

NEW DEVELOPMENTS IN POSITRON ANNIHILATION SPECTROSCOPY
TECHNIQUES: FROM EXPERIMENTAL SETUPS TO ADVANCED PROCESSING
SOFTWARE

Petr Stepanov

A Dissertation

Submitted to the Graduate College of Bowling Green
State University in partial fulfillment of
the requirements for the degree of

DOCTOR OF PHILOSOPHY

April 2020

Committee:

Farida Selim, Advisor

Ellen Gorsevski,
Graduate Faculty Representative

Alexander Tarnovsky

Mikhail Zamkov

Copyright ©April 2020

Petr Stepanov

All rights reserved

ABSTRACT

Farida Selim, Advisor

Fully-digital Coincidence Doppler broadening (CDB) spectrometer with a software coincidence unit and energy resolution function of 1.2 keV at 511 keV is assembled at Bowling Green State University. A computer program – TLIST Processor – that fits and subtracts background on the two-dimensional energy spectrum and exports CDB spectrum is developed. Another program (SW Calculator) that performs deconvolution of the CDB spectrum into different contributions (e^+ annihilation on conduction band, valence and core electrons, para-Ps annihilation in pores) is developed. Program evaluates S and W parameters of the CDB spectra and allows calculation of the Fermi energy for simple metals.

Experimental spectra of pure and well annealed Al, Fe, Cu and Zn samples are measured and processed with a help of the developed software. The obtained values of the Fermi energies and binding energies of core electrons are in a good agreement with the reference values for the investigated metals. This result validates the correct operation of the CDB setup.

Tuning of electronic circuits and optimization of geometry of the detection unit of the conventional analog lifetime (LT) spectrometer were performed annually. Three e^+ sources were manufactured from aqueous solution of $^{22}\text{NaCl}$. A convenient technology that allows sealing the activity in between of thin Kapton foils is suggested. New computer software RooPositron that allows processing the lifetime spectra is developed. Program accounts on a type of the studied materials (metals, powders, liquids) and positron reactions therein. The advantage of the program is ability to integrate custom fitting models with meaningful physical parameters that describe e^+ behavior in the studied medium.

LT spectra acquired at different recording time intervals and CDB spectra of Al_2O_3 nanopowders (0.05, 0.3, 1 and 3 μm) were measured and interpreted by means of the RooPositron software. It was shown that consistent interpretation of the data is possible when thermalization process of the “hot” Ps atom in the intercrystalline space in nanopowders is taken into

account. Kinetics of the Ps thermalization is essentially non-exponential, but the developed software is able to proceed with this.

More detailed model of the Ps formation in liquids is suggested. It takes into account formation of the intermediate/transient Ps state, the quasifree positronium, which further transforms into the Ps bubble state. It provides reasonable explanation of the deviation of I_1/I_3 ratio from the value of 1/3 when conventional 3-exponential decomposition of the LT spectra is applied. It also explains the “juvenile broadening” effect observable in ACAR experiments. Interpretation of the LT spectra in water, i-octane, c-hexane and i-propanol with a help of the developed RooPositron program allowed to obtain the reaction rate constants of the Ps oxidation and Ps ortho-para conversion in these liquids with various concentrations of dissolved O₂.

All the program code developed in current research is publicly available.

This dissertation is dedicated to my dad Serge and my mom Anna whose love, support and encouragement have inspired me to pursue and complete my research.

"Life is like riding a bicycle. To keep your balance you must keep moving."

– Albert Einstein

ACKNOWLEDGMENTS

First I would like to thank my committee members Mikhail Zamkov, Aleksander Tarnovskiy, and Ellen Gorsevski.

I would like to express my deepest gratitude to people that assisted me to achieve success in this study. Without these people this dissertation would not exist.

My advisor Dr. Farida Selim, who provided me an opportunity to join her research group and continue my scientific career. I'm very thankful to my advisor for providing guidance and financial support and encouragement along the way.

A very special thanks to my dad Sergey who contributed a lot of his time and efforts in this work. Thanks for visiting and spending your vacation time here in our research lab at BGSU as Research Collaborator three years in a row. Thanks to my mom for coming out here with my day, providing support and cooking best Russian pancakes and pierogi.

Thanks for my girlfriend Heather Kish for helping me in tough moments of depression and providing support and hope for the better future.

Last but not least I want to thank my fellow classmates and students from our research group that made the school feel like home and brought a lot of fun and excitement.

Table of Contents

	Page
Introduction and background	2
Aims and tasks	5
Chapter 1 Brief review of basis of e^+e^- annihilation	9
1.1 Discovery of the e^+ . Two-photon annihilation of e^+e^- pair	9
1.2 Observable values: annihilation rates and electron momentum distribution .	12
1.3 Energy and momentum conservation laws for two-photon annihilation . .	15
1.4 Positronium and hydrogen atoms	19
1.5 Positronium in a constant magnetic field	23
1.6 Relative contact density in the Ps atom	26
Chapter 2 Examples of calculation of 2γ -annihilation rates and momentum distributions	29
2.1 Annihilation of the para-positronium in vacuum	29
2.2 Pick-off annihilation of the ortho-positronium	30
2.3 Annihilation of quasi-free positrons in metals	33
Chapter 3 Positron sources and experimental methods of PAS	39
3.1 e^+ sources	39
3.2 Positron Annihilation Lifetime Spectroscopy (PALS)	41
3.3 Angular Correlation of Annihilation Radiation (ACAR)	45
3.4 Doppler Broadening of Annihilation Radiation (DBAR)	48
3.5 Coincidence Doppler Broadening Spectroscopy (CDB)	50
3.6 Assembling of the CDB setup and developing new routine for processing two-dimensional CDB spectra	56
3.7 Brief conclusion on this chapter	68
Chapter 4 Positron trapping models	69
4.1 Standard trapping model (one type of the defects)	70

	viii	
4.2	Standard trapping model (two types of the defects)	75
4.3	Diffusion trapping model	76
4.4	Formation of “hot” Ps in intergrain space in nanopowders and its subsequent thermalization	78
4.5	Brief conclusion on this chapter	85
Chapter 5	Interaction of Ps with dissolved oxygen in liquids	87
5.1	Experimental	89
5.2	Ortho-para conversion and oxidation of Ps in the presence of dissolved O ₂ .	90
5.3	Concentrations of dissolved O ₂ in the studied liquids	97
5.4	Determination of the Ps-O ₂ reaction rate constants	97
5.5	Processing of the spectra through a model taking into account the formation of qf-Ps	100
5.6	Brief conclusion on this chapter	104
Chapter 6	Development of the software for processing of LT and CDB spectra . .	106
6.1	ROOT installation on macOS and Linux	108
6.1.1	Install from a precompiled binary	109
6.1.2	Compile libraries from source	110
6.2	ROOT installation on Windows 10	111
6.2.1	Setup of the Windows Subsystem for Linux	112
6.3	CERN ROOT GNU Makefile structure	114
6.3.1	Specifying Dictionary entries in LinkDef.h	115
6.3.2	Dictionary generation	116
6.3.3	Compiling the shared library	117
6.3.4	Compiling source code files	117
6.3.5	Linking	117
6.4	Makefile targets	118

6.5	Makefile syntax	119
6.6	Setting up an IDE for a CERN ROOT project with existing Makefile	129
6.6.1	Installing Eclipse	130
6.6.2	Increasing Eclipse heap	130
6.6.3	Configuring the Eclipse Build Environment	131
6.6.4	Importing existing ROOT project	131
6.6.5	Setting headers search path	131
6.6.6	Adding ROOT source files	132
6.6.7	Creating Build Configurations	133
6.6.8	Setting Launch Configuration	134
6.7	Model View architecture	135
6.7.1	Simple MVP implementation in CERN ROOT GUI	138
6.8	RooPositron program	155
6.8.1	Installation	155
6.8.2	How to start the fit	156
6.8.3	Integrated fitting models	159
6.8.4	How to adjust model fitting parameters	160
6.8.5	How to implement a custom fitting Model	160
6.8.6	How to contribute	163
Summary		164
References		167
The simplest view on γ -spectroscopy		180
Making positron sources from $^{22}\text{NaCl}$ aqueous solution		187
Adjustment and tuning of the Positron Annihilation Lifetime Setup		193

.1	Choice of the appropriate high voltage (HV) for Hamamatsu H3177 photo-multipliers (PMTs)	193
.2	Measurements of the amplitude spectra	194
.3	Calibration of the Time-to-Amplitude Converter (TAC)	195
.4	Determination of the source correction and parameters of the resolution function	196
.5	Final tuning of the LT setup	198
	Calculation of the positron flux towards the grain boundary	200
	Calculation of expressions $a \sum_{n=1}^{\infty} \exp(-an^2)$ and $\frac{6}{\pi^2} \sum_{n=1}^{\infty} \frac{\exp(-an^2)}{n^2}$	204
	Thermalization kinetics of the positronium atom due to its collisions with crystallites and molecules of air in the intergrain space	206
	Positron annihilation in Al_2O_3 nanopowders of a different dispersion	208
	Experimental guide for the Coincidence Doppler Broadening Spectrometer	216
.6	Coincidence Doppler spectrometer setup	217
.6.1	High purity Germanium detectors	218
.6.2	Lynx Multichannel Analyzers	219
.6.3	Observing the coincidence count rate	220
.7	Geometry of the experiment	220
.8	Initial configuration	223
.8.1	Setting up the device Friendly Names	223
.8.2	Getting started with the ProSpect software	224
.8.3	Clearing the analyzer error status	225
.8.4	Ramping the voltage	225
.8.5	Timing signal shape adjustment	226
.8.6	Analyzer calibration	227
.9	Setting discriminator levels	229

.10 Two-dimensional energy spectrum acquisition	230
.10.1 Hard drive requirements for spectrum acquisition	230
.10.2 Setting up the Prospect with separate physical drive	231
.10.3 Acquisition in TLIST mode	232

Список иллюстраций

Figure	Page
1.1 Observation of the positron in a Wilson chamber (1993). Saturated steam condenses on the track ions produced by a flying charged particle. The chamber was built by prof. R.A. Milliken and C. Anderson. The magnetic field applied in the chamber was 15 kG. The dark line in the middle is a 6 mm lead plate. A thin dashed curved line going from the bottom up is the positron track. According to the authors' interpretation, the track on the bottom belongs to a 63 MeV positron. After crossing the plate positron's energy is equal to 23 MeV [20].	9
1.2 Feynman diagram of the two-photon annihilation of the electron-positron pair.	10
1.3 Annihilation of the e^+e^- pair when momentum of the center of mass is zero (left, like in e^+e^- collider) and non-zero (right).	14
1.4 Momentum conservation during the two-photon annihilation of the e^+e^- pair. The momentum of the thermalized positron is much less compared to the momentum of the electron \mathbf{p}_e that participates in the annihilation. \mathbf{p}_1 and \mathbf{p}_2 – momentums of the annihilation photons.	16
1.5 The energy region on a two-dimensional energy spectrum that contain CDB events is highlighted with yellow. E_1 и E_2 are the registered energies of the photons. I is the ionization potential of the core electrons.	19
1.6 Example of the two-dimensional spectrum of aluminum. The region for the CDB events is selected according to 1.24). Namely $ E_2 - E_1 < 25$ keV and -3.5 keV $< E_1 + E_2 - 2mc^2 < 1.9$ keV.	20
1.7 Martin Deutsch (1917–2002) in his laboratory at the Massachusetts Institute of Technology (c. 1952) with a pair of early scintillation counters of the type used in the discovery of positronium (1951). “There was nothing in life that he didn't want to understand” [news.mit.edu/2002/deutsch].	21

1.8	Comparison of the parameters of H-atom and positronium	22
1.9	The Breit-Rabi diagram for the Ps: dependence of the energy levels of the singlet and triplet states vs. magnitude of the external magnetic field. Here, the energy axes is presented in the units of the Ps hyperfine splitting, $\Delta E = 8.4 \cdot 10^{-4}$ eV. This quantity is taken as the unit of energy [27]	27
2.1	The Tao-Eldrup Ps bubble model (Ps in liquids). Ps is located in an infinitely deep spherically symmetric potential well of radius $R_\infty = R + \delta$. $\Psi(r)$ is its center-of-mass wave function. R is the free-volume radius of the bubble. δ is the typical penetration depth of valence electrons into the bubble. P_R is the overlapping area of the positron wave function and the electron density of surrounding molecules.	32
2.2	Dependence of the Ps pick-off annihilation rate vs. surface tension in different liquids. The solid curve illustrates the Tao-Eldrup formula for the optimal value of the parameter $\delta = 1.66$ Å. The dashed curve is an approximate relation $\lambda_{po} \propto \sigma^{1/2}$	33
2.3	Contributions to CDB spectrum from the simplest e^- wave functions considered here: 1 – Eq. (2.17), 2 – (2.19) and 3 – (2.21). All the functions are normalized on 1 at $\delta = 0$	38
3.1	Scheme of the nuclear transformations of ^{22}Na and ^{44}Ti	40
3.2	Scheme of the PAL spectrometer: Sc – scintillator, PMT – photomultiplier, CFDD – constant fraction differential discriminator. Energies of the “start” and “stop” photons correspond to the ^{22}Na -based positron source.	42

3.3 An example of a LT annihilation spectrum of positrons measured in pure water at room temperature [35]. The solid lines show deconvolution of the spectrum into three exponential components: $I_1 = 25.2 \%$, $\tau_1 = 194(2)$ ps, $I_2 = 49.3(4) \%$, $\tau_2 = 0.42(1)$ ns and $I_3 = 25.5(3) \%$, $\tau_3 = 1.80(1)$ ns. The source correction was 13% (in this experiment the ^{44}Ti positron source was used, activity was welded into a $10 \mu\text{m}$ titanium foil). Contribution from e^+ annihilation in the source was also represented by three exponents.	44
3.4 Scheme of 1D-ACAR setup (1D = one dimensional; ACAR = angular correlation of annihilation radiation). The left arm is movable and the right one is fixed.	45
3.5 Left: angular distributions of annihilation photons in metals (Zn, Mn) [36]. The spectra are decomposed into a sum of the parabolic and Gaussian components. The insets show the angular resolution functions.	47
3.6 Схема позитронного спектрометра для измерения доплеровских спектров аннигиляционных фотонов (DBAR – Doppler Broadening of Annihilation Radiation).	48
3.7 Left: CDB spectrum in aluminum [37]. Right: Momentum dependence of the ratio of e^+ annihilation events on impurity atoms to the number of e^+ annihilations on electrons in pure Al [P.Asoka-Kumar et al., 1997].	51
3.8 Dependence of the Doppler shift of the peak of the annihilation photons in n-hexane vs. applied electric field [38, 39].	54
3.9 Scheme of the Doppler spectrometer built in Idaho accelerated center. Hard γ -radiation is generated as a result of the retardation of 6 MeV electrons in a tungsten target [40].	55

3.10 Left: γ -spectrum from Pb sample, measured by HPGe detector. On a bell-like Compton background one may see X-ray lines from Pb fluorescence at 75 keV, annihilation line at 511 keV and well known line emmitid after e-capture of ^{40}K nuclei. Right: LT spectrum in Pb obtained, obtained as a result of the time-base scanning of the 511-peak shown in the left figure.	55
3.11 Scheme of the digital Doppler coincidence spectrometer.	56
3.12 To the determination of the energy resolution of the CDB setup at about 500 keV.	58
3.13 γ -lines of the nearest to the 511-line isotopes (Ba-133 and Cs-137). Upper lines measures by the detector No 1; bottom lines – detector No 2.	59
3.14 Asymmetry of the photopeak absorption line (511-line in metallic Al).	60
3.15 To the approximation of the γ -line of Cs-137.	62
3.16 TLIST Processor application fits and subtracts background from the two-dimensional CDB energy spectrum. Ridge profile for $E > 511$ keV (area “C”) consists of contribution from Compton scattered 1.27 MeV photons, pile-up effect and in-flight annihilation. At $E < 511$ keV (area “B”) there are a number of processes discussed in the text. Left: convoluted and fitted background is represented by the overlay mash. Right: events from the yellow band of a width $1022 \text{ keV} - E_b - 2\delta < E_1 + E_2 < 1022 \text{ keV} + 2\delta$ are selected to construct final single-dimensional CDB spectrum. Here E_b stands for the typical binding energy of core electrons in Al and 2δ is the energy resolution of both γ -detectors.	63
3.17 Contribution of the background events to the experimental CDB spectrum. .	64
3.18 Doppler spectra of simple metals deconvoluted into a set of contributions of annihilation on Fermi gas electrons (inverted parabola) and Gaussian components. Contribution from annihilation in positron source is subtracted from spectra. Convolution with the energy resolution function of 1.2 keV FWHM is applied.	67

4.1	Potentials for e^+ and e^- in a crystal lattice.	69
4.2	Scheme of e^+ annihilation in a metal when there is only one type of the defects, capable to trap positrons.	71
4.3	Formation of different positron states in Al_2O_3 nanopowders.	79
5.1	The parameters of 3-exponential deconvolution of the LT spectra in cyclohexane, isooctane, isopropanol and water before and during their bubbling with argon, oxygen and air at room temperature. The lifetime of the shortest (τ_1) component was a “common free” parameter for each stage of the gas bubbling.	96
5.2	Dependencies of λ_o (data taken from Tab. 5.1) vs. concentration of dissolved oxygen in different liquids. Solid lines – Eq. (5.19).	99
5.3	The linear dependence of the rate constants $k_{\text{Ps}+\text{O}_2}$ of the Ps reaction with dissolved oxygen in different liquids vs. the inverse viscosity, $1/\eta$ Eq. (5.20). Black circles ● are taken from [71]; red symbols ▲, ■ – from Tab. 5.2 and 5.3. All the data correspond to room temperature.	99
5.4	Screenshots of the RooPositron software [17] depicting series of spectra fitted with a model derived from equations (5.1)-(5.4).	101
5.5	The effect of the presence of O_2 on the shape of lifetime annihilation spectra in cyclohexane. Blue – blowing argon, black – blowing with air, red – blowing oxygen. Source contribution and background are subtracted from the spectra. The spectra are normalized to 10^6 counts.	103
6.1	Specificity of building a ROOT based C++ program.	114
6.2	Diagram of the Makefile targets and file locations for the production version of the application. Files involved in a certain Makefile target are enclosed in horizontal rows. Arrows denote the move operations.	119

6.3	Diagram of the Makefile targets and corresponding file locations for the development version of the application. Files infolvwd in a certain Makefile target reside in the horizontal rows. Solid arrows denote move operations. Dashed arrows represent relative shared library search path for the executable.	120
6.4	Setting Eclipse build environment variables on Linux. On macOS use DYLD_LIBRARY_PATH and LD_LIBRARY_PATH on Linux.	131
6.5	Importing project with Makefile on Linux	132
6.6	Specifying the search path for ROOT headers	132
6.7	Adding ROOT source files to the project	133
6.8	Setting up Eclipse build configurations	134
6.9	Run and Debug configurations	135
6.10	Model-View architectural patterns. Solid lines represent function calls. Dashed lines stand for interactions defined by Publisher-Subscriber pattern [113].	137
6.11	Diagram of the signals and function calls of the root-mvp-gui program. It illustrates a trivial implementation of the MVP pattern within the ROOT framework. Source code is available on GitHub.	139
6.12	Editing fitting parameter values and limits in plain text editor.	160
13	γ -spectrum and the decay scheme of Cs-137. This isotope emits photons with $E_\gamma = 662$ keV. In green we have shown the background γ -spectrum in our laboratory.	183
14	Position of the γ -source and the lead shielding of the sensitive volume of the HPGe γ -detector.	183
15	Dependencies of cross-sections of the photoelectric effect, Compton effect and pair production vs. energy of the incident γ -quanta irradiated metallic copper.	184

16	γ -spectrum of K-40 and its decay scheme. Since the energy of the emitted photons is quite high (1460 keV), the pair production process is possible. Single-escape and double-escape peaks are located to the left of the photopeak on 511 and 1022 keV, respectively. The characteristic Compton edge is at $E_e^{max} = 1243$ keV and the backscattering peak is at $E_{BS} = E_\gamma - E_e^{max} = 1460 - 1243 = 217$ keV [Idaho National Laboratory “Gamma-ray Spectrum Catalogue” https://gammaray.inl.gov/SiteAssets/catalogs/ge/pdf/k40.pdf] .	185
17	γ -spectrum and the decay scheme of ^{22}Na . As a result of β^+ -decay an excited state of ^{22}Ne is formed. Within 3.7 ps it emits 1.274 MeV quantum and goes to the ground state. Annihilation of positrons leads to formation of 511 keV γ -quanta. Both these lines and other peculiarities at $E_e^{max} = 1062$ keV, $E_{BS} = E_\gamma - E_e^{max} = 1274 - 1062 = 212$ keV are seen on the spectrum. The γ -background in our laboratory is shown in green.	186
18	Shipping invoice for aqueous solution of radioactive $^{22}\text{NaCl}$ salt.	187
19	Dose rate at 10 cm distance far from the vial with $^{22}\text{NaCl}$	188
20	Typical count rate from the original vial with radioactive salt $^{22}\text{NaCl}$	188
21	Punching the kapton tape and attaching 8 μm kapton film to the double-side kapton tape.	190
22	Dropping water into a vial with ^{22}Na activity.	190
23	Dropping $^{22}\text{NaCl}$ aqueous solution on the Kapton film.	191
24	Ready-to-use ^{22}Na positron source.	192

25	Left: Anode signals from the Detector 1 (s/n BA 1773; see signals on the channel No.1, upper curves). This detector is supposed to be the START detector, because its signals are somewhat lower then that for the Detector 2. Right: Anode signals from the Detector 2 (s/n BA 1739; see signals on the channel No.2, lower curves). This detector is supposed to be the STOP detector, because its signals are higher then that from the Detector 1.	193
26	Anode and dynode signals from both detectors (D1 -- channels 1, 2; D2 -- channels 3 and 4).	194
27	Amplitude spectra from the START and STOP detectors. All spectra were measured with the CFDD external delay cable =25 cm.	195
28	Time calibration of TAC (June 19, 2019). Duration of 1 MCA channel is 6.176 ps.	196
29	LT spectrum of well-annealed iron (reference sample).	197
30	Measuring of the dose rate from the e^+ sources for LT (left) and CDB (right) experiments.	197
31	The LT spectrum of the defect-free Al.	199
32	Diffusion of a positron towards a grain boundary.	200
33	Approximations of the sums $a \sum_{n=1}^{\infty} \exp(-an^2)$ and $\frac{6}{\pi^2} \sum_{n=1}^{\infty} \frac{\exp(-an^2)}{n^2}$ at different a	205
34	SEM images of the investigated Al_2O_3 powders (left to right: 50 nm, 300 nm, 1 μm and 3 μm).	211
35	CDB spectrum of a Al_2O_3 powder (50 nm powder size) deconvoluted into gaussian components. The most narrow component (3rd gauss) corresponds to annihilation of the p-Ps atoms.	212
36	Coincidence Doppler spectrometer setup diagram.	217

37	Cross section of a coaxial Ge detector.	218
38	Coincidence Doppler spectrometer setup diagram.	220
39	Doppler spectrometer setup at Farida Selim lab at BGSU. (a, b) positioning the sample with respect to the detectors' orientation with the help of the pointer; (c) two-detector experiment setup; correct horizontal alignment of the detectors is asserted with the help of bubble levels	222
40	Assigning a unique Friendly Name for the Lynx analyzer.	224
41	Connecting to Lynx Analyzers in ProSpect application.	225
42	Clearing the device fault in the ProSpect application.	226
43	Ramping voltage on the preamplifiers.	227
44	Screenshot of the ProSpect calibration interface displaying spectrum and cal- ibration points.	228
45	Specifying axis binning for two-dimensional energy spectrum.	233

Список таблиц

Table	Page
3.1 β^+ -isotopes used in the e^+ sources	39
3.2 Obtained values of the Fermi energies and electron binding energies (wave functions approximated by Gaussians). Experimental values for the Fermi energy (a) are taken from ref. [49]. Theoretical electron binding energies (b) are taken from ref. [50]. Integration ranges (in keV) for S and W parameters were following: S [-1.6, 1.6] and for W [-11.52,-5.52] and [5.52, 11.52].	66
5.1 Parameters of the 3-exponential decomposition of the LT spectra of the initially aerated isoctane, cyclohexane, isopropanol and water, and also after their bubbling with argon, oxygen and air at room temperature. τ_1 is considered as a “common free” parameter for each gas bubbling. Statistical uncertainties of the fitting parameters are indicated in parenthesis.	98
5.2 Values of the Ostwald coefficients $c_{O_2}^{(L)}/c_{O_2}^{(G)}$, concentrations of O_2 in liquids after their bubbling with oxygen and air at room temperature ($20\text{ }^\circ\text{C}$) and pressure 1 atm. Values of k_{Ps+O_2} and λ_{po} were obtained by fitting the data shown in Fig. 5.2, using Eq. (5.19).	98
5.3 Parameters of the model Eqs. (5.5-5.10) obtained as a result of fitting of the LT spectra of liquids with different O_2 contents, $\lambda_{qf} = \lambda_+$, $\lambda_b = 20\text{ ns}^{-1}$, $\lambda_{2\gamma} = 1/0.16\text{ ns}^{-1}$ (in accordance with the magnetic quenching experiments [77,78]), $\tau_+ = 1/\lambda_+$, $\tau_{po} = 1/\lambda_{po}$. Statistical uncertainties of the fitting parameters are indicated in parenthesis.	103
6.2 List of fitting models supported by RooPositron	161
3 The Compton-edge energies and energies of backscattered photons for some γ -emitters, calculated according to Eqs. (3)-(4).	181

4	Results of fitting of LT and CDB spectra of Al ₂ O ₃ powders.	214
5	List of radioactive isotopes and their photon energies used for calibration. . .	227
6	Binning properties of analyzers to be used in TLIST Data Scanner application.	230

List of Abbreviations:

ACAR	– Angular Correlation of Annihilation Radiation
BGSU	– Bowling Green State University
CFDD	– Constant Fraction of Annihilation Radiation
DBAR	– Doppler Broadening of Annihilation Radiation
DTM	– Diffusion Trapping Model
CDB	– Coincidence Doppler Broadening
CDBAR	– Coincidence Doppler Broadening of Annihilation Radiation
CFDD	– Constant Fraction Differential Discriminator
HPGe	– High purity Germanium
HV	– High Voltage
LT	– lifetime
MCA	– MultiChannel Analyzer
PAS, PALS	– Positron Annihilation (Lifetime) Spectroscopy
PMT	– Photo Multiplier Tube
Ps, p-Ps, o-Ps	– positronium; para-, ortho-positronium
qf	– quasi-free
SEM	– Scanning Electron Microscopy
STM	– Standard Trapping Model
TAC	– Time-to-Amplitude Converter
cps	– counts per second

Introduction and background

Over the past few decades, positron annihilation spectroscopy (PAS) has found use in numerous applications in condensed matter physics. More specifically, PAS has been used in studies of radiation physics [1, 2], chemistry [3–5], radiobiology and medicine [6, 68, 69]. There are even several elegant PAS experiments that test fundamental principles of quantum electrodynamics [9, 10].

Essence of the PAS method is following. Positrons (e^+) are either implanted into the studied samples by fast sub-nanosecond pulses or produced via pair-production when sample is positioned next to the high-energy gamma target. The latter approach is the simplest. Subsequent annihilation radiation is registration. Throughout its lifetime in a substance positron can experience one or many different changes of its state.

Initially, a positron created from a β^+ -decay is produced with a high kinetic energy, typically on the order of 0.1-1 MeV. Following implantation into a target material, within a timespan of about 1 ps, the positron rapidly loses its kinetic energy. Due to the acts of ionization and electronic excitation positron becomes thermalized with its surroundings. In polar liquids positrons end up in solvated state. In materials with crystal structure positron can become bounded in point defects. Formation of the positron-molecular or positron-ionic complexes is also possible. Additionally, a thermalized positron in a dielectric media may form a positronium atom (Ps) – a chemically-active bound state of an e^+e^- pair, which is essentially the lightest analog of the hydrogen atom. In a molecular gas the positron can become temporarily attached to a molecule via Feshbach resonances. It can then either be

ejected as the molecule de-excites or can annihilate while attached [11]. If the positrons are present in sufficient density, they can form Ps_2 in the pores of a dielectric material [12]. Several polyelectron Ps^- and Ps^+ ions can be formed that are routinely used in experiments [13].

It is important that in every particular state mentioned above the positron sends specific “signals” reflected in the energy and momentum of the annihilation radiation. By registering the energy of the annihilation radiation and measuring the lifetime of the positron in the material we can identify the nature of the e^+ states.

Due to the fact that the vacancy type point defects in materials lack repulsive positively charged cores that make up the lattice, majority of them become a trap for the positrons. Positron lifetime in a defect is longer due to the lower electron density of the surrounding. Therefore a positively charged positron is a probe of the vacancy-type defects. Application of PAS provides possibilities to study the following processes in materials: creation and accumulation of vacancies under the influence of various types of radiation; annealing and aging of defects in construction materials (steels, alloys, semiconductors and polymeric materials); estimating the concentration of point-defects.

Doppler positron spectroscopy studies the momentum of pairs of annihilation γ -quanta. Parameters of Doppler annihilation spectra are related to the electronic structure of the annihilation sites of the positron. It is possible to identify physical and chemical properties of the material at the annihilation sites. Parameters of the annihilation spectra are sensitive to chemical composition, temperature, pressure, and presence of external electric and magnetic fields.

It is essential that PAS is non-destructive technique. The energy of a positron or annihilation gamma quanta is not enough to move an atom out of the lattice in solids. It is possible to utilize the same samples in subsequent experiments involving different characterization methods.

Common sources of positron radiation, are: ^{22}Na isotope that provides positrons with energies up to 0.54 MeV with the mean of 0.22 MeV; ^{44}Ti with e^+ energies less than 1.47

MeV is widely used in PAS experiments in liquids; ^{18}F with a short half-life time of 109 minutes is used in medicine and radiobiological experiments.

In non-conductive media positrons form tracks – arrays of ion-electron pairs distributed along the trajectory of a positron, also known as spurs. When positron energy drops to about 500 eV its energy loss approaches the Bragg peak and positron trajectory becomes non-linear. The terminal part of the positron track is named the blob. It is a large “cloud”, consisting of 20-40 ion-electron pairs. When the positron becomes thermalized, it may form a bound state with one of the intratrack electrons and create a Ps atom. Usually Ps formation occurs either within the e^+ blob, or in its nearest vicinity. Both e^+ and Ps atoms may “explore” the positron blob and potentially participate in chemical reactions therein with other radiolytic products produced by the “hot” e^+ during its slowdown. Therefore, PAS can be a convenient tool for studies of radiation-chemical processes in the positron track, giving supplementary information about radiation chemistry, usually obtained in pulsed radiolysis experiments.

Porosity experiments involving the Ps atom were held for a number of decades. The Ps atom gained the status of a probe of a “free volume” in solid molecular media, particularly in polymers. Ps atoms have a preference to localize in nanometer sized pores and voids. This effect occurs due to: 1) the exchange repulsion of the Ps electron from the surrounding molecular electrons and 2) e^+ Coulomb repulsion from nuclei of the atoms. Furthermore, once within a network, the confinement energy of these channels will result in the thermal Ps becoming trapped within larger pores. Ps is unable to re-enter narrower channels – it does not have sufficient energy to overcome the barrier.

In liquid media, Ps usually forms a nanobubble around itself (or the “Ps bubble”). We shall see that the ortho-Ps lifetime strongly depends on the distance to the nearest (to Ps) molecular electrons. Therefore, measuring its lifetime, researchers can estimate the size of nanopores (free volume elements) in material. This is important for understanding the structure of polymers and amorphous, glassy and porous media.

Despite of the successful application of PAS in the above studies, the PAS experiments

face some significant challenges. The conventional analog positron spectrometer is composed from fast timing electronic components that often need precise tuning. This requires experience in nanosecond electronics and understanding of nuclear physics of the experiment. Recently the digital positron spectrometers appeared on the market. Digital processing of the signals leads to significant improve in timing resolution of spectrometers. However, they come with their own challenges. Digital spectrometers require experience with digital signal processing and development of the software. Fortunately, the application of PAS becomes more accessible as some manufacturers now offer “all-in-one” systems. These hardware components are paired with software that is sufficient for the simplest processing of annihilation spectra [14].

The rise of experimental capabilities of PAS has stimulated the development of its theoretical basis. Theoretical models describing e^+ behavior in various media and conditions have been developed and published in literature [1–5]. Nevertheless their usage is hindered because of a lack of appropriate user-friendly software, which allows to obtain physically meaningful parameters from raw experimental data. In some cases, an elaboration of more adequate models is still required.

Current research goals are aimed at two problems. At first, we contributed to the development of the theoretical models that describe e^+ and Ps kinetics in various media. Secondly, we developed a number of open-source software that allows application of the above models for processing of the registered lifetime and Doppler-broadening annihilation spectra [?, ?, 17].

Aims and tasks

My research at BGSU during 2014-2020 consisted of carrying out some theoretical studies in positron spectroscopy field as well as working with lifetime and Doppler positron experimental setups and writing corresponding software products.

At first, we assembled and fine-tuned the digital Doppler broadening spectrometer, which measures the energy spectra of annihilation photons in the coincidence mode (Coincidence Doppler Broadening – CDB). The spectrometer is assembled from two high-purity Ge detec-

tors operating at 4.5 kV and a pair of Lynx multichannel analyzers manufactured by Mirion Technologies (former Canberra Industries). Each analyzer supports up to 32768 channels which corresponds to a channel width of about 60 eV. The energy resolution of the detectors is 1.3 keV at 0.5 MeV.

My responsibilities were following: wiring up the components and setting up the communication between the devices; ensuring the transmission of the signals from germanium γ -detectors to the energy analyzers; calibration of the analyzers' energy scale; resolving technical software and hardware issues; setting up acquisition in two-detector coincidence time-stamp mode – registering pair of annihilation photons, which deposit energy in both detectors simultaneously.

A number of software programs were developed to allow the interpretation of the Doppler positron experimental spectra. First program TLIST Processor [15] imports two-dimensional Doppler energy spectrum, subtracts the background and exports the conventional single-dimensional CDB spectrum.

Another program SW Calculator [16] imports the CDB spectrum, calculates the S and W line shape parameters and evaluates energies of the core and valence electrons as well as the Fermi energy in metals.

Along with the digital Doppler spectrometer we carried out the lifetime experiments with conventional analog positron annihilation lifetime spectrometer. The apparatus consists of two Hamamatsu H3177 γ -quanta photomultipliers equipped with BaF₂ scintillators. Signal processing is performed by the ORTEC fast-timing electronic units: pair of discriminators (583), time-delay box (DB463), time-to-amplitude converter (567) and multichannel analyzer (926). The routine maintenance that includes optimization, adjustments, diagnostics and replacement of the analog components was performed. The quality of the experimental spectra were considerably improved by tuning the geometry of the experiment.

The essential part of the positron annihilation experiments is fabricating the radioactive sources. In this research we made a number of e⁺ sources from aqueous solution of a ra-

dioactive salt $^{22}\text{NaCl}$. The solution of activity of $100 \mu\text{Ci}$ (3.7 MBq) was obtained from the PerkinElmer supplier. Radioactive solution was deposited on a Kapton foil of a thickness of $8 \mu\text{m}$. In order to preserve the small diameter of the radioactive area in the source, a set of iterative depositions followed by the drying cycle was performed. A syringe of a volume of $10 \mu\text{L}$ was used to deposit a single drop of the radioactive solution at a time. After the desired amount of radioactive $^{22}\text{NaCl}$ salt was deposited and dried on the Kapton film, the source was sealed by another Kapton foil of a same thickness. In order to connect the Kapton foils together a doule-sided Kapton tape with silicon adhesive on the each side (MIL-P-46112 Type I) was used. Thickness of the tape is $25 \mu\text{m}$. The glue residue on each side is $38 \mu\text{m}$ thick. In total we made three e^+ sources following the above technique. All of the sources were used in the PAS experiments in this research carried out in the F. Selim laboratory at BGSU.

Additionally, the improvements to the sample holder mechanism for precise positioning of the positron source and studied samples assembly in both CDB and lifetime (LT) spectrometers were introduced.

A significant part of current research is related to fitting and interpretation of raw annihilation spectra. Unfortunately there was no positron lifetime spectra fitting software that allows integration of the custom fitting models. Therefore, the new software for fitting of raw experimental positron lifetime spectra is developed [17].

The processing of the LT spectra is often narrowed to their deconvolution into a set of two or three exponential decays. In conductive materials, these exponential decays are associated either with positron annihilation in an “ideal” crystal lattice (in a bulk of the crystal), or with annihilation of e^+ , trapped in the positronophilic defects. In dielectric media, where Ps formation is possible, these exponents are also associated with annihilation of para- and ortho-Ps atoms.

The simplest multi-exponential deconvolution of the LT spectra is not always fair from the viewpoint of physics. Annihilation kinetics turns out to be more complicated, especially

when e^+ is involved in diffusion processes, such as: reaching and trapping of e^+ at the grain boundaries; Ps diffusion towards micelles in solutions. Nonexponential kinetics also takes place when epithermal Ps thermalizes in nanopowders (in intergrain space). Moreover, in molecular media it is necessary to consider Ps formation process in more details. It is important to account that Ps localization in a nanobubble or nanopore does not happen instantly, but takes certain time. Ignorance of these intermediate states and effects lead to incorrect spectra interpretation and the obtained results.

In order to resolve these problems the RooPositron computer program is developed [17]. It supports experimental spectra fitting with conventional multi-exponential, standard trapping and diffusion-trapping models, and allows implementation of the custom parameterized decay models.

Two models for fitting the lifetime spectra of liquids, molecular media and nanopowders are formulated and included in the RooPositron software.

Chapter 1 Brief review of basis of e^+e^- annihilation

1.1 Discovery of the e^+ . Two-photon annihilation of e^+e^- pair

The existence of a positron – a particle having a mass and spin of an electron but with an opposite charge – was predicted by P.A.M Dirac in 1930 [19]. It was a first anti-particle that was predicted theoretically. Positron is lepton – a pure elementary particle. It is described by the Fermi-Dirac statistics and it participates in three types of interactions (gravitational, electromagnetic, and weak) excluding the strong one. Positron itself is a stable particle but when it collides with an electron, the annihilation happens. Two or more γ -quanta are produced. The total rest energy of the positron-electron pair is transferred into the energy of the annihilation photons.

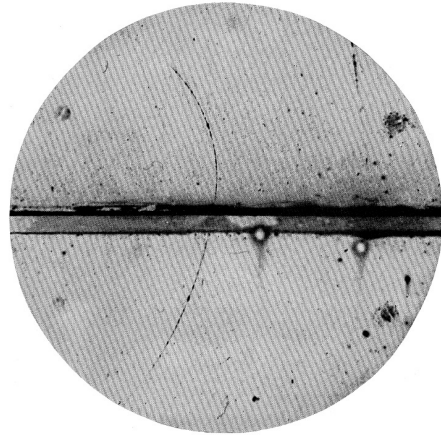


Fig. 1.1 Observation of the positron in a Wilson chamber (1933). Saturated steam condenses on the track ions produced by a flying charged particle. The chamber was built by prof. R.A. Milliken and C. Anderson. The magnetic field applied in the chamber was 15 kG. The dark line in the middle is a 6 mm lead plate. A thin dashed curved line going from the bottom up is the positron track. According to the authors' interpretation, the track on the bottom belongs to a 63 MeV positron. After crossing the plate positron's energy is equal to 23 MeV [20].

Three years later Carl Anderson discovered positrons while analyzing the tracks of cosmic

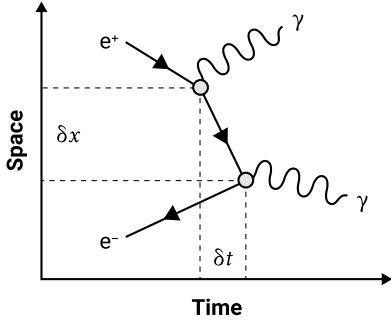


Fig. 1.2 Feynman diagram of the two-photon annihilation of the electron-positron pair.

rays in a Wilson chamber [20] (Fig. 1.1). Observation of two tracks with the same starting point and curved in opposite directions in magnetic field speaks for the birth of a new particle.

In the majority of cases in condensed matter positron and electron annihilate into two photons. Generally speaking the number of produced gamma-quanta is arbitrary and governed by the conservation laws:

$$e^+ + e^- \rightarrow n\gamma, \quad n = 0, 1, 2, \dots \quad (1.1)$$

Annihilation that emits one quanta requires existence of a third object. For instance, a nucleus of a mass M that receives part of momentum.

In condensed matter two-photon annihilation takes the least amount of time. Two photons is a minimum number that does not require existence of a third object. Three-photon annihilation is a much slower process.

The process of two-photon annihilation of the electron and positron on a Feynmann diagram (Fig. 1.2)

$$e^+ + e^- \rightarrow 2\gamma \quad (1.2)$$

consists of two stages: a particle (say, positron) emits a photon and transforms into a virtual positron that travels towards the electron. During a certain moment of time δt a photon with energy mc^2 , electron and virtual positron exist together. After the virtual e^+ reaches

the electron, they transform into a photon. The value of the δt can be estimated from the uncertainty principle ($\delta x \cdot \delta p \sim \hbar/2$):

$$\delta t \sim \frac{\hbar}{mc^2}, \quad \frac{\hbar}{mc^2} = 1.32 \cdot 10^{-21} \text{ s.} \quad (1.3)$$

The virtual particle (a signal, annihilation notification) travels with the speed of light. Therefore we can estimate the size of the annihilation area:

$$\delta x \sim c\delta t \sim \frac{\hbar}{mc}, \quad \frac{\hbar}{mc} = 3.86 \cdot 10^{-11} \text{ cm.} \quad (1.4)$$

Notice that the value of a Compton electron wavelength is $2\pi\hbar/mc = 2.4 \cdot 10^{-10}$ cm. The linear size of the annihilation area \hbar/mc is three orders of magnitude smaller than the typical atomic size. The annihilation duration δt is four orders of magnitude smaller than the period of rotation of an electron around the Bohr orbit, $a_B/\alpha c \sim 2.4 \cdot 10^{-17}$ s (here $\alpha = e^2/\hbar c = 1/137$). Thereby it is rather correct to speak of the annihilation process happening “instantly” at a certain “point of space”.

In quantum electrodynamics the two-gamma annihilation cross section of a non-relativistic positron with an electron of opposite spin orientation (the sum of the spins of e^- and e^+ should be 0) is [21]:

$$\sigma_{2\gamma} = 4\pi r_0^2 \frac{c}{v}. \quad (1.5)$$

Here $r_0 = e^2/mc^2 = 2.8 \cdot 10^{-13}$ cm is the classical radius of the electron, m – mass, e – elementary charge, v – relative speed of the positron with respect to the electron. v is equal to the speed of the positron when its energy is much greater than the energy of the electrons of the media.

Three-photon annihilation is about 1000 times slower compared to 2γ -annihilation.

1.2 Observable values: annihilation rates and electron momentum distribution

Typically the experimentally measured value is not the annihilation cross-section, but the corresponding annihilation rate. In a simple case it is given by following expression:

$$\lambda_{2\gamma} = \sigma_{2\gamma} v n_e = 4\pi r_0^2 c n_e, \quad (1.6)$$

where n_e is the contact density – the density of electrons in the vicinity of the positron (averaged within the positron spatial distribution). Only electrons of the opposite spin to the e^+ contribute significantly into the equation. It is assumed that electrons are stationary; a fast positron with velocity v flies through electrons.

A hot positron injected into a material loses the bulk of its energy by ionizing the atoms it encounters. Eventually it becomes a thermal particle. Typical time of the ionization slow down is 10 ps. When the positron no longer has sufficient kinetic energy to cause ionization, it continues to thermalize towards a thermal energy of about $kT \sim 1/40$ eV. Thermalization takes less than 1 ps.

Apparently a positron located inside a studied material at a room temperature can annihilate with electrons of a different momentum $\mathbf{p} = m\mathbf{v}$ (or wave vectors $\mathbf{k} = \mathbf{p}/\hbar$). Therefore in formula (1.6) the n_e must be replaced by an average (with the function $n(\mathbf{k})$) over the wave vectors of all electrons:

$$\lambda_{2\gamma} = \pi r_0^2 c \int n(\mathbf{k}) \frac{d^3 k}{(2\pi)^3}. \quad (1.7)$$

Strictly speaking here $\mathbf{p} = \hbar\mathbf{k}$ is the momentum of e^+e^- pair at a time moment of annihilation (the momentum of the center-of-mass of the pair). Just this quantity is converted to the momentum of the pair of annihilation photons at annihilation (Fig. 1.3). However, if the positron is thermalized, \mathbf{p} is actually reduced to the momentum of the electron.

Note that there might be a number of favorable localization spots for the e^+ – vacancies,

dislocations, grain boundaries. These areas can have different electron density and different momentum distribution $n(\mathbf{k})$. That is why PAS is very sensitive to the presence of the structural defects in the studied samples.

In multi-electron media only a 1/4 of all electrons form a singlet state with a positron (total spin 0) and therefore, annihilate into two photons. The rest 3/4 of all electrons form triplet state with total spin $1 \cdot \hbar$. The triplet state has a much longer lifetime (in this particular case – infinitely longer) and annihilates into an odd number of photons. Since in equation (1.5) the function $n(\mathbf{k})$ provides momentum distribution of all electrons in the media but we want to consider only two-gamma annihilation, we intentionally divided Eq. (1.7) by 4.

The normalization of the $n(\mathbf{k})$ function is following. Its integral across all \mathbf{k} in (1.7) gives the concentration of electrons in the medium:

$$\int n(\mathbf{k}) \frac{d^3 k}{(2\pi)^3} = n_e. \quad (1.8)$$

In order to understand the relation between $n(\mathbf{k})$ and the electron's wavefunctions we shall remind the following. According to quantum mechanics, the momentum distribution of the particle is determined by the square of the Fourier transform of its wave function in the coordinate space. So in order to calculate $n(\mathbf{k})$ we must decompose the e^+e^- wavefunction into plain waves $\exp(-i\mathbf{k}(\mathbf{r}_+ + \mathbf{r}_-)/2)$ (which correspond to its propagation with the total momentum $\hbar\mathbf{k}$). Then the correspondent coefficient squared gives the annihilation probability with the given momentum. We must also take into account that annihilation of an electron and positron pair can only happen when their spatial coordinates match. We will address this further using the Dirac delta-function $\delta(\mathbf{r}_+ - \mathbf{r}_-)$. All these lead to the following correlation between $n(\mathbf{k})$ and the wave function $\Psi_{+-}(\mathbf{r}_+, \mathbf{r}_-)$ of the annihilating electron-positron pair:

$$n(\mathbf{k}) = \left| \int \Psi_{+-}(\mathbf{r}_+, \mathbf{r}_-) \delta^3(\mathbf{r}_+ - \mathbf{r}_-) e^{i\mathbf{k}(\mathbf{r}_++\mathbf{r}_-)/2} \cdot d^3 r_+ d^3 r_- \right|^2 = \left| \int \Psi_{+-}(\mathbf{r}, \mathbf{r}) \cdot e^{i\mathbf{k}\mathbf{r}} d^3 r \right|^2, \quad (1.9)$$

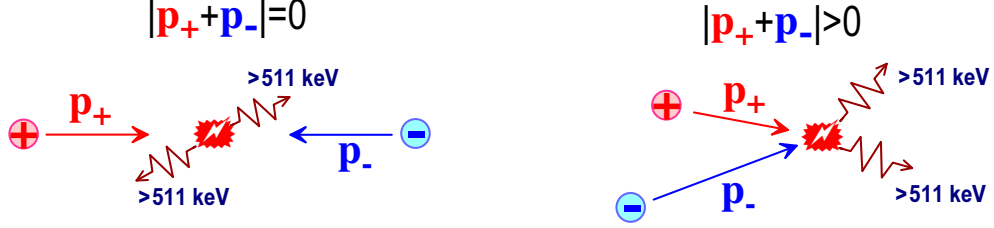


Fig. 1.3 Annihilation of the e^+e^- pair when momentum of the center of mass is zero (left, like in e^+e^- collider) and non-zero (right).

$$\iint |\Psi_{+-}(\mathbf{r}_+, \mathbf{r}_-)|^2 d^3 r_+ d^3 r_- = 1.$$

If a positron is surrounded by a large number of electrons, the above expression has to account for the contributions from all electrons that the positron can annihilate with. Within the approximation of non-interacting particles Ψ_{+-} becomes a product of separate wave functions:

$$\Psi_+(\mathbf{r}_+) \cdot \prod_{\mu=1}^N \Phi_\mu(\mathbf{r}_\mu).$$

Here $\Phi_\mu(\mathbf{r}_\mu)$ is the wavefunction of a nearest electron in state μ . Taking into account the spin factors the electron part of the wave function should be anti-symmetric with respect to the possible electron rearrangements. Additionally the correlation factor $\gamma(\mathbf{k})$ that stands for the attraction of the positron and electron should be accounted for.

The contribution to the momentum distribution of the e^+e^- pair from annihilation on the μ electron is given by:

$$\int \Psi_+(\mathbf{r}_+) \Phi_\mu(\mathbf{r}_\mu) \delta^3(\mathbf{r}_+ - \mathbf{r}_\mu) e^{i\mathbf{k}(\mathbf{r}_++\mathbf{r}_\mu)/2} \cdot d^3 r_+ d^3 r_\mu = \int \Psi_+(\mathbf{r}) \Phi_\mu(\mathbf{r}) e^{i\mathbf{k}\mathbf{r}} d^3 r.$$

Taking a sum of contributions of all electrons that can annihilate with the positron, we obtain $n(\mathbf{k})$:

$$n(\mathbf{k}) \approx \sum_{\mu=1}^N \left| \int \Psi_+(\mathbf{r}) \Phi_\mu(\mathbf{r}) e^{i\mathbf{k}\mathbf{r}} d^3 r \right|^2. \quad (1.10)$$

To obtain the 2 γ -annihilation rate we integrate $n(\mathbf{k})$ by variable $d^3 k$. We will use the

expression (1.9)):

$$\begin{aligned}
\int n(\mathbf{k}) \frac{d^3 k}{(2\pi)^3} &= \int \frac{d^3 k}{(2\pi)^3} \left| \int \Psi_{+-}(\mathbf{r}, \mathbf{r}) \cdot e^{i\mathbf{kr}} d^3 r \right|^2 = \\
&= \int \frac{d^3 k}{(2\pi)^3} \int \Psi_{+-}^*(\mathbf{r}', \mathbf{r}') e^{-i\mathbf{kr}'} d^3 r' \cdot \int \Psi_{+-}(\mathbf{r}, \mathbf{r}) e^{i\mathbf{kr}} d^3 r = \\
&= \int \int \Psi_{+-}^*(\mathbf{r}, \mathbf{r}) \Psi_{+-}(\mathbf{r}', \mathbf{r}') d^3 r d^3 r' \cdot \int e^{i\mathbf{k}(\mathbf{r}-\mathbf{r}')} \frac{d^3 k}{(2\pi)^3} = \int |\Psi_{+-}(\mathbf{r}, \mathbf{r})|^2 d^3 r. \quad (1.11)
\end{aligned}$$

Here we used standard integral representation of the delta-function:

$$\int e^{i\mathbf{k}(\mathbf{r}-\mathbf{r}')} \frac{d^3 k}{(2\pi)^3} = \delta^3(\mathbf{r} - \mathbf{r}').$$

Therefore the 2γ -annihilation rate (1.7) becomes:

$$\lambda_{2\gamma} = \pi r_0^2 c \int n(\mathbf{k}) \frac{d^3 k}{(2\pi)^3} = \pi r_0^2 c \int |\Psi_{+-}(\mathbf{r}, \mathbf{r})|^2 d^3 r. \quad (1.12)$$

If we integrate the expression (1.10) by $d^3 k$ we will obtain:

$$\lambda_{2\gamma} = \pi r_0^2 c \sum_\mu \int d^3 \mathbf{r} |\Psi_+(\mathbf{r})|^2 |\Phi_\mu(\mathbf{r})|^2. \quad (1.13)$$

Next we will consider some examples of calculation of $n(\mathbf{k})$ and $\lambda_{2\gamma}$ for p-Ps annihilation, pick-off annihilation of the o-Ps and e^+ annihilation with the “free” electrons in metals.

1.3 Energy and momentum conservation laws for two-photon annihilation

During the annihilation process following terms must be conserved: energy-mass, momentum, angular momentum and spin. Let's consider the annihilation of the e^+e^- pair into two photons. We will consider the positron to be thermalized. We will neglect the positron kinetic energy because it is rather small, about $k_B T$, at room temperature $k_B T \approx 1/40$ eV. Additionally we will take the energies of polarization and coulomb interaction out of scope.

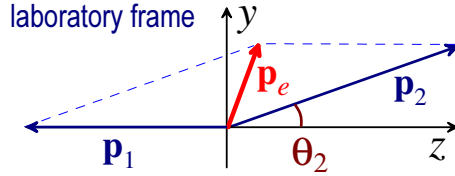


Fig. 1.4 Momentum conservation during the two-photon annihilation of the e^+e^- pair. The momentum of the thermalized positron is much less compared to the momentum of the electron \mathbf{p}_e that participates in the annihilation. \mathbf{p}_1 and \mathbf{p}_2 – momentums of the annihilation photons.

Then the energy and momentum conservation laws look like:

$$mc^2 + \sqrt{m^2c^4 + c^2p_e^2} - U_e = cp_1 + cp_2, \quad \mathbf{p}_e = \mathbf{p}_1 + \mathbf{p}_2, \quad \mathbf{p}_e = \frac{m\mathbf{v}_e}{\sqrt{1 - v_e^2/c^2}}. \quad (1.14)$$

Here U_e is potential energy of an electron in the atom (taken to be a positive value), $E_1 = cp_1$ and $E_2 = cp_2$ – energies of the annihilation photons, v_e - the speed of an electron in non-relativistic approximation $\sqrt{m^2c^4 + c^2p_e^2} = \frac{mc^2}{\sqrt{1-v_e^2/c^2}} \rightarrow mc^2 + p_e^2/2m$, and $E_b = |p_e^2/2m - U_e|$ is the binding energy of an electron in the atom.

In case of two-photon annihilation we can always select the plane YZ to be lined up with the trajectories of the annihilating photons (see Fig. 1.4). Then

$$\text{energy conservation : } 2mc^2 + p_e^2/2m - E_b = cp_1 + cp_2, \quad (1.15)$$

$$\text{z-projection : } p_{ez} = -p_1 + p_{2z}, \quad (1.16)$$

$$\text{y-projection : } p_{ey} = p_{2y}. \quad (1.17)$$

If the momentum of the electron is assumed to be given (p_{ey} , p_{ez}) then the desired value will be the momenta of the annihilation photons: p_1 and (p_{2y}, p_{2z}) . In the particular case when $p_e = 0$, the photons are emitted strictly in opposite directions along the z axis. Moreover, to within the binding energy of the electron in the atom $cp_1 = cp_2 = mc^2$.

Taking into account $p_2^2 = p_{2y}^2 + p_{2z}^2$ we can exclude p_{2y} from the energy conservation law.

Next we obtain the equation for the desired value p_{2z} from (1.14):

$$2mc^2 - E_b = c(p_{2z} - p_{ez}) + c\sqrt{p_{ey}^2 + p_{2z}^2}.$$

Squaring this equation and collecting similar terms together, we obtain:

$$p_{2z} = \frac{2mc - E_b/c + p_{2z}}{2} - \frac{cp_{ey}^2}{2(2mc - E_b/c + p_{2z})}.$$

We can neglect the last term as $p_{ez} \gg p_{ey}^2/2mc$. This gives:

$$p_{2z} = mc - \frac{E_b}{2c} + \frac{p_{2z}}{2}.$$

On the other hand, equations (1.16) and (1.17) give:

$$p_1 = p_{2z} - p_{ez} = mc - \frac{E_b}{2c} - \frac{p_{2z}}{2}, \quad p_{2y} = p_{ey}. \quad (1.18)$$

Thus we obtain the momentum of the second photon:

$$p_2^2 = p_{2z}^2 + p_{2y}^2 \Rightarrow p_2 \approx mc - \frac{E_b}{2c} + \frac{p_{ez}}{2}. \quad (1.19)$$

It is easy to obtain the expression for the θ_2 angle to the first order approximation of v/c . This angle is measured in the angular correlation experiments.

$$\theta_2 \approx \frac{p_{2y}}{p_2} \approx \frac{p_{ey}}{mc}. \quad (1.20)$$

In one-dimensional Doppler experiments, the measured value is the energy of one of the annihilation photons, $cp_2 \approx mc^2 + cp_{ez}/2$. In two-dimensional coincident experiments both

photon energies are registered: $E_1 = cp_1$ and $E_2 = cp_2$. From (1.18) and (1.19) we obtain:

$$E_2 - E_1 = cp_2 - cp_1 \approx cp_{ez} \approx \sqrt{2mc^2I/3}. \quad (1.21)$$

Here as a rough estimate we took $\frac{p_{ez}^2}{2m} \approx \frac{1}{3} \cdot \frac{p_e^2}{2m} \approx \frac{I}{3}$, where I is the ionization potential (minimum energy required to remove the valence electron).

Then the difference in the energies $E_2 - E_1$ can vary in a certain interval depending on which electron was involved in the annihilation. For instance, for Fe $I = 10$ eV to 7 keV and the energy interval is -49 keV to 49 keV.

On the other hand the sum energy of the annihilation photons is given by the energy conservation law. If we calculate the binding energy in the atom as $E_b = |U_e| - \frac{p_e^2}{2m}$ and assume that it is equal to the ionization potential $I = E_b$ of the same e^- , we will obtain:

$$c(p_1 + p_2) = 2mc^2 - I.$$

We can estimate the size of the area of interest on the two-dimensional E_1, E_2 diagram. The annihilation events that contribute into the CDB (Coincident Doppler Broadening) spectrum reside within this area. The conditions that define the area are following:

$$|E_2 - E_1| < \sqrt{2mc^2I/3}, \quad 2mc^2 - I < E_1 + E_2 < 2mc^2 \quad (1.22)$$

It turns out that the desired region of interest is represented on the E_1, E_2 spectrum by a narrow region of the experimental data (see Fig.1.5). The area of the region must be increased somewhat to account for the finite energy resolution of the detectors. Namely, each border along the axis should be broadened by the sum of the energy resolutions of the two detectors.

$$|E_2 - E_1| < \sqrt{2mc^2I/3} + 2\delta, \quad -I - 2\delta < E_1 + E_2 - 2mc^2 < 2\delta. \quad (1.23)$$

For example, the ionization potential of the inner K-electrons for aluminum is 1.56 keV [22].

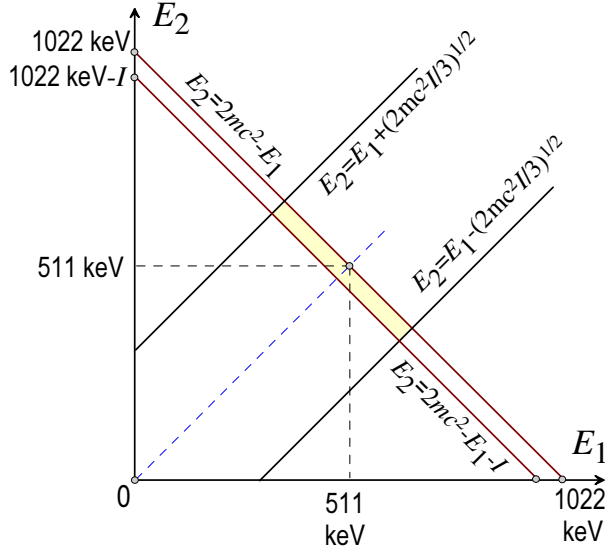


Fig. 1.5 The energy region on a two-dimensional energy spectrum that contain CDB events is highlighted with yellow. E_1 и E_2 are the registered energies of the photons. I is the ionization potential of the core electrons.

Then the desired region for the events for CDB spectrum is following (Fig. 1.6):

$$|E_2 - E_1| < 25 \text{ keV}, \quad -3.5 \text{ keV} < E_1 + E_2 - 2mc^2 < 1.9 \text{ keV}. \quad (1.24)$$

Acquisition and interpretation of the γ -spectra is not a trivial procedure. It is important to shield the detectors from the background radiation, maintain clean radiochemical environment in the laboratory. Correct calibration of the detectors with reference samples' should be carried out: peaks can have uneven Compton background on each side. There is specificity of interaction of the γ -quanta with the active detector volume. These questions are addressed in the Appendix 6.8.6.

1.4 Positronium and hydrogen atoms

In vacuum, in gases, as well as in non-conducting condensed matter, a positron and an electron can form an electrically neutral atomic-like bound state called positronium (chemical symbol Ps). The possibility of its existence was pointed out by Stepan Mokhorovich in 1934, shortly after the discovery of the positron. However, experimental confirmation of this prediction was obtained by Martin Deutsch only in 1951 in experiments on positron slowing down in gases [23, 24], Fig. 1.7.

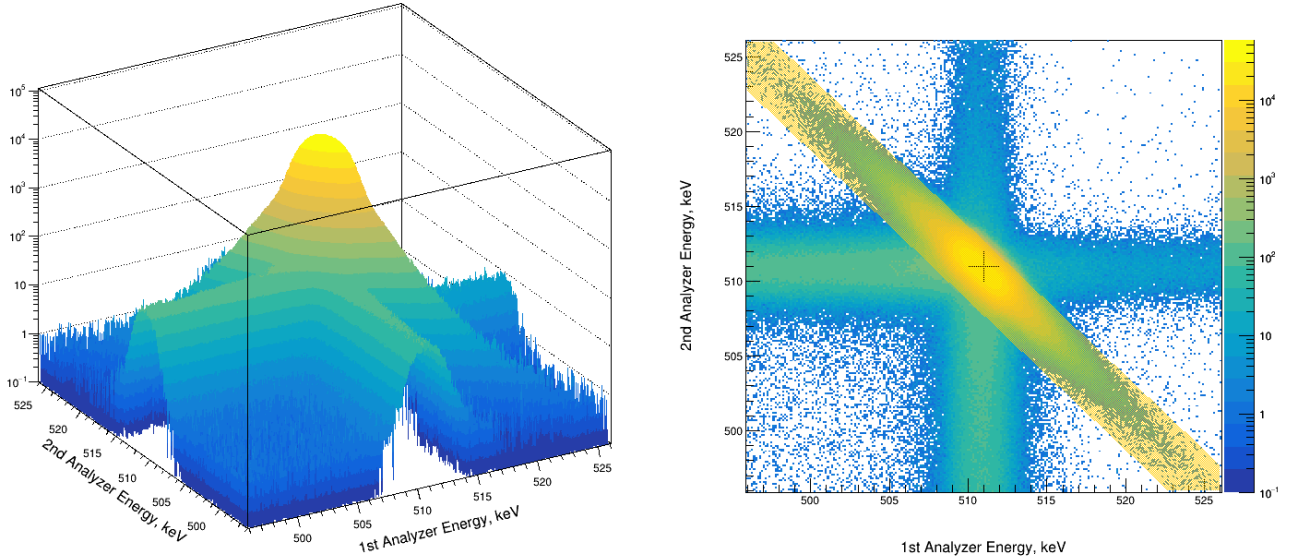


Fig. 1.6 Example of the two-dimensional spectrum of aluminum. The region for the CDB events is selected according to 1.24). Namely $|E_2 - E_1| < 25$ keV and -3.5 keV $< E_1 + E_2 - 2mc^2 < 1.9$ keV.

The mass of a Ps atom, to good approximation, is equal to twice the the electron mass 1022 keV/ c^2 . Strictly speaking, the e^- mass is $510.998950(1)$ keV/ c^2 , therefore $2m_e = 1021.9979$ keV/ c^2 . In vacuum, the Ps mass, m_{Ps} should be less by 6.8 eV/ c^2 . However, it is not practical to experimentally observe this difference yet.

The Schrödinger equation, which describes in nonrelativistic approximation the relative motion of e^+ and e^- in the Ps atom, after separation of the variable center of mass Ps, takes the following form:

$$\left(-\frac{\hbar^2}{2\mu m} \nabla^2 - \frac{e^2}{\varepsilon r} \right) \psi^{\text{Ps}}(\mathbf{r}) = E^{\text{Ps}} \psi^{\text{Ps}}(\mathbf{r}) \quad (1.25)$$

It is similar to the equation for the hydrogen atom. The difference lies only in the value of the reduced mass factor, μ , which is $1/2$ for Ps, and $\mu \approx 1$ for H. For more generality, we added the dielectric permittivity constant ε of the medium, to the term describing Coulombic attraction of the particles.

If we compare Eq. (1.25) with the usual equation for the H-atom, we see that μ just renor-

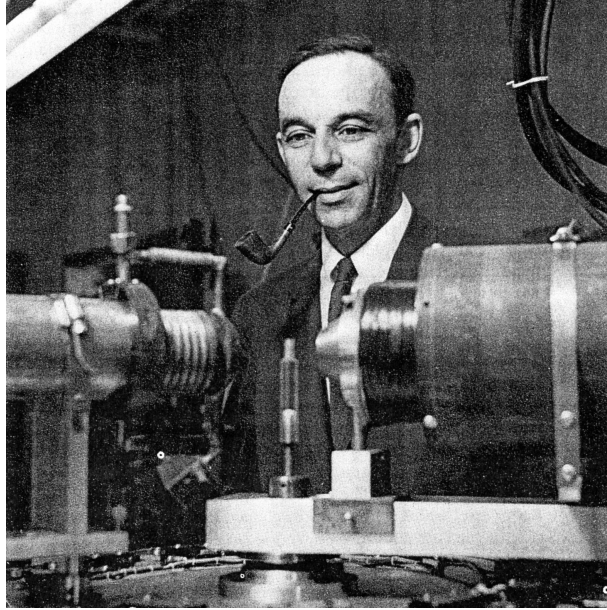


Fig. 1.7 Martin Deutsch (1917–2002) in his laboratory at the Massachusetts Institute of Technology (c. 1952) with a pair of early scintillation counters of the type used in the discovery of positronium (1951). “There was nothing in life that he didn’t want to understand” [news.mit.edu/2002/deutsch].

malizes the mass $m \rightarrow \mu m$, and ε renormalizes the square of the electric charge $e^2 \rightarrow e^2/\varepsilon$. After scaling transformation of the spatial variable, Eq. (1.25) reduces to the Schrödinger equation for $\mu = 1$, that is just the H-atom problem. Thus, the wave functions and energy levels for the atom Ps can be written similarly to the functions and levels of H:

$$\psi_{nlm}^{\text{Ps}}(\mathbf{r}) = \psi_{nlm}^{\text{H}}\left(\frac{\mu \mathbf{r}}{\varepsilon a_B}\right), \quad E_{nlm}^{\text{Ps}} \approx E_{nlm}^{\text{H}}/2, \quad (1.26)$$

where $a_B = \hbar^2/me^2 \approx 0.53 \text{ \AA}$ is the Bohr radius. It follows from Eq. (1.26) that in vacuum all the Ps bound states (1s, 2s, 2p, ...) are bound with half the energy of the corresponding states in H. For the Ps ground state

$$\psi_{100}^{\text{Ps}}(r) = \frac{1}{\sqrt{8\pi\varepsilon^3 a_B^3}} \exp\left(-\frac{r}{2\varepsilon a_B}\right) \quad (1.27)$$

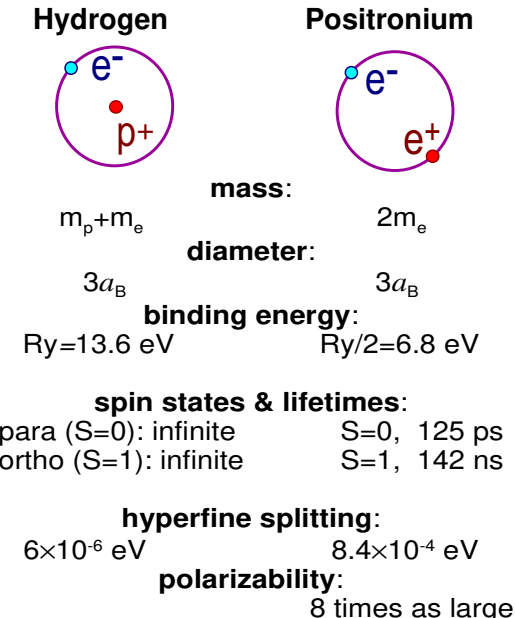


Fig. 1.8 Comparison of the parameters of H-atom and positronium

where the average value of the relative e^+e^- coordinate r is

$$\langle \psi_{100}^{\text{Ps}} | \mathbf{r} | \psi_{100}^{\text{Ps}} \rangle = \frac{3\epsilon}{2\mu} a_B \Rightarrow 3a_B \text{ (Ps in vacuum).}$$

This means that the $\langle \mathbf{r} \rangle$ for the Ps atom in vacuum is twice as large as that of the H atom. Note that $\langle \mathbf{r} \rangle$ represents Ps diameter, but in case of the hydrogen atom this value is actually its radius. Thus, the linear sizes of both atoms are same [18].

Similar to hydrogen, the Ps atom has two spin states – singlet (parapositronium, p-Ps) and triplet (orthopositronium, o-Ps). In orthopositronium, the vector sum of the spin of the e^+ and e^- is equal to 1, whereas in parapositronium the net spin is zero. The difference in the energies of these states is associated with the interaction of the magnetic moments of the positron and electron. It is called the energy of the hyperfine splitting. In the 1s-state, it is $203.4 \text{ GHz} = 0.8418 \text{ meV}$. Parapositronium (being in s-states) annihilates into even number of γ -rays, and orthopositronium – into an odd number of photons. Therefore, p-Ps decays mainly into two gammas, but o-Ps – into three. In the next section, based on Eq. (1.7), we

will show that in vacuum the p-Ps lifetime in the ground state is 125.2 ps. The lifetime of o-Ps is almost 1000 times longer – 142.0 ns.

The situation differs if Ps resides in a medium, but not in vacuum. The observed o-Ps lifetime decreases significantly. Here the lifetime is dictated by the pick-off annihilation, where the e^+ annihilates with one of the nearby electrons of the medium. Annihilation of the positron, which is a part of the ortho-Ps, most likely occurs not with its own electron, but with one of the electrons in the medium, that has a spin direction opposite to that of the positron. Prompt $2\gamma e^+e^-$ annihilation is possible in this case. This process is called pick-off annihilation. For para-Ps, the pick-off process is not so important, because the positron in para-Ps can annihilate into two gammas with its own electron within ~ 0.1 ns.

1.5 Positronium in a constant magnetic field

In the previous section, the Schrodinger equation was written for a e^+e^- pair (or Ps atom) in the nonrelativistic approximation (1.25). Taking account of the magnetic field effects requires a more rigorous approach, since magnetism is essentially of a relativistic nature. It should be based on the relativistic Dirac equation. In the case of low velocities (in the first order in v^2/c^2), it reduces to the Breit equation (G. Breit, 1929). The correct derivation of this equation for the electron+positron system was proposed by L.D. Landau and V.B. Berestetskiy in 1949 [25]. The Breit Hamiltonian contains many terms (kinetic, Coulomb, spin-orbit, spin-spin terms, contact interactions etc.). It is beyond of the scope of this work to detail the expressions for each of these terms. In particular, basing on this equation, one can calculate the energy difference of the triplet spin state and the singlet state: $\Delta E \approx 7\alpha^4 mc^2/12 = 8.41 \cdot 10^{-4}$ eV (hyperfine energy splitting, $\alpha = 1/137$). In the nonrelativistic limit, Eq. (1.25) is obtained from the Breit equation. The following term of the Breit Hamiltonian describes interaction of e^+e^- pair with a constant external magnetic field B (the field is directed along the z axis):

$$\mathcal{H}_B = -\hat{\mu}\hat{B} = \frac{e}{mc}B(\hat{s}_{ze} - \hat{s}_{zp}). \quad (1.28)$$

Here $\hat{\mu}$ is the operator of the magnetic moment of the pair, and the spin operators \hat{s}_{ze} and \hat{s}_{zp} (in essence, they are just the Pauli matrices) have the following properties (for the positron and electron, respectively) [26]:

$$\hat{s}_z |\uparrow\rangle = \frac{\hbar}{2} |\uparrow\rangle, \quad \hat{s}_z |\downarrow\rangle = -\frac{\hbar}{2} |\downarrow\rangle, \quad \hat{s}_z = \frac{\hbar}{2} \begin{pmatrix} 1 & 0 \\ 0 & -1 \end{pmatrix}, \quad |\uparrow\rangle = \begin{pmatrix} 1 \\ 0 \end{pmatrix}, \quad |\downarrow\rangle = \begin{pmatrix} 0 \\ 1 \end{pmatrix}. \quad (1.29)$$

The arrows $|\uparrow\rangle$ and $|\downarrow\rangle$ mean that the spin of the particle (electron or positron) is either directed up ($m_s = \frac{1}{2}$), or down ($m_s = -\frac{1}{2}$).

The wave function (1.26) of the Ps atom, including the spin part, can be written as

$$\psi_{nlm}^{\text{Ps}}(\mathbf{r}) \chi_{\mathbf{SM}_s}(\sigma), \quad (1.30)$$

where n , l and m are the spatial atomic quantum numbers of the pair, and S and M_s are its spin numbers (full spin and its projection onto the quantization axis). In the absence of a magnetic field, the spin states of e^+e^- pairs are characterized by a definite total spin S and its projection onto the z axis:

$$\begin{aligned} \chi_{00} &= \frac{|\uparrow_e\rangle|\downarrow_p\rangle - |\downarrow_e\rangle|\uparrow_p\rangle}{\sqrt{2}}, \\ \chi_{11} &= |\uparrow_e\rangle|\uparrow_p\rangle, \quad \chi_{10} = \frac{|\uparrow_e\rangle|\downarrow_p\rangle + |\downarrow_e\rangle|\uparrow_p\rangle}{\sqrt{2}}, \quad \chi_{1,-1} = |\downarrow_e\rangle|\downarrow_p\rangle. \end{aligned} \quad (1.31)$$

It is easy to check that all these states are orthogonal and normalized, i.e. $\langle \chi_{00} | \chi_{00} \rangle = 1$, $\langle \chi_{00} | \chi_{10} \rangle = 0$ and so on.

However, not all of these states remain eigenstates, when a e^+e^- pair interacts with an external permanent magnetic field B . Using these rules, it is easy to prove that

$$(\hat{s}_{ze} - \hat{s}_{zp}) \chi_{00} = \hbar \chi_{10}, \quad \mathcal{H}_B \chi_{00} = \mu_B B \chi_{10},$$

$$(\hat{s}_{ze} - \hat{s}_{zp})\chi_{11} = 0, \quad \mathcal{H}_B\chi_{11} = 0,$$

$$(\hat{s}_{ze} - \hat{s}_{zp})\chi_{10} = \hbar\chi_{00}, \quad \mathcal{H}_B\chi_{10} = \mu_B B\chi_{00},$$

$$(\hat{s}_{ze} - \hat{s}_{zp})\chi_{1,-1} = 0, \quad \mathcal{H}_B\chi_{1,-1} = 0, \quad (1.32)$$

where $\mu_B = \frac{e\hbar}{2mc}$ is the Bohr magneton. Thus, the magnetic field mixes the states χ_{00} and χ_{10} , which now are not the eigenstates of the Hamiltonian (1.28). A magnetic field does not disturb the states with collinear spins, because in this case the total magnetic moment is zero (magnetic moments of e^+ and e^- cancel out each other).

Let us find the eigenfunctions and eigenvalues of the Hamiltonian $\mathcal{H}_0 + \mathcal{H}_B$ (\mathcal{H}_0 is the Hamiltonian of the e^+e^- pair in the absence of magnetic field), choosing suitable linear combinations of the initial states χ_{00} and χ_{10} :

$$\tilde{\chi}_{00} = a\chi_{10} - \sqrt{1-a^2}\chi_{00}, \quad \tilde{\chi}_{10} = \sqrt{1-a^2}\chi_{10} + a\chi_{00}. \quad (1.33)$$

Here, the orthonormality of the new states is automatically taken into account: $\langle \tilde{\chi}_{00} | \tilde{\chi}_{00} \rangle = \langle \tilde{\chi}_{10} | \tilde{\chi}_{10} \rangle = 1$, $\langle \tilde{\chi}_{00} | \tilde{\chi}_{10} \rangle = 0$. Strictly speaking, these states are no longer characterized by certain values of the total spin of the pair and its projection on the z -axis. But if we consider the parameter a to be small (which actually takes place at typical values of magnetic fields achievable under laboratory conditions), then each of the new linear combinations will still be dominated by one of the wave functions: χ_{00} or χ_{10} . Therefore, we store indexes 00 and 10 at $\tilde{\chi}_{00}$ and $\tilde{\chi}_{10}$. So, let us act on these functions by the hamiltonian $\mathcal{H}_0 + \mathcal{H}_B$:

$$(\mathcal{H}_0 + \mathcal{H}_B)\tilde{\chi}_{00} = \tilde{E}_{00}\tilde{\chi}_{00}, \quad (\mathcal{H}_0 + \mathcal{H}_B)\tilde{\chi}_{10} = \tilde{E}_{10}\tilde{\chi}_{10}, \quad (1.34)$$

$$\mathcal{H}_0\chi_{00} = E_{00}\chi_{00}, \quad \mathcal{H}_0\chi_{10} = E_{10}\chi_{10}, \quad \Delta E = E_{10} - E_{00}.$$

Here \tilde{E}_{00} and \tilde{E}_{10} are the magnetic energy terms of the new states $\tilde{\chi}_{00}$ and $\tilde{\chi}_{10}$, ΔE is the hyperfine splitting in the positronium atom in vacuum without a magnetic field. In Eqs.

(1.34) we collect together and equate to zero the sum of all the coefficients at χ_{00} and χ_{10} , respectively. As a result, we obtain the following relations:

$$\frac{\Delta E}{\mu_B B} = \frac{1 - 2a^2}{a\sqrt{1 - a^2}}, \quad \tilde{E}_{00} = E_{00} - \frac{a\mu_B B}{\sqrt{1 - a^2}}, \quad \tilde{E}_{10} = E_{10} + \frac{a\mu_B B}{\sqrt{1 - a^2}}. \quad (1.35)$$

From the first relation we obtain the quadratic equation on a^2 :

$$y^2(1 - 2a^2)^2 = a^2(1 - a^2), \quad y = \frac{\mu_B B}{\Delta E} \approx \frac{B, \text{ kG}}{145.3}, \quad \mu_B = 5.79 \cdot 10^{-9} \text{ eV/G}.$$

From here it follows, that

$$a^2 = \frac{1}{2} \left(1 - \frac{1}{\sqrt{1 + 4y^2}} \right) \stackrel{y \ll 1}{\approx} y^2.$$

Dependence of the energy levels of the Ps singlet and triplet states vs. magnitude of the external magnetic field is shown in Fig. 1.9. As we have mentioned above, energy levels of the states $\chi_{1,1}$ and $\chi_{1,-1}$ do not change in the presence of the magnetic field. Moreover, because the magnetic field does not affect these states, they will annihilate into three photons as before. So annihilation rates of the states $\tilde{\chi}_{00}$ and $\tilde{\chi}_{10}$ will be proportional to the corresponding partial contributions of the states with a certain spin (χ_{00} and $\chi_{1,0}$):

$$\lambda^{\tilde{\chi}_{00}}(B) = (1 - a^2)\lambda_{2\gamma}^{\text{p-Ps}} + a^2\lambda_{3\gamma}^{\text{o-Ps}},$$

$$\lambda^{\tilde{\chi}_{10}}(B) = (1 - a^2)\lambda_{3\gamma}^{\text{o-Ps}} + a^2\lambda_{2\gamma}^{\text{p-Ps}}, \quad (1.36)$$

where $\lambda_{2\gamma}^{\text{p-Ps}}$ and $\lambda_{3\gamma}^{\text{o-Ps}}$ are the annihilation rates of para- and orthopositronium in the absence of the field. Therefore, these states can annihilate into two or three photons as well.

1.6 Relative contact density in the Ps atom

If the Ps atom resides in a medium, its wave function obviously differs from its wave function in vacuum. In this case, the Ps annihilation rate is determined by the relative

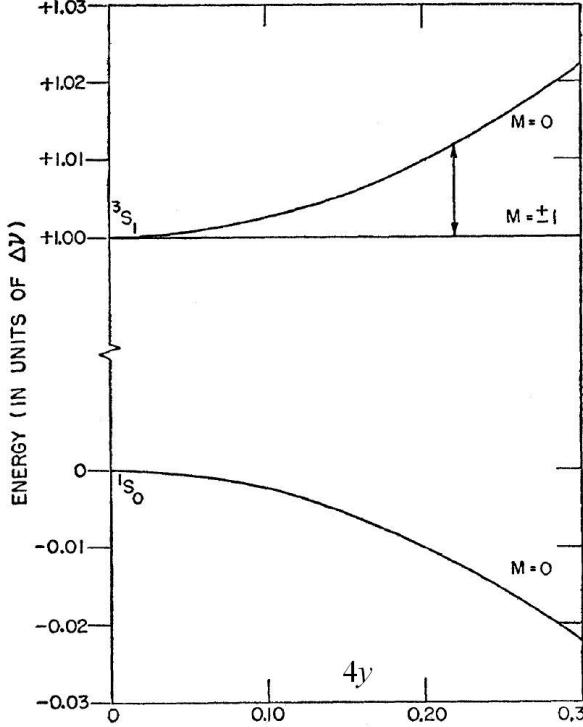


Fig. 1.9 The Breit-Rabi diagram for the Ps: dependence of the energy levels of the singlet and triplet states vs. magnitude of the external magnetic field. Here, the energy axes is presented in the units of the Ps hyperfine splitting, $\Delta E = 8.4 \cdot 10^{-4}$ eV. This quantity is taken as the unit of energy [27]

contact density η_c in the Ps atom:

$$\eta_c = \frac{\int \int d^3\mathbf{r}_+ d^3\mathbf{r}_- |\Psi_{+-}(\mathbf{r}_+, \mathbf{r}_-)|^2 \delta(\mathbf{r}_+ - \mathbf{r}_-) }{\int \int d^3\mathbf{r}_+ d^3\mathbf{r}_- |\Psi_{+-}^{vac}(\mathbf{r}_+, \mathbf{r}_-)|^2 \delta(\mathbf{r}_+ - \mathbf{r}_-) } = \frac{\int d^3\mathbf{r}_+ |\Psi_{+-}(\mathbf{r}_+ = \mathbf{r}_-)|^2}{\int d^3\mathbf{r}_+ |\Psi_{+-}^{vac}(\mathbf{r}_+ = \mathbf{r}_-)|^2}. \quad (1.37)$$

Here $\Psi_{+-}(\mathbf{r}_+, \mathbf{r}_-)$ is the Ps wave function in the medium, $\Psi_{+-}^{vac}(\mathbf{r}_+, \mathbf{r}_-)$ is its wave function in vacuum, having the form (1.27), and \mathbf{r}_+ and \mathbf{r}_- are the radius-vectors e^+ and e^- . Since integration over \mathbf{r}_+ and \mathbf{r}_- in the denominator (1.37) can be replaced by integration over the variables of the center of mass and relative distance

$$\int \int d^3\mathbf{r}_+ d^3\mathbf{r}_- \dots = \int \int d^3\mathbf{R}_{cm} d^3\mathbf{r} \dots,$$

then

$$\int \int |\Psi_{+-}^{vac}(\mathbf{r}_+, \mathbf{r}_-)|^2 \delta(\mathbf{r}_+ - \mathbf{r}_-) d^3\mathbf{r}_+ d^3\mathbf{r}_- = \int_V |\psi_{100}^{\text{Ps}}(r=0)|^2 |\Psi_{cm}^{vac}(\mathbf{R})|^2 d^3\mathbf{R} = |\psi_{100}^{\text{Ps}}(0)|^2 = \frac{1}{8\pi a_B^3}.$$

Here we took into account the normalization condition $\Psi_{cm}^{vac}(\mathbf{R})$: $\int_V |\Psi_{cm}^{vac}(\mathbf{R})|^2 d^3R = 1$.

Thus, we obtain

$$\eta_c = 8\pi a_B^3 \int \int d^3\mathbf{r}_+ d^3\mathbf{r}_- |\Psi_{+-}(\mathbf{r}_+, \mathbf{r}_-)|^2 \delta(\mathbf{r}_+ - \mathbf{r}_-) = 8\pi a_B^3 \int d^3\mathbf{r} |\Psi_{+-}(\mathbf{r}, \mathbf{r})|^2. \quad (1.38)$$

If we assume that the psi-function Ψ_{+-} of the Ps localized in the medium has the form similar to (1.27), but with a different value of the parameter a , which characterizes the decrease in the wave function of the pair with increasing distance between e^+ and e^- , then

$$\Psi_{+-}(\mathbf{r}, \mathbf{r}) = \Psi_{cm}(\mathbf{R}) \cdot \frac{1}{\sqrt{8\pi a^3}}.$$

Then substituting this expression into Eq. (1.38) and accounting for the normalization condition for Ψ_{cm} , we obtain the following expression for the relative contact density:

$$\eta_c = a_B^3/a^3. \quad (1.39)$$

Chapter 2 Examples of calculation of 2γ -annihilation rates and momentum distributions

2.1 Annihilation of the para-positronium in vacuum

To calculate the two-photon p-Ps annihilation rate in vacuum (the singlet pair e^+e^- with zero spin), we write its wave function in a “hydrogen-like” form:

$$\Psi_{+-}(\mathbf{r}_+, \mathbf{r}_-) = \Psi_{cm}(\mathbf{R}_{cm}) \cdot \psi_{100}^{\text{Ps}}(\mathbf{r}_+ - \mathbf{r}_-), \quad (2.1)$$

where $\Psi_{cm}(\mathbf{R}_{cm})$ is the wave function depending on the center-of-mass coordinate, $\mathbf{R}_{cm} = (\mathbf{r}_+ + \mathbf{r}_-)/2$, of the pair and ψ_{100}^{Ps} is the wave function, depending on the relative coordinate of the pair, $\mathbf{r}_+ - \mathbf{r}_-$. The function Ψ_{+-} has conventional normalization:

$$\int |\Psi_{+-}(\mathbf{r}_+, \mathbf{r}_-)|^2 d^3r_+ d^3r_- = 1, \quad \int d^3r_+ d^3r_- \dots = \int d^3R_{cm} d^3r \dots$$

As was indicated in (1.9), the p-Ps momentum distribution has the form:

$$n(\mathbf{k}) = \left| \int \Psi_{+-}(\mathbf{r}, \mathbf{r}) e^{i\mathbf{kr}} d^3r \right|^2, \quad (2.2)$$

and the rate of 2γ -annihilation (1.12):

$$\lambda_{2\gamma} = \pi r_0^2 c \int n(\mathbf{k}) \frac{d^3k}{(2\pi)^3} = \pi r_0^2 c \int |\Psi_{+-}(\mathbf{r}, \mathbf{r})|^2 d^3r. \quad (2.3)$$

Taking into account that, with respect to the center-of-mass coordinate of the pair (i.e. for the p-Ps atom), we have a uniform spatial distribution ($\Psi_{cm}(\mathbf{R}_{cm}) = 1/\sqrt{V}$), then

$$\Psi_{+-}(\mathbf{r}, \mathbf{r}) = \frac{1}{\sqrt{V}} \cdot \psi_{100}^{\text{Ps}}(0) = \frac{1}{\sqrt{V}} \cdot \frac{1}{\sqrt{8\pi a_B^3}}. \quad (2.4)$$

By squaring this expression and substituting it into Eq. (2.3), we obtain expression for $\lambda_{2\gamma}$. In this case, we should not forget to restore the multiplier “4”. Since we consider here the e^+ annihilation with its own electron only (and obviously it is in the “right” spin state with respect to the positron (in this case, there are no any other electrons)):

$$\lambda_{2\gamma}^{p\text{-Ps}} = 4\pi r_0^2 c \int_V |\Psi_{+-}(\mathbf{r}, \mathbf{r})|^2 d^3r = 4\pi r_0^2 c |\psi_{100}^{\text{Ps}}(0)|^2 = \frac{cr_0^2}{2a_B^3} = 8 \text{ ns}^{-1}, \quad (2.5)$$

Here we took into account that $r_0 = 2.8 \cdot 10^{-13}$ cm and $a_B = 0.53 \cdot 10^{-8}$ cm. Thus, we obtain that the p-Ps lifetime is $1/8 \text{ ns} = 125 \text{ ps}$.

The p-Ps atom in a liquid, being in a “bubble” state, is described by the “bell-shaped” wave function Ψ_{cm} with respect to the center-of-mass variable. The momentum distribution of annihilation photons is expressed through the Fourier transform of Ψ_{cm} . When Ps is localized in a bubble, it usually turns out that the contact density in the Ps atom (i.e., the electron density on the positron) is less than in vacuum. Would we consider Ps as a point particle, we have to adopt that the contact density in Ps does not change (i.e. equal to 125 ps, as it is in p-Ps). It usually turns out that in a medium the Coulomb attraction between e^+ and e^- weakens (for example, due to dielectric screening by the electrons of the medium). Therefore, both the contact density and the p-Ps annihilation rate also decrease, and the p-Ps lifetime increases.

2.2 Pick-off annihilation of the ortho-positronium

Two-photon annihilation of ortho-positronium assumes that e^+ annihilation occurs not with its own “intrinsic” e^- (that is a part of Ps), but with one of the electrons of the surrounding molecules of the medium (spin direction of this e^- should be opposite to the e^+ spin). In this case, 2γ -annihilation is possible. If $\Psi_{+-}(\mathbf{r}_+, \mathbf{r}_-)$ is the wavefunction of the Ps in a medium, and $\Phi_\mu(\mathbf{r}_\mu)$ describes one of the e^- of the medium, with which the positron will annihilate, then Eqs. (1.10) and (1.11) for the momentum distribution of the annihilating

pair reduces to (the e^+ coordinate must coincide with the electron coordinate):

$$\int n(\mathbf{k}) \frac{d^3 k}{(2\pi)^3} = \sum_{\mu} \int d^3 \mathbf{r}_+ \int d^3 \mathbf{r}_- |\Psi_{+-}(\mathbf{r}_+, \mathbf{r}_-)|^2 |\Phi_{\mu}(\mathbf{r}_+)|^2.$$

Thus the expression for the 2γ -annihilation (1.10) or better to say for the pick-off annihilation may be written as

$$\lambda_{po} = \pi r_0^2 c \int n(\mathbf{k}) \frac{d^3 k}{(2\pi)^3} = \pi r_0^2 c \sum_{\mu} \int d^3 \mathbf{r}_+ \int d^3 \mathbf{r}_- |\Psi_{+-}(\mathbf{r}_+, \mathbf{r}_-)|^2 |\Phi_{\mu}(\mathbf{r}_+)|^2.$$

Here we make summation over all electrons of the nearest molecules with which the positron may annihilate. If we assume that the overall electron density of these molecules has a stepwise profile:

$$\sum_{\mu} |\Phi_{\mu}(\mathbf{r})|^2 = n_e \theta(r > R), \quad (2.6)$$

where R is the Ps bubble radius (strictly speaking, the radius of the “free volume” of the Ps bubble), then the λ_{po} becomes the following:

$$\lambda_{po} = \lambda_+ P_R, \quad P_R \approx \int_{r_+ > R} d^3 \mathbf{r}_+ \int d^3 \mathbf{r}_- |\Psi_{+-}(\mathbf{r}_+, \mathbf{r}_-)|^2. \quad (2.7)$$

Here $\lambda_+ = \pi r_0^2 c n_e$ is the annihilation rate of “free” positron. In a majority of molecular liquids $\lambda_+ \approx 2 \text{ ns}^{-1}$.

The Tao-Eldrup model [28]. Let us consider a simplest case – a “point-like” (structureless) positronium localized in a spherically-symmetric rectangular infinitely deep potential well (R_{∞} is the radius of the well). This is a common model for the Ps “bubble”-state in liquids or for the Ps localized in (spherical) pores in dielectric media.

In the above expressions, we can adopt that \mathbf{r}_+ and \mathbf{r}_- at any time moment are very close to each other and practically coincide with the center-of-mass coordinate R_{cm} of the e^+e^- pair. It means that the integral $\int d^3 \mathbf{r}_- |\Psi_{+-}(\mathbf{r}_+, \mathbf{r}_-)|^2$ can be replaced with $|\Psi_{cm}(\mathbf{r}_+)|^2$.

In other words, this is the same if we adopt $|\Psi_{+-}(\mathbf{r}_+, \mathbf{r}_-)|^2 = \Psi_{cm}^2(R_{cm}) \cdot \delta^3(r)$.

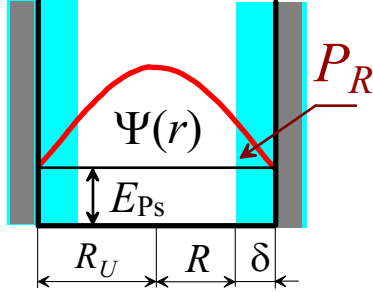


Fig. 2.1 The Tao-Eldrup Ps bubble model (Ps in liquids). Ps is located in an infinitely deep spherically symmetric potential well of radius $R_\infty = R + \delta$. $\Psi(r)$ is its center-of-mass wave function. R is the free-volume radius of the bubble. δ is the typical penetration depth of valence electrons into the bubble. P_R is the overlapping area of the positron wave function and the electron density of surrounding molecules.

Using the well-known expression for the wave function of a point particle in a spherical infinitely-deep potential well:

$$\Psi_{cm}(r) = \frac{\sin(\pi r/R_\infty)}{\sqrt{2\pi R_\infty} r}, \quad (2.8)$$

and substituting it into (2.7), we obtain the Tao-Eldrup formula for the pick-off annihilation rate of Ps (Fig. 2.1):

$$\frac{\lambda_{po}}{\lambda_+} = \int_R^{R_\infty} |\Psi_{cm}(r)|^2 4\pi r^2 dr = 1 - \frac{R}{R_\infty} + \frac{\sin(2\pi R/R_\infty)}{2\pi} = \frac{\delta}{R_\infty} - \frac{\sin(2\pi\delta/R_\infty)}{2\pi}. \quad (2.9)$$

Here we introduced the parameter $\delta = R_\infty - R$, which characterizes the thickness of the near-wall layer of the bubble (or cavity) where the positron can annihilate with the electrons of the surrounding molecules (which form the Ps bubble). Following to R. Ferrell [29], one may minimize the Ps quantum-mechanical energy E_{Ps} of positronium and the energy of the reorganization of a liquid medium ($4\pi R_\infty^2 \sigma$, where σ is the surface tension coefficient), then

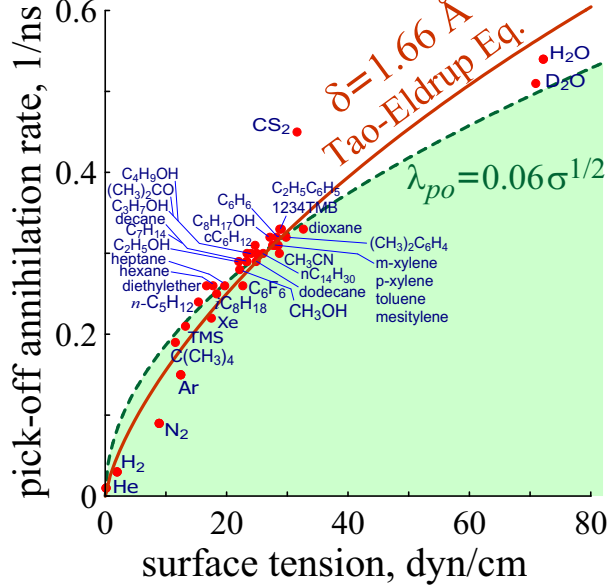


Fig. 2.2 Dependence of the Ps pick-off annihilation rate vs. surface tension in different liquids. The solid curve illustrates the Tao-Eldrup formula for the optimal value of the parameter $\delta = 1.66 \text{ \AA}$. The dashed curve is an approximate relation $\lambda_{po} \propto \sigma^{1/2}$.

we find the following expression for the equilibrium radius Ps of the bubble:

$$\frac{\pi^2 a_B^2}{R_\infty^2} \text{Ry} + 4\pi R_\infty^2 \sigma \leftrightarrow \min \text{ over } R_\infty \quad \Rightarrow \quad R_\infty = a_B \left(\frac{\pi \text{Ry}}{8\sigma a_B^2} \right)^{1/4}.$$

Substituting R_∞ into Eq. (2.9), we obtain a relationship between the pick-off annihilation rate and σ , which includes only one parameter δ . If we proceed with the fitting of the experimental data on Ps pick-off annihilation lifetimes in liquids, using this relationship $\lambda_{po}(\sigma)$, Fig. 2.2, [30], it turns out that $\delta \approx 1.66 \text{ \AA}$, and λ_+ is as before $\approx 2 \text{ ns}^{-1}$.

2.3 Annihilation of quasi-free positrons in metals

Discussing e^+ annihilation in conducting media, it is necessary to write down the wave function of the positron and surrounding electrons. Within the framework of the independent particle model, the wave function of the system is the product of the wave functions of the

positron and individual electrons¹:

$$\Psi_+(\mathbf{r}_+) \cdot \prod_{\mu=1}^N \Phi_\mu(\mathbf{r}_\mu).$$

Expression (1.10) in this case gives the momentum distribution of the annihilating pairs

$$n(\mathbf{k}) = \sum_{\mu=1}^N \left| \int \Psi_+(\mathbf{r}) \Phi_\mu(\mathbf{r}) e^{i\mathbf{kr}} d^3r \right|^2, \quad (2.10)$$

and Eq. (1.13) is the 2γ -annihilation rate of a “free” positron in a metal:

$$\lambda_+ = \pi r_0^2 c \sum_{\mu=1}^N \int |\Psi_+(\mathbf{r})|^2 |\Phi_\mu(\mathbf{r})|^2 d^3r. \quad (2.11)$$

Assuming that the electron concentration is constant in space and equal to

$$\sum_{\mu=1}^N |\Phi_\mu(\mathbf{r})|^2 \approx n_e, \quad (2.12)$$

we obtain the Sommerfeld result for the annihilation rate of the quasifree positrons [31] (the normalization condition for the positron wave function $\int |\Psi_+(\mathbf{r})|^2 d^3r = 1$ is taken into account):

$$\lambda_+ = \pi r_0^2 c n_e. \quad (2.13)$$

Momentum distribution in the case of e^+ annihilation on conduction electrons. To obtain theoretical expressions for the shape of ACAR and DBAR spectra, it is necessary to have an explicit form of $n(\mathbf{k})$. If we assume that positrons in metals are thermalized, we can move its wave function $\Psi_+(\mathbf{r}) \approx 1/\sqrt{V}$ before the integration in Eq. (2.10), because $\Psi_+(\mathbf{r})$ varies slowly. Then the momentum distribution of the e^+e^- pair will depend on the wave functions of the electrons only.

¹Strictly speaking, the electron wave function, taking into account spin factors, must be antisymmetrized with respect to all permutations of electrons.

It is generally believed that the wave functions of conduction electrons can be approximated by the plane waves $\Phi_\mu(\mathbf{r}) = \exp(-i\mathbf{k}_\mu \cdot \mathbf{r})/\sqrt{V}$. The wave vectors \mathbf{k}_μ (as well as the positron momentum) are determined from the Born-Karman boundary conditions in the cube of periodicity cube V . With this we come to the Fermi distribution:

$$\int_V \Phi_\mu(\mathbf{r}) e^{i\mathbf{k}\cdot\mathbf{r}} d^3r = \int_V \frac{e^{-i\mathbf{k}_\mu \cdot \mathbf{r}}}{\sqrt{V}} e^{i\mathbf{k}\cdot\mathbf{r}} d^3r = \sqrt{V} \delta_{\mathbf{k}_\mu, \mathbf{k}},$$

$$n(\mathbf{k}) = \frac{1}{V} \sum_{\mu}^{k_\mu < k_F} |\sqrt{V} \cdot \delta_{\mathbf{k}_\mu, \mathbf{k}}|^2 \propto \vartheta(k < k_F). \quad (2.14)$$

Integration of this function over k gives the concentration of conduction electrons:

$$\int n(k) \frac{d^3k}{(2\pi)^3} = \frac{4\pi k_F^3/3}{(2\pi)^3} = n_e.$$

Momentum distribution of e^+e^- pairs in case of e^+ annihilation on internal electrons of the atoms. Let us consider e^+ annihilation on internal (core) electrons. In this case $\Phi_\mu(\mathbf{r})$ cannot be approximated by plane waves, but it should look like atomic wave functions. Below we consider the simplest expressions for the wave functions of core electrons in the hydrogen-like potential $U = -Ze/r$ (Z is the effective charge of the nucleus) and calculate corresponding expressions for $n(\mathbf{k})$ and contributions to the CDB spectra [32].

1) exponential wave function:

$$\Phi_\mu(r) = \frac{e^{-r/a}}{\sqrt{\pi a^3}}, \quad \int |\Phi_\mu(r)|^2 d^3r = 1, \quad \Psi_+ = \frac{1}{\sqrt{V}}. \quad (2.15)$$

The minimization condition for the total (kinetic and potential) energy of an electron described by this wave function, $\langle \Phi_\mu | K + U | \Phi_\mu \rangle - \min$, gives the following relationship between Z and a : $Z = a_B/a$. Moreover, the minimal value of the total electron energy is $\langle \Phi_\mu | K + U | \Phi_\mu \rangle = -Z^2 \text{Ry} = -(a_B/a)^2 \text{Ry}$.

As before, we believe that the momentum distribution of the annihilating pair is solely due to momentum of the electron:

$$\begin{aligned} \int \Phi_\mu(r) e^{i\mathbf{kr}} d^3r &= \int \frac{e^{-r/a}}{\sqrt{\pi a^3}} e^{i\mathbf{kr}} d^3r = \frac{8\sqrt{\pi a^3}}{(1+k^2a^2)^2}, \\ d^3r &= r^2 dr d\vec{\Omega}, \quad d\vec{\Omega} = \sin\theta d\theta d\phi, \quad \int e^{i\mathbf{kr}} d\vec{\Omega} = 4\pi \frac{\sin kr}{kr}, \\ n(\mathbf{k}) &= \frac{1}{V} \left| \int \Phi_e(\mathbf{r}) e^{i\mathbf{kr}} d^3r \right|^2 = \frac{1}{V} \frac{64\pi a^3}{(1+k^2a^2)^4}. \end{aligned} \quad (2.16)$$

To verify the correctness of the obtained formula for the electron momentum distribution function, one can integrate Eq. (2.16) over d^3k and make sure that $\int n(\mathbf{k}) d^3k / (2\pi)^3 = 1/V$.

It will be shown below (see Eq. (3.14)) that in a spherically symmetric case the contribution to the CDB spectrum can be calculated by knowing the function $n(\mathbf{k})$ as follows: $C(\Delta = E_2 - E_1) \propto \int_{|\Delta|/c\hbar}^{\infty} kn(k) dk$. In this case, this contribution has the form of the Lorentzian cubed:

$$C(\Delta = E_2 - E_1) \propto \frac{1}{(1+\delta^2)^3}, \quad \delta = \frac{a\Delta}{c\hbar}. \quad (2.17)$$

2) the Gaussian wave function:

$$\Phi_\mu(r) = \frac{2^{3/4}}{\pi^{3/4} a^{3/2}} e^{-r^2/a^2}, \quad \int |\Phi_\mu(r)|^2 d^3r = 1. \quad (2.18)$$

In this case, the total energy minimization condition (with respect to a) gives the following relationship between Z and a : $Z = \frac{3\sqrt{\pi}}{2^{3/2}} \frac{a_B}{a}$ and the minimal energy value is equal to $-\frac{8}{3\pi} Z^2 \text{Ry}$ or $-3\frac{a_B^2}{a^2} \text{Ry}$. Then we calculate the Fourier transform of this wave function (in Cartesian coordinates, $k^2 = k_x^2 + k_y^2 + k_z^2$, $d^3k = dk_x dk_y dk_z$):

$$n(k) = (2\pi)^{3/2} a^3 \exp\left(-\frac{k^2 a^2}{2}\right).$$

After that, using Eq. (3.14), we get the corresponding contribution to the observed CDB spectrum:

$$C(\Delta = E_2 - E_1) \propto e^{-\delta^2}, \quad \delta = \frac{a\Delta}{c\hbar}. \quad (2.19)$$

3) the wave function which corresponds to e^- in an excited state:

$$\Phi_\mu(r) = \frac{re^{-r/a}}{\sqrt{3\pi a^5}}, \quad \int |\Phi_\mu(r)|^2 d^3r = 1. \quad (2.20)$$

The total energy minimization condition gives $Z = 2a_B/3a$, and the minimal value of the total electron energy is $-3Z^2\text{Ry}/4 = -\text{Rya}_B^2/3a^2$.

Calculation of the electron momentum distribution gives

$$n(k) \propto \frac{(3 - k^2 a^2)^2}{(1 + k^2 a^2)^6},$$

so the corresponding contribution to CDB spectrum is

$$C(\Delta = E_2 - E_1) \propto \frac{16}{5(1 + \delta^2)^5} - \frac{2}{(1 + \delta^2)^4} + \frac{1}{3(1 + \delta^2)^3}, \quad \delta = \frac{a\Delta}{c\hbar}. \quad (2.21)$$

All these three expressions (2.17), (2.19) and (2.21), Fig. 2.3 are used in the SW Calculator [16] program for fitting experimental CDB spectra as possible components describing annihilation of positrons on core electrons.

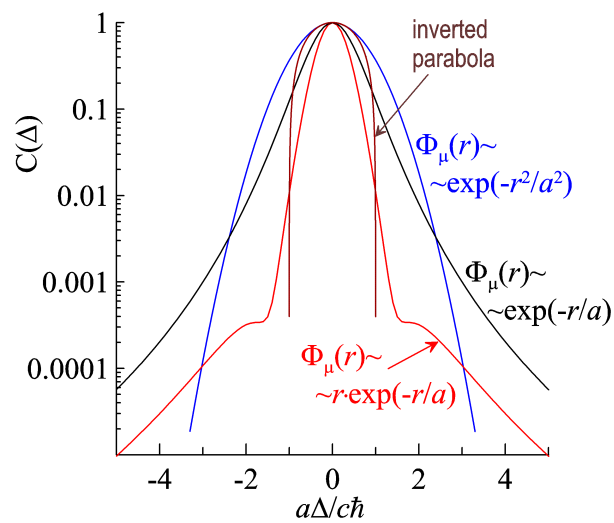


Fig. 2.3 Contributions to CDB spectrum from the simplest e^- wave functions considered here: 1 – Eq. (2.17), 2 – (2.19) and 3 – (2.21). All the functions are normalized on 1 at $\delta = 0$.

Chapter 3 Positron sources and experimental methods of PAS

3.1 e⁺ sources

The choice of the positron source is determined according to the goals of the study. For medical applications (PET – Positron Emission Tomography) one needs the short-lived isotopes, which rapidly decay with emission of a positron. It is important because of reduction of the radiation load on a patient. The most popular isotope is ¹⁸F, which enters fluorodeoxyglucose (18F-FDG). This is an analogue of ordinary glucose, where one of the OH-groups is replaced by ¹⁸F. This compound is used to visualize tumors, because cancer cells consume glucose more actively than the ordinary cells.

For material science research, much more long-lived β^+ -isotopes are used, Table 3.1. The most common e⁺ source is the ²²Na isotope. It is usually shipped in the form of aqueous solution of ²²NaCl salt. This salt is deposited and sealed in between two thin Kapton films (8 μm) or (4-5 μm) titanium foils. During the last 4 years, I have made three e⁺ sources using ²²Na isotope. The manufacturing process is described in detail in Appendix 6.8.6.

Table 3.1 β^+ -isotopes used in the e⁺ sources

¹¹ C	–	20 min	¹⁹ Ne	–	17.4 s	⁵⁸ Co	–	71 day
¹³ N	–	10 min	²² Na	–	2.6 y	⁵⁷ Ni	–	36 h
¹⁵ O	–	123 min	²⁶ Al	–	$8 \cdot 10^5$ y	⁶⁴ Cu	–	12.8 h
¹⁸ F	–	110 min	⁴⁴ Ti	–	59 y	⁶⁸ Ge	–	275 days

For ACAR experiments the activity of the e⁺ source should be very high, of order of 1 Curie (1 Curie = $3.7 \cdot 10^{10}$ Bq, 1 Becquerel (Bq) has one nuclear decay per second). For the LT measurements, it is sufficient to have 3-4 orders of magnitude less intensive source. The half-life of ²²Na is 2.6 years, so the positron flux during an experiment can be considered as constant.

It is important that β^+ -decay of ²²Na is accompanied by formation of the excited nucleus,

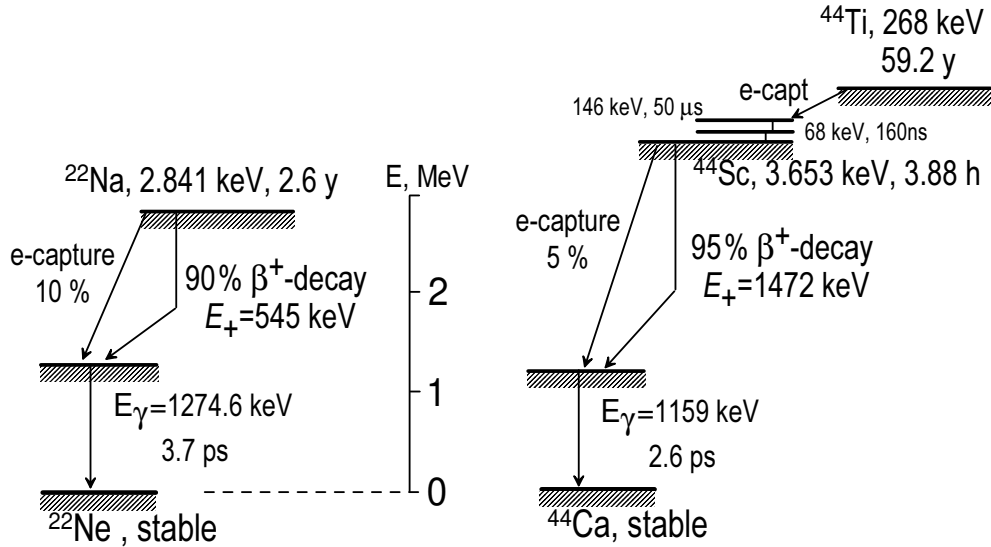


Fig. 3.1 Scheme of the nuclear transformations of ^{22}Na and ^{44}Ti .

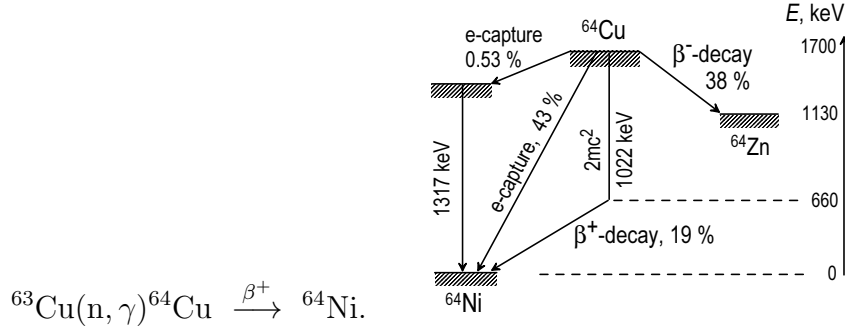
$^{22}\text{Ne}^*$, which promptly (3.7 ps) transfers to its ground state, emitting 1.274 MeV γ -quantum, Fig. 3.1. It is difficult to overestimate this peculiarity of the ^{22}Na β^+ -decay. Registration of this photon (it appears almost immediately after the e^+ birth) gives the start signal, which triggers the PAL setup.

In ACAR and DBAR measurements, registration of the time moment of the e^+ birth is not needed. Moreover, in these cases 1.274 MeV γ -quanta from $^{22}\text{Ne}^*$ introduce an additional background. In this case, the isotope ^{68}Ge may be more preferable as the e^+ source, despite of the short half-life of this nucleus.

A serious problem that must be kept in mind when doing positron annihilation experiments (LT, DBAR or ACAR) is the account for the e^+ annihilation within the material of the positron source itself (the source correction). The number of such adverse annihilation events can be reduced by choosing the β^+ -emitter with a higher e^+ initial energy. From this viewpoint the e^+ source based on ^{44}Ti might be good for the LT experiments (the half-life is 59 years, the β^+ -end-point energy is 1.47 MeV and there is the “start” γ -quantum – 1.16 MeV).

There are several positron annihilation apparatuses installed near nuclear reactors. So it

is possible to use reactor radiation for the e^+ production. For example, one may irradiate metallic copper with the reactor (the capture cross-section of thermal neutrons by ^{63}Cu is about 4.5 barn):



After about 1 day irradiation, copper is transferred to a special chamber of the positron spectrometer. In such a way it is possible to obtain e^+ activity, sufficient for doing ACAR measurements (NRNU MEPhI, Moscow).

There are several setups in which positrons are born directly in the studied samples owing to the phenomenon of e^+e^- pair production. In this case the studied sample (could be thick!) is irradiated by high-energy γ -rays (some MeV). When they fly in the Coulombic electric field of the nuclei, the positrons arise.

The last possibility of the e^+ production are the positron beams. In this case a tungsten target (usually) is irradiated with the high-energy gammas (generated by bremsstrahlung of a high-energy electron beam, or one may use nuclear fission gammas in a nuclear reactor). As a result of pair production in tungsten some small fraction of positrons thermalize therein and escape from it. These positrons could be captured and accelerated by external electric field. As a result one may produce rather bright low-energy monochromatic positron beams, which are successfully used in surface physics studies [33, 34].

3.2 Positron Annihilation Lifetime Spectroscopy (PALS)

Entering a medium, fast positrons lose their kinetic energy down to the thermal one within 10 ps or so. The main mechanism of energy losses is the ionization slowing down.

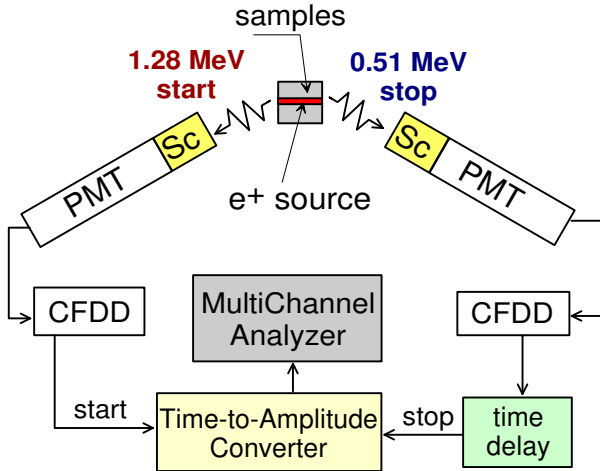


Fig. 3.2 Scheme of the PAL spectrometer: Sc – scintillator, PMT – photomultiplier, CFDD – constant fraction differential discriminator. Energies of the “start” and “stop” photons correspond to the ^{22}Na -based positron source.

When the positron energy becomes $\lesssim 10$ eV, such positrons mainly excite intra- and intermolecular vibrations. Ionization energy losses determine the positron penetration into the studied sample (the depth is 0.1-4 mm). So this allows to study the electronic and structural bulk properties of different materials.

Of course, the slowing down time and the penetration depth depend on initial e^+ energy and properties of the studied samples. After thermalization, positrons may freely diffuse in a substance. The e^+ diffusion length in a defect-free material is limited by its lifetime before annihilation (in metals it is 100-200 ps), so the e^+ diffusion length could be hundreds of nanometers.

In dielectric and molecular media at the end of the positron track the Ps formation is quite possible. In its turn Ps can react with both intratrack radiolytic products and with the dissolved substances.

In LT experiments the time intervals between the start and stop signals (photons) accompanying e^+ production and annihilation ($e^+ + e^- \rightarrow 2\gamma$) are measured. Scheme of the positron annihilation lifetime setup is shown in Fig. 3.2.

Fig. 3.3 shows an example of the LT spectrum measured in pure water at room temperature. It is quite common that processing of LT spectra (using PalsFIT or LT programs) consist in their deconvolution into several (usually three) exponentials, decreasing with time. For instance, in liquids the shortest component approximately corresponds to the p-Ps an-

nihilation ($\tau_1 \sim 0.15\text{-}0.2$ ns), the second component describes “free” positrons ($\tau_2 = 0.4\text{-}0.5$ ns) and the long-lived component ($\tau_3 \gtrsim 2$ ns) comes from o-Ps annihilation, respectively:

$$C_{theor}(t) = \Delta t \left[C_{tot} \sum_i \frac{I_i}{\tau_i} \exp\left(-\frac{t}{\tau_i}\right) \right] = \Delta t \left[C_{tot} \sum_i \lambda_i I_i \exp(-\lambda_i t) + B \right], \quad (3.1)$$

$$\int_0^\infty C(t) dt = C_{tot}, \quad \sum_i I_i = 1.$$

For a correct comparison of the theoretical model with the measured spectra, one needs to take into account contribution from e^+ annihilation within the positron source (so called “source correction”), $C_{source}(t)$. It is also necessary to take into account a background BG from random start-stop coincidences. Usually the source correction can also be represented as a set of decreasing exponentials. It should be determined in advance in experiments with the reference (pure, well annealed, defect-free) samples, having well-known e^+ lifetime (monoexponential decay). They could be iron, aluminum, copper, tungsten and so on.

After that, it is necessary to convolute the theoretical model with the time-resolution function of the setup, $f_{res}(\tau)$:

$$C_{exp}(t) = \int_{-\infty}^\infty [C_{theor}(\tau) + C_{source}(\tau)] f_{res}(t - \tau) d\tau + BG. \quad (3.2)$$

From here one can conclude about the meaning of the time resolution function. It describes the shape of the LT spectrum, if “start” and “stop” photons enter detectors simultaneously.

Thus, $C_{exp}(t)$ is the number of positron annihilations registered in the corresponding channel of the multichannel analyzer (the time moment t corresponds to the center of the channel, and Δt is the channel duration).

Sometimes one may find in the literature the statement that intensities of shortest and long-lived components of LT spectra in a molecular medium obey the so-called “three-to-one” ratio: $I_3/I_1 = 3/1$. It has the following motivation. During a β -decay, energetic positrons are generated with 100% polarization. It means that their spin $| \uparrow_p \rangle$ is directed along the

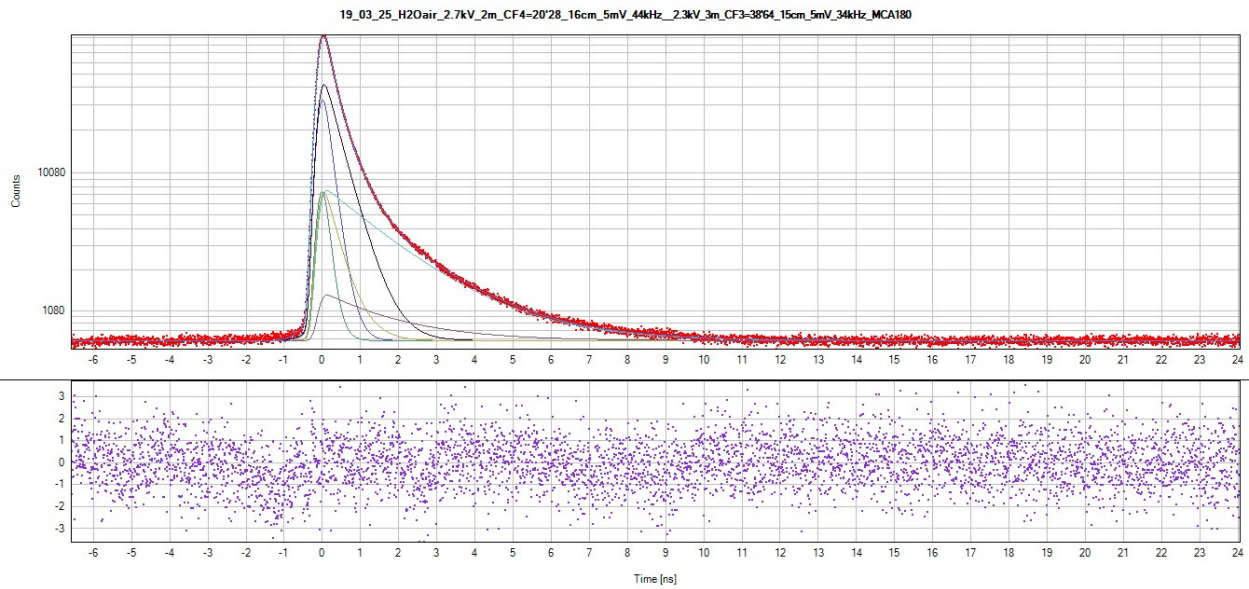


Fig. 3.3 An example of a LT annihilation spectrum of positrons measured in pure water at room temperature [35]. The solid lines show deconvolution of the spectrum into three exponential components: $I_1 = 25.2\%$, $\tau_1 = 194(2)$ ps, $I_2 = 49.3(4)\%$, $\tau_2 = 0.42(1)$ ns and $I_3 = 25.5(3)\%$, $\tau_3 = 1.80(1)$ ns. The source correction was 13% (in this experiment the ^{44}Ti positron source was used, activity was welded into a $10\ \mu\text{m}$ titanium foil). Contribution from e^+ annihilation in the source was also represented by three exponents.

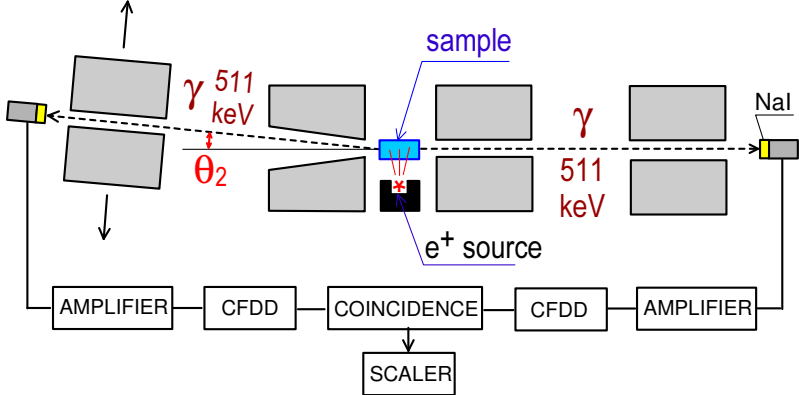


Fig. 3.4 Scheme of 1D-ACAR set-up (1D = one dimensional; ACAR = angular correlation of annihilation radiation). The left arm is movable and the right one is fixed.

direction of the e^+ momentum when it escapes the nucleus. When this positron combines with one of the electrons in a medium, two following spin states may form with equal probability: $|\uparrow_e\uparrow_p\rangle$ and $|\downarrow_e\uparrow_p\rangle$. The first is orthopositronium, o-Ps $^{m=1}$, with the projection of its spin onto the quantization axis equal to 1, and the second state is the sum of o-Ps with $m = 0$ and p-Ps. Both these states are taken with equal weights: $|\downarrow_e\uparrow_p\rangle = (\chi_{10} - \chi_{00})/\sqrt{2} = (|o\text{-Ps}^{m=0}\rangle - |p\text{-Ps}\rangle)/\sqrt{2}$. Thus, from the viewpoint of spin statistics, a polarized (spin up) positron forms ortho- and para-states according to 3:1 ratio. Obviously, the same thing will happen for the opposite polarization of the positron (spin-down), i.e. 3-to-1 ratio must exist anyway. Sometimes this motivation is used for fixing the ratio $I_3/I_1 = 3/1$ when fitting annihilation spectra. However, more rigorous consideration of the Ps formation mechanism given in the Chapter 5 shows that this ratio does not hold.

3.3 Angular Correlation of Annihilation Radiation (ACAR)

ACAR spectrometer has two arms with two γ -detectors: one is fixed and the other movable, Fig. 3.4. The moving arm may move on a certain angle. Both detectors work in a coincidence, registering angular deviation from 180° of two annihilation γ -quanta.

As was noted above, the observable value in ACAR experiments is the flying-out angle of annihilation photons, θ_2 : $\theta_2 = \frac{p_{ey}}{mc} = \frac{\hbar k_{ey}}{mc}$, where p_{ey} is the y -component of the pair momentum (hereinafter we will write θ instead of θ_2 , and p_y instead of p_{ey}).

Formally, calculation of the shape of the ACAR spectrum reduces to finding the distribution function of one random variable, if we know the distribution function of another

random variable, which depends on the first one. For example, let we know the momentum distribution of the electrons, $n(\mathbf{p})$, then we want to know the distribution function for one of the momentum component, say, p_y or $\theta = p_y/mc$. This could be done as follows:

$$C\left(\theta = \frac{p_y}{mc}\right) \propto \int n(\mathbf{p}) \delta\left(\theta - \frac{p_y}{mc}\right) d^3p. \quad (3.3)$$

Assuming that $n(p)$ is spherically symmetric (.e. n depends only on the modulus of p), we obtain:

$$C(\theta) \propto \int n\left(\sqrt{p_x^2 + p_z^2 + (mc\theta)^2}\right) dp_x dp_z. \quad (3.4)$$

Now let us replace the differential of the “square” $dp_x dp_z$ by $2\pi p_{xz} dp_{xz}$, so we can proceed with integration over p :

$$\begin{aligned} C(\theta) &\propto 2\pi \int_0^\infty n\left(\sqrt{p_{xz}^2 + (mc\theta)^2}\right) p_{xz} dp_{xz} = \pi \int_0^\infty n\left(\sqrt{p_{xz}^2 + (mc\theta)^2}\right) dp_{xz}^2 = \\ &\stackrel{p^2=p_{xz}^2+(mc\theta)^2}{=} \pi \int_{(mc\theta)^2}^\infty n(p) dp^2 = 2\pi \int_{mc\theta}^\infty n(p) pdp. \end{aligned} \quad (3.5)$$

Substituting here the spherically symmetric Fermi distribution for electrons in metals $n(p) \propto \vartheta(p < p_F)$, we find that the ACAR spectrum (in the case of annihilation of thermal e^+ on conduction electrons) must have the form of the inverted parabola:

$$C(\theta < p_F/mc) \propto 1 - \left(\frac{mc\theta}{p_F}\right)^2, \quad C(\theta > p_F/mc) = 0. \quad (3.6)$$

This parabola intersects the abscissa (axis of θ) at the point $\theta_F = p_F/mc$. Then knowing p_F (the Fermi momentum) we can determine the Fermi energy and the density of the conduction electrons:

$$n_e = p_F^3 / (3\pi^2 \hbar^3), \quad E_F = \frac{p_F^2}{2m} = \frac{mc^2}{2} \theta_F^2, \quad (E_F, \text{ eV}) = 0.255 \cdot (\theta_F, \text{ mrad})^2.$$

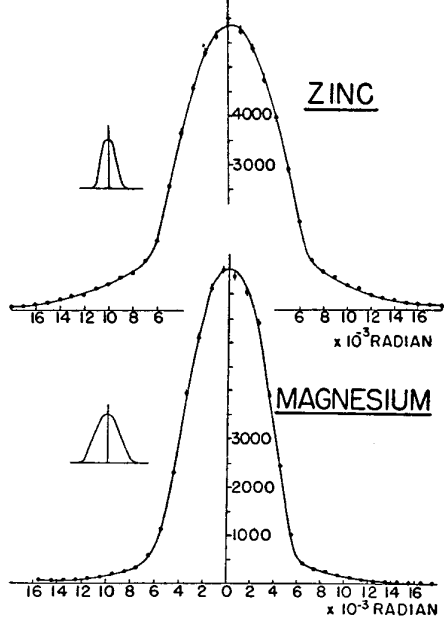


Fig. 3.5 Left: angular distributions of annihilation photons in metals (Zn, Mn) [36]. The spectra are decomposed into a sum of the parabolic and Gaussian components. The insets show the angular resolution functions.

Note that it is possible to solve the inverse problem: to reconstruct the e^- momentum distribution, $n(k_y)$, along y -axis, knowing shape of the experimental ACAR spectrum:

$$\rho(n_y) \propto \frac{1}{\theta} \cdot \frac{dC(\theta)}{d\theta}. \quad (3.7)$$

Of course, if we substitute here $C(\theta)$ in the form of the inverted parabola, Eq. 3.6, we immediately reproduces the stepwise Fermi distribution.

In the absence of theoretical predictions about the shape of the angular spectrum, it is usually decomposed into a set of Gaussian components:

$$C(\theta) \propto \sum_i Y_i \exp(-\theta^2/2M_{2i}). \quad (3.8)$$

Here values of the second moments M_{2i} of the Gaussians can be easily related to the full widths at half maximum: $\Theta_i = 2\sqrt{2M_{2i} \ln 2} \approx 2.355\sqrt{M_{2i}}$.

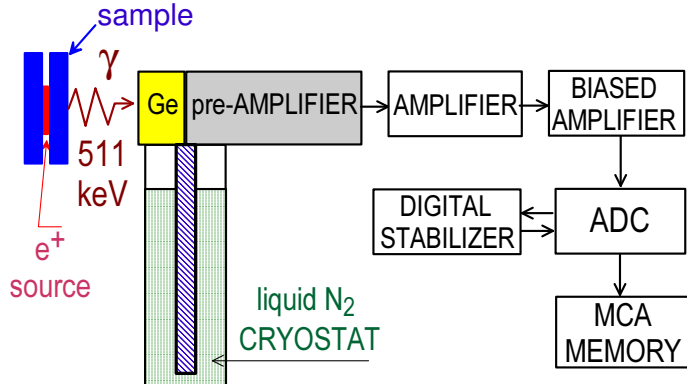


Fig. 3.6 Схема позитронного спектрометра для измерения доплеровских спектров аннигиляционных фотонов (DBAR – Doppler Broadening of Annihilation Radiation).

3.4 Doppler Broadening of Annihilation Radiation (DBAR)

In conventional DBAR experiments (Fig. 3.6) the observable quantity is the energy of one of the annihilation γ -quanta. Their total energies slightly differ from $mc^2 = 511$ keV because of their binding and kinetic energies in the atoms. This deviation leads to the so-called Doppler broadening of the 511-annihilation peak when 2 γ -annihilation occurs. Basing on the energy and momentum conservation laws, it was shown that, Eq. (1.19):

$$E_2 = cp_2 \approx mc^2 - E_b/2 + cp_z/2.$$

The calculation of the shape of both the DBAR and ACAR spectra is a difficult task. It can be solved analytically only in the simplest cases. In fact, to do that we must take into account that e^+ can annihilate with different electrons, having different momenta. So first of all we need to know momentum distribution $n(\mathbf{k})$ of the annihilating e^+e^- pair, which appears in Eq. (1.7). Then it is possible to calculate the shape of the spectrum. In independent particle approximation (independent positron and electrons), the momentum

distribution has the form (2.10):

$$n(\mathbf{k}) = \sum_{\mu=1}^N \left| \int \Psi_+(\mathbf{r}) \Phi_\mu(\mathbf{r}) e^{i\mathbf{kr}} d^3r \right|^2. \quad (3.9)$$

Formally calculation of the shape of DBAR (and ACAR) spectra reduces to the problem of finding the distribution function of one random variable, in case we know the distribution function of another random variable, which depends on the first one. This can be done in the following standard way. Similarly to Eq. (3.3), the shape of the DBAR spectrum (number of counts at a given energy of an annihilation photon) can be written as:

$$C(E_2) \propto \int n(\mathbf{p}) \cdot \delta \left(E_2 - mc^2 + \frac{E_b}{2} + \frac{cp_z}{2} \right) d^3p, \quad (3.10)$$

where p_z is the z -component of the e^- momentum (the positron annihilates with this electron).

In a spherically symmetric case, when $n(\mathbf{p})$ depends only on p (module of \mathbf{p}), one can obtain much simpler expression for the DBAR spectrum:

$$C(\Delta) \propto \int_0^\infty n(p) p^2 dp \int_0^\pi 2\pi \sin \theta d\theta \cdot \delta \left(\Delta - \frac{cp \cos \theta}{2} \right), \quad \Delta = mc^2 - E_b/2 - E_2, \quad p_z = p \cos \theta.$$

Integration over angular variables (actually over $\cos \theta$) can be carried out using the following relation

$$\int_{-1}^1 \delta \left(\Delta - \frac{cp x}{2} \right) dx = \begin{cases} 2/cp, & |\Delta| < cp/2, \\ 0, & |\Delta| > cp/2. \end{cases}$$

Thus we obtain

$$C(\Delta) \propto \int_{2|\Delta|/c}^\infty p n(p) dp. \quad (3.11)$$

For example, when using the Fermi distribution $n(p) = \vartheta(p < p_F)$ (quasi-free electron

gas + “stopped” positron), the final expression is:

$$C\left(|\Delta| < \frac{cp_F}{2}\right) \propto \int_{2|\Delta|/c}^{p_F} pdp = 1 - \left(\frac{2\Delta}{cp_F}\right)^2, \quad C\left(|\Delta| > \frac{cp_F}{2}\right) = 0. \quad (3.12)$$

From here it follows that the DBAR spectrum in simple metals (as well as the ACAR spectrum) must have a parabolic component corresponding to annihilation of thermalized positrons on “free” electrons. This parabola cuts out on the energy axis the interval $[-cp_F/2, cp_F/2]$. From here one may find the Fermi momentum p_F , Fermi energy and free electron density.

3.5 Coincidence Doppler Broadening Spectroscopy (CDB)

At the end of the last century, a two-detector-type of the DBAR spectroscopy has been developed. The second γ -detector registers the second annihilation 511-photon in the coincidence mode with the first detector (in fact, a pair of photons E_1, E_2 must hit the detectors within a certain time interval. Modern digital setups support simultaneous registration of the photons within a 100 ns time window. This makes possible to reduce significantly the background under the 511 keV photopeak. It allows to observe positron annihilation on internal (core) electrons and to identify the chemical nature of the atoms, on which e^+e^- annihilation takes place, Fig. 3.7.

After registering the two-dimensional distribution, $C(E_1, E_2)$, it is usually moved to the one-dimensional spectrum, $C(E_1 - E_2)$, which depends on the energy difference $\Delta = E_1 - E_2$ of two annihilation photons. According to (1.21) this difference is equal to the z -component of annihilating pair (mostly it is the momentum of the electron):

$$\Delta = E_1 - E_2 = cp_z, \quad E_{1,2} = mc^2 - E_b/2 \pm cp_z/2.$$

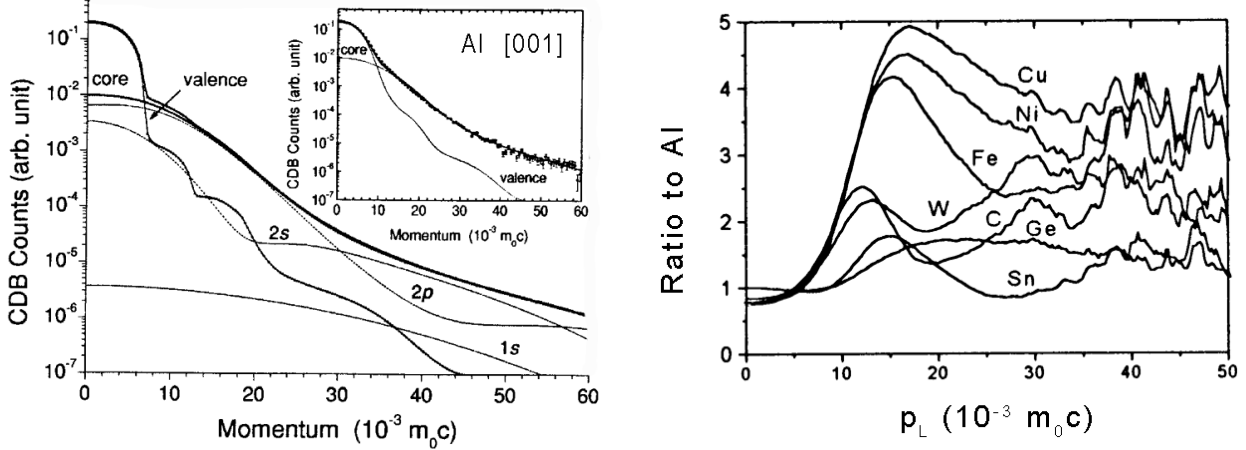


Fig. 3.7 Left: CDB spectrum in aluminum [37]. Right: Momentum dependence of the ratio of e^+ annihilation events on impurity atoms to the number of e^+ annihilations on electrons in pure Al [P.Asoka-Kumar et al., 1997].

Similar to Eq. (3.10), one may write down an expression of the CDB spectrum as follows:

$$C(\Delta = E_2 - E_1) \propto \int n(\mathbf{p}) \delta(\Delta - cp_z) d^3 p. \quad (3.13)$$

In a spherically symmetric case, the calculation of this integral is similar to Eqs. (3.10-3.11), but now the lower limit in the integration is different (!):

$$C(\Delta = E_2 - E_1) \propto \int_{|\Delta|/c}^{\infty} pn(p) dp. \quad (3.14)$$

When positrons annihilate on conduction electrons (in metals, alloys), the CDB spectrum also has a form of the inverted parabola (but the coefficient before Δ is different):

$$C(\Delta = E_2 - E_1) \propto 1 - \left(\frac{\Delta}{cp_F} \right)^2, \quad |\Delta| < cp_F, \quad C(|\Delta| > cp_F) = 0. \quad (3.15)$$

This parabola cuts on the energy axis $E_2 - E_1$ twice as large interval: $2cp_F = | -cp_F, cp_F |$, but again, from here we can find the Fermi momentum, energy etc.

In the case of annihilation of a thermalized positron on internal (core) electrons, the

momentum distribution of the e^+e^- pair, $n(p)$, is determined by the Fourier transform of the electron wave function (the positron wave function can be approximated as a constant on this scale). Several examples of calculating of $n(p)$ in the simplest cases of electron wave functions (exponentially decaying, Gaussian, r times an exponent) were given in the previous chapter, see Eqs. (2.17), (2.19) and (2.17).

Accounting for the energy resolution of the CDB spectrometer. The obtained above theoretical expressions for $C(\Delta = E_2 - E_1)$, which describe contributions to the CDB spectrum should be convoluted with two energy resolution functions of the γ -detectors. We will approximate them by Gaussians:

$$C_{exp}(\epsilon_1, \epsilon_2) = \iint C(E_1, E_2) G(\epsilon_1 - E_1) G(\epsilon_2 - E_2) dE_1 dE_2, \quad (3.16)$$

$$G(\epsilon_1 - E_1) = \frac{e^{-(\epsilon_1 - E_1)^2 / 2M_2}}{\sqrt{2\pi M_2}}.$$

Here for simplicity we assume that the detector resolution functions are same (and can be approximated as a gaussian with the second moment M_2). In the case of CDB-spectroscopy when the theoretical prediction for $C(\Delta)$ depends on the difference $\Delta = E_1 - E_2$:

$$C_{exp} = \iint C(\Delta) G(\epsilon_1 - E_1) G(\epsilon_2 - E_2) dE_1 dE_2 = \iint C(\Delta) G(\epsilon_1 - \Delta - E_2) G(\epsilon_2 - E_2) dE_1 dE_2,$$

we can easily integrate over E_2 :

$$\int G(\epsilon_1 - \Delta - E_2) G(\epsilon_2 - E_2) dE_2 = \int_{-\infty}^{\infty} e^{-x^2} e^{-(x+b)^2} \frac{dx}{\pi\sqrt{2M_2}} = \frac{e^{-b^2/2}}{\sqrt{4\pi M_2}}, \quad b = \frac{\epsilon_2 - \epsilon_1 + \Delta}{\sqrt{2M_2}}.$$

Thus, $C(\Delta)$ must be convoluted with the Gaussian function with twice as large the second moment:

$$C_{exp}(\epsilon_1 - \epsilon_2) = \int C(\Delta) \frac{\exp\left[-\frac{(\epsilon_2 - \epsilon_1 + \Delta)^2}{4M_2}\right]}{\sqrt{4\pi M_2}} d\Delta.$$

For correct comparison with the experimental data, we have to add to C_{exp} a contribution of e^+ annihilation within the e^+ -source as well as a constant random coincidence background.

We know that in dielectric media, the Ps formation is quite possible. Often an analysis of the CDB and ACAR spectra is reduced to deconvolution into three components (usually they are approximated by Gaussians):

$$C(\Delta) = \sum_i C_i(\Delta) \rightarrow \sum_i D_i \exp\left(-\frac{\Delta^2}{2\langle\Delta^2\rangle_i}\right). \quad (3.17)$$

The “narrow” component is usually associated with p-Ps annihilation. Wider components are associated with annihilation of “free” e^+ (on surrounding electrons) and with o-Ps annihilation (the pick-off process). If the momentum distributions of the pair in these states are characterized by the function $n_i(p)$, we can relate the second moment of the i -th component of the CDB spectrum

$$\langle\Delta^2\rangle_i = \frac{\int \Delta^2 C_i(\Delta) d\Delta}{\int C_i(\Delta) d\Delta}, \quad C_i(\Delta) \propto \int_{|\Delta|/c}^{\infty} p n_i(p) dp, \quad (3.18)$$

with the corresponding mean square of the e^+e^- momentum, $\langle p^2 \rangle_i = \int p^2 n_i(p) d^3p$. Performing integration by parts¹, we obtain:

$$\langle\Delta^2\rangle_i = \frac{c^2 \langle p^2 \rangle_i}{3}. \quad (3.19)$$

For example, knowing the second moment of the “narrow” (para-positronium) component of the CDB spectrum, $\langle\Delta^2\rangle_{pPs}$, we can easily calculate the mean kinetic energy of the p-Ps

¹

$$\begin{aligned} \int \Delta^2 C_i(\Delta) d\Delta &= \int_0^\infty \Delta^2 \int_{\Delta/c}^\infty p n_i(p) dp \cdot d\Delta = 0 + \frac{c^3}{4\pi} \int_0^\infty p^2 n_i(p) d^3p = \frac{c^3}{4\pi} \langle p \rangle_i, \\ \int C_i(\Delta) d\Delta &= \int_0^\infty \int_{\Delta/c}^\infty p n_i(p) dp \cdot d\Delta = 0 + \frac{c}{4\pi} \int_0^\infty n_i(p) d^3p = \frac{c}{4\pi}. \end{aligned}$$

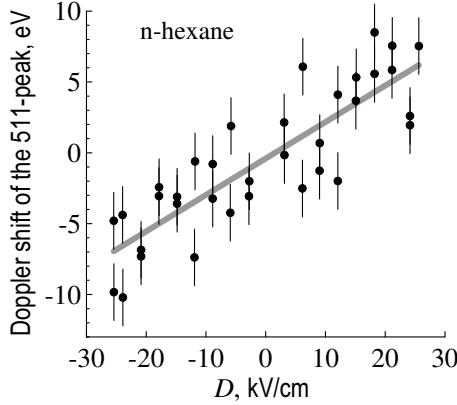


Fig. 3.8 Dependence of the Doppler shift of the peak of the annihilation photons in n-hexane vs. applied electric field [38, 39].

atom

$$\frac{\langle p^2 \rangle_{\text{pPs}}}{4m} = \frac{3\langle \Delta^2 \rangle_{\text{pPs}}}{4mc^2}.$$

Usually sensitivity of the DBAR installations is noticeably less than that of the ACAR. Angular resolution of the ACAR spectrometers is about $\Delta\theta \approx 0.5$ mrad. Converting this value ($\Delta\theta = \Delta p_y/mc$) to the p-Ps energy we obtain $E_{\text{pPs}} \approx 3\Delta p_y^2/4m \approx 0.1$ eV. On the other hand typical energy resolution of the Doppler setup is 10 times worse $\Delta p_z c/2 \approx 1\text{-}1.2$ keV. So the minimal energy of the e^+e^- pair, which can be observed, is about 0.4-0.5 eV.

e^+ mobility. Small modification of the Doppler spectrometer makes it possible to measure e^+ mobility μ_p in matter. To do this, an external electric field up to several tens of kV/cm must be applied to the sample along the axis of the spectrometer. Then the free positrons can be accelerated by the field E . They acquire additional momentum along the electric field, and the position of the center of the Doppler spectrum is shifted by $mc\mu_p E/2$. Measuring this shifting, one can determine the e^+ mobility, Fig. 3.8, [38, 39].

Positrons via pair production. Due to relatively small e^+ penetration depth into matter (about 1 mm), PAS cannot study thick samples. To overcome this shortcoming, γ -ray induced positron annihilation spectroscopy was developed. In this case, e^+e^- pairs are generated directly in the studied sample when it is irradiated by high-energy γ -quanta (and they penetrate to a much greater depth than fast positrons), Fig. 3.9.

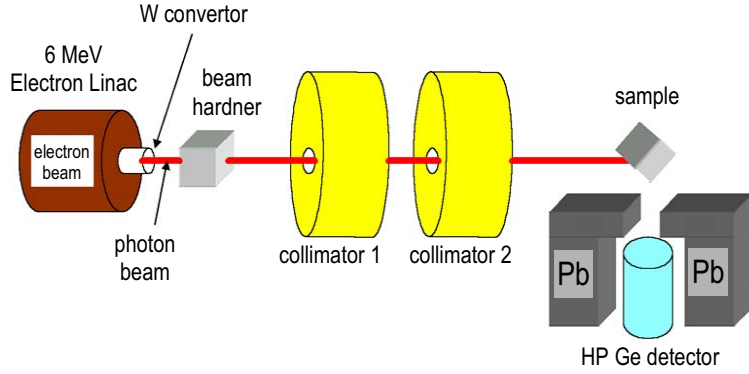
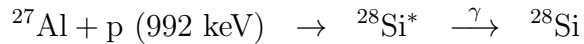


Fig. 3.9 Scheme of the Doppler spectrometer built in Idaho accelerated center. Hard γ -radiation is generated as a result of the retardation of 6 MeV electrons in a tungsten target [40].

It is also possible to generate a monoenergetic beam of γ -quanta as a result of irradiation of a target by accelerated protons. In [41] the Al target was irradiated by 1.5 MeV protons. As a result of proton capture by ^{27}Al nuclei



the excited $^{28}\text{Si}^*$ nuclei are formed. Then they emit prompt gammas (within 1 ps) with the energies of 3.2, 2.8, and 1.78 MeV. As a result they irradiate the studied sample (thick piece of lead) and generate electron-positron pairs therein, Fig. 3.10.

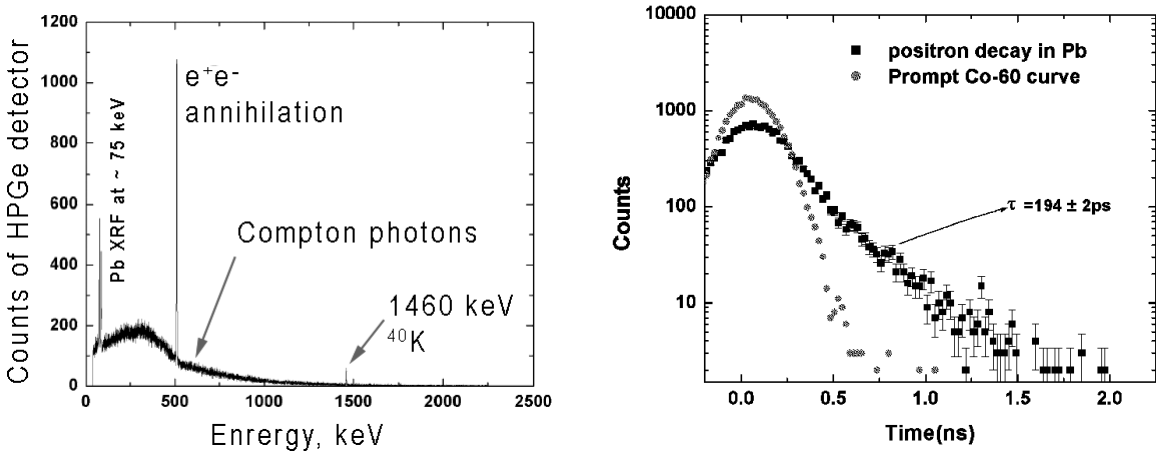


Fig. 3.10 Left: γ -spectrum from Pb sample, measured by HPGe detector. On a bell-like Compton background one may see X-ray lines from Pb fluorescence at 75 keV, annihilation line at 511 keV and well known line emmitid after e-capture of ^{40}K nuclei. Right: LT spectrum in Pb obtained, obtained as a result of the time-base scanning of the 511-peak shown in the left figure.

3.6 Assembling of the CDB setup and developing new routine for processing two-dimensional CDB spectra

As we have mentioned above in CDB experiments the energies E_1 and E_2 of a pair of annihilation photons related to the annihilation of the same positron are simultaneously registered (within a 100 ns time window), Fig. 3.11. Raw CDB spectrum consists of the energy pairs (E_1, E_2) that satisfy the condition (1.22): $-E_b - 2\delta < E_1 + E_2 - 1022 \text{ keV} < 2\delta$, where E_b is the binding energy of the lowest core electrons and 2δ is the energy resolution of both γ -detectors. Simultaneous registration of two annihilation photons allows to reduce significantly the background under the 511 keV photopeak. Due to this reason (unlike the single-detector DBAR) the CDB spectroscopy becomes a unique tool for analyzing chemical environment at the positron annihilation site.

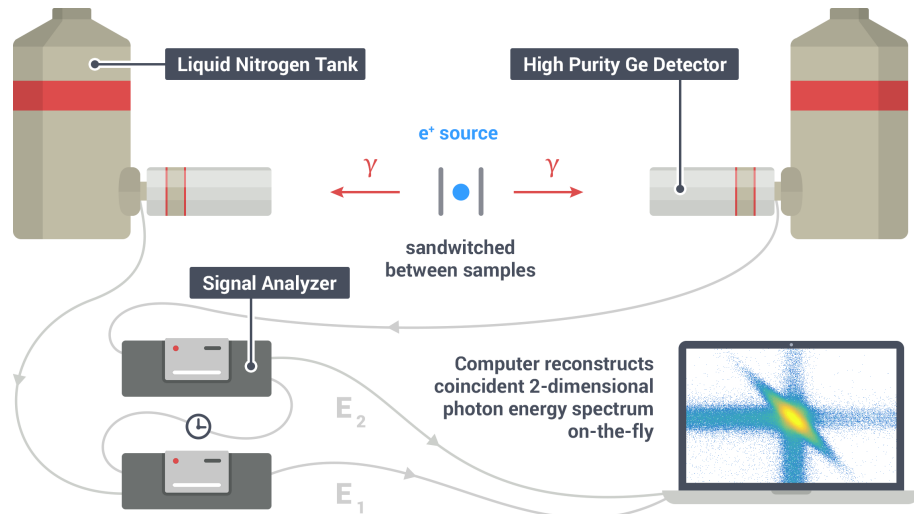


Fig. 3.11 Scheme of the digital Doppler coincidence spectrometer.

Experimental setup. A digital CDB spectrometer has been installed at Bowling Green State University in 2016. It is assembled from two high-purity Ge detectors operating at 4.5 kV and a pair of Lynx multichannel analyzers manufactured by Canberra Industries. Each

analyzer supports up to 32768 channels. This results in a channel width of a 60 eV. The energy resolution of the detectors is about 1.2 keV at 0.5 MeV. Detailed description of its assembling and tuning is given in Appendix .5.

The novelty of Canberra's spectrometer is absence of the coincidence unit. Analyzers are connected to each other and share an internal clock single. Every device continuously saves independent series of energy and time events to the hard drive. The two-dimensional energy spectrum is reconstructed on-the-fly during acquisition with Canberra's TLIST Scanner software. This application imports time-stamped energy data files from both analyzers, matches energy values registered within a time interval of 100 ns and reconstructs two-dimensional energy histogram.

Activity of the positron source used in CDB experiments is usually smaller, then in PALS. In our case activity of the $^{22}\text{NaCl}$ salt was about $10 \mu\text{Ci} = 0.37 \text{ MBq}$. It was capped in between of two $8 \mu\text{m}$ Kapton foils sealed with a silicon glue. The sample-source sandwich was placed in the middle of two HPGe detectors facing towards each other. The distance between detectors was about 1 m. Detectors' dead time was 4.5%. The count rate registered by each analyzer was 3000 counts/s. Acquisition at such relatively low count rate (≈ 50 cps) prevents notable pileup effects and preamplifier saturation.

Energy resolution. The width of the γ -lines (including the annihilation one) is due to random distribution of the energy losses of photoelectrons generated due to the photoelectric effect. Energy of the photoelectrons is mostly spent on ionization losses, but a smaller fraction is spent on heating of the the crystal of the detector. Uncertainty of such a redistribution leads to broadening of the observed line in the γ -spectrum. Typical broadening (FWHM = Full Width at Half Maximum) is about 1 keV. However, the energy resolution of the spectrometer depends on the energy itself. Near the annihilation line (511 keV), it can be determined by interpolation of the FWHM of the nearest γ -lines or FWHM of the lines of artificial γ -emitters having close energy, for example, Ba-133 (436.9 keV) and Cs-137 (661.5

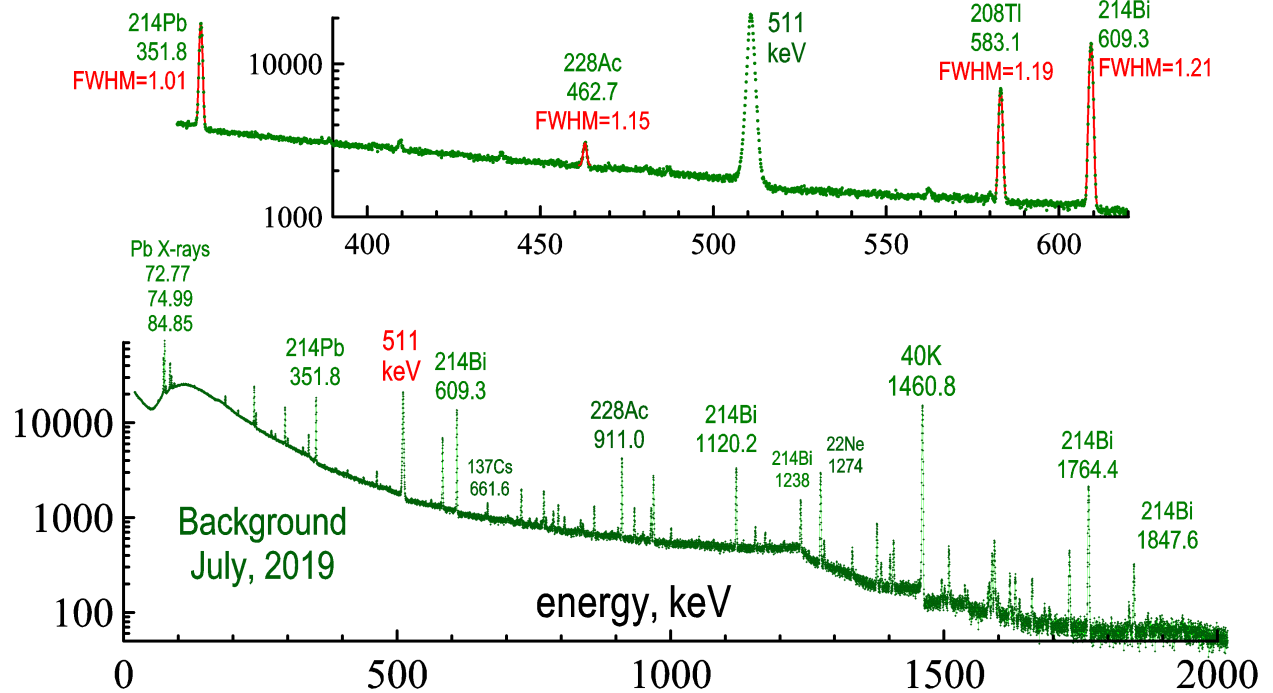


Fig. 3.12 To the determination of the energy resolution of the CDB setup at about 500 keV.

keV), Figs. 3.12, 3.13.

Subtraction of the background. Subtraction of two-dimensional background in CDB spectra were reported by E. do Nascimento et. al. [42–44]. However that software is not open for public use. So we have to develop similar desktop software (TLIST Processor) which subtracts two-dimensional background from the raw CDB spectra. Let us start with consideration of the effects, which contribute to the background in case of one-dimensional γ -spectra and the DBAR spectra particularly [45, 46], Appendix 6.8.6.

It is clearly seen that any photoabsorption γ -line (below we shall consider the annihilation 511 keV line) is asymmetric, that is, the background level (or the count rate) on the left and on the right from the peak is significantly different, Fig. 3.14. What is the reason for that? Obviously, the Compton photons generated by the scattering of 1.27 MeV photons (they accompany e^+ birth in the $^{22}\text{NaCl}$ source) give approximately constant contribution in the energy region close to the annihilation peak (450-550 keV; Fig. 3.14). What are the main

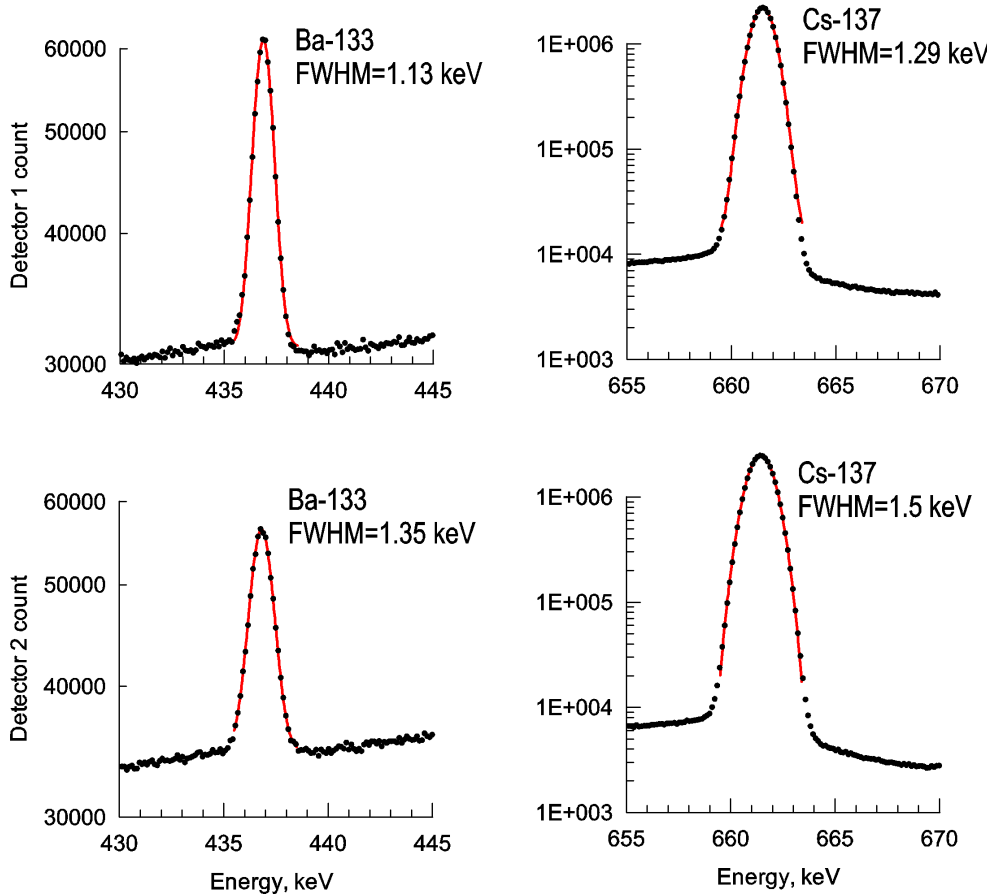


Fig. 3.13 γ -lines of the nearest to the 511-line isotopes (Ba-133 and Cs-137). Upper lines measures by the detector No 1; bottom lines – detector No 2.

factors causing this asymmetry?

- 1) Small angle Compton scattering of annihilation photons. It occurs in any substance arranged on the flight trajectory of the annihilation photons from the assembly (e^+ source and samples) up to the active substance of the detector (i.e. samples, sample holder, housing of the detector and the active substance of the detector itself). When annihilation photons scatter at small angles, they lose small portion of energy, so they arrive on the left wing of the 511 keV peak [47], which distorts the line shape and leads to its asymmetry. This contribution to the background of the 511-line can be approximated by a step function [45];
- 2) Incomplete charge collection. Within the detector volume the free charge carriers (secondary electrons) may randomly disappear because of the electron-hole recombination,

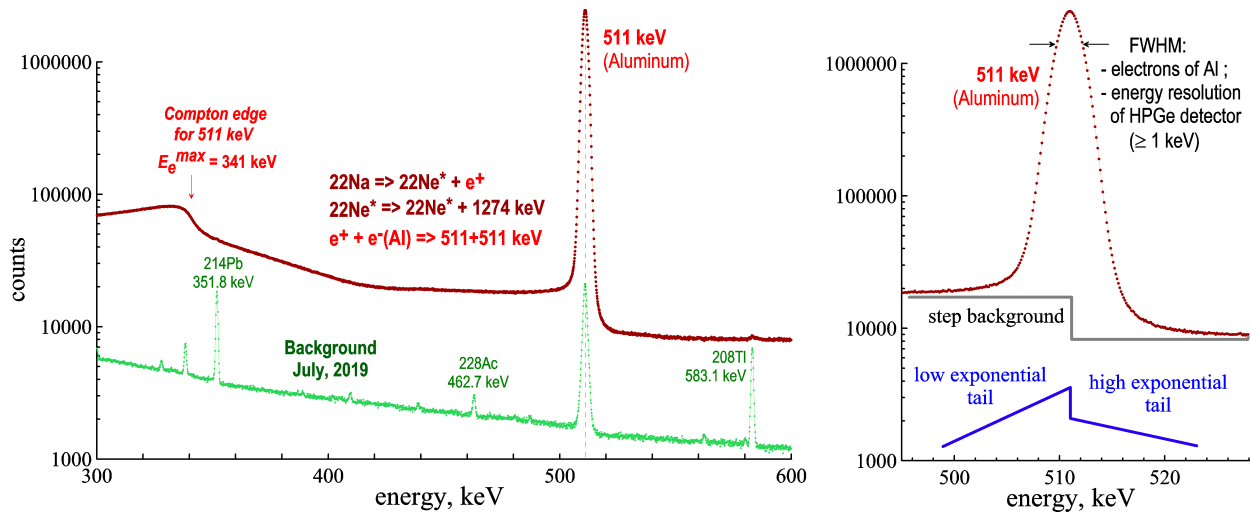


Fig. 3.14 Asymmetry of the photopeak absorption line (511-line in metallic Al).

e^- trapping on impurities, e^- escape on the crystal boundary and so on. Efficiency of these processes depends on the place where the photoabsorption effect took place (close to the crystal boundary or in its bulk; in the “death” area of the electrode, which collects charges or not, and so on). For HPGe detectors with the large crystals it is also important to take into account the so-called the “ballistic deficit” effect. Propagation of the produced free carriers to the electrode (which collects them) takes some time. If the photoelectric absorption took place far from the electrode, the charge collection time becomes longer, so not all charge carriers will be collected (within a fixed detector shaping time, about $1 \mu\text{s}$). Both these effects lead to underestimation of the registered energy of the 511-gammas;

3) The pile-up effect. It is a combination of 511-photon with some low energy photon (there are many of them which hit the detector). As a result the respond may appear at energies higher than 511 keV γ -line. Contribution of this effect decreases with increase of energy (it can be represented by an exponent with a negative slope [43, 45]);

4) In-flight annihilation. Most of the positrons become thermalized before annihilation, but a small fraction of e^+ annihilate (with a low-momentum electron) “in-flight”, having large

kinetic energy K_+ . In this case with the total energy of two annihilating photons is

$$E_1 + E_2 = 2mc^2 + K_+ - E_b \approx 2mc^2 + K_+, \quad K_+ = \frac{p^2}{2m}$$

This effect contribute to the right wings of both one-dimensional DBAR and two-dimensional CDB spectra;

5) 3γ -annihilation. For the annihilation line, there is also a contribution, which comes from 3γ -annihilation. It also increases the background on the left wing of the 511-line. In fact, small fraction of e^+ may form with e^- a triplet state which annihilate into 3 photons (one of which may have energy slightly less 511 keV and also increase background on the left). The software we developed can approximate this 3γ -contribution profile with the Ore-Powell formula [48]. But it seems this effect is negligible because of large separation between detectors in our case.

There could be more complicate combination of these effects, which contribute to the shape of the background. Here we mentioned only the basic ones. The problem of the background subtraction is not easy and directly affects on the results, obtained from the CDB spectra.

An example of the simplest background simulation which takes into account the above mentioned effects in case of the Cs-137 photo-absorption line is given in Fig. 3.15. The background contribution is approximated by a step-function and two exponential wings, while the central part of the line is gaussian:

$$C(E) = BG(E < E_0) + C_0 \exp \left[- \left(\frac{E - E_0}{\text{FWHM}} \right)^2 \right] + BG(E > E_0), \quad (3.20)$$

$$C_0 = 1473000, \quad E_0 = 661.65 \text{ keV}, \quad \text{FWHM} = 1.32 \text{ keV},$$

$$BG(E < E_0) = 2460 + 3130 \cdot \exp(-(E_0 - E)/E_L), \quad E_L = 4.6 \text{ keV},$$

$$BG(E > E_0) = 344 + 4669 \cdot \exp(-(E_0 - E)/E_R), \quad E_R = 2.47 \text{ keV}.$$

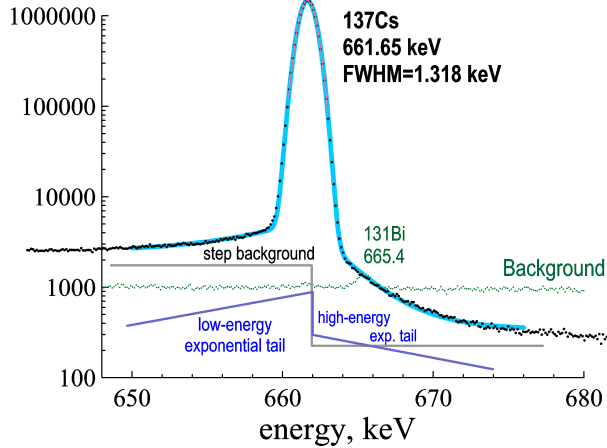


Fig. 3.15 To the approximation of the γ -line of Cs-137.

The background of the two-dimensional CDB spectrum is simulated with two ridge profiles (the step-like function and two exponential tails similar to Eq. 3.20) crossed at 90° at $E_1 = E_2 = 511$ keV on the energy plane, Fig. 3.16. In a perpendicular direction the ridges are broadened by two Gaussian functions with different dispersions and intensities. To take into account the energy resolution of the γ -detectors, the background function is convoluted with two Gaussian functions with FWHMs equal to the energy resolutions of the corresponding detectors. To proceed with CDB background subtraction we developed the TLIST Processor – a desktop GUI application written in C++ built with CERN ROOT scientific framework. The source code is available on GitHub (<https://github.com/petrstefanov/tlist-processor>) and distributed under GNU Public License 3.0.

After the background subtraction from the raw two-dimensional CDB spectrum, $C(E_1, E_2)$, the TLIST generates one-dimensional CDB spectrum, i.e. counts vs. $\Delta = E_1 - E_2$. As a result one obtains the CDB spectrum with almost zero background. From this spectrum it is possible to extract electron momentum distribution and obtain some parameters of the defects.

The one-dimensional CDB spectrum of aluminum and its subtracted background is shown in Fig. 3.17. This spectrum includes contribution of e^+ annihilation in the e^+ source itself (in the Kapton film) which is about 12% from total annihilation events. This contribution may also be subtracted with a help of TLIST.

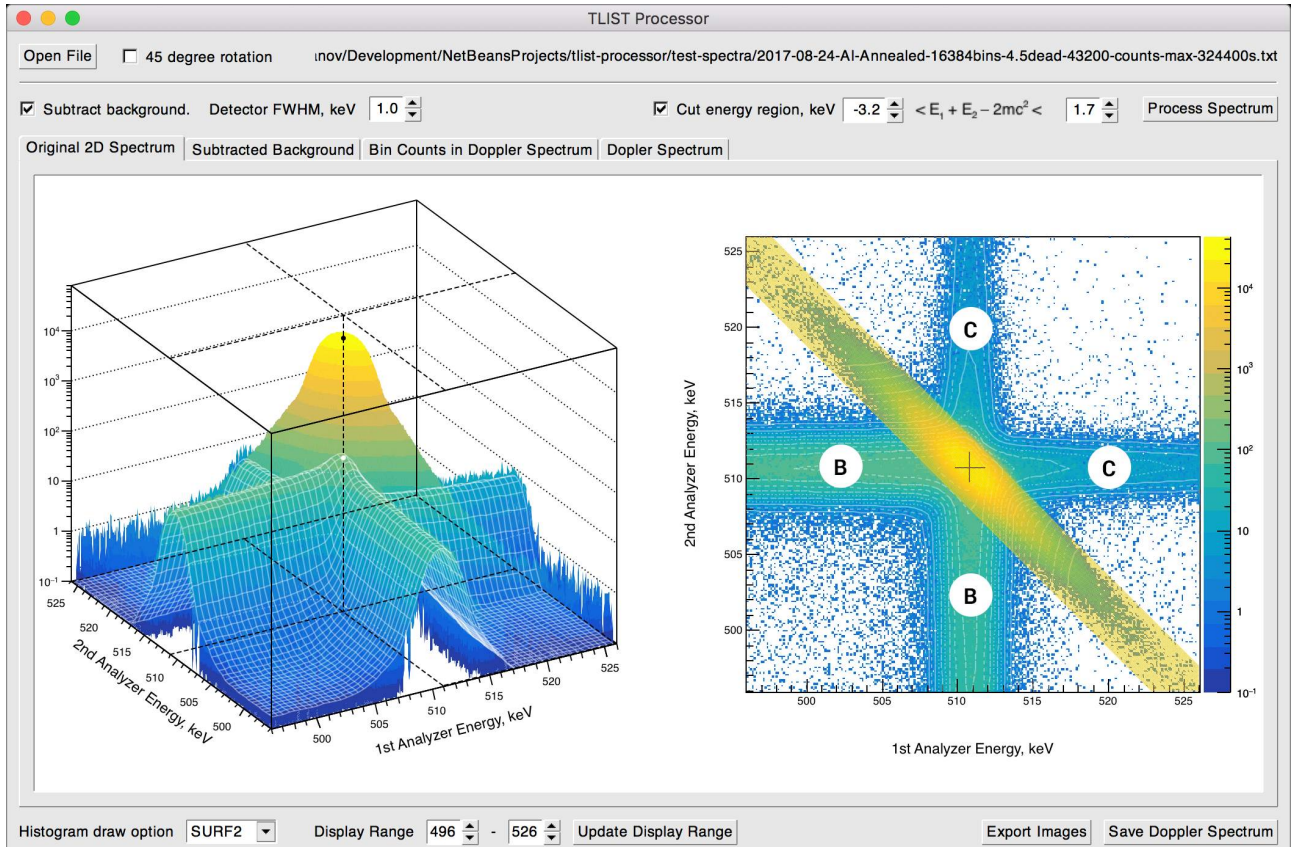


Fig. 3.16 TLIST Processor application fits and subtracts background from the two-dimensional CDB energy spectrum. Ridge profile for $E > 511$ keV (area “C”) consists of contribution from Compton scattered 1.27 MeV photons, pile-up effect and in-flight annihilation. At $E < 511$ keV (area “B”) there are a number of processes discussed in the text. Left: convoluted and fitted background is represented by the overlay mesh. Right: events from the yellow band of a width $1022 \text{ keV} - E_b - 2\delta < E_1 + E_2 < 1022 \text{ keV} + 2\delta$ are selected to construct final single-dimensional CDB spectrum. Here E_b stands for the typical binding energy of core electrons in Al and 2δ is the energy resolution of both γ -detectors.

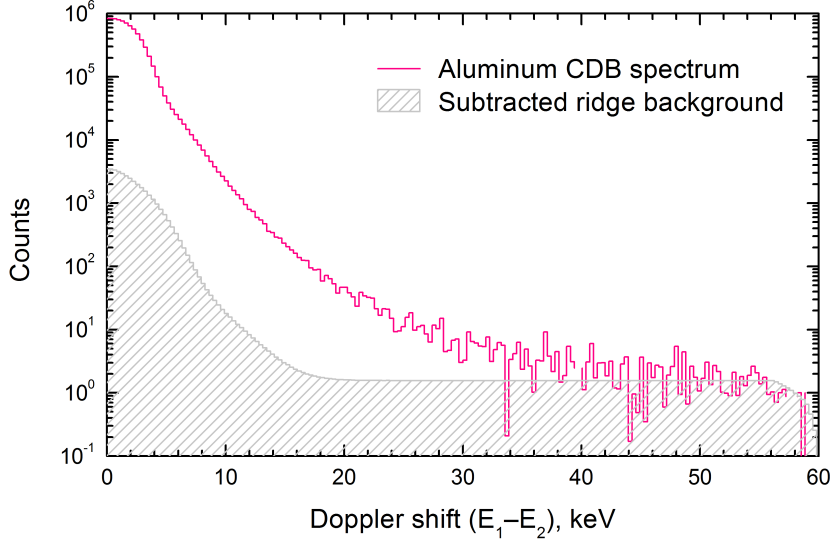


Fig. 3.17 Contribution of the background events to the experimental CDB spectrum.

Deconvolution of the CDB spectra. Theoretical calculation of the CDB spectrum is a complicated quantum-mechanical problem. To proceed with this we need to know the momentum distribution $n(\mathbf{p})$ of the e^+e^- pair at a time of annihilation. In most cases, as we have mentioned above, a positron is fully thermalized, so $n(\mathbf{p})$ is defined by the momentum distribution of the electrons. Using energy and momentum conservation laws, one may relate the energy difference of annihilation photons with z -projection of the momentum (the longitudinal momentum) of the electron that participated in the annihilation process $E_2 - E_1 = cp_z$, see for example Eqs. (3.13) and (3.14).

Our aim when developing the software for CDB spectra processing was not just to decompose them into a set of simple (bell-like) functions, for example, into several Gaussians, but to proceed with more realistic, physically meaningful components. In Chapter 2, we examined some simplest cases: e^+ annihilation on conduction electrons and on “core” electrons. Their wave functions can be roughly approximated by simple analytical expressions, namely $\propto \exp(-r/a)$, $\propto r \cdot \exp(-r/a)$, $\propto (r - b) \exp(-r/a)$, and gaussian. For each of them we have calculated analytically corresponding electron momentum distribution $n(\mathbf{p})$ (taking the

Fourier transforms of the electron wave functions) and obtained respective contributions to the CDB spectrum, Fig. 2.3.

It is important to note that the obtained contributions substantially differ from the Gaussian components. It means that the extracted parameters (results of the fitting of the spectra, for example, energies of core electrons on which positrons annihilate) will also be different.

In order to check the goodness of the data acquired by our CDB spectrometer and the developed software, we measured CDB spectra of the annealed metals – Al, Cu, Zn and Fe. For fitting the spectra, we developed a special software (SW Calculator), which deconvolutes one-dimensional CDB spectra into separate contributions from conduction, valence and core electrons according to our theoretical model mentioned above. Source code and can be downloaded for free from GitHub (<https://github.com/petrstepanov/sw-calculator>). The software accounts for a certain energy resolution of the HPGe detectors, Eq. 3.16. The energy resolution function we have determined separately, Figs. 3.12 and 3.13, $\text{FWHM} = 1.2 \text{ keV}$.

A CDB spectrum of Al ($1s^2 2s^2 2p^6 3s^2 3p^1$) is shown in Fig. 3.17. Elementary electron Fermi gas theory predicts the following relation between the Fermi energy and the concentration of the conduction electrons [49]:

$$E_F = \text{Ry} \cdot (3\pi^2 n_e a_B^3)^{2/3}. \quad (3.21)$$

If we adopt that the conduction electron number density in Al is $n_e = 3/\Omega_{\text{Al}}$, (3 is the number of outer electrons $3s^2 3p^1$, which are transferred to the conduction band, and $\Omega_{\text{Al}} = 16.7 \text{ \AA}^3$ is the volume per one atom in Al). The contribution of these conduction electrons to $C(\Delta)$ is described by the inverted parabola, from which (with a help of Eq. 3.21) we obtain the Al Fermi energy $12.3(5) \text{ eV}$, Table 3.2. It agrees well with the literature value $E_F = 11.7 \text{ eV}$ [49].

Table 3.2 Obtained values of the Fermi energies and electron binding energies (wave functions approximated by Gaussians). Experimental values for the Fermi energy (a) are taken from ref. [49]. Theoretical electron binding energies (b) are taken from ref. [50]. Integration ranges (in keV) for S and W parameters were following: S [-1.6, 1.6] and for W [-11.52,-5.52] and [5.52, 11.52].

	Al	Fe	Cu	Zn
Fermi energy, [eV]	12.3 ± 0.5 11.7^a	9.36 ± 0.08 11.1^a	7.6 ± 0.4 7.00^a	9.36 ± 0.06 9.47^a
Three inner shell electron binding energies, [eV]	40 ± 8 —	24.89 ± 0.08 59^b	23 ± 6 80^b	31.2 ± 0.5 91^b
	80 ± 30 77 ^b	65.6 ± 1.1 61^b	46 ± 13 82^b	75.9 ± 2.1 94^b
	215 ± 200 121 ^b	250 ± 9 98^b	250 ± 60 127^b	309 ± 6 141^b
S parameter, [arb.u.]	$0.55314 \pm 2.4 \times 10^{-4}$	$0.4341 \pm 3 \times 10^{-4}$	$0.4839 \pm 4 \times 10^{-4}$	$0.51211 \pm 2.1 \times 10^{-4}$
W parameter, [arb.u.]	$0.02010 \pm 1.5 \times 10^{-4}$	$0.06544 \pm 9 \times 10^{-5}$	$0.05653 \pm 1.3 \times 10^{-4}$	$0.05242 \pm 5 \times 10^{-5}$

Inner shell electrons ($1s^2$ $2s^2$ $2p^6$) have following binding energies 1564 eV, 121 eV and 77 eV. On the first step we approximated the inner electron wave functions with Gaussians. It results in gaussian contributions to the CDB spectrum and gives a crude estimation of the electron binding energies, Table 3.2 and Fig. 3.18. Fitting of the CDB spectra using components calculated above is now underway.

Experimental Doppler spectra of aluminum, iron, copper and zinc were measured and processed by our software, Fig. 3.18. The annihilation spectrum in Kapton was measured separately. It is subtracted from the every spectrum of the metals with a certain intensity obtained from PALS measurements (12%). Corresponding core electron binding energies obtained from the fit are given in Table 3.2.

Fermi energies obtained from the fit are in an agreement with the reference values [49]. Reasonable agreement with the known electron binding energies [50] is obtained.

We are looking forward to apply more realistic expressions for the inner electron wave functions include angular dependencies. These improvements are expected to give better agreement for valence and core electron binding energies. We also plan to include in the software simple description of a positron in structural defects (vacancies). Trapped positron can be considered as a particle in a potential well and its contribution into the CDB spectra

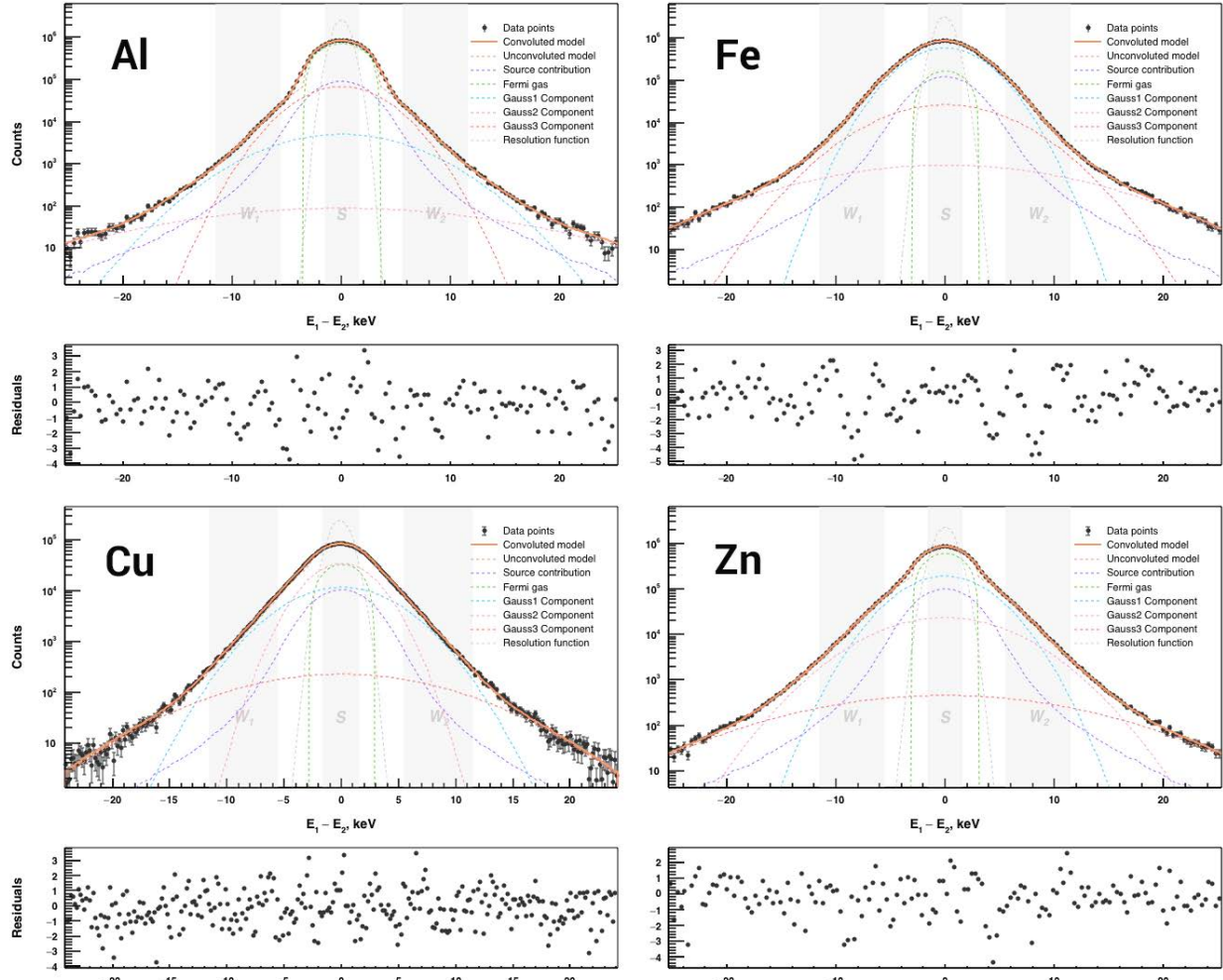


Fig. 3.18 Doppler spectra of simple metals deconvoluted into a set of contributions of annihilation on Fermi gas electrons (inverted parabola) and Gaussian components. Contribution from annihilation in positron source is subtracted from spectra. Convolution with the energy resolution function of 1.2 keV FWHM is applied.

can be roughly calculated. We also plan to proceed with a simultaneous fitting of PALS and CDB spectra. This will result in a better understanding of the defect structure of the studied materials.

3.7 Brief conclusion on this chapter

This chapter provides a brief overview on positron sources used in the positron annihilation spectroscopy, as well as its main experimental methods.

Fully-digital CDB spectrometer (energy resolution is 1.2 keV) with a software coincidence unit is set up and tested at Bowling Green State University. Detailed description of its assembling and tuning is given in Appendix .5. Special attention is paid to the estimation of the energy resolution of the spectrometer and different background contributions in the region close to the annihilation line (511 keV). Original software (TLIST Processor) that fits and subtracts the two-dimensional background from raw CDB spectra is developed. It also allows to export one-dimensional CDB spectrum suitable for further processing/interpretation (the software is available for public use).

We suggest to deconvolute one-dimensional CDB spectra into contributions from e^+ annihilation on conduction and inner shell electrons (several typical contributions to CDB spectrum are calculated analytically). This approach is realized by means of another desktop software (SW Calculator). This program calculates also S- and W-parameters of the CDB spectra, extracts Fermi energies and binding energies of core electrons.

Experimental spectra of pure and well annealed Al, Fe, Cu and Zn samples are measured and processed with a help of our software. The obtained parameters are in a good agreement with the reference values for the investigated metals.

Chapter 4 Positron trapping models

We have already mentioned that PAS is very convenient tool for studying vacancy-type defects in solids. Having positive charge, free positrons are strongly repelled from positively charged nuclei. Therefore, vacancy-type defects (which are just empty space) easily trap positrons, so they are “positronophilic” defects. Moreover, some vacancies may be negatively charged, which increase their affinity to positrons.

A positron annihilates in a substance being in one of the two states: in thermalized “free” state (quasifree positron, qf-e⁺) or trapped in a defect. Since probability of the e⁺ annihilation is proportional to the electron density, the positron lives longer in the vacancy-type defects, because low electron density therein.

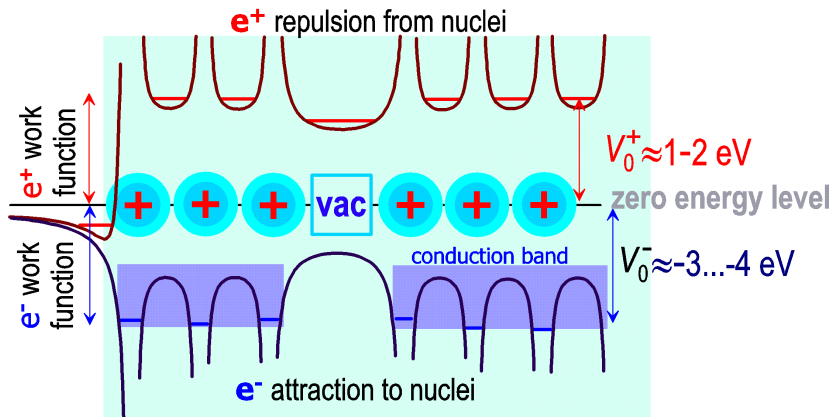


Fig. 4.1 Potentials for e⁺ and e⁻ in a crystal lattice.

Motion of a thermalized (quasifree) positron in a medium can be described in terms of a wave packet. The positron wave function can be roughly approximated with a help of a Gaussian-like function, having a characteristic width of order of its de Broglie wavelength, $\lambda = \hbar/m_e v_{th}$. When $T = 300$ K and $3k_B T/2 \approx m_e v_{th}^2/2$, we obtain $v_{th} \simeq 10^7$ cm/s – the e⁺ thermal velocity, so $\lambda = \hbar/m_e v_{th} \approx 10$ Å. qf-e⁺ motion may be considered as diffusion-like with the diffusion coefficient, $D_+ \simeq \lambda v_{th}/6 \approx \hbar/6m_e \approx 1/6$ cm²/s.

Diffusion displacement $L_d \sim \sqrt{4D_+\tau_+}$ of a thermalized e⁺ during its lifetime τ_+ (100-200

ps) before annihilation is about $1000 \text{ \AA} = 0.1 \mu\text{m}$. If we simulate the qf-e⁺ with a sphere of a diameter λ , then we obtain that the lowest defect concentration that qf-e⁺ can sense is about 0.1 ppm (probably 1 ppm is more realistic number).

Kinetics of the positron trapping on defects depends on their concentration c_d . If c_d is high enough, that is, when the average distance between defects is comparable with the “size” of the positron ($c_d > 1/\lambda^3 > 10^4$ ppm), then the positron for any small time interval dt can annihilate in a bulk of the studied sample and/or can be captured by a defect (in other words, when at least one defect at any time is present within the e⁺ “region of sensitivity”). This situation is called as “kinetic control”. In this case the Standard Trapping Model (STM) is definitely applicable [51, 52]. One may say that the main approximation of STM is that the e⁺ trapping can be described in terms of the probability (or trapping rate), which is independent of the positron location in the bulk.

When concentration of defects is small ($< 10^4$ ppm), e⁺ trapping by a defect depends on how quickly the positron can meet the defect. This situation is called as “diffusion control”. Such a model is called as the Diffusion Trapping Model (DTM) [53–56].

4.1 Standard trapping model (one type of the defects)

Let us consider formulation of the STM, when only one type of the defects (vacancies) is presented. Suppose that qf-e⁺ annihilates in an “ideal” bulk of the studied sample (“ideal” means defect-free crystal lattice without structural defects) with the rate λ_b . At the same time positrons can be trapped by defects (let \varkappa_d is the trapping probability) and then annihilate from the trapped state (let λ_d is the e⁺ annihilation rate from the trapped state), Fig. 4.2.

Annihilation kinetics of the positrons obeys the following balance equations, which are written in terms of probabilities (or populations) of different positron states, namely, the probability of finding a positron in the quasifree state in a bulk, n_b , and the probability of finding a positron in a trapped state in a defect, n_d :

$$\dot{n}_b(t) = -\lambda_b n_b - \varkappa_d n_b, \quad n_b(0) = 1, \quad (4.1)$$

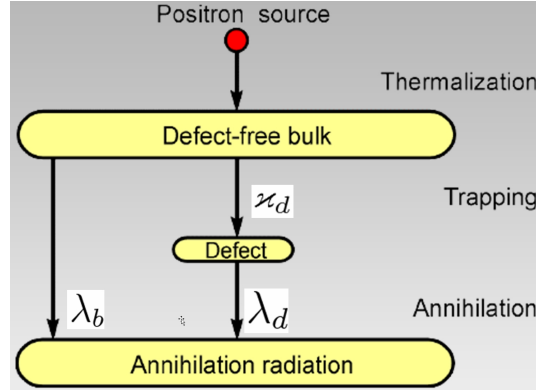


Fig. 4.2 Scheme of e^+ annihilation in a metal when there is only one type of the defects, capable to trap positrons.

$$\dot{n}_d(t) = \kappa_d n_b - \lambda_d n_d, \quad n_d(0) = 0. \quad (4.2)$$

Solutions of these equations are the following:

$$n_b(t) = e^{-(\lambda_b + \kappa_d)t}, \quad n_d(t) = \frac{\kappa_d}{\lambda_b + \kappa_d - \lambda_d} [e^{-\lambda_d t} - e^{-(\lambda_b + \kappa_d)t}]. \quad (4.3)$$

Now let us calculate the number of annihilation events recorded in the n -th channel of the multichannel analyzer (MCA), that is, during the time interval $[t_n, t_n + \Delta t]$. To do this, it is necessary to integrate over the time two terms describing positron annihilation (Δt is the time duration of the MCA channel):

$$C \left(t = \frac{t_n + t_{n+1}}{2} \right) \propto \int_{t_n}^{t_{n+1}} (\lambda_b n_b + \lambda_d n_d) dt \approx [\lambda_b n_b(t) + \lambda_d n_d(t)] \Delta t. \quad (4.4)$$

This expression is a theoretical prediction for the shape of the lifetime (LT) annihilation spectrum. After collecting similar terms, one gets:

$$C(t) \propto \Delta t \left[\left(\lambda_b - \frac{\lambda_d \kappa_d}{\lambda_b + \kappa_d - \lambda_d} \right) e^{-(\lambda_b + \kappa_d)t} + \frac{\lambda_d \kappa_d}{\lambda_b + \kappa_d - \lambda_d} e^{-\lambda_d t} \right]. \quad (4.5)$$

We may rewrite it as:

$$C(t) \propto \lambda_1 I_1 e^{-\lambda_1 t} + \lambda_2 I_2 e^{-\lambda_2 t}, \quad \text{where} \quad \lambda_1 = \lambda_b + \varkappa_d, \quad \lambda_2 = \lambda_d, \quad (4.6)$$

$$I_1 = \frac{\lambda_b - \lambda_d}{\lambda_b + \varkappa_d - \lambda_d}, \quad I_2 = \frac{\varkappa_d}{\lambda_b + \varkappa_d - \lambda_d}, \quad I_1 + I_2 = 1.$$

With these definitions of intensities, I_1 has a meaning of probability that the positron will annihilate from a quasifree state, and I_2 is the probability that e^+ will annihilate from a localized state.

For comparison of this theoretical model with the experimental LT spectra, it is necessary to add to $C(t)$ contribution from e^+ annihilation in the positron source, $C_{source}(t)$, and also take into account the presence of the background BG due to random coincidences. After all we must convolve the obtained “theoretical” spectrum with the time resolution function of the spectrometer, $f_{res}(\tau)$:

$$C_{exp}(t) = \int_{-\infty}^{\infty} [C(\tau) + C_{source}(\tau)] f_{res}(t - \tau) d\tau + BG. \quad (4.7)$$

From here one may understand the meaning of the resolution function. It gives the shape of the LT spectrum when registering pairs of photons fall into the “start” and “stop” detectors at the same time moment.

Let us make a comment concerning random spatial distribution of acceptors (for example, vacancy-type defects in the crystal lattice) and the end-point position of the thermalized positron. Unlike the previous consideration, let the concentration of the traps be not too high, so the positron needs some time to reach the defect in a diffusive way. Without delving into derivation of the kinetics of e^+ disappearance in this case, we present the final formula [57, 58] and discuss the meaning of the terms written below:

$$n_b(t) = \exp \left(-\lambda_b t - \frac{4\pi}{3} c_d R^3 - 8c_d R^2 \sqrt{\pi D_+ t} - 4\pi D_+ c_d R t \right), \quad t \gg R^2/D_+. \quad (4.8)$$

The factor $e^{-\lambda_b t}$ takes into account the qf-e⁺ annihilation in a defect-free volume. The next term (“initial step-down”) corresponds to the situation when the positron is thermalized (“stopped”) very close to the acceptor (inside a reaction sphere with the radius equal to R – the sum of the reaction radii of the acceptor and the positron). The square-root-term in time describes disappearance of “close pairs” (positron + acceptor) when the positron stopped near the acceptor (but not within the reaction sphere). Such pairs decay rather quickly. The last term (exponential in time) corresponds to the case when qf-e⁺ stopped being at the “average” distance to the nearest acceptor, $\simeq c_d^{-1/3}$. This last term ($\varkappa_d n_b$) is taken into account in the STM equations (4.1). In the frameworks of the theory of diffusion-controlled reactions, the value \varkappa_d (more precisely $4\pi D_+ R$) is the rate constant of the scavenging chemical reaction.

Basing on Eq. (4.8), one can refine the STM by taking into account the “time dependence” of the reaction rate constant of this chemical reaction (e⁺ trapping). It means the following. Let differentiate over time Eq. (4.8) (we assume that $\varkappa_d = 4 \pi D_+ R c_d$): members:

$$\dot{n}_b(t) = -\lambda_b n_b - \varkappa_d \left(1 + \frac{R}{\sqrt{\pi D_+ t}} \right) n_b, \quad n_b(0) = 1. \quad (4.9)$$

Here (in the initial condition) we neglected the term of the initial step-down, assuming that $n_b(0) = 1$. The last term on the right side of this equation is a correction of the e⁺ trapping kinetics. It takes into account e⁺ trapping by defects in “close pairs” (positron + acceptor). Obviously, the similar term appears in Eq. (4.2) for n_d :

$$\dot{n}_d(t) = \varkappa_d \left(1 + \frac{R}{\sqrt{\pi D_+ t}} \right) n_b - \lambda_d n_d, \quad n_d(0) \approx 0. \quad (4.10)$$

Substituting here typical numbers for parameters ($R \simeq 10 \text{ \AA}$, $D_+ \simeq 0.3 \text{ cm}^2/\text{s}$), we obtain that at $t > 1 \text{ ps}$ the expression $R/\sqrt{\pi D_+ t}$ turns out to be much less than 1. Thus, Eqs. (4.9-4.10) are reduced to Eqs. (4.1).

Knowing the e^+ trapping rate, one may estimate concentration of the defects, c_d . It can be done using the Smoluchowski expression for the diffusion-controlled reaction rate-constant:

$$\varkappa_d = 4\pi D_+ R c_d. \quad (4.11)$$

Substituting $D_+ \simeq 1/6 \text{ cm}^2/\text{s}$, $R \simeq 10 \text{ \AA}$ one obtains

$$\varkappa_d \simeq 3 \cdot 10^{-7} [\text{cm}^3/\text{s}] \cdot c_d.$$

Quite often concentration of defects is expressed not as their number per 1 cm^3 , but as a number of defects per one atom in the matrix.

For example, in a crystalline silicon the quantity $c_d \Omega_{\text{Si}}$ is the so-called “defect atomic fraction”, where $\Omega_{\text{Si}} = 20 \text{ \AA}^3$ is the volume per one Si atom. So e^+ trapping rate can be rewritten as follows:

$$\varkappa_d = \mu c_d \Omega_{\text{Si}}, \quad \mu = 4\pi D_+ R / \Omega_{\text{Si}} \simeq 10^{16}, \text{ s}^{-1}.$$

In the book by R.Krause-Rehberg [1] on p.103 one may find experimental values for μ for some electrically neutral defects in semiconductors. It is seen that the value 10^{16} 1/s is about 10 times as large than μ -values given there. It is because our estimation took into account the diffusion control only. We assumed that any collision between e^+ and a defect immediately leads to the e^+ trapping. In fact, it is not true. There is also the so-called “kinetic control”, which is associated with the need of energy transfer from the positron to the lattice, when e^+ getting trapped in a defect. This circumstance reduces probability of the e^+ trapping. Formally it can be expressed as a diminishing of the reaction radius R (by a factor of 10, i.e. $R \simeq 1 \text{ \AA}$). With this we obtain correct estimation of μ : $\simeq 10^{15} \text{ 1/s}$.

4.2 Standard trapping model (two types of the defects)

The above model can be easily generalized on the case when two types of defects are present in the studied sample (for example, monovacancies and divacancies). Let n_{d1} and n_{d2} are probabilities of finding a positron trapped either by the first or the second type of defects. \varkappa_{d1} and \varkappa_{d2} stand for the corresponding positron trapping rates, and λ_{d1} and λ_{d2} are the e^+ annihilation rates from the trapped states. In this case, equations describing kinetics of positron annihilation and trapping are the following:

$$\dot{n}_b = -\lambda_b n_b - (\varkappa_{d1} + \varkappa_{d2}) n_b, \quad n_b(0) = 1, \quad (4.12)$$

$$\dot{n}_{d1} = \varkappa_{d1} n_b - \lambda_{d1} n_{d1}, \quad n_{d1}(0) = 0; \quad \dot{n}_{d2} = \varkappa_{d2} n_b - \lambda_{d2} n_{d2}, \quad n_{d2}(0) = 0.$$

Solutions of these equations are similar to Eqs. (4.3):

$$\begin{aligned} n_b(t) &= e^{-(\lambda_b + \varkappa_{d1} + \varkappa_{d2})t}, & n_{d1}(t) &= \frac{\varkappa_{d1}[e^{-\lambda_{d1}t} - e^{-(\lambda_b + \varkappa_{d1} + \varkappa_{d2})t}]}{\lambda_b + \varkappa_{d1} + \varkappa_{d2} - \lambda_{d1}}, \\ n_{d2}(t) &= \frac{\varkappa_{d2}[e^{-\lambda_{d2}t} - e^{-(\lambda_b + \varkappa_{d1} + \varkappa_{d2})t}]}{\lambda_b + \varkappa_{d1} + \varkappa_{d2} - \lambda_{d2}}. \end{aligned} \quad (4.13)$$

Now similar to Eq. (4.4) one may calculate the theoretical shape of the LT spectrum:

$$C \left(t = \frac{t_n + t_{n+1}}{2} \right) \propto \lambda_b n_b(t) + \lambda_{d1} n_{d1}(t) + \lambda_{d2} n_{d2}(t). \quad (4.14)$$

Substituting here Eqs. (4.13), it is possible to reduce it to:

$$C(t) \propto \lambda I_1 e^{-\lambda t} + \lambda_{d1} I_2 e^{-\lambda_{d1} t} + \lambda_{d2} I_3 e^{-\lambda_{d2} t}, \quad (4.15)$$

where

$$\lambda = \lambda_b + \varkappa_{d1} + \varkappa_{d2}, \quad I_1 = \frac{\lambda_b - \lambda_{d1} I_1 - \lambda_{d2} I_2}{\lambda}, \quad I_2 = \frac{\varkappa_{d1}}{\lambda - \lambda_{d1}}, \quad I_3 = \frac{\varkappa_{d2}}{\lambda - \lambda_{d2}}. \quad (4.16)$$

It is easy to check, that $I_1 + I_2 + I_3 = 1$.

Knowing trapping rates \varkappa_{d1} and \varkappa_{d2} one may estimate concentrations of the both type of the defects.

4.3 Diffusion trapping model

In PAS investigations of polycrystalline samples (or powders) with the grain size up to $1 \mu\text{m}$, one can expect that positrons, moving in a diffusive way, may reach the crystallite boundary, localize and annihilate therein. This will lead to appearance of the long-lived component in LT spectra. This process can be described by simulating a grain by a sphere of the radius L [53–56]. Presence of defects (vacancies) uniformly distributed within grains and are able to trap positrons, are taken into account in the framework of the standard trapping model. In this case, the positron can exist in the following three states:

- a) the quasi-free positron in the bulk, e_b^+ . Its survival probability at time t is $n_b(t)$. Its annihilation rate is λ_b ;
- b) the positron captured by a vacancy, e_v^+ . The survival probability of e_v^+ is $n_v(t)$. Its annihilation rate is λ_v ;
- c) the positron, which reached a grain boundary and localized there, e_g^+ . We denote its survival probability as $n_g(t)$ and its annihilation rate is λ_g .

Let \varkappa_v is the trapping rate of e_b^+ by vacancies. We denote the diffusion flux of the quasifree positrons on the grain boundaries as $J(t)$ (expression for $J(t)$ is obtained in Appendix .5).

Then the set of equations describing evolution of the positron states is as follows:

$$\begin{cases} \dot{n}_b(t) = -(\lambda_b + \varkappa_v)n_b - J(t), & n_b(0) = 1, \\ \dot{n}_v(t) = \varkappa_v n_b - \lambda_v n_v, & n_v(0) = 0, \\ \dot{n}_g(t) = J(t) - \lambda_g n_g, & n_g(0) = 0 \end{cases} \quad (4.17)$$

where

$$J(t) = \frac{6\lambda_J e^{-(\lambda_b + \varkappa_v)t}}{\pi^2} \sum_{m=1}^{\infty} e^{-\lambda_J m^2 t}, \quad \text{where } \lambda_J = \frac{\pi^2 D_+}{L^2}, \quad (4.18)$$

Solution of the first of the equation is (see Eq. 13)):

$$n_b(t) = \frac{6e^{-(\lambda_b + \kappa_v)t}}{\pi^2} \sum_{m=1}^{\infty} \frac{e^{-\lambda_J m^2 t}}{m^2}. \quad (4.19)$$

Now we can integrate the second and third equations:

$$n_v(t) = \frac{6\kappa_v}{\pi^2} \sum_{m=1}^{\infty} \frac{e^{-\lambda_v t} - e^{-(\lambda_b + \kappa_v + \lambda_J m^2)t}}{m^2(\lambda_b + \kappa_v + \lambda_J m^2 - \lambda_v)}, \quad (4.20)$$

$$n_g(t) = \frac{6\lambda_J}{\pi^2} \sum_{m=1}^{\infty} \frac{e^{-\lambda_g t} - e^{-(\lambda_b + \kappa_v + \lambda_J m^2)t}}{\lambda_b + \kappa_v + \lambda_J m^2 - \lambda_g}. \quad (4.21)$$

Note that when $\lambda_J = 0$ (no e_b^+ diffusion), $n_g(t)$ is equal to zero, and expressions for n_b and n_v coincide with equations (4.3) obtained in the framework of the standard trapping model.

Shape of the LT spectrum is calculated exactly in the same way as it was done for STM, Eq. (4.4). The number of annihilation start-stop coincidences in the k 's channel of the analyzer is:

$$C \left(t = \frac{t_k + t_{k+1}}{2} \right) \propto \int_{t_k}^{t_{k+1}} (\lambda_b n_b + \lambda_v n_v + \lambda_g n_g) dt \approx [\lambda_b n_b(t) + \lambda_v n_v + \lambda_g n_g(t)] \Delta t. \quad (4.22)$$

Integration of $C(t)$ over t from zero to infinity gives unity. This reflects the fact that at $t = 0$ there is only one positron in the system, and after a long period of time the positron will inevitably annihilate, which increases counts by unity in one of the MCA channels.

Equation (4.22) is a theoretical prediction for the shape of the LT annihilation spectrum in the case when e^+ trapping by vacancies and by grain boundaries is taken into account. Our model contains 5 adjustable parameters: λ_b , λ_v , λ_g , the “diffusion rate” $\lambda_J = \pi^2 D_+/L^2$ and the e^+ trapping rate by vacancies – κ_v .

Although the expressions for the positron states (and the observed spectrum) are represented in the form of infinite exponential series, apparently only the first few terms in the series are really important, because the series converge rather well.

4.4 Formation of “hot” Ps in intergrain space in nanopowders and its subsequent thermalization

It is well known that a positronium atom (Ps) is not formed in conducting substances (including polycrystalline). This is because of the presence of a large number of quasifree electrons near the positron, none of which spend enough time close e^+ to talk about the formation of the Ps atom. In dielectric substances Ps formation is quite possible, which leads to the presence of a long-time component in the LT (lifetime) spectra. Below, we consider the most typical scenario of the formation and annihilation of various positron states in nanodispersed powders (particularly in Al_2O_3 powders). The proposed model is based on the work of Ch. Dauwe [60, 61] and will be used for fitting of the LT and CDB (Coincidence Doppler Broadening) spectra of various powders using the software that we are developing [32, 62, 63].

A scheme of formation of various states e^+ in Al_2O_3 nanopowders is shown in Fig. 4.3. During e^+ ionization slowing down, the positron creates many ion-electron pairs. Then it becomes thermalized and stays for a short time (about 50-100 ps) in a quasi-free state (qf- e^+). qf- e^+ can either annihilate with a rate of λ_b , or be captured by a vacancy-type defect (as a result vac- e^+ is formed). qf- e^+ can also reach a crystallite boundary and be localized there in the surface-bound state, surf- e^+ . Moreover, qf- e^+ can interact with one of the secondary (track) electrons and form a quasi-free positronium atom, qf-Ps, which diffuses in the bulk of crystallite and may reach its boundary. After that qf-Ps flies into the space in between the crystallites, having excess kinetic energy (1-2 eV). It occurs due to the fact that qf-Ps is an electrically neutral particle and, unlike a positron, does not experience polarization attraction to the surface of the crystallite. So Ps atom does not form a surface-bound state. In the inter-crystallite space we must distinguish two different spin states of the Ps atom – ortho-Ps and para-Ps (o-Ps, p-Ps), since their annihilation rate significantly differs when they reside in-between the crystallites.

Below, we do not consider a short initial time interval (some tens of ps) during which

thermalized e^+ may meet one of the track e^- and form qf-Ps. Subsequent evolution of the positron states, including qf- e^+ capture by vacancy-type defects, formation of surf- e^+ as well as o-Ps and p-Ps is described by the following equations:

$$n_b(t) = (1 - P_{Ps})e^{-(\lambda_b + \kappa_v)t}, \quad (4.23)$$

$$n_v(t) = (1 - P_{Ps}) \frac{\kappa_v [e^{-\lambda_v t} - e^{-(\lambda_b + \kappa_v + \kappa_s)t}]}{\lambda_b + \kappa_v + \kappa_s - \lambda_v}, \quad (4.24)$$

$$n_s(t) = (1 - P_{Ps}) \frac{\kappa_s [e^{-\lambda_s t} - e^{-(\lambda_b + \kappa_v + \kappa_s)t}]}{\lambda_b + \kappa_v + \kappa_s - \lambda_s}, \quad (4.25)$$

$$\dot{n}_{Ps}(t) = -P_{Ps}J(t) - \lambda_{Ps}n_{Ps}, \quad n_{Ps}(0) = P_{Ps}, \quad (4.26)$$

$$\dot{n}_o(t) = \frac{3P_{Ps}J(t)}{4} - \left(\lambda_{3\gamma} + \lambda_{po} + \frac{\lambda_{opc}(t)}{4} \right) n_o, \quad n_o(0) = 0, \quad (4.27)$$

$$\dot{n}_p(t) = \frac{P_{Ps}J(t)}{4} + \frac{\lambda_{opc}(t)}{4} n_o - (\lambda_{2\gamma} + \lambda_{po}) n_p, \quad n_p(0) = 0. \quad (4.28)$$

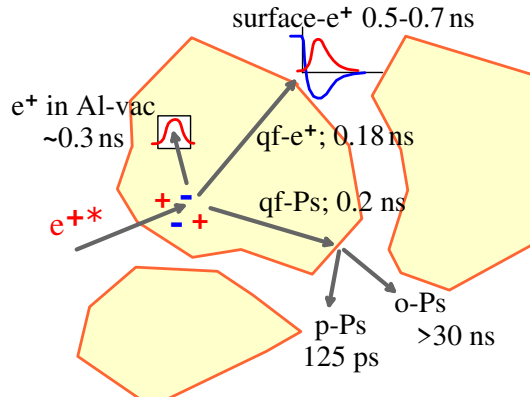


Fig. 4.3 Formation of different positron states in Al_2O_3 nanopowders.

Here $n_b(t)$, $n_v(t)$, $n_s(t)$ and $n_{Ps}(t)$ are the probabilities to observe qf- e^+ , vac- e^+ , surf- e^+ and qf-Ps at a time t ; λ_b , λ_v , λ_s and λ_{Ps} are the annihilation rates of e^+ in these states. P_{Ps} is the qf-Ps formation probability, κ_v is the qf- e^+ trapping rate by vacancy-type defects (here they are Al monovacancies), κ_s is the rate of reaching the crystallite boundary by qf- e^+ (as a result qf- e^+ transforms into surf- e^+). Actually the first three equations describe

behavior of positrons, escaping formation of qf-Ps. $n_o(t)$ and $n_p(t)$ are probabilities to find o-Ps and p-Ps in inter-crystallite space. $\lambda_{3\gamma} \approx 0.007 \text{ ns}^{-1}$ and $\lambda_{2\gamma} \approx 8 \text{ ns}^{-1}$ are the o-Ps 3γ -annihilation rate and p-Ps 2γ -annihilation rate in vacuum. λ_{po} is the pick-off annihilation rate of Ps, related with its short stayings in a crystallite near-surface layer, where e^+ wave-function overlaps with the wave function of e^- of the Al_2O_3 molecules of the top-surface layer of the crystallites. $\lambda_{opc}(t)$ is the ortho-to-para-Ps conversion rate. This process of Ps spin-conversion is due to the presence of the paramagnetic centers on the crystallite surface (adsorbed O_2 molecules). $J(t)$ is the diffusion flux of qf-Ps to the crystallite boundary (it determines o-Ps and p-Ps formation probabilities in the intercrystallite space).

Now let us estimate λ_{po} rate and demonstrate that one may neglect it below. Actually, according to the Tao-Eldrup model $\lambda_{po} \approx 2 \text{ ns}^{-1} \cdot 2\delta_{TE}/\ell$, where $\delta_{TE} = 1.66 \text{ \AA}$ and ℓ is the characteristic distance between the crystallites (comparable with the size of crystallites). Assuming that $\ell \simeq 100\text{-}200 \text{ nm}$, we obtain $\lambda_{po} \approx 0.003\text{-}0.006 \text{ ns}^{-1}$. So it leads to $\lambda_{po} < \lambda_{3\gamma} \approx 0.007 \text{ ns}^{-1}$. In more coarse powders, it will be even less. Note, that λ_{po} does not depend on o-Ps velocity (when Ps velocity decreases, both the Ps time-of-flight between the crystallites and the Ps residence time in the crystallite near-surface electron layer increase proportionally). On the contrary, the ortho-para conversion rate, λ_{opc} , essentially depends on the Ps velocity. It is proportional to the frequency of Ps collisions with paramagnetic centers. In such collisions, the spin coupling between e^+ and e^- is broken and then restores again similar to how it occurs at Ps formation. So each act of ortho-para-conversion decreases $n_o(t)$ by a factor $3/4$ in accordance with the spin statistics: $n_o \rightarrow 3n_o/4$. We do not take into account the inverse process of converting para-Ps to ortho-Ps state because of the very fast 2γ self-annihilation of p-Ps.

The diffusion flux $J(t)$ of qf-Ps on the grain boundary entered Eq. (4.26), as well as Eq. (4.26) itself, may be obtained by solution of the diffusion equation on the concentration of qf-Ps for the spherical grain (crystallite) having the radius L (D_{Ps} is the qf-Ps diffusion

coefficient, λ_{Ps} is its annihilation rate):

$$J(t, \lambda_{Ps}, \lambda_J) = \frac{6\lambda_J e^{-\lambda_{Ps}t}}{\pi^2} \sum_{m=1}^{\infty} e^{-\lambda_J m^2 t}, \quad \text{where} \quad \lambda_J = \frac{\pi^2 D_{Ps}}{L^2}. \quad (4.29)$$

This expression is obtained in Appendix .5. In Appendix .5 we obtained simple, but accurate analytical approximation:

$$\sum_{m=1}^{\infty} e^{-m^2 \lambda_J t} \approx \sqrt{\frac{\pi}{2\lambda_J t}} \cdot e^{-\sqrt{33\lambda_J t}} + e^{-\lambda_J t} + e^{-4\lambda_J t}, \quad (4.30)$$

which speeds up numerical calculations.

Kinetics of qf-Ps annihilation can be expressed as follows:

$$n_{Ps}(t) = P_{Ps} e^{-\lambda_{Ps}t} \left[1 - \int_0^t J(\tau) e^{\lambda_{Ps}\tau} d\tau \right], \quad (4.31)$$

$$\int_0^t J(\tau) e^{\lambda_{Ps}\tau} d\tau = \frac{6}{\pi^2} \sum_{m=1}^{\infty} \lambda_J \int_0^t e^{-\lambda_J m^2 \tau} d\tau = \frac{6}{\pi^2} \sum_{m=1}^{\infty} \frac{1 - e^{-m^2 \lambda_J t}}{m^2} = 1 - \frac{6}{\pi^2} \sum_{m=1}^{\infty} \frac{e^{-m^2 \lambda_J t}}{m^2}.$$

For this sum, it is possible to suggest rather accurate analytical approximation, which simplifies carrying out numerical calculations when processing the spectra (Appendix .5):

$$n_{Ps}(t) = P_{Ps} e^{-\lambda_{Ps}t} \frac{6}{\pi^2} \sum_{m=1}^{\infty} \frac{e^{-m^2 \lambda_J t}}{m^2} \approx P_{Ps} e^{-\lambda_{Ps}t} (0.39 e^{-3.27 \sqrt{\lambda_J t}} + 0.61 e^{-\lambda_J t}). \quad (4.32)$$

Before discussing expressions for o-Ps and p-Ps, we make one simplification. In fact, the entire picture of the e^+ annihilation in nanopowders may be divided into two stages. The first stage is the annihilation of qf- e^+ , vac- e^+ , surf- e^+ and qf-Ps. The second stage is the thermalization and annihilation of Ps atoms in intergranular space. The duration of the first stage is about several nanoseconds. The second stage lasts much longer. Therefore, when all qf-Ps escape the intergranular space, the following equations can be used:

$$\dot{n}_o(t) = - \left(\lambda_{3\gamma} + \lambda_{po} + \frac{\lambda_{opc}(t)}{4} \right) n_o, \quad n_o(0) = \frac{3P_{Ps}}{4} \int_0^{\infty} J(t) dt, \quad (4.33)$$

This integral from $J(t)$ (it is the qf-Ps escape from the crystallite bulk) can be calculated exactly [59]:

$$\begin{aligned} \int_0^\infty J(\tau)d\tau &= \frac{6}{\pi^2}\lambda_J \sum_{m=1}^\infty \int_0^\infty e^{-m^2\lambda_J\tau-\lambda_{\text{Ps}}\tau}d\tau = \frac{6}{\pi^2} \sum_{m=1}^\infty \frac{1}{\lambda_{\text{Ps}}/\lambda_J + m^2} = \\ &= \frac{3}{\pi^2} \sqrt{\frac{\lambda_J}{\lambda_{\text{Ps}}}} \left(\pi \coth \pi \sqrt{\frac{\lambda_{\text{Ps}}}{\lambda_J}} - \sqrt{\frac{\lambda_J}{\lambda_{\text{Ps}}}} \right), \quad \int_0^\infty J(\tau)d\tau \Big|_{\lambda_{\text{Ps}}/\lambda_J \rightarrow 0} = 1. \end{aligned} \quad (4.34)$$

Then

$$n_o(t) = n_o(0) \exp \left(-\lambda_{3\gamma}t - \lambda_{po}t - \int_0^t \frac{\lambda_{opc}(\tau)}{4} d\tau \right). \quad (4.35)$$

To find the p-Ps annihilation kinetics, one may use that p-Ps 2γ -annihilation rate is substantially greater than all other annihilation rates. So we can assume that all p-Ps which were formed during the time interval $t \dots t+dt$ annihilate during the same time interval (i.e. $\dot{n}_p(t) \approx 0$). Then

$$n_p(t) \approx \frac{1}{\lambda_{2\gamma} + \lambda_{po}} \left[\frac{P_{\text{Ps}}}{4} J(t) + \frac{\lambda_{opc}(t)}{4} n_o(t) \right]. \quad (4.36)$$

For the sum entering expression for $J(t)$ in Eq. (4.29), we also obtained the analytical approximation. Then the first term in (4.36) takes the form:

$$\frac{P_{\text{Ps}}}{4(\lambda_{2\gamma} + \lambda_{po})} J(t) \approx \frac{P_{\text{Ps}}}{4(\lambda_{2\gamma} + \lambda_{po})} \cdot \frac{6\lambda_J e^{-\lambda_{\text{Ps}}t}}{\pi^2} \left[\sqrt{\frac{\pi}{2\lambda_J t}} \cdot e^{-\sqrt{33\lambda_J t}} + e^{-\lambda_J t} + e^{-4\lambda_J t} \right].$$

Thermalization kinetics of Ps atoms ejected into intercrystalline space requires separate consideration. These Ps atoms lose their kinetic energy in collisions with the surface of the crystallites. Since the energy loss rate of the Ps atoms is small due to the large mass difference of Ps and colliding object, the thermalization kinetics is rather slow [60]. Assuming the ortho-para conversion rate is proportional to the frequency of Ps collisions with O₂ molecules, one

obtains the following expression for $\lambda_{opc}(t)$:

$$\lambda_{opc}(t) = \frac{\mu v(t)}{\ell} = \frac{\mu v_{th}}{\ell} \cdot \frac{1 + \nu e^{-\alpha t}}{1 - \nu e^{-\alpha t}}, \quad \nu = \frac{v_0 - v_{th}}{v_0 + v_{th}}, \quad \alpha = \frac{2m v_{th}}{M\ell}. \quad (4.37)$$

Here μ characterizes efficiency of ortho-para conversion at each collision, m is the mass of Ps, and M is the mass of the object with which it collides (for example, when Ps collides with a single Al_2O_3 molecule, $m/M = 10^{-5}$), the recoil energy will be less, if Ps collides with a heavier object. v_0 is the initial Ps velocity at the moment when Ps escapes outside the crystallite (if Ps escapes having kinetic energy of 1 eV, then $v_0 \approx 4.2 \cdot 10^7$ cm/s. $v_{th} \approx 8 \cdot 10^6$ cm/s is the thermal velocity of Ps at room temperature. It is clear that the ratio $\nu = \frac{v_0 - v_{th}}{v_0 + v_{th}}$ is very close to 1. With increase of time, the rate λ_{opc} decreases from $\mu v_0/\ell$ down to $\mu v_{th}/\ell$.

The integral vs. $\lambda_{opc}(t)$ over t , entering Eq. (4.35), is calculated analytically:

$$\int_0^t \frac{\lambda_{opc}(\tau)}{4} d\tau = \frac{\mu v_{th} t}{4\ell} + \frac{\mu M}{4m} \ln \frac{1 - \nu e^{-\alpha t}}{1 - \nu}. \quad (4.38)$$

If we assume that $\ell \simeq 100$ nm and the typical time of λ_{opc} variation is 10 ns (it means that $\alpha = \frac{2m v_{th}}{M\ell} \simeq 0.1$ ns⁻¹), we can estimate m/M ratio: $m/M \simeq 10^{-6}$. It means that when Ps collides with the surface of crystallites, approximately 10 Al_2O_3 molecules take on the recoil energy of the Ps atom.

Fitting the spectra we have found that $\mu \simeq 10^{-5}\text{--}10^{-4}$, so that the fraction of collisions in which Ps interacts with O_2 molecules adsorbed on the surface is small.

Shape of the LT spectrum is calculated in a conventional way. According to (4.23)-(4.28), the number of annihilations in the k channel of the time analyzer is:

$$\begin{aligned} C_{th} \left(t = \frac{t_k + t_{k+1}}{2} \right) &\propto [\lambda_b n_b + \lambda_v n_v + \lambda_s n_s + \lambda_{\text{Ps}} n_{\text{Ps}} + (\lambda_{3\gamma} + \lambda_{po}) n_o + (\lambda_{2\gamma} + \lambda_{po}) n_p] \Delta t = \\ &= \left[\lambda_b n_b + \lambda_v n_v + \lambda_s n_s + \lambda_{\text{Ps}} n_{\text{Ps}} + \left(\lambda_{3\gamma} + \lambda_{po} + \frac{\lambda_{opc}(t)}{4} \right) n_o + \frac{P_{\text{Ps}}}{4} J(t) \right] \Delta t. \end{aligned} \quad (4.39)$$

To compare this expression with the experimental data, we must convolute it with the resolution function of the spectrometer and add the random coincidences background. If the experiments are done in air, the o-Ps quenching rate by air $\lambda_{air} \approx 0.004 \text{ ns}^{-1}$ [64] should be added to $\lambda_{3\gamma}$ (mostly oxygen is involved in this process).

This model also allows to calculate the intensity of the para-positronium (“narrow”) component observed in CDB experiments:

$$Y_p = \int_0^\infty \lambda_{2\gamma} n_p(t) dt \approx \frac{\lambda_{2\gamma}}{4(\lambda_{2\gamma} + \lambda_{po})} \left[P_{\text{Ps}} \int_0^\infty J(t) dt + \int_0^\infty \lambda_{opc}(t) n_o(t) dt \right]. \quad (4.40)$$

In case of $\lambda_{3\gamma} + \lambda_{po} \ll \lambda_{opc}(t)$ and taking into account Eq. (4.38), the last term is reduced to:

$$n_o(0) \int_0^\infty \frac{\lambda_{opc}(t)}{4} \exp \left(- \int_0^\infty \frac{\lambda_{opc}(\tau)}{4} d\tau \right) dt = n_o(0) \left[1 - \exp \left(- \int_0^\infty \frac{\lambda_{opc}(t)}{4} dt \right) \right] = n_o(0). \quad (4.41)$$

Thus, taking into account Eqs. (4.33) and (4.34), we arrive to ($\lambda_{2\gamma} \gg \lambda_{po}$):

$$Y_p \approx P_{\text{Ps}} \int_0^\infty J(t) dt = \frac{3P_{\text{Ps}}}{\pi^2} \sqrt{\frac{\lambda_J}{\lambda_{\text{Ps}}}} \left(\pi \coth \pi \sqrt{\frac{\lambda_{\text{Ps}}}{\lambda_J}} - \sqrt{\frac{\lambda_J}{\lambda_{\text{Ps}}}} \right). \quad (4.42)$$

This expression has simple physical meaning. In this model the o-Ps atoms, which fly in the space in-between crystallites, do not annihilate by themselves ($\lambda_{3\gamma} \rightarrow 0$). Colliding with O₂, these o-Ps atoms convert to p-Ps atoms, which then decay into two 511 keV photons. Therefore, in this particular case all Ps atoms, which escape the crystallites and annihilate there, contributes to the narrow component of the CDB spectrum.

The developed model contains the following adjustable parameters: λ_b , λ_v , λ_s , P_{Ps} , \varkappa_v , \varkappa_s , as well as μ and m/M . However, one may take into account that the annihilation rates of qf-e⁺ and qf-Ps must be close to each other $\lambda_{\text{Ps}} \approx \lambda_b$. Eq. (4.42) also imposes additional relation on the parameters. Parameter λ_b is determined (and fixed) from the fit of the coarse-grain defect-free powder. Also, if we assume that $D_{\text{Ps}} \approx 1 \text{ cm}^2/\text{s}$, then $\lambda_J = \pi^2 D_{\text{Ps}} / L^2$ also

becomes fixed.

Let us note in conclusion that on the basis of the developed model, we wrote a computer code which allows to fit annihilation (LT and CDB) spectra in nanosized dielectric powders. An example of processing annihilation spectra in Al_2O_3 nanopowders is given in Appendix .5 and in [63]. The program takes into account the possibility of e^+ trapping by vacancy-type defects, formation of surface-bound e^+ states, as well as Ps formation and Ps thermalization in between the crystallites. As a result we succeeded to obtain e^+ annihilation parameters within the crystallites, kinetics of Ps thermalization and ortho-para conversion reaction (when Ps collides with O_2 molecules in air and O_2 molecules adsorbed on the surface of crystallites).

4.5 Brief conclusion on this chapter

This chapter provides a brief overview of the models, describing the fate of positrons implanted into solids (standard trapping models and diffusion trapping models). All this models are well-known and we incorporated them into the RooPositron software [17] which fits lifetime and CDB spectra.

For interpretation of the annihilation spectra in nanopowders we have to combine the trapping model with the model describing thermalization of hot Ps atoms in inter-crystallite space. To do this we considered in more details the Ps formation process within in crystallites: to have a self-consistent model we introduced an intermediate state – quasi-free positronium (which is formed as a result of combination of thermalized positron end one of the track electrons) and took into account its diffusion to outer boundary of the crystallites.

For incorporation of this unified model into the spectra fitting software, we obtained of analytical approximations (simple, but quite accurate) for the series appearing in the model. It allows to proceed with fitting of the spectra within a reasonable time.

Taking into account of the Ps thermalization stage is important for consistent interpretation of the spectra because an individual 3-exponential fits of the spectra (for 50 nm and 100 nm Al_2O_3 powders) measured at different recording intervals (50, 100 and 200 ns), do

not provide consistent values of the e+ lifetimes and intensities (it is vary notable for the long-lived component, Appendix .5). However, account for the Ps thermalization stage (non-exponential kinetics) issues consistent values for the fitting parameters (especially describing the thermalization stage).

Chapter 5 Interaction of Ps with dissolved oxygen in liquids

Positron annihilation spectroscopy (PAS) has numerous applications in material science such as studies of structural defects, free volume, porosity of materials. At the same time PAS is also applied to study radiolytic processes in chemistry, radiobiology and medicine [66].

In experiments with radioisotope positron sources, positrons are born and injected into the studied material with continuous energy distribution, with the end point energies 1.47 MeV for ^{44}Ti - ^{44}Sc - ^{44}Ca -source and 0.54 MeV for ^{22}Na - ^{22}Ne -source. During ionization the slowing down positrons form tracks (clusters of ion-electron pairs along their trajectory), and after getting thermalized e^+ start to explore the surrounding medium. Because typical lifetimes of the positron states (0.1-10 ns) are of the order of characteristic times of the intratrack processes in molecular media, the positron turns out to be a convenient probe for radiation phenomena.

In nonconducting (molecular) substances, a thermalized e^+ easily forms Ps, which is a bound state of e^+ and e^- (the lightest analog of a hydrogen atom). The formation of Ps occurs in the final part of the e^+ track (the positron blob) as a result of the combination of a thermalized positron with one of the track electrons. Depending on the relative orientation of e^+ and e^- spins, the Ps atom can exist either in the para-state (p-Ps) with a spin equal to zero, or in the ortho-state (o-Ps) with a spin equal to $1\cdot\hbar$ [3].

In most molecular liquids, the o-Ps lifetime is much shorter than it is in vacuo (142 ns). It is decreased to a few ns, because of the so-called pick-off process, when the positron (in Ps) undergoes 2γ -annihilation with one of the nearest molecular electrons, whose spin is anti-parallel to the positron's spin. Nevertheless, the o-Ps atom can take part in chemical reactions not only with intratrack radiolytic products (in water, these are hydrated electrons, H_3O^+ , OH-radicals), but also with dissolved substances, for example, with molecular oxygen, O_2 [67].

Recently, some interest in the phenomenon of shortening of the o-Ps lifetime (Ps quench-

ing) in various liquids due to its interaction with dissolved oxygen has reemerged. This effect seems to be important when testing healthy and carcinogenic tissues by means of PAS because the oxygen content therein noticeably differs [68]. The reason is the so-called oxygen effect: there are relatively few blood tubes in cancerous tumors, so cancer cells develop under oxygen-lacking conditions. This explains enhanced radioresistance of the cancer cells, since just the products of interaction of dissolved oxygen with the chemically active radicals (which appear because of irradiation) destroys the tumor. PAS studies in this direction are partially stimulated because of the development of a new type of positron annihilation tomographer at the Jagiellonian University in Krakow, Poland [69, 70].

The interaction of Ps with oxygen molecules (as well with some molecules possessing oxidizing properties, such as Cl_2 , Br_2 , I_2) is more important than with other neutral molecules (for example, N_2). The interaction with neutral molecules through elastic collisions leads to the pick-off annihilation of Ps: the time of such collision is very short. By contrast, Ps interaction with oxygen molecules results in the formation of an activated, unstable, complex (or compound, PsO_2 or $e^+\text{O}_2^-$): the time involved can thus be much longer. The O_2 molecule can either oxidize Ps atom ($\text{Ps} + \text{O}_2 \rightarrow e^+ + \text{O}_2^-$), or stimulate its ortho-para conversion ($\text{Ps} \rightarrow 1/4 \text{ p-Ps} + 3/4 \text{ o-Ps}$), because O_2 molecule has a magnetic moment. All these processes lead to an observable decrease of the o-Ps lifetime (Ps quenching) [71–75]. Using conventional methods of processing of the positron annihilation lifetime (LT) spectra it is impossible to distinguish between oxidation and spin-conversion reactions.

Experiments with magnetic fields indicated the importance of the Ps ortho-para conversion and allowed to estimate a decrease of the Ps contact density parameter ($\eta_c = |\Psi_{liquid}^{\text{Ps}}(0)|^2 / |\Psi_{vacuum}^{\text{Ps}}(0)|^2$) only in few liquids: water (0.8; 0.65), benzene (0.84), methanol (0.68) and hexane (0.82) [77, 78]. So we adopt here that η_c is about 0.75-0.8 in all liquids studied here. It means that para-Ps being in a bubble state in a liquid lives about 160 ps (longer than in vacuum) before it undergoes the 2γ -annihilation.

In this paper, we present the results of our PAS experiments in organic liquids (cyclo-

hexane, isoctane, isopropanol) and in water in order to identify the nature of the Ps-O₂ interaction (oxidation or conversion). Values of the reaction rate constants are obtained with the help of new software, which uses an advanced model of Ps formation for processing of LT annihilation spectra.

5.1 Experimental

All the reagents used were purchased from Russian Chemist (www.rushim.ru). Unlike previous studies [72, 73] we did not use the freeze-thaw method to remove dissolved O₂ to avoid the risk of damaging the positron source during freezing and evacuation. Therefore, oxygen was removed from the liquid phase by its bubbling with chemically pure argon. For determination of the rate constants of the Ps+O₂ reactions, the liquids were bubbled either with air or pure oxygen to increase the O₂ concentration.

The gases were previously cleaned by means of blowing them through dry alkali KOH and then through nanosieves Metrohm 0.3 nm previously kept for 24 h in forvacuum at 250 °C. Next, the purified gas was fed into a hermetically sealed vial containing the studied liquid. Input/output of the gas was performed by means of two long medical needles, tightly inserted into the lid of the vial.

The positron source was made from a 10 mm diameter, 0.2 mm thick titanium washer. Its central part (6 mm diameter) was welded on both sides with 10 μm titanium foils. In-between them a radioactive powder of TiCl₄, containing about 7.5 MBq of ⁴⁴Ti, was deposited. The positron source was fixed in the center of the vial using stainless steel clip. The clip itself was tightly fixed in the lid of the vial. The source correction was determined in a series of separate measurements of the reference (pure, well-annealed) samples (Al, Si, Fe and W). From these measurements we concluded that for the present experiments with liquids the source correction is 13%. It consists of the following components I1=32%, t1=0.15 ns; I2=50%, t2=0.38 ns; I3=18% and t3=1.8 ns.

The lifetime annihilation spectra were recorded using two γ-detectors with BaF₂ scintillators and fast timing nanosecond electronic units from ORTEC. The time resolution of

the annihilation spectrometer was 280 ps. Spectra were recorded sequentially for each hour during one day. The total number of “start-stop” coincidence in each spectrum was about 1 million. All measurements were done at 20 °C.

The spectra were first analyzed through 3-exponential deconvolution. The lifetime of the shortest (parapositronium) component was fixed to the lifetime of p-Ps in a vacuum, 125 ps. Then, a more accurate model was used, taking into account formation of a quasi-free positronium and its subsequent transformation into a bubble state.

5.2 Ortho-para conversion and oxidation of Ps in the presence of dissolved O₂

Immediately after its birth, as a result of radioactive transformations of ⁴⁴Ti-⁴⁴Sc-⁴⁴Ca radioactive nuclei, the positron has a rather large kinetic energy (about 1 MeV). Within the next 10 ps, it loses its energy down to thermal energy because of ionization slowing down. At the end of its track in molecular media, the thermalized positron can combine with one of the electrons knocked out through ionization along the track. This process results in the formation of the quasi-free positronium, qf-Ps, a delocalized weakly bound state of e⁺ and e⁻, which also moves in a liquid at thermal velocity [79, 80]. Note that there is no need to specify the spin state of qf-Ps, because the contact density of its electron at the level of the positron is rather small. Therefore, the main channel of qf-Ps annihilation is annihilation of e⁺ with one of the electrons of the surrounding molecules. Within 50-100 ps, qf-Ps transforms into a localized state (Ps bubble formation time) [81, 82]. Although the typical qf-Ps lifetime is rather short, this state is important for explaining of the extreme behavior of the S-parameter time dependence in AMOC experiments.

In the scheme to follow, we neglect initial picosecond-scale processes like electron and positron solvation, qf-Ps formation. The initial moment ($t = 0$) of the following system

describing transformation of the positron states is the time moment of formation of qf-Ps:

$$\dot{n}_+(t) = -\lambda_+ n_+ + \lambda_{ox} n_o, \quad n_+(0) = 1 - P_{qf}, \quad (5.1)$$

$$\dot{n}_{qf}(t) = -\lambda_q n_{qf}, \quad n_{qf}(0) = P_{qf}, \quad \lambda_q = \lambda_{qf} + \lambda_b, \quad (5.2)$$

$$\dot{n}_o(t) = \frac{3\lambda_b}{4} n_{qf} - \lambda_o n_o, \quad n_o(0) = 0, \quad \lambda_o = \lambda_{po} + \frac{\lambda_{opc}}{4} + \lambda_{ox}, \quad (5.3)$$

$$\dot{n}_p(t) = \frac{\lambda_b}{4} n_{qf} + \frac{\lambda_{opc}}{4} n_o - \lambda_p n_p, \quad n_p(0) = 0, \quad \lambda_p = \lambda_{2\gamma} + \lambda_{po}. \quad (5.4)$$

Here, $n_+(t)$ and $n_{qf}(t)$ are probabilities of existence of the thermalized solvated positron and qf-Ps at a time t , respectively; $n_o(t)$ and $n_p(t)$ are the probabilities of observing the Ps atom localized in a bubble in ortho- and para-state, respectively; $\lambda_b = 1/(0.05...0.1 \text{ ns})$ is the rate constant of the qf-Ps transformation into positronium localized in a nanobubble, P_{qf} is the formation probability of qf-Ps, λ_{qf} and λ_+ are the annihilation rate constants of the qf-Ps and solvated positrons, λ_{po} is the pick-off annihilation rate constant of Ps and $\lambda_{ox} = k_{ox} c_{O_2}^{(L)}$ and $\lambda_{opc} = k_{opc} c_{O_2}^{(L)}$ are the oxidation and ortho-para conversion rate constants. $c_{O_2}^{(L)}$ being the concentration of molecular oxygen. $\lambda_{2\gamma} \approx 8 \text{ ns}^{-1}$ is the 2γ annihilation of p-Ps. In the above equations we neglect the para-to-ortho process, since, due to the rather low O₂ concentrations used, this reaction appears kinetically negligible as compared to the fast 2γ -decay of p-Ps. Solving Eqs. (5.1-5.4) gives the following equations for all 4 positron states:

$$n_{qf}(t) = P_{qf} e^{-\lambda_q t}, \quad n_o(t) = \nu (e^{-\lambda_o t} - e^{-\lambda_q t}), \quad \nu = \frac{3P_{qf}}{4} \frac{\lambda_b}{\lambda_q - \lambda_o}, \quad (5.5)$$

$$n_+(t) = (1 - P_{qf}) e^{-\lambda_+ t} + \nu \frac{\lambda_{ox}}{\lambda_+ - \lambda_o} (e^{-\lambda_o t} - e^{-\lambda_+ t}) - \nu \frac{\lambda_{ox}}{\lambda_q - \lambda_+} (e^{-\lambda_+ t} - e^{-\lambda_q t}), \quad (5.6)$$

$$n_p(t) = \frac{P_{qf}}{4} \frac{\lambda_b}{\lambda_q - \lambda_p} (e^{-\lambda_p t} - e^{-\lambda_q t}) + \nu \frac{\lambda_{opc}/4}{\lambda_p - \lambda_o} (e^{-\lambda_o t} - e^{-\lambda_p t}) - \nu \frac{\lambda_{opc}/4}{\lambda_q - \lambda_p} (e^{-\lambda_p t} - e^{-\lambda_q t}). \quad (5.7)$$

2γ -annihilation of these four positron states gives the following contribution to the shape of the LT spectrum:

$$C_{2\gamma}(t) \propto \lambda_{qf}n_{qf} + \lambda_+n_+ + \lambda_pn_p + \lambda_{po}n_o. \quad (5.8)$$

Thus, in this case the LT spectrum consists of 4 exponentials:

$$C_{2\gamma}(t) \propto \lambda_qI_0e^{-\lambda_q t} + \lambda_pI_1e^{-\lambda_p t} + \lambda_+I_2e^{-\lambda_+ t} + \lambda_oI_3e^{-\lambda_o t}. \quad (5.9)$$

Of course, to compare this with the experiment, we must add contribution from e^+ annihilation within the positron source, convolute $C_{2\gamma}(t)$ with the resolution function of the spectrometer, and add a random coincidence background. Combining the terms corresponding to the same exponents, we find the intensities:

$$\begin{aligned} I_0 &= P_{qf}\frac{\lambda_{qf}}{\lambda_q} - \frac{P_{qf}}{4}\frac{\lambda_p\lambda_b}{\lambda_q(\lambda_q - \lambda_p)} + \nu\frac{\lambda_p\lambda_{opc}/4}{\lambda_q(\lambda_q - \lambda_p)} + \nu\frac{\lambda_+\lambda_{ox}}{\lambda_q(\lambda_q - \lambda_+)} - \nu\frac{\lambda_{po}}{\lambda_q}, \\ I_1 &= \frac{P_{qf}}{4}\frac{\lambda_b}{\lambda_q - \lambda_p} - \nu\frac{\lambda_{opc}/4}{\lambda_p - \lambda_o} - \nu\frac{\lambda_{opc}/4}{\lambda_q - \lambda_p}, \\ I_2 &= 1 - P_{qf} - \nu\frac{\lambda_{ox}}{\lambda_+ - \lambda_o} - \nu\frac{\lambda_{ox}}{\lambda_q - \lambda_+}, \\ I_3 &= \nu\frac{\lambda_p\lambda_{opc}/4}{\lambda_o(\lambda_p - \lambda_o)} + \nu\frac{\lambda_+\lambda_{ox}}{\lambda_o(\lambda_+ - \lambda_o)} + \nu\frac{\lambda_{po}}{\lambda_o}. \end{aligned} \quad (5.10)$$

Particularly when there are no reactions between Ps and oxygen ($\lambda_{opc} = \lambda_{ox} = 0$), these expressions are reduced to:

$$\begin{aligned} I_0 &= P_{qf}\frac{\lambda_{qf}}{\lambda_q} - \frac{P_{qf}}{4}\frac{\lambda_p\lambda_b}{\lambda_q(\lambda_q - \lambda_p)} - \frac{3P_{qf}}{4}\frac{\lambda_{po}\lambda_b}{\lambda_q(\lambda_q - \lambda_{po})}, \\ I_1 &= \frac{P_{qf}}{4}\frac{\lambda_b}{\lambda_q - \lambda_p}, \quad I_2 = 1 - P_{qf}, \quad I_3 = \frac{3P_{qf}}{4}\frac{\lambda_b}{\lambda_q - \lambda_{po}}. \end{aligned} \quad (5.11)$$

It is easy to verify that in this case the qf-Ps formation probability is $P_{qf} = I_0 + I_1 + I_3$ and $\sum_{i=0}^3 I_i = 1$. In case of very fast formation of the Ps bubble ($\lambda_b \rightarrow \infty, \lambda_q \rightarrow \infty$) Eqs. 5.11

give $I_0 = 0$, $I_1 = P_{qf}/4$, $I_2 = 1 - P_{qf}$, $I_3 = 3P_{qf}/4$.

Usually in positron lifetime experiments the short-lived components I_0 and I_1 cannot be resolved using the conventional exponential deconvolution, so these intensities are combined in one short-lived component, which is incorrectly identified with the probability of p-Ps formation. As a result, a wrong conclusion is made about violation of the “one-to-three” ratio of p-Ps and o-Ps formation probabilities:

$$\frac{I_0 + I_1}{I_3} = \frac{1}{3} + \frac{4(\lambda_{qf} - \lambda_{po})}{3\lambda_b}. \quad (5.12)$$

Substituting here the probable values of the rates $\lambda_{qf} \simeq 2$, $\lambda_{po} \simeq 0.5$ and $\lambda_b \simeq 15\text{-}20 \text{ ns}^{-1}$, this ratio increases from $1/3$ to $\simeq 1/2$ in accordance with experimental observations in Fig. 5.1. Thus, an increase in this ratio is a consequence of the formation and presence of qf-Ps over several dozens of picoseconds, before its transformation into a bubble state.

In essence, the proposed model contains only 5 adjustable parameters: P_{Ps} , $\lambda_{qf} \approx \lambda_+$, λ_{po} , k_{opc} , k_{ox} since we fixed λ_b to 20 ns^{-1} based on AMOC experiments [81, 82].

The conventional approach for processing the LT spectra in liquids consists in their deconvolution into three exponentials decreasing with time. This can be derived from Eqs. 5.10, if we neglect the existence of qf-Ps, (assuming that the rate constant of the Ps bubble formation λ_b is very large). In this case Eqs. (5.1-5.4):

$$\dot{n}_p(t) = \frac{\lambda_{opc}}{4}n_o - \lambda_p n_p, \quad \lambda_p = \lambda_{2\gamma} + \lambda_{po}, \quad n_p(0) = \frac{P_{\text{Ps}}}{4}, \quad (5.13)$$

$$\dot{n}_+(t) = \lambda_{ox}n_o - \lambda_+ n_+, \quad n_+(0) = 1 - P_{\text{Ps}}, \quad (5.14)$$

$$n_o(t) = \frac{3P_{\text{Ps}}}{4}e^{-\lambda_o t}, \quad \lambda_o = \lambda_{po} + \frac{\lambda_{opc}}{4} + \lambda_{ox}. \quad (5.15)$$

Here P_{Ps} is already the probability of Ps formation just in a bubble state. The equations on

n_+ and n_p can be easily solved

$$n_p(t) = \frac{P_{\text{Ps}}}{4} e^{-\lambda_p t} + \frac{3P_{\text{Ps}}}{4} \cdot \frac{\lambda_{\text{opc}}/4}{\lambda_p - \lambda_o} (e^{-\lambda_o t} - e^{-\lambda_p t}).$$

$$n_+(t) = (1 - P_{\text{Ps}}) e^{-\lambda_+ t} + \frac{3P_{\text{Ps}}}{4} \cdot \frac{\lambda_{\text{ox}}}{\lambda_+ - \lambda_o} (e^{-\lambda_o t} - e^{-\lambda_+ t}),$$

after which it comes out that the LT spectrum consists of three exponents:

$$C_{2\gamma}(t) \propto \lambda_+ n_+ + \lambda_p n_p + \lambda_{po} n_o = \lambda_p I_1 e^{-\lambda_p t} + \lambda_+ I_2 e^{-\lambda_+ t} + \lambda_o I_3 e^{-\lambda_o t}, \quad (5.16)$$

$$I_1 = \frac{P_{\text{Ps}}}{4} - \frac{3P_{\text{Ps}}}{4} \cdot \frac{\lambda_{\text{opc}}/4}{\lambda_p - \lambda_o}, \quad I_2 = 1 - P_{\text{Ps}} - \frac{3P_{\text{Ps}}}{4} \frac{\lambda_{\text{ox}}}{\lambda_+ - \lambda_o}, \quad (5.17)$$

$$I_3 = \frac{3P_{\text{Ps}}}{4} \left[\frac{\lambda_{po}}{\lambda_o} + \frac{\lambda_+}{\lambda_o} \frac{\lambda_{\text{ox}}}{\lambda_+ - \lambda_o} + \frac{\lambda_p}{\lambda_o} \frac{\lambda_{\text{opc}}/4}{\lambda_p - \lambda_o} \right], \quad I_1 + I_2 + I_3 = 1, \quad \tau_1 = \frac{1}{\lambda_p}, \quad \tau_2 = \frac{1}{\lambda_+}, \quad \tau_3 = \frac{1}{\lambda_o}. \quad (5.18)$$

Such a simplified model (without qf-Ps) cannot explain the observed values of the ratio I_1/I_3 (larger than 1/3). It is seen from Eqs. 5.17-5.18 taking account of the Ps reactions with oxygen (conversion and oxidation; non-zero λ_{ox} and λ_{opc}) reduces even more the I_1/I_3 ratio and brings this model into conflict with experiment. Therefore, for a formal description of the LT spectra, these quantities I_1 , I_2 , I_3 , τ_1 , τ_2 and τ_3 are often considered as free adjustable parameters.

In Fig. 5.1 and Tab. 5.1 we have shown the results of such a formal treatment of the LT spectra measured in cyclohexane, iso-octane, isopropanol and water before and after bubbling argon, oxygen and air through these liquids. The p-Ps lifetime τ_1 was assumed to be a “common free” parameter for each stage of gas bubbling. Comparison with the fit when τ_1 was fixed to 125 ps (p-Ps lifetime in vacuum) is given in the Supplementary information file. The obtained e⁺ and o-Ps lifetimes are in agreement with the results of

previous measurements [72, 73] done with deaerated liquids.

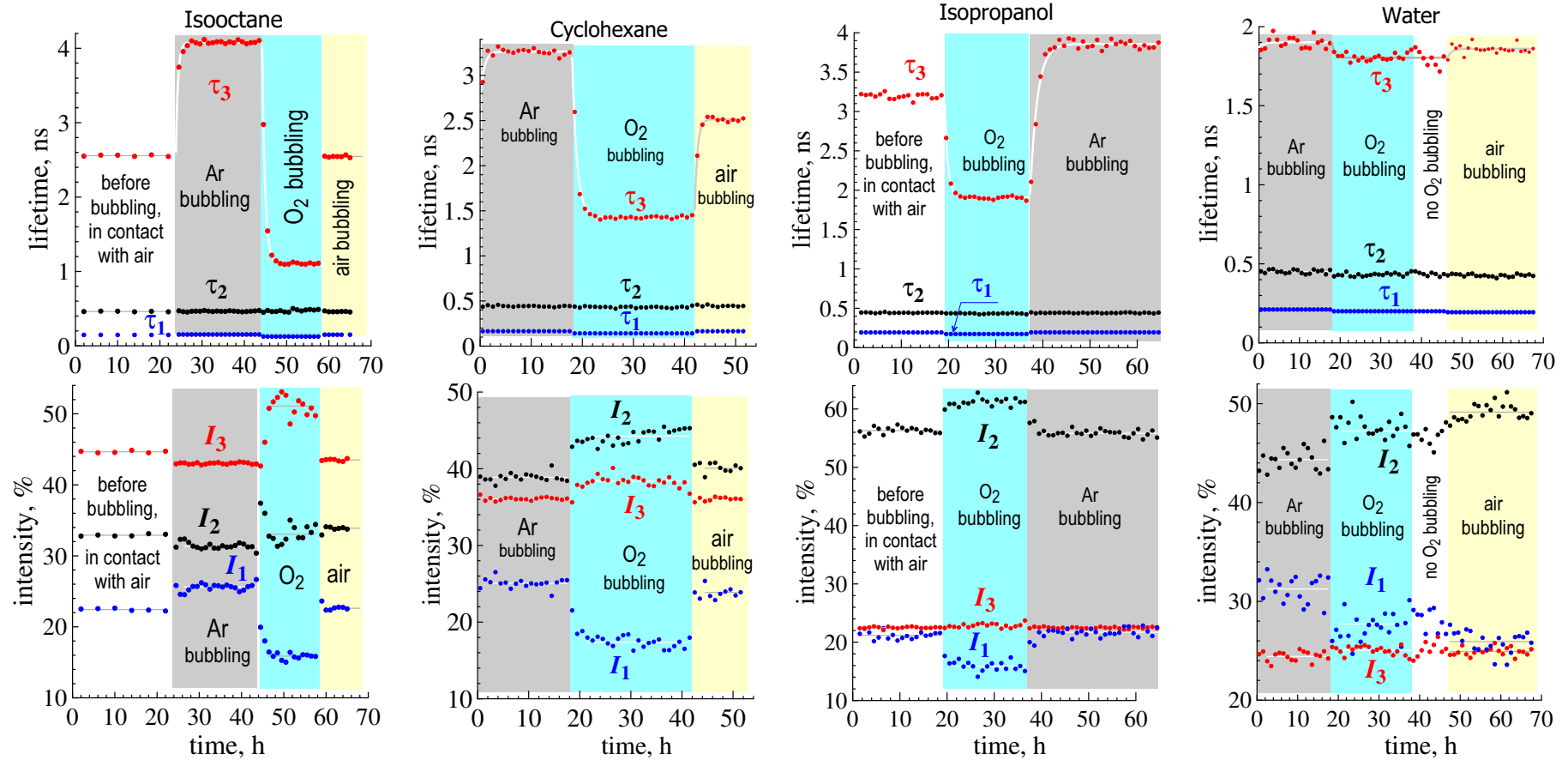


Fig. 5.1 The parameters of 3-exponential deconvolution of the LT spectra in cyclohexane, isooctane, isopropanol and water before and during their bubbling with argon, oxygen and air at room temperature. The lifetime of the shortest (τ_1) component was a “common free” parameter for each stage of the gas bubbling.

5.3 Concentrations of dissolved O₂ in the studied liquids

Gas solubility is often expressed by the Ostwald coefficient, L , which is the ratio of the gas concentration in the gas phase to its concentration in the liquid: $L = c_{\text{O}_2}^{(L)}/c_{\text{O}_2}^{(G)}$ (in some papers, the Ostwald coefficient is defined as $c_{\text{O}_2}^{(G)}/c_{\text{O}_2}^{(L)}$).¹

When pure oxygen is bubbled through a liquid, its partial pressure is 1 atm and its gas phase concentration is $c_{\text{O}_2}^{(G)} \approx 1/24.1$ mole/liter, since at 20 °C 1 mole of an ideal gas occupies 24.1 liters. The concentrations of O₂ in liquids can be easily obtained, knowing values of the Ostwald coefficients (Table 5.2): $L = c_{\text{O}_2}^{(L)}/c_{\text{O}_2}^{(G)}$. When air is blown through a liquid, the O₂ concentration in the gas phase is 0.21 times less: $c_{\text{O}_2}^{(G)} = 0.0087$ mole/liter (since partial O₂ pressure in air is 0.21 atm). The O₂ concentration in the liquid phase decreases in the same proportion.

In our experiments dissolved oxygen is completely removed from a liquid phase after 2 hours bubbling of argon through the liquid.

5.4 Determination of the Ps-O₂ reaction rate constants

If we neglect any influence of the intratrack radiolytic products on Ps (which can also promote Ps oxidation and conversion, although mostly on a short time-scale) and in the absence of dissolved oxygen, the o-Ps lifetime is determined only by the pick-off annihilation of e⁺ with one of the electrons of nearby molecules. In the presence of O₂, the o-Ps lifetime can also be shorten because of conversion to the para-state and Ps oxidation:

$$\lambda_o(c_{\text{O}_2}^{(L)}) = \lambda_{po} + \frac{\lambda_{opc}}{4} + \lambda_{ox} = \lambda_{po} + k_{\text{Ps+O}_2} \cdot c_{\text{O}_2}^{(L)}, \quad k_{\text{Ps+O}_2} = \frac{k_{opc}}{4} + k_{ox}. \quad (5.19)$$

Our experimental data for $\lambda_o(c_{\text{O}_2}^{(L)})$ at different O₂ concentrations in liquids are summarized in Tables 5.1 and 5.2. Approximating these dependencies using Eq.(5.19), one can determine the values of the “total” rate constant $k_{\text{Ps+O}_2}$ reaction with oxygen and the pick-off

¹Gas solubility may also be expressed in terms of the mole fraction, x , which is the ratio of the number of moles of the solute (gas molecules) to the total number of moles of all substances per unit volume of the solution.

Table 5.1 Parameters of the 3-exponential decomposition of the LT spectra of the initially aerated isooctane, cyclohexane, isopropanol and water, and also after their bubbling with argon, oxygen and air at room temperature. τ_1 is considered as a “common free” parameter for each gas bubbling. Statistical uncertainties of the fitting parameters are indicated in parenthesis.

Liquid	I_1 , %	τ_1 , ps	I_2 , %	τ_2 , ns	I_3 , %	τ_3 , ns	$\lambda_o = 1/\tau_3$, ns ⁻¹
Isooctane							
– Ar bubbling	24.6	148(1)	32.3(1)	0.45(1)	43.1(1)	4.01(1)	0.249(3)
– air bubbling	21.8	145(1)	34.4(2)	0.45(1)	43.8(1)	2.51(1)	0.398(5)
– before bubbling	22.6	149(1)	32.7(1)	0.46(1)	44.7(1)	2.546(3)	0.393(2)
– O ₂ bubbling	14	116(3)	31(1)	0.43(1)	55(2)	1.077(6)	0.929(6)
Cyclohexane							
– Ar bubbling	25	165(2)	38.9(4)	0.44(1)	36.1(4)	3.26(4)	0.307(12)
– air bubbling	23.9	165(2)	40.1(4)	0.45(1)	36.1(4)	2.515(40)	0.398(16)
– O ₂ bubbling	17.4	141(2)	44.3(4)	0.43(1)	38.4(4)	1.42(4)	0.703(29)
Isopropanol							
– Ar bubbling	21.7	194(3)	56(1)	0.44(2)	22.5(1)	3.75(10)	0.267(26)
– before bubbling	21	193(3)	56(1)	0.44(2)	22.5(10)	3.2(1)	0.313(30)
– O ₂ bubbling	16	173(4)	61(1)	0.43(2)	22.9(8)	1.905(10)	0.525(6)
Water							
– Ar bubbling	31	213(4)	44(4)	0.44(2)	25(4)	1.833(16)	0.546(9)
– air bubbling	25	194(3)	49(1)	0.42(2)	25.5(1)	1.802(15)	0.555(9)
– O ₂ bubbling	27	200(3)	47(4)	0.42(1)	26(3)	1.746(14)	0.573(8)

Table 5.2 Values of the Ostwald coefficients $c_{\text{O}_2}^{(L)}/c_{\text{O}_2}^{(G)}$, concentrations of O₂ in liquids after their bubbling with oxygen and air at room temperature (20 °C) and pressure 1 atm. Values of $k_{\text{Ps+O}_2}$ and λ_{po} were obtained by fitting the data shown in Fig. 5.2, using Eq. (5.19).

Liquid	$c_{\text{O}_2}^{(L)}/c_{\text{O}_2}^{(G)}$	$c_{\text{O}_2}^{(L)}$, M O ₂ bubbling $c_{\text{O}_2}^{(G)} = 0.0415$ M	$c_{\text{O}_2}^{(L)}$, M air bubbling $c_{\text{O}_2}^{(G)} = 0.0087$ M	$k_{\text{Ps+O}_2}$, M ⁻¹ s ⁻¹	λ_{po} , 1/ns
Isooctane	0.362 [83] 0.3725 [84]	0.0148 0.0154	$3.2 \cdot 10^{-3}$	$4.50(6) \cdot 10^{10}$	0.25(1)
Cyclohexane	0.27 [83, 85]	0.0112	$2.35 \cdot 10^{-3}$	$3.51(7) \cdot 10^{10}$	0.31(1)
Isopropanol	0.2463 [84]	0.010	$2.1 \cdot 10^{-3}$	$2.61(6) \cdot 10^{10}$	0.26(1)
Water	0.0334 [83]	0.00139	$2.9 \cdot 10^{-4}$	$1.86(10) \cdot 10^{10}$	0.55(2)

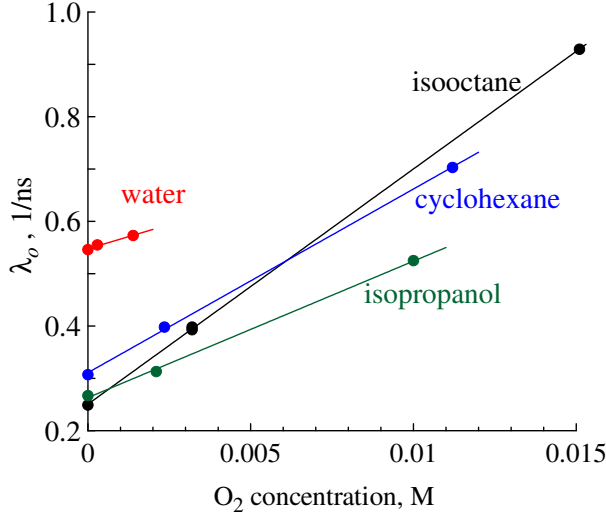


Fig. 5.2 Dependencies of λ_o (data taken from Tab. 5.1) vs. concentration of dissolved oxygen in different liquids. Solid lines – Eq. (5.19).

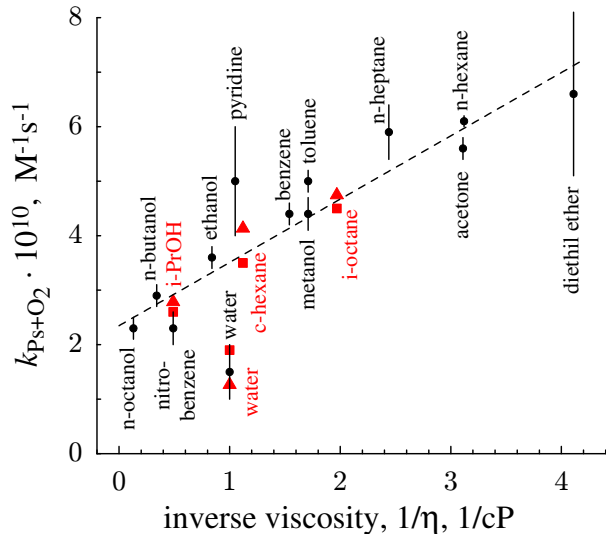


Fig. 5.3 The linear dependence of the rate constants $k_{\text{Ps}+\text{O}_2}$ of the Ps reaction with dissolved oxygen in different liquids vs. the inverse viscosity, $1/\eta$ Eq. (5.20). Black circles ● are taken from [71]; red symbols ▲, ■ – from Tab. 5.2 and 5.3. All the data correspond to room temperature.

annihilation rate λ_{po} (see Table 5.2 and Fig. 5.2).

In Fig. 5.3 our data for $k_{\text{Ps}+\text{O}_2}$ are plotted vs. the inverse dynamic viscosity $1/\eta$ of the liquids together with the previous data for other liquids [71]. Linear dependence of $k_{\text{Ps}+\text{O}_2}$ over T/η indicates that the $\text{Ps}+\text{O}_2$ reaction is diffusion-controlled:

$$k_{\text{Ps}+\text{O}_2} = 4\pi(D_{\text{Ps}} + D_{\text{O}_2})(R_{\text{Ps}} + R_{\text{O}_2}), \quad D_{\text{Ps}} + D_{\text{O}_2} = \frac{k_B T}{4\pi\eta R_{\text{Ps}}} + \frac{k_B T}{6\pi\eta R_{\text{O}_2}} \propto \frac{T}{\eta}. \quad (5.20)$$

Here k_B is the Boltzmann constant, T is the absolute temperature, D_{Ps} and D_{O_2} are the diffusion coefficients of the reactants, $R_{\text{Ps}} \approx 3\text{-}4 \text{ \AA}$ and $R_{\text{O}_2} \approx 2 \text{ \AA}$ are bubble radii of Ps and O_2 .

Eq. 5.20 brings us two problems. The first one is that the rate constant should tend to zero with increasing viscosity of the solvent, whereas Fig. 5.3 shows that it is not ($k_{\text{Ps}+\text{O}_2}$ remains finite at high viscosity). This means that the interaction of Ps and O₂ occurs not only at a distance of a direct contact of the reactants, but also at greater distances (for example, electron or Ps as a whole may tunnel to the oxygen molecule) [86]. The second problem is that the predicted value of the slope of the dependence $k_{\text{Ps}+\text{O}_2}$ versus $1/\eta$ according to Eq. (5.20) is several times smaller than it really is in Fig. 5.3. It may indicate that we must distinguish between reaction radii of the reagents and their “hydrodynamic” radii entering the diffusion coefficients. Seemingly, the reaction radii are larger than the hydrodynamic ones.

5.5 Processing of the spectra through a model taking into account the formation of qf-Ps

In the present study, we take into account that Ps atoms are not formed in nanobubbles instantly. It takes a certain time to find a pre-existing place suitable for localization (Section 3). More subtle effects such as the time-dependence of the rate constant $k_{\text{Ps}+\text{O}_2}$ according to the Smoluchowski theory are not considered in this paper [88].

In section 5 we discussed only values of the “total” rate constants $k_{\text{Ps}+\text{O}_2}$ (but not k_{opc} and k_{ox} separately) because it is hardly possible to distinguish the interaction mechanisms of the Ps with O₂ (conversion or oxidation) on the sole basis of the quenching rate constant $\lambda_o(c_{\text{O}_2}^{(L)})$. However, the equations developed in Section 3 show that the processes of Ps ortho-para conversion and Ps oxidation result in different redistribution of the lifetime components (I_i) of the LT spectra. This makes it possible to determine the dominant mechanism of the Ps+O₂ interaction.

In the mid 60’s of the last century the Ps+O₂ interaction was generally accepted to be just conversion [71]. However after the ACAR experiments in deairated and oxygenated n-hexane [89], this viewpoint was rejected. No increase of the “narrow” parapositronium component in O₂ saturated n-hexane was observed. This result points to Ps oxidation by O₂ as the dominant process. However, the questions remain about this experiment [89], as the

o-Ps lifetime found in oxygen-saturated n-hexane (1 ns) was almost two times less than that obtained by other authors [71–73].

Unfortunately existing software products like LT-10 [76] or PALSfit3 [90] (<http://palsfit.dk/>) do not include fitting models that account for the physical behavior outlined in Section 3. Therefore in order to shed some light onto the interaction mechanisms of Ps and O_2 , we developed a special computer software “RooPositron” for processing lifetime annihilation spectra (<https://github.com/petrstepanov/roopositron>).

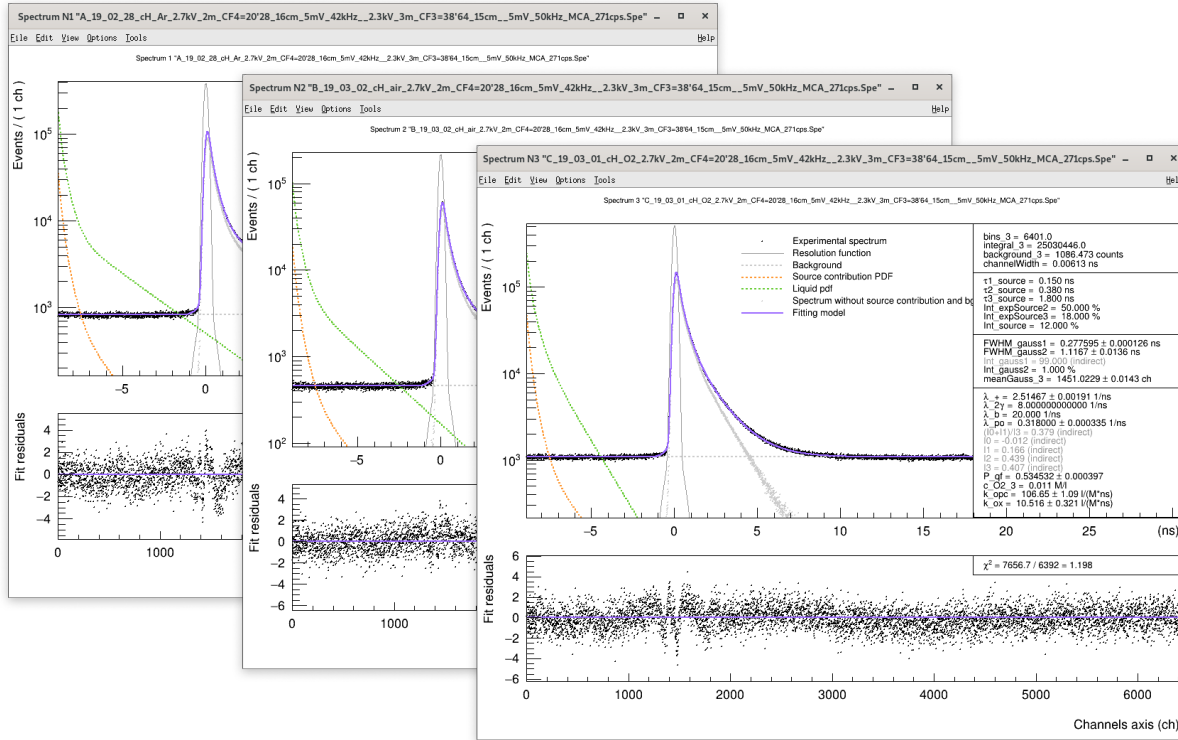


Fig. 5.4 Screenshots of the RooPositron software [17] depicting series of spectra fitted with a model derived from equations (5.1)–(5.4).

The program is written in C++ language and utilizes the ROOT framework [91] developed by CERN. ROOT is a set of object-oriented classes that provide a vast functionality for analyzing scientific data. The RooFit [92] package allows the user to built up custom fitting models based on corresponding parameters and performs simultaneous fits of multiple spectra by minimizing the chi-square.

In RooPositron we implemented functionality that is similar to the existing products on the market, such as: simultaneous spectra fitting, ability to fit spectra with various channel width, introduced common and fixed fitting parameters, graphical visualization of the fit and residuals (Fig. 5.4), and plots export to ASCII files.

Some competitive features of RooPositron program that make it outstanding with respect to the existing solutions include:

- RooPositron's code is open-source and program is distributed free of charge. Any researcher in the field can contribute and improve the functionality.
- Program supports integration of custom fitting models that correspond to meaningful physical parameters of the environment.
- Fitting models support calculation of indirect parameters as functions of the regular parameters of the model.
- Various types of minimizer functions can be used in order to fit the spectra (MINUIT, FUMILI and some others).
- User has a control on the convolution operation parameters. By adjusting the convolution binning user can either select a quicker fitting speed or obtain higher fit precision.

Program comes with a detailed instructions that covers installation, usage and explain how to add custom models. RooPositron is hosted on GitHub (<https://github.com/petrstepanov/roopositron>)

Currently RooPositron can perform conventional multiexponential fits, trapping model, and diffusion-trapping model. In this work the program was extended with a fitting model of formation of Ps atom in liquid media that accounts for the qf-Ps state as formulated in Section 3. The integrity of the fitting equations added into the program was additionally verified by means of Wolfram Mathematica computing system. Parameters P_{Ps} , $\lambda_{qf} = \lambda_+$,

Table 5.3 Parameters of the model Eqs. (5.5-5.10) obtained as a result of fitting of the LT spectra of liquids with different O₂ contents, $\lambda_{qf} = \lambda_+$, $\lambda_b = 20 \text{ ns}^{-1}$, $\lambda_{2\gamma} = 1/0.16 \text{ ns}^{-1}$ (in accordance with the magnetic quenching experiments [77, 78]), $\tau_+ = 1/\lambda_+$, $\tau_{po} = 1/\lambda_{po}$. Statistical uncertainties of the fitting parameters are indicated in parenthesis.

Liquid	$\lambda_+ = \lambda_{qf}; \text{ns}^{-1}$	$\tau_+ \text{ ns}$	$\lambda_{po} \text{ ns}^{-1}$	$\tau_{po} \text{ ns}$	P_{qf}	$k_{opc}, 10^{10} \text{ M}^{-1} \text{s}^{-1}$	$k_{ox}, 10^{10} \text{ M}^{-1} \text{s}^{-1}$	$k_{opc}/4 + k_{ox}, 10^{10} \text{ M}^{-1} \text{s}^{-1}$
i-octane	2.430(1)	0.412(1)	0.252(1)	3.968(4)	0.639(2)	9.62(9)	2.37(3)	4.78(5)
c-hexane	2.568(2)	0.389(1)	0.320(3)	3.125(10)	0.542(1)	12.6(2)	1.02(4)	4.17(5)
i-propanol	2.509(1)	0.399(1)	0.276(2)	3.622(10)	0.340(2)	9.8(1)	0.35(5)	2.82(5)
water	2.516(8)	0.397(4)	0.556(1)	1.799(2)	0.451(3)	1(1)	1.1(4)	1.3(8)

λ_{po} , k_{opc} , k_{ox} are set as free during the fit. The rate constant of Ps bubble formation λ_b is fixed to 20 ns⁻¹ to be in agreement with the AMOC data [81, 82].

All experimental spectra were analyzed and fitted by the proposed model. The obtained parameters including values of the Ps spin-conversion rate constant (ortho-Ps ⇌ para-Ps) and Ps oxidation rate constant (Ps + O₂ ⇒ e⁺ + O₂⁻) are given in Table 5.3. Oxidation of the Ps atom turned out to be about 5-10 times less favorable process. In conventional three-exponential deconvolution of the spectra, the Ps-O₂ interaction manifests only in a variation of only one parameter – the o-Ps annihilation rate λ_o vs. O₂ concentration. It does not allow to distinguish between conversion and oxidation.

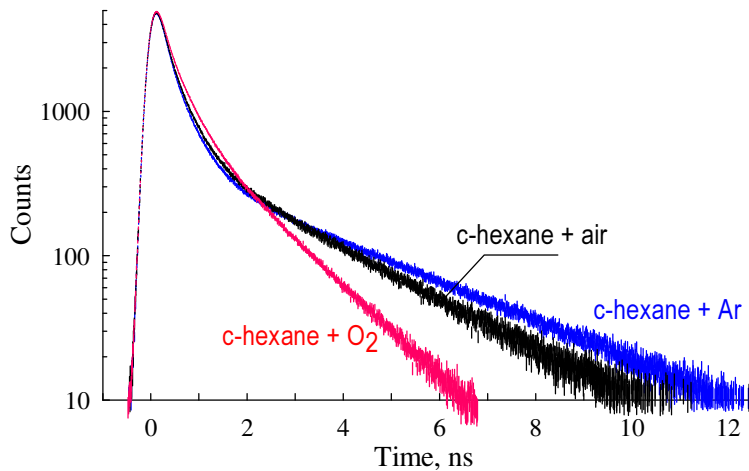


Fig. 5.5 The effect of the presence of O₂ on the shape of lifetime annihilation spectra in cyclohexane. Blue – blowing argon, black – blowing with air, red – blowing oxygen. Source contribution and background are subtracted from the spectra. The spectra are normalized to 10⁶ counts.

5.6 Brief conclusion on this chapter

The interaction of the Ps atom with oxygen dissolved in liquid media is a rather complex problem. In fact it is a special case of a general problem of random walks of a particle and its acceptors when they can interact on a random distance [87]. The problem is even more complex because formation of Ps atoms in nano-bubbles does not happen at the same moment of time (say, $t = 0$). Instead every formation event happens to have a certain random time delay. These delays occur due to existence of a delocalized intermediate transient state of an e^+e^- pair named quasi-free positronium (qf-Ps). The localization event of qf-Ps is preceded by a process of seeking for a suitable preexisting trap in the solvent. This aspect is studied in current paper.

Following the spin statistics, it has long been thought that the formation of the ortho- and para-states of Ps should strictly result in the ratio $I_1/I_3 = 1/3$. However, by taking into account the existence of the qf-Ps, as a precursor of the ensuing bubble state of Ps, we were able to explain the anomalously high ratio for I_1/I_3 (at 1/2 or more) as it is usually found through conventional analysis of the LT spectra into 3 decaying exponential components. Moreover, the proposed model, which takes into account formation of qf-Ps naturally explains the extremal behavior of the $S(t)$ parameter (juvenile broadening) observed in AMOC experiments.

The presence of oxygen does not affect the lifetime of “free” positrons, $\tau_+ = 1/\lambda_+$. It is mostly determined by the structure of the solvated state e^+ and the average electron density of the solvent.

A new open-source program RooPositron that fits lifetime annihilation spectra is developed [17]. The software supports integration of custom fitting models. A model derived from Eqs. (5.5-5.10) is integrated into the new program as a fitting function. By contrast with the conventional multiexponential deconvolution, the new fitting model parameters represent values with real physical meaning (such as Ps reaction rate constants, annihilation rate constants of the various positron states, probability of qf-Ps formation, localization rate of

qf-Ps in a nanobubble). Application of the RooPositron program revealed the ortho-para-conversion of Ps atom to be a dominant process of the interaction between Ps atom and dissolved oxygen. Oxidation of the Ps atom turned out to be about 5-10 times less favorable. In conventional three-exponential analysis it is not possible to distinguish between conversion and oxidation.

Spectra of water with dissolved oxygen show almost no difference in shape and fitting parameters with respect to pure water spectra. This is explained by a very low solubility of O₂ molecules. Therefore pure water is often used as a “reference” medium for testing the operation of the lifetime positron spectrometers.

Chapter 6 Development of the software for processing of LT and CDB spectra

The development of the programs for the Doppler and lifetime spectra processing and fitting was in C++ language. The software framework of our choice was selected to be CERN ROOT [93].

ROOT is a C++ framework developed by the European Organization for Nuclear Research (CERN). It is a set of open-source libraries, the primary purpose of which is data analysis for the high-energy physics experiments.

The RooFit and RooStats packages provide a set of tools for defining fitting models, performing multidimensional fitting and variety of statistical analysis. In RooFit [94] mathematical concepts such as variables, model parameters, probability density functions (PDFs) and integrals are represented as C++ objects. There is a built-in support for performing numerous operations with PDFs such as addition, multiplication, convolution and more. This provides a great opportunities for building flexible fitting models with custom logic. One of the most important features of RooFit are following:

- Powerful support for following histogram operations: input and output to the hard drive, arithmetical operations, and visualization capabilities.
- Rich data plotting functionality: support for two and three-dimensional plots, arranging multiple plots on the canvas, setting logarithmic axis scale, display of error bars, support for plot legends and many more.
- RooFit natively supports parallel calculations which significantly affects the fitting speed.
- Variety of the fitting algorithms for data sets including maximum likelihood fit as well as minimization of chi-square values. A number of fitting minimizers is available: MINUIT, MINUIT2, FUMILI and some others.

- A precise control of the fitting parameters during the fit. Support for parameter value limits.
- Ability to perform simultaneous fits of a number of data sets that have common parameters.
- FFTW3 library provides a robust algorithm for performing convolution operation. The control over the convolution operation parameters allows optimizing the fitting process for either fitting speed or fitting precision.
- The ROOT Graphical User Interface (GUI) is very similar to the Qt library; it offers a rich set of user interface (UI) elements, controls and dialogs.
- Cross-platform compatibility: Linux, macOS and Windows. A standalone executable is compiled with gcc (Linux) or clang (macOS) using GNU makefile. On windows the conventional way is to use MSVC's cl.exe compiler and nmake utility.

The above advantages of the ROOT framework lead towards our decision to select it as the framework of choice for the development of the applications for processing and fitting the Doppler and lifetime positron spectra.

Along with some advantages of the ROOT framework it comes with a handful of problems:

- The framework is enormously large and contains about 3 million lines of code. This makes the learning curve very steep.
- The library setup and use might be overwhelming for a beginner as it requires some knowledge of command-line tools.
- Development and compilation the standalone ROOT-based C++ applications requires understanding of the C++ language, GNU Makefile syntax and setting up the Integrated Development Environment (IDE).

In this chapter we will comprehensively address the above issues to instruct the researchers to be able to utilize and collaborate on the software that was developed.

6.1 ROOT installation on macOS and Linux

There are two ways of installing ROOT libraries on a personal computer.

The easiest approach is to perform the ROOT installation from a precompiled binary that matches your operating system and compiler versions. This option is ideal for users that only intend to compile source code and run an existing ROOT application.

The other common installation method is to compile the ROOT libraries from source code. This is a more complex approach, but is critical for developers that want to create ROOT-based applications or want to contribute to the existing code base. Compiling ROOT from source will provide a rich source code debugging capabilities. Also, compiling from sources may be your only option if ROOT binaries for your operation system are not hosted on the official repository [96].

The setup of the ROOT libraries on a personal computer begins with installing the build prerequisites. These are specific to the type of the operating system installed on the computer.

On macOS it is required to install Xcode Developer Package and XQuartz. Xcode can be obtained through App Store. After the install of the Xcode is completed run following command in Terminal to install Xcode command line tools: `sudo xcodebuild -license && xcode-select --install`. Next download and install xQuartz from official website [97].

Setup of the prerequisites on a computer with a Linux system is performed in the Terminal. For the Ubuntu Linux v18.04 family the command is following:

```
sudo apt-get install build-essential git dpkg-dev cmake g++ gcc binutils libx11-dev
libxpm-dev libxft-dev libxext-dev gfortran libssl-dev libpcre3-dev xlibmesa-glu-dev
libglew1.5-dev libftgl-dev libmysqlclient-dev libfftw3-dev libcfitsio-dev
graphviz-dev libavahi-compat-libdnssd-dev libldap2-dev python-dev libxml2-dev
```

```
libkrb5-dev libgsl0-dev libqt4-dev
```

For the Fedora Linux family v31 the prerequisites can be installed with following command:

```
sudo dnf install @development-tools git cmake gcc-c++ gcc binutils libX11-devel  
libXpm-devel libXft-devel libXext-devel install gcc-gfortran openssl-devel  
pcre-devel mesa-libGL-devel mesa-libGLU-devel glew-devel ftgl-devel mysql-devel  
fftw-devel cfitsio-devel graphviz-devel avahi-compat-libdns_sd-devel python-devel  
libxml2-devel openldap gsl-devel
```

The list of the prerequisites for some other operating systems can be found on the official website [98].

6.1.1 Install from a precompiled binary

Precompiled binaries are available on the official website [96]. In order to avoid compatibility issues it is important to ensure that for the version of the operating system (OS) and C++ compiler to match with the versions in the downloaded ROOT binary distribution. The OS and C++ compiler versions on macOS computer can be obtained by executing following command in the terminal:

```
sw_vers && clang --version
```

ROOT binary releases are not always published up-to-date with the recent Xcode and clang compiler versions. Therefore it may happen that Xcode version installed on the macOS provides a newer compiler version than the one used in the binary. In this case depending on the clang version used to compile the ROOT binary determine the Xcode version you have to downgrade to. A reference between Xcode and clang versions can be found on the MacPorts website [?]. Older Xcode versions can be obtained on Apple Developer website [100].

After mounting the .dmg disk image a graphical interface for the binary distribution install should be available on macOS.

It is important to update your system environment variables after the ROOT is installed. Special ROOT's script thisroot.sh adds ROOT executable files to system \$PATH, defines

the \$ROOTSYS variable and appends the path of the ROOT shared libraries directory to the system's \$DYLD_LIBRARY_PATH variable.

On newer macOS the shell should be changed to bash instead of the zsh. In order to source the script on macOS run:

```
echo source 'find $(pwd) -name "thisroot.sh"' >> ~/.bash_profile
source ~/.bash_profile
```

At this point the user should be able to run ROOT from Terminal with the root command.

Installation of the root from the binary distribution on Linux system is almost identical. Operation system and the C++ compiler versions can be obtained with the following command:

```
lsb_release -a && gcc --version
```

Download the corresponding version of the ROOT binary and extract its contents. It is good practice to extract the archive in the ~/Applications folder following the macOS pattern.

User-specific environment variables on Linux are traditionally defined in the ~/.profile file; for distributions with bash login shell the ~/.bash_profile can be used instead. However due to some security issues on Ubuntu 18 and Fedora 31 and newer versions the thisroot.sh script has to be sourced in ~/.bashrc.

```
echo source 'find $(pwd) -name "thisroot.sh"' >> ~/.bashrc
source ~/.bashrc
```

6.1.2 Compile libraries from source

Having the required ROOT prerequisites installed on the system we can now compile ROOT libraries from source. The source code can be obtained on the GitHub repository:

```
mkdir -p ~/Downloads && cd ~/Downloads
git clone https://github.com/root-project/root.git
```

A conventional location for the compiled binaries on Linux is /Applications folder. The directory for the build can be created with the following command:

```
mkdir -p ~/Applications/root && cd ~/Applications/root
```

Configuration of the ROOT build is controlled by the list of CMAKE variables that is published on the official website [101]. It is necessary to turn on the internal build of the FFTW3 library in order to make use of the FFT convolution class. For the application developers to be able to debug ROOT it is necessary to set the build type to "Debug" to be able to debug ROOT classes:

```
cmake -Dbuiltin_fftw3=ON -DCMAKE_BUILD_TYPE=Debug ~/Downloads/root
```

When proceeding with the build it's important to specify number of CPU cores used in the compilation process. This can significantly reduce the compilation time:

```
cmake --build . -- -j`nproc`
```

Lastly to set up the environment variables, follow the instructions outlined in the previous section.

To prevent accidental changes to the ROOT source files it is best to remove the write privileges from the source folder and enclosed files recursively:

```
chmod -R -w ~/Downloads/root
```

6.2 ROOT installation on Windows 10

MacOS and Linux operation systems both evolved from the UNIX family. They have different compilers installed by default, namely clang on macOS and gcc in Linux. Nevertheless both operation systems support GNU Autotools environment. So it is possible to compile and install the program with the same GNU Makefile that contains some conditionals.

Microsoft windows not only has a different compiler (Microsoft C/C++ Optimizing Compiler cl) but also has its own make utility, NMAKE – which has a different syntax than GNU make.

In 2019 ROOT version 6 introduced support for Windows. There are several ways to compile a C++ program that utilizes ROOT Libraries on Windows from sources:

- Set up the compilation and linking in the Microsoft Visual Studio project.
- Write the native Windows Makefile with the NMAKE syntax.
- Use CMAKE, a cross-platform build system.
- Take advantage of the Microsoft Windows Subsystem for Linux (WSL).

In Windows 10 Microsoft introduced the WSL feature. It provides a compatibility environment that allows Linux tools and programs to run inside of Windows. Once you install it you get access to a terminal window, where you can run bash scripts, compilers and any Linux applications.

Historically it happened that we developed ROOT programs on macOS and Linux first and the Makefile was written in GNU Automake. The easiest way to run the existing programs on Windows is to use the Microsoft Windows Subsystem for Linux (WSL). Once the WSL is set up, the compilation of the source files and linking process is identical to the Linux.

Additionally, the Crostini feature from Google [103] that makes it possible now to run ROOT apps on a Chromebook.

6.2.1 Setup of the Windows Subsystem for Linux

The install of the WSL should be performed on an up-to-date version of the Windows 10.

To enable the Linux Bash shell environment the “Developer mode” option needs to be enabled in Windows. Feature is located in Start → Settings → Update and Security → For

developers.

The Windows Subsystem For Linux feature has to be marked for the installation on the system. It is located in Start → Windows System → Control Panel → Programs and Features → Turn Windows features on or off. The computer will require a restart for these changes to take effect.

Linux distribution has to be installed in Windows. In order to do so navigate to “<http://aka.ms/wslstore>” using the web browser. It is recommended to install the Ubuntu Linux as it is the most popular distribution. After installation is complete, access the Ubuntu from menu Start → Ubuntu.

A new user account will automatically be created when Linux is first started. The new user will be added to the “sudo” group and set as a default user.

Linux needs to be updated with the following Terminal command:

```
sudo apt-get update && sudo apt-get upgrade
```

The default X server needs to be set up by exporting the \$DISPLAY environment variable:

```
echo export DISPLAY=\"localhost:0\" >> ~/.bashrc
```

In order to get GUI applications to work the libtiff-tools package needs to be installed on Ubuntu via Terminal command:

```
sudo apt-get install libtiff-tools
```

A Windows alternative to the Linux X.Org Server needs to be installed on Windows 10. A distribution can be found on the official repository on sourceforge [104]. The Xming-fonts package hosted on the same resource needs to be installed to ensure the correct rendering of the linux fonts. Default Xming settings need to be set by running the XLaunch application and following the wizard.

It is useful to add Xming to the list of Windows startup programs. Open startup applications folder by typing the following command in the Windows command prompt:

explorer %APPDATA%\Microsoft\Windows\Start Menu\Programs\Startup

Drag the Xming shortcut from the start menu into the File Explorer's window. Next, follow the instructions on installing CERN ROOT on Linux outlined in the section 6.1.

The Linux hard drive on the windows machine can be accessed in following location:

%userprofile%\AppData\Local\Packages\CanonicalGroupLimited.UbuntuonWindows\
LocalState\rootfs

6.3 CERN ROOT GNU Makefile structure

Generally speaking a trivial C++ GNU Makefile consists of two steps: individual compilation of the sources and linking the object files. However some extra build steps are required if your C++ code takes advantage of the CERN ROOT libraries. The diagram below represents the build steps of a program that makes use of such ROOT features like GUI, ClassDef and ClassImp macros.

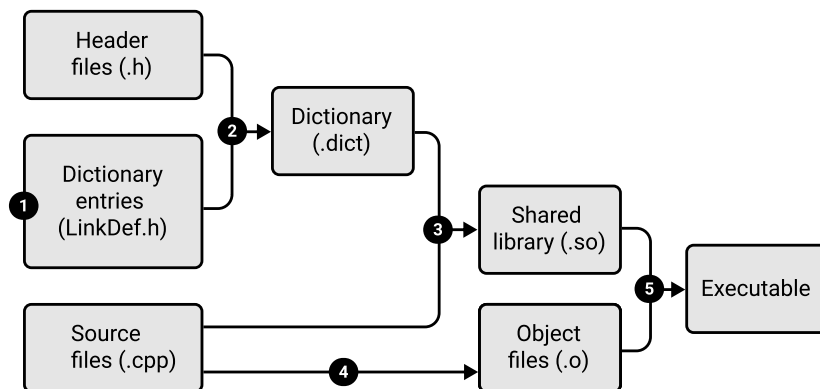


Fig. 6.1 Specificity of building a ROOT based C++ program.

1. A list of program Class names that require creating a Dictionary has to be specified in the file named LinkDef.h. Every program Class that inherits from TQObject or utilizes the ClassImp macro needs to be in this list.
2. A dictionary file (.dict) is created by passing the LinkDef.h file along with all the program header files (.h) to the rootcint interpreter.

3. Shared library (.so) file needs to be compiled from the list of the source files and the dictionary.
4. Just like for any other C++ application the sources are individually compiled into the object files.
5. Finally the compiler links object files, shared library and other ROOT shared libraries together into an executable.

6.3.1 Specifying Dictionary entries in LinkDef.h

There are two types of classes which need to be specified in the LinkDef.h file: classes that utilize ClassDef and ClassImp macros; classes with Signal and Slot mechanism inherited from TQObject base class.

ROOT macros ClassDef and ClassImp are used to register declaration and implementation of some static members of the class inherited from TObject. For example, ClassDef and ClassImp macros are used in custom RooFit PDF classes inherited from RooAbsPdf. Some of the non-inline members generated by ClassDef in header files need to have an implementation. ROOT generates them automatically as part of the Dictionary.

The Signal and Slot mechanism in CERN's ROOT GUI allows communication between a signal – e.g. button click event and slot – a corresponding method that is called when the event fires. ROOT's class TQObject is the base class that implements this communication mechanism. Every class that utilizes the Signal and Slot mechanism has to be specified in the LinkDef.h. Otherwise the communication won't work. For example, if you are writing a GUI application then your main class that inherits from TGMainFrame should be on the list.

The common structure of the LinkDef.h file is as follows. The first six lines takes the required header:

```
// All Linkdef.h files start with this preamble
```

```
#ifdef __CINT__
#pragma link off all globals;
#pragma link off all classes;
#pragma link off all functions;
#pragma link C++ nestedclasses;

// List all your classes that require Dictionary generation:
#pragma link C++ class MyClassWithClassImpMacro1
#pragma link C++ class MyClassWithClassImpMacro2
// ...
#pragma link C++ class MyClassInheritedFromTQObject1;
#pragma link C++ class MyClassInheritedFromTQObject2;
// ...
#endif
```

After the default LinkDef.h header class names that qualify the above conditions must be stated.

6.3.2 Dictionary generation

The rootcling program generates the Dictionary for the selected list of headers specified in the LinkDef.h file and is executed with the following command:

```
rootcling -f app-dictionary.cxx Header1.h Header2.h ... LinkDef.h
```

where \$(CXXFLAGS) is a set of compiler flags; -f flag stands for overwriting the existing output file; LinkDef.h has to be the last parameter in the list of input header files. Along with the Dictionary *.cxx file the *_rdict.pcm file is created. The latter file is fundamental for the correct functioning of the dictionary at runtime. It should be located in the directory where the shared library is installed in which the compiled dictionary resides [105].

6.3.3 Compiling the shared library

After the Dictionary is generated a shared library *.so needs to be compiled. The final executable will be linked against it along with the other ROOT libraries. The necessary syntax for the library compilation is following:

```
$(CXX) -shared -o app-library.so $(LDFLAGS) $(CXXFLAGS) $(LIBS) -I$(INCDIR)
Source1.cpp Source2.cpp ...
```

where \$(CXX) is the compiler command – g++ GNU C++ Compiler on Linux or clang++ on macOS; the -shared flag tells the compiler to produce a shared object which can then be linked with other objects to form an executable; flag -o app-library.so specifies the location and name of the output file; the \$(LDFLAGS) variable represents the linker flags; macOS C++ compiler requires linking against ROOT shared libraries \$(LIBS); flag -I specifies the additional search path of the ROOT include files; we will provide the path in \$(INCDIR) variable.

6.3.4 Compiling source code files

Every *.cpp source file is compiled individually. The required syntax of the command is:

```
$(CXX) -c $(CXXFLAGS) Source1.cpp -o Source1.o
$(CXX) -c $(CXXFLAGS) Source2.cpp -o Source2.o
...
```

Here the -c flag directs the compiler to compile and assemble only, and not perform linking.

6.3.5 Linking

The final step is linking all the object files against ROOT’s shared libraries and the application shared library that was generated previously. Syntax of the command is following:

```
$(CXX) -o app-name Source1.o Source2.o ... app-library.so $(LIBS)
```

where app-name is the name of the output executable file; variable \$(LIBS) will contain the list of ROOT libraries used for linking. Libraries must contain the regular ROOT libraries and all extra ROOT libraries used in the program: RooFit, GUI and others.

6.4 Makefile targets

The Makefile for the programs developed during this research contains a number of targets that serve different purposes:

- The default target – all – builds the production version of the application. This executable is compiled with full optimization. The search path of the shared library in the executable is system default – \$DYLD_LIBRARY_PATH on macOS or \$LD_LIBRARY_PATH on Linux.
- The install target installs the application on the system. It copies production executable to a standard directory on Unix-like operating systems that contains executable files (typically /usr/bin/). Shared library *.so and dictionary *.cxx and *.pcm files are copied to the \$ROOTSYS/lib - search path for the ROOT shared libraries.
- Two targets – release and debug – build the development version of the program. These targets are used by the developers to test the production release or debug the program respectively.

The build and install processes of the production version of the program is outlined schematically in Fig. 6.2.

It is important to understand the difference between the production executable versus the debug and release development executable files. Development executable files are located in the program's child folder – ./dist/ and they are not installed on the system. The shared library search path in the development executable files is set to be relative (they reside in the same folder). This approach separates the development executable and production version of the program installed on the computer. The locations and relationships of the various program files of the development build are illustrated in Fig. 6.3.

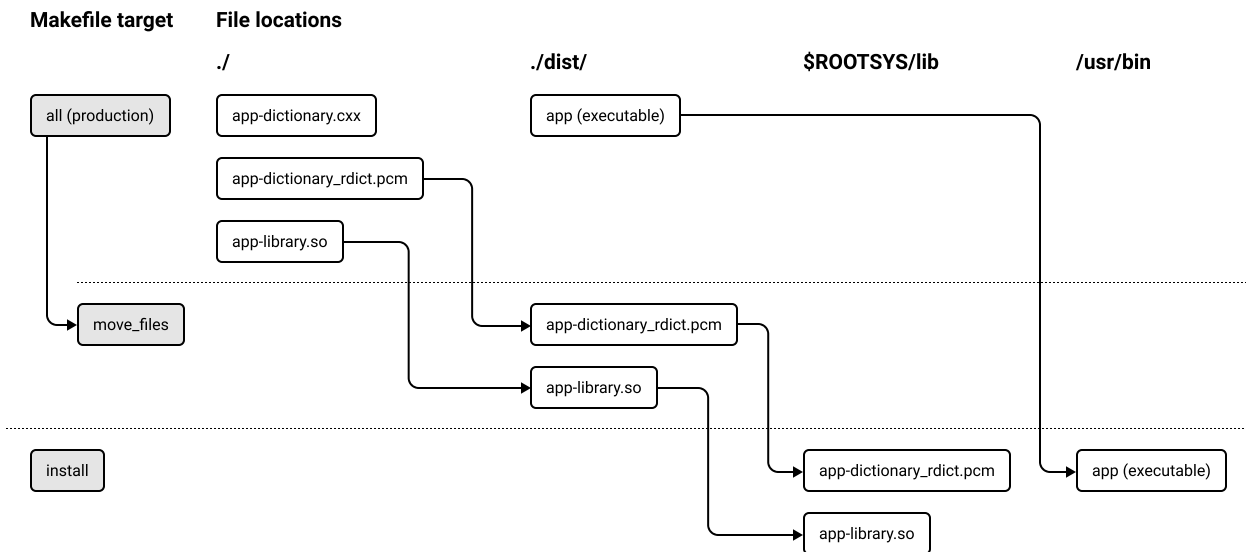


Fig. 6.2 Diagram of the Makefile targets and file locations for the production version of the application. Files involved in a certain Makefile target are enclosed in horizontal rows. Arrows denote the move operations.

To summarize, the default build target – all – followed by the install target are used to build and install the production version of the application on the system. The release and debug targets are typically used within the IDE to test the release and compile the binary with debug symbols.

6.5 Makefile syntax

This section describes the complete syntax of the Makefile used in the programs developed at BGSU. The Makefile starts with definition of the \$CXX, which is used to invoke the compiler. Please note that the indentation in the Makefile syntax needs to be done with TAB characters.

```

1 # Select compiler command depending on environment
2 OS=$(shell uname)
3   CXX=g++
4 ifeq ($OS),Darwin)
5   CXX=clang++
```

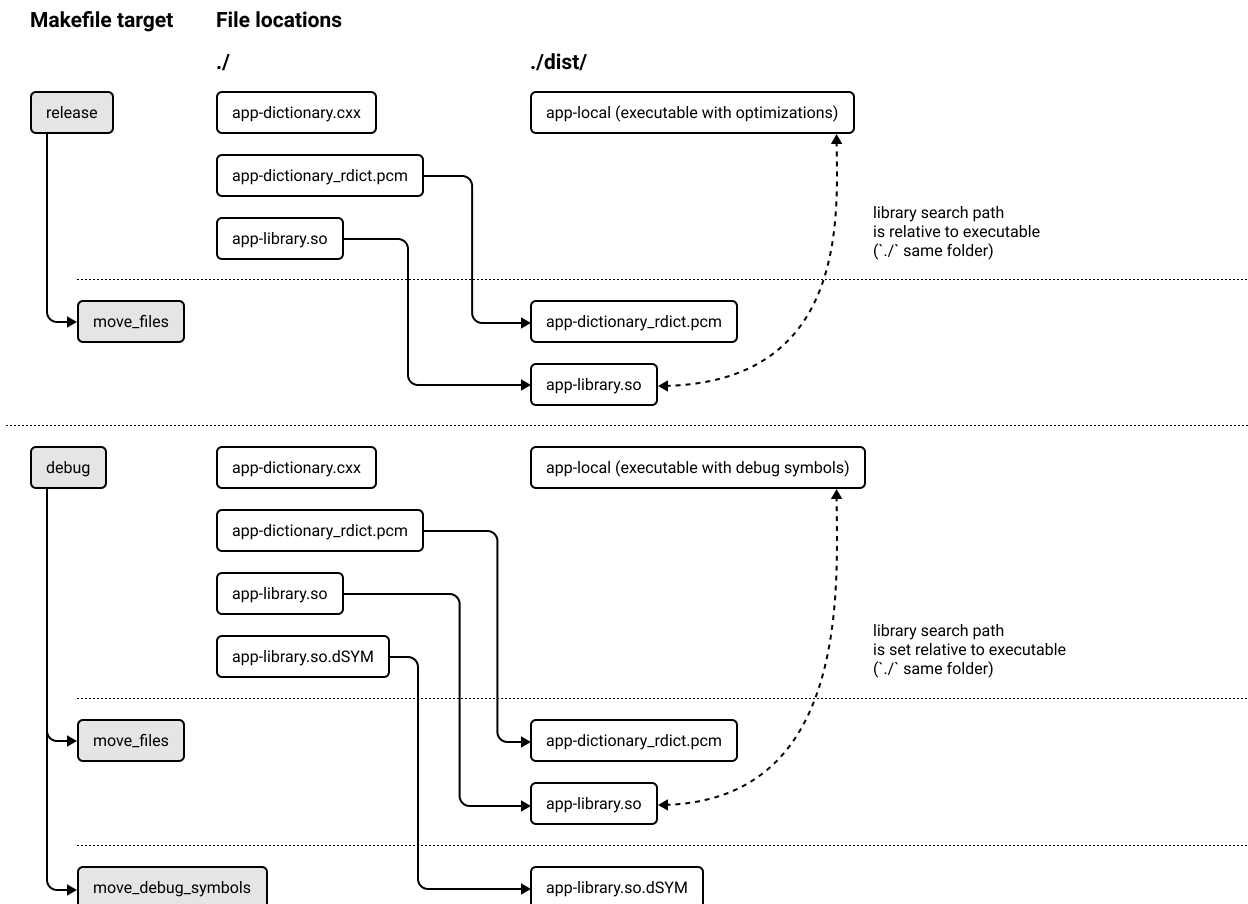


Fig. 6.3 Diagram of the Makefile targets and corresponding file locations for the development version of the application. Files involved in a certain Makefile target reside in the horizontal rows. Solid arrows denote move operations. Dashed arrows represent relative shared library search path for the executable.

6 endif

The C++ compiler commands are different on macOS(clang++) and Linux (g++). Depending on the output of the uname shell command we set the corresponding value of the \$CXX variable.

We define variables that stand for: compiler flags, linker flags, location of the ROOT header files and list of the ROOT libraries used by the executable.

7 # Variables for compiling and linking
8 CXXFLAGS='root-config --cflags' -fPIC

```

9 LDFLAGS='root-config --ldflags'
10 INCDIR='root-config --incdir'
11 LIBS='root-config --glibs ' -lRooFit -lRooFitCore -lHtml -lMinuit -lFumili

```

The root-config command is a utility program that prints corresponding; The -fPIC flag ensured that the code built into the shared library is position independent (it is not required but advised for predictable results). Note that root-config --glibs only outputs the list of regular and GUI ROOT libraries. Our programs take advantage of RooFit and other libraries that must be manually appended to the list.

Variables that correspond to project folder structure, file names of the dictionary, shared library and the binary executable are defined in the following set of variables:

```

12 # Define variables for directories
13 SRC_DIR=src
14 OBJ_DIR=build
15 BIN_DIR=dist
16
17 # Set the name of your executable
18 APP_NAME=app
19
20 # Set variables with dictionary .cxx and .pcm filenames
21 DICT_CXX_FILENAME=$(APP_NAME)-dictionary.cxx # app-dictionary.cxx
22 DICT_PCM_FILENAME=$(APP_NAME)-dictionary_rdict.pcm #
23             app-dictionary_rdict.pcm
24
25 # Shared library and its debug symbols filenames
26 SHARED_LIBRARY=$(APP_NAME)-library.so    # app-library.so
27 SHARED_LIBRARY_DS=$(APP_NAME)-library.so.dSYM # app-library.so.dSYM

```

```

27
28 # Binary executable file names with path
29 EXECUTABLE=$(BIN_DIR)/$(APP_NAME)      # dist/app
30 EXECUTABLE_LOCAL=$(BIN_DIR)/$(APP_NAME)-local # dist/app-local

```

The shell find command is used to automatically create lists of all header *.h and source *.cpp files located in the project folder. These lists are saved \$HEADERS and \$SOURCES variables respectively.

```

31 # Define list of header files (.h), source files (.cpp) and object files (.o)
32 H_EXT = h
33 HEADERS = $(shell find $(SRC_DIR) -type f -name *.$(H_EXT))
34 HEADERS := $(filter-out $(SRC_DIR)/LinkDef.h,$(HEADERS))
35
36 SRC_EXT = cpp
37 SOURCES = $(shell find $(SRC_DIR) -type f -name *.$(SRC_EXT))
38
39 OBJECTS_TEMP = $(SOURCES:.cpp=.o)
40 OBJECTS = $(patsubst $(SRC_DIR)/%, $(OBJ_DIR)/%, $(OBJECTS_TEMP))

```

The LinkDef.h file is excluded from the list of header variables. This is intended as the LinkDef.h file needs to be the last parameter in the list of headers when generating the dictionary. It will be appended manually later.

The list of object files .o is created automatically from the list of source files by replacing the extension and the directory name.

Below we declare the dir_guard convenience variable – a shorthand used for automatic directory creation. It is helpful if source files are organized in sub-directories.

```

41 # Convenience variable for creating new directories
42 dir_guard=@mkdir -p $(@D)

```

```

43
44 # Path for installing the shared library and dictionary .pcm
45 # Tip: macOS system integrity protection blocks access
46 # to $(DYLD_LIBRARY_PATH) so we use $(ROOTSYS)/lib instead
47 DYNAMIC_LIBRARY_PATH = $(ROOTSYS)/lib
48
49 # Path for installing the executable binary
50 ifeq ($(PREFIX),)
51     PREFIX := /usr/local
52 endif

```

The last two variables, namely \$DYNAMIC_LIBRARY_PATH and \$PREFIX are used in the install target to install the production executable and its shared library on the system.

For every build target – production, release and debug we set additional compiler flags and specify corresponding set of prerequisites.

```

53 # Default target builds production executable
54 all: production
55
56 # Add -O3 optimization level for the production release
57 production: CXXFLAGS+=-O3
58 production: directories $(DICT_CXX_FILENAME) $(SHARED_LIBRARY)
59             $(OBJECTS) $(EXECUTABLE) move_files
60
61 # Add -O3 optimization level for the test release
62 release: CXXFLAGS+=-O3
63 release: directories $(DICT_CXX_FILENAME) $(SHARED_LIBRARY)
64             $(OBJECTS) $(EXECUTABLE_LOCAL) move_files

```

```

63
64 # Also might add flags for debug optimizations: -Og -ggdb -DDEBUG
65 debug: CXXFLAGS+=-g
66 debug: directories $(DICT_CXX_FILENAME) $(SHARED_LIBRARY) $(OBJECTS)
      $(EXECUTABLE_LOCAL) move_files move_debug_symbols

```

The default target – all builds production executable; it is compiled with the highest -O3 optimization compiler flag. The executable and its shared library that are compiled in this target are installed on the system with the install target later.

Executables compiled with release and debug targets have different file name — \$EXECUTABLE_LOCAL. They will be linked with the shared library located in the same directory ./dist via relative path. This simplifies the development process – no install needed. Also this local build will not interfere with the production version of the program that might be installed on the computer.

The debug target above requires -d compiler flag. Extra -Og flag can be added to the debug compiler flags for optimization level.

The syntax for the target that created dictionary .cxx and .pcm files follows:

```

67 # Target for dictionary generation (creates .cxx and .pcm)
68 $(DICT_CXX_FILENAME): $(HEADERS) $(SRC_DIR)/LinkDef.h
69   rootcling -f $@ $^

```

The last prerequisite in the command above needs to be \$(SRC_DIR)/LinkDef.h. It was explicitly removed from the list of header .h files \$(HEADERS) previously.

The \$@ automatic variable stands for the file name of the target of the rule. Variable \$^ corresponds to the names of all the prerequisites, with spaces between them [106]. These are shortcut functions and user does not have to substitute them.

Prerequisites for compilation of the the shared library are dictionary .cxx file and the list of sources:

```

70 # Target for the shared library compilation
71 $(SHARED_LIBRARY): $(DICT_CXX_FILENAME) $(SOURCES)
72   $(CXX) -shared -o $@ $(LDFLAGS) $(CXXFLAGS) $(LIBS) -I$(INCDIR) $^

```

Here the parameter `$(LIBS)` is required by the macOS clang++ compiler, but it is optional for Linux g++.

The target for compilation of every program's source file has the following syntax:

```

73 # Target for compiling the object files
74 $(OBJ_DIR)/%.o: $(SRC_DIR)/%.cpp
75   $(dir_guard)
76   $(CXX) -c $(CXXFLAGS) $< -o $@

```

The `$(dir_guard)` convenience variable makes sure that the directories in the output object path exist. The `$<` automatic variable represents the source file (name of the first prerequisite) [106].

The executable binary is linked against ROOT's shared libraries and application shared library. For the production executable the syntax is straightforward.

```

77 # Target for linking the production executable
78 $(EXECUTABLE): $(OBJECTS) $(SHARED_LIBRARY)
79   $(CXX) -o $@ $(OBJECTS) $(SHARED_LIBRARY) $(LIBS)

```

The shared library file `$(SHARED_LIBRARY)` along with the list of the ROOT shared libraries are appended to the list of program object files. The shared library search path for the production executable will be the same as for other ROOT libraries, namely `$DYLD_LIBRARY_PATH` or `$LD_LIBRARY_PATH` – depending on the operating system.

The linking process for the development and testing release targets is more complex. There is no cross-platform way to specify the relative search path of the shared library. On macOS it is achieved by executing the `install_name_tool` command after the linking. On

Linux the relative location of the shared library is set with the `-Wl,-rpath` linker option [107].

```

80 # Target for linking the test release and development executable
81 # The relative runtime search path (./) is set for the shared library
82 $(EXECUTABLE_LOCAL):
83 ifeq ($(OS),Darwin)
84     # for macOS
85     $(CXX) -o $@ $(OBJECTS) $(SHARED_LIBRARY) $(LIBS)
86     install_name_tool -change $(SHARED_LIBRARY)
87             @executable_path/$(SHARED_LIBRARY) $(EXECUTABLE_LOCAL)
88 else
89     # for Linux
90     $(CXX) -o $@ $(OBJECTS) $(SHARED_LIBRARY) $(LIBS)
91             -Wl,-rpath,'$$ORIGIN'
92 endif

```

The dictionary files *.cxx and *.pcm, shared library *.so and shared library debug symbols *.so.dSYM (generated on macOS only when compiling with debug symbols) are copied to the ./dist/ folder. The dictionary .cxx file can be removed from the file system.

```

91 # Target moves .so and .pcm files to ./dist
92 move_files:
93     # move .so library to ./ dist folder
94     mv $(SHARED_LIBRARY) $(BIN_DIR)/$(SHARED_LIBRARY)
95     # move dictionary .pcm to ./dist folder , remove dictionary .cxx
96     mv $(DICT_PCM_FILENAME) $(BIN_DIR)/$(DICT_PCM_FILENAME)
97     # remove dictionary .cxx code (don't need it anymore)
98     rm $(DICT_CXX_FILENAME)
99

```

```

100 # Target moves .so.dSYM debug symbols to /dist folder
101 move_debug_symbols:
102 ifeq ($(OS),Darwin)
103     mv $(SHARED_LIBRARY_DS) $(BIN_DIR)/$(SHARED_LIBRARY_DS)
104 endif

```

The install target copies production executable and the shared library to the corresponding locations on the file system:

```

105 # Target installs the executable and moves shared library to $ROOTSYS/lib
106 install :
107     # run 'make install' or 'sudo -E make install' to preserve user environment
108     sudo install -m 755 $(EXECUTABLE) $(DEstdir)$(PREFIX)/bin/
109     sudo install -m 755 $(BIN_DIR)/$(SHARED_LIBRARY)
110             $(DYNAMIC_LIBRARY_PATH)/
111     sudo install -m 755 $(BIN_DIR)/$(dict_pcm_filename)
112             $(DYNAMIC_LIBRARY_PATH)/

```

The Makefile must follow GNU conventions and support the \$DEstdir variable. It can be specified by the user on the make command line to alter the install path. For example:

```
make DEstdir=/tmp/stage install
```

A set of tools xdg-utils that simplify the integration of the applications into the Linux desktop environment is used to install the application icon and create the desktop launcher:

```

111 # Target to copy the application icon and create the launcher on Linux
112 install -linux-launcher:
113     xdg-icon-resource install --context apps --size 128 ./resources/app.png app
114     xdg-desktop-menu install ./resources/app.desktop

```

The pixel dimensions of the application's icon app.png need to correspond to the value specified in the --size parameter. The application desktop launcher must satisfy the freedesktop.org [108] desktop entry specification [109].

Targets that do not update or create a file, but are rather a sequence of shell commands to be executed are named PHONY targets. Typically they are listed in the very end of the Makefile.

```

115 # Target that cleand the buld
116
117 clean:
118     rm -f -r $(OBJ_DIR)
119     rm -f -r $(BIN_DIR)
120     rm -f $(DICT_CXX_FILENAME)
121     rm -f $(DICT_PCM_FILENAME)
122     rm -f $(SHARED_LIBRARY)
123
124 # Target for creating the ./build and ./dist directories
125
126 directories :
127     mkdir -p $(OBJ_DIR)
128
129     mkdir -p $(BIN_DIR)
130
131 # Target for test output
132
133 echo:
134     $(info SOURCES: $(SOURCES))
135     $(info HEADERS: $(HEADERS))
136
137
138 # List of special targets that do not generate files
139 .PHONY: clean directories move_files move_debug_symbols echo

```

This is the end of the Makefile. A ROOT-based program with the above Makefile syntax can be installed on macOS or Linux operating system with following commands:

```
make
```

```
make install
```

In order to run the program user must type the name of the program executable file in the Terminal. This name was set in the \$APP_NAME variable in the Makefile.

Optionally on the Linux system user can add the program to the applications menu by running the command:

```
make install-linux-launcher
```

The complete code of the Makefile discussed in this section can be obtained on my GitHub page [16].

6.6 Setting up an IDE for a CERN ROOT project with existing Makefile

In this section we setup an IDE to be able to debug and test a CERN ROOT based C++ project with an existing Makefile. The IDE of our choice is Eclipse for the sake of the following benefits: open-source – available free of charge; cross-platform – makes the development possible on any operating system; supports C++ projects with custom Makefiles. An alternative option would be to use NetBeans IDE. However Eclipse has a better support of the system Environment variables. Eclipse install comes with following prerequisites:

- Install Java Runtime Environment (JRE) or Java Development Kit (JDK). The macOS binary is available on the official Java website [110]. On Linux Java is installed with the following command in Terminal: sudo apt install default-jdk for Debian based systems; for Fedora based distributions use sudo dnf install java-11-openjdk.
- Install gdb program to provide debugging capabilities. Eclipse will be a front-end for gdb. On macOS debugger must be installed from Homebrew package manager. It also requires a code signing procedure [111]. On Linux gdb is installed in Terminal:

sudo apt install gdb for Debian systems and sudo dnf install gdb for Fedora based operating systems.

6.6.1 Installing Eclipse

The Eclipse installer for macOS can be downloaded from the official website [112]. During the install the “Eclipse IDE for C/C++ Developers” option should be selected.

Ubuntu v.18.04 based distributions include an outdated Eclipse version in official repositories that does not work. An up to date version should be obtained from the official website [112].

Due to some technical issues in Fedora 31 the Eclipse install requires enabling a module:

```
sudo dnf module enable eclipse:latest
sudo dnf install eclipse
```

After Eclipse installation is completed the C/C++ Development Tool (CDT) plugin needs to be installed. “Install new Software” dialog is located under the Eclipse “Help” menu. “All Available Sites” should be specified in the repository select box. Under “Programming Languages” the “C/C++ Development Tools” item needs to be selected for installation.

6.6.2 Increasing Eclipse heap

The default Eclipse heap size is not enough to index ROOT classes. In order to increase the heap memory size, the following parameters in the eclipse.ini file need to be changed:

```
-Xms2048m
-Xmx2048m
```

Additionally in Eclipse Preferences → C/C++ → Indexer set the “Cache limits” to 50% and 2048MB. It is reasonable to allocate a limit of about half of the computer RAM amount available after the system start up. A minimum value value of 2 Gb is recommended to be able to debug ROOT programs.

6.6.3 Configuring the Eclipse Build Environment

In order to be able to process the program Makefile Eclipse has to have access to the user's PATH, ROOTSYS, LD_LIBRARY_PATH (or DYLD_LIBRARY_PATH on macOS) environment variables. Eclipse IDE installed on macOS or via flatpak on Linux cannot access the above variables. Therefore their values have to be specified manually in Eclipse Preferences dialog under C/C++ → Build → Environment (see Fig.6.4). Variable values can be obtained from the Terminal by running the echo \$PATH command (substitute \$PATH with the name of the corresponding variable).

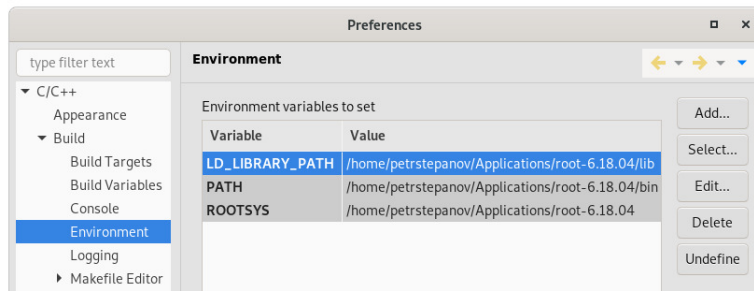


Fig. 6.4 Setting Eclipse build environment variables on Linux. On macOS use DYLD_LIBRARY_PATH and LD_LIBRARY_PATH on Linux.

6.6.4 Importing existing ROOT project

The project can be imported from the following menu item: File → New → Makefile Project with Existing Code. Project name and source code location need to be specified in the modal dialog. Check only “C++” under the Languages selection. Select “MacOSX GCC” as Toolchain on MacOS and “Linux GCC” on Linux (see Fig. 6.5).

6.6.5 Setting headers search path

The location of the ROOT header files need to be specified in project Properties → C/C++ General → Paths and Symbols. On the “Includes” tab the “GNU C++” language has to be selected. Add \${ROOTSYS}/include path to the list of “Include directories” (see Fig. 6.6).

After the header search path was modified the project index needs to be rebuilt. The

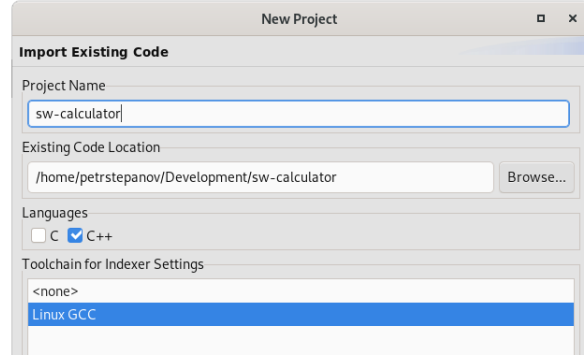


Fig. 6.5 Importing project with Makefile on Linux

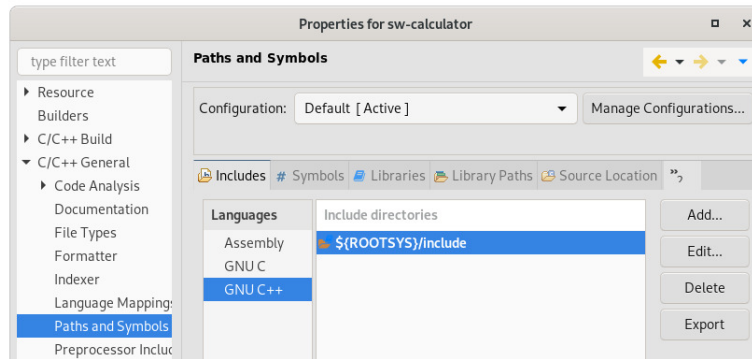


Fig. 6.6 Specifying the search path for ROOT headers

project index can be manually rebuilt in Eclipse menu: Project → C/C++ Index → Rebuild.

6.6.6 Adding ROOT source files

ROOT source files provide useful documentation. Adding source files to the project allows access to the ROOT source files through Eclipse user interface and in-depth debugging capabilities. In project Properties → C/C++ General → Paths and Symbols the “Source Location” tab needs to be opened. The folder containing ROOT source files needs to be linked with the “Link Folder...” button. In the modal dialog the “Link to folder on the file system” checkbox needs to be selected (see Fig. 6.7). If the ROOT was built from sources the location of the source files used to build ROOT should be specified. Otherwise source files can be obtained from the official website [96].

CERN ROOT contains thousands of source files. It takes about an hour of time to perform the indexing process.

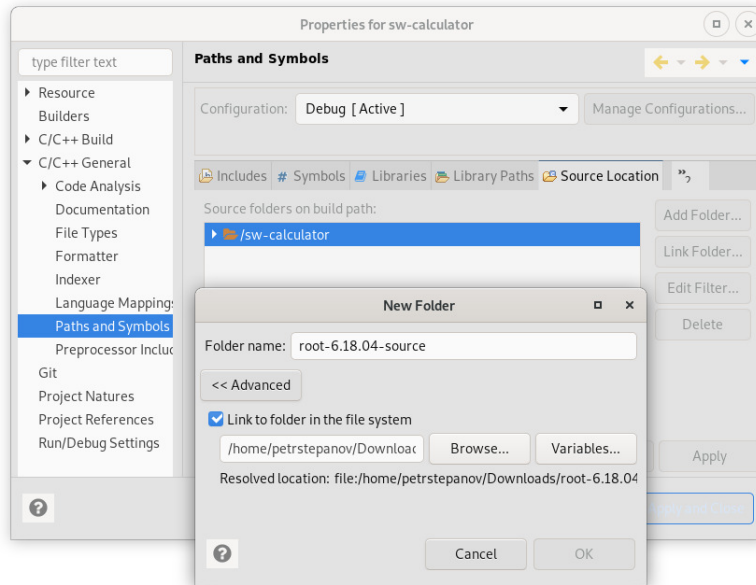


Fig. 6.7 Adding ROOT source files to the project

6.6.7 Creating Build Configurations

Two build configurations need to be set up in Eclipse. Release configuration will invoke the release Makefile target. This configuration builds local executable with full compiler optimizations. This executable is not supposed to be installed on the system; it is designed for testing purposes and linked with its shared library with a relative path. Debug configuration will invoke the debug target which is compiled with debug symbols.

Build configurations are managed in the “C/C++ Build” in the project properties dialog. Two configurations need to be created: Release and Debug. Corresponding Makefile targets – release and debug – need to be assigned for each configuration on the “Behavior” tab in the “Build (Incremental Build)” input field (see Fig. 6.8).

For the sake of simplicity the Makefile outputs both – debug and release executables to the same `./dist/` project folder. Therefore the clean target needs to be invoked when switching between build configurations.

The desired build configuration can be selected in Eclipse menu: Project → Build Configurations → Set Active. The build must be started in Project → Build Project menu item.

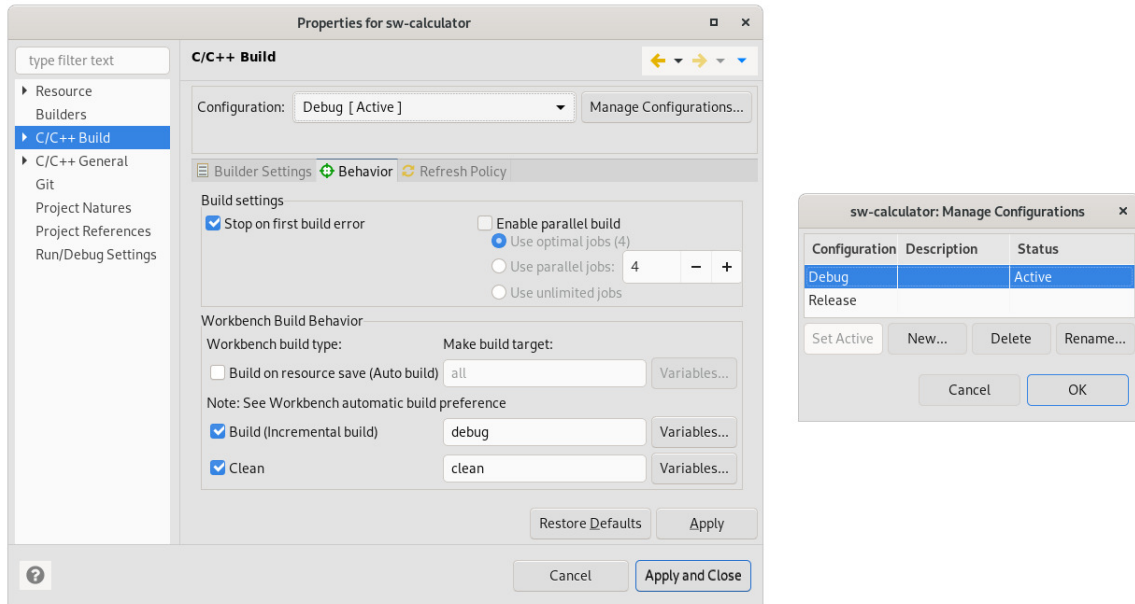


Fig. 6.8 Setting up Eclipse build configurations

After the successful build the executable file will be generated and it will be possible to proceed with setting up the Launch configuration.

6.6.8 Setting Launch Configuration

To be able to run or debug the program executable a setup of a new Launch configurations required. It includes following settings: location of the executable file; program arguments; environment variables for the launch and debugger settings. A new configuration needs to be created in Eclipse menu “Run → Debug Configurations...”. In the “Debug Configurations” the “C/C++ Application” option needs to be selected and the “New configuration” button clicked.

On the “Main” tab the location of the executable needs to be specified. The Makefile discussed in this chapter outputs the executable file to the ./dist/ project folder. It is advised to select the “Disable auto build” option. Otherwise Eclipse will rebuild the project upon every launch.

The environment variables set up in the previous subsection only affect the build process. Environment for the launch configuration needs to be specified separately. In order to launch

the program the only required variable is the location of the ROOT shared libraries. On the “Environment” tab the LD_LIBRARY_PATH on Linux and DYLD_LIBRARY_PATH on macOS system need to be specified (see Fig. 6.9).

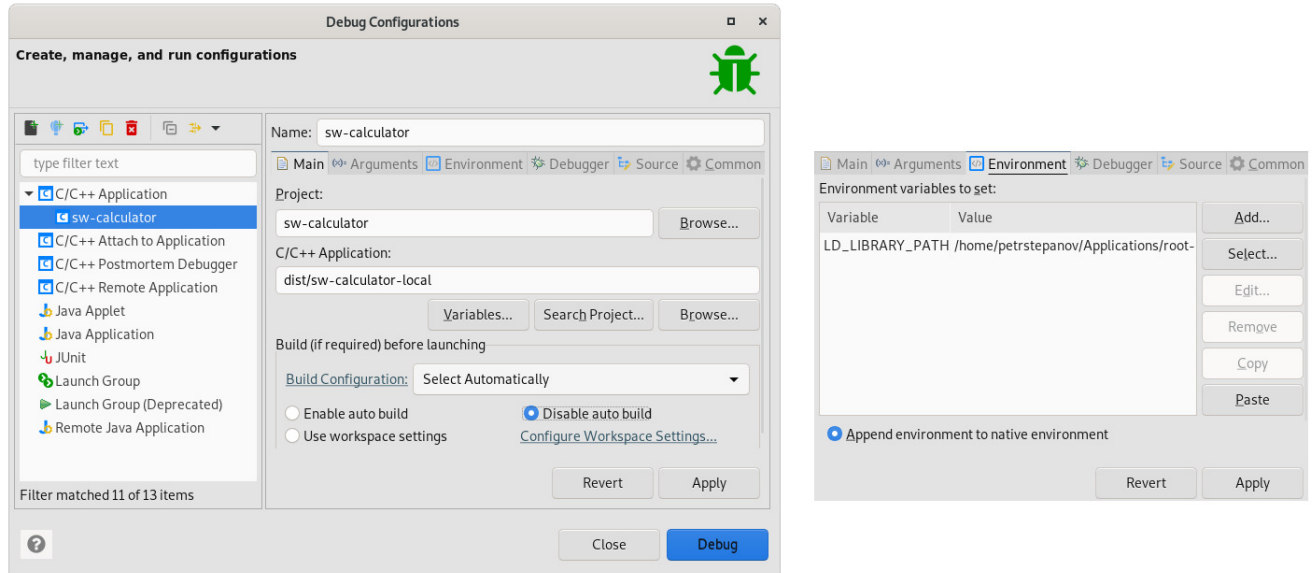


Fig. 6.9 Run and Debug configurations

6.7 Model View architecture

Usually applications developed with the Graphical User Interface (GUI) use specific architectural patterns of the code organization that are named Model-View patterns. They are represented by a set of rules that govern the relationship between the data in the program and the way it is presented to the user. In this section, we give introduction to the model/view paradigm, and outline the involved concepts.

Let's consider a trivial example that reveals the model-view paradigm. A program stores an experimental spectrum as a set of two-dimensional data points (bin, count) – each having a bin number and a corresponding count in the bin. This data is named Model. The visual representation of the spectrum data can be different. For instance, it can be a graph on a two-dimensional axis. Alternatively, the same data could be represented as a two-column table. Therefore, two different View objects utilizing the same data set can take place. In order to avoid program code duplication the Views logic is separated from the Model they

are interacting with.

The separation of functionality – decoupling the Model and View instances from each other – introduced by this architecture has following advantages:

- Ability to reuse code in the program and avoid code duplication.
- Greater flexibility to customize the presentation of the data.
- Parallel development (multiple developers working on the same code base).
- Easier testing and code maintenance.

There is a variety of implementations of the Model-View pattern. The oldest pattern for achieving the separation of concerns is Model-View-Controller (MVC). It consists of three layers: Model, View and Controller. In addition to dividing the application into these components, the MVC pattern defines interactions between them (see Fig. 6.10):

- Controller receives the user input (interaction with an input field, button or other control). Upon receiving the event from the user, Controller optionally validates the input and manipulates the data stored in the Model.
- Model manages and stores the data in the application. It also defines the rules that govern data manipulation. Model is not the data itself; it is rather responsible for reading, creating and deleting entries in the database.
- View does not have any knowledge of or reference to the controller. View receives event notifications from the Model. When the application data was changed, View updates the presentation.

Another common architectural pattern is Model-View-Presenter. Its principles are similar to the MVC but have more distinct separation of concerns.

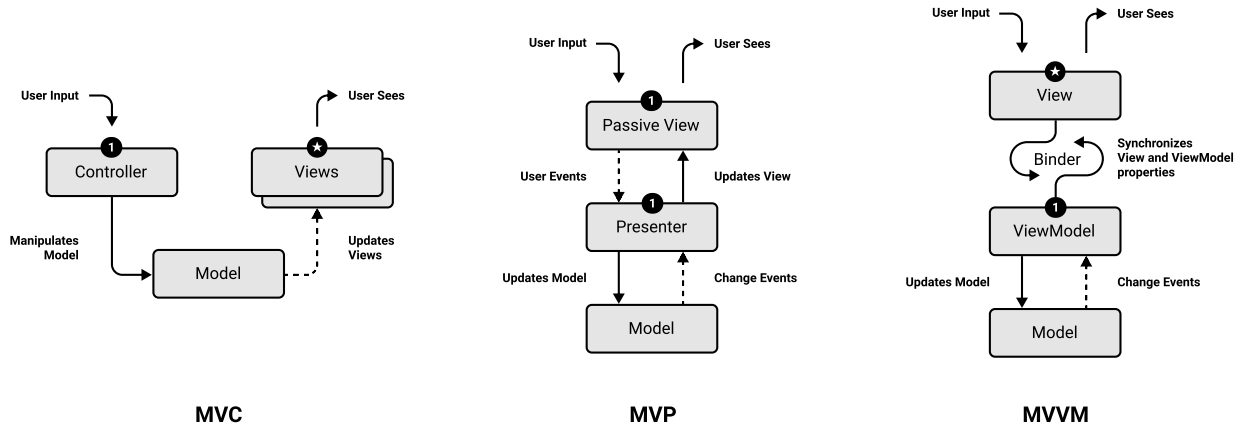


Fig. 6.10 Model-View architectural patterns. Solid lines represent function calls. Dashed lines stand for interactions defined by Publisher-Subscriber pattern [113].

- The View is named Passive View; It contains very little or no logic at all, delegating as much responsibility to the Presenter as possible. Usually the View implementation instantiates the corresponding Presenter object. View provides Presenter a reference to itself and exposes its methods for the Presenter to interact with the UI.
- The Presenter is responsible for addressing all the UI events. Sometimes it is referred to as a Supervising Controller. Presenter works as a middle-man between the View and the Model. Usually there is a one-to-one mapping between the Presenter and corresponding View. It receives data from the View and passes it to the Model. It also retrieves data from the Model, and formats it for display in the View.
- The Model is not aware of existence of the View. Model communicates with the Presenters through the publisher-subscriber algorithm [113]. When a change in the Model happens it publishes an event with a corresponding name. Presenters are subscribed to these events and update the Views' UI accordingly.

MVP framework is utilized by the well-known frameworks like Laravel (PHP) and Swing (Java). It is considered to be a more advanced architecture than MVC for the following reasons:

- Logic (like event handlers and user interface state) can be moved from the view to the presenter.
- The user interface can be unit tested in terms of the presenter, since it describes the user interface state. Inside the unit test, we replace the view with a test driver that makes calls to the presenter.
- The user interface is isolated from the application logic, both can be developed independently

The most recently announced architectural pattern is named Model-View-ViewModel (MVVM). Sometimes it is referred to as Model-View-Binder (see Fig. 6.10). The View and Model components have the same functionality as in the MVP pattern. However, the Presenter is replaced by a combination of the Binder and the ViewModel.

Binder provides a two-way binding mechanism between the UI fields in the View and their values stored in the ViewModel. When any input field in the View is changed, the Binder updates its value in the ViewModel. The opposite way, when any value in the ViewModel is changed, all the Views fields binded to the corresponding value are updated. This frees the developers from writing the communication logic that synchronizes View and Model in the MVP approach. UI frameworks that utilize the MVVM pattern are often referred to as “reactive”. Modern JavaScript frameworks like Vue.js and ReactJS use MVVP architecture.

6.7.1 Simple MVP implementation in CERN ROOT GUI

The MVP pattern was selected as an architectural pattern of use in the ROOT GUI applications for positron spectroscopy that I developed during the course of the research presented here (SW Calculator [16] and TLIST Precessor [15]) due to following reasons:

- MVP architecture provides a better maintainable and extendable code than MVC.
- MVVM’s binder mechanism is considered to be an overkill for simple UI applications.

Unfortunately, CERN ROOT GUI documentation and example programs do not refer to any Model-View architectural pattern. Thereby the implementation of the the MVP pattern in CERN ROOT framework was written as a part of current research.

In order to graphically illustrate the MVP implementation in the ROOT GUI classes a program named `root-mvp-gui` is developed [114]. This program is trivial though it completely reveals the essence of the MVP pattern and its integration with the ROOT GUI classes. In this section we provide the full code of the program.

Understanding the root-mvp-gui source code is essential for developers to be able to collaborate on the open-source programs developed in this research.

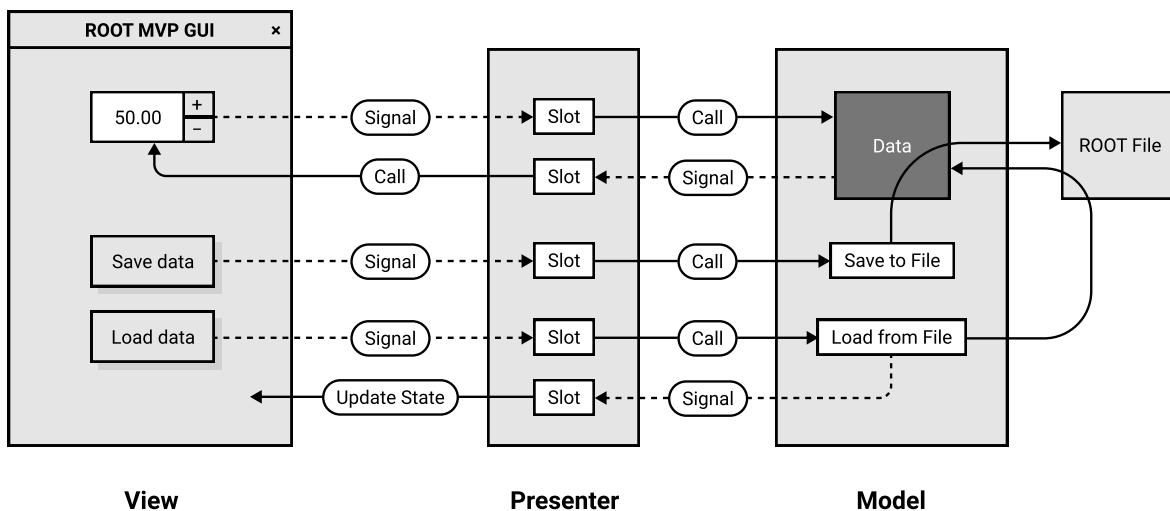


Fig. 6.11 Diagram of the signals and function calls of the root-mvp-gui program. It illustrates a trivial implementation of the MVP pattern within the ROOT framework. Source code is available on GitHub.

The interface of the root-mvp-gui program consists of a single View with an input field. The MVP architectural pattern works as follows:

- The user interaction event with the input field attached to the View changes its value.
 - View sends the signal to the Presenter; upon receiving the notification Presenter passes the input field value to the Model

- Model saves the corresponding value in a data structure and sends the success signal back to the Presenter.
- Presenter triggers the update of the View's state; View reflects the updated value of the input field.
- Additionally the Model has capabilities of saving and reading the data structure to a local file on the hard drive. This allows saving and restoring different states of the application.

The implementation of the MVP pattern is based on three fundamental classes. Abstract classes for the View (AbstractView), Presenter (AbstractPresenter) and a singleton class for the Model (Model).

The View abstract class inherits ROOT's default class TGCompositeFrame – the base class for composite widgets. Therefore, it is possible to attach child widgets to the AbstractView implementations. The ROOT GUI elements are created attached to the View in the initializeUI() method.

The AbstractView is a template class which allows storing a reference to the Presenter object of a generic type. The View implementation instantiates the concrete presenter object, providing a reference to itself in the method instantiatePresenter().

```

1 #ifndef ABSTRACTVIEW_H
2 #define ABSTRACTVIEW_H
3
4 #include <TGFrame.h>
5 #include <iostream>
6
7 template<class P> class AbstractView: public TGCompositeFrame {
8 public:
9     AbstractView(const TGWindow *w = 0) : TGCompositeFrame(w) {

```

```

10         presenter = nullptr;
11     }
12
13     ~AbstractView() {
14         delete presenter;
15     }
16
17 protected:
18     P* presenter;
19
20     virtual P* instantiatePresenter()=0;
21     virtual void connectPresenterSignals()=0;
22     virtual void initializeUI ()=0;
23
24     ClassDef(AbstractView,0)
25 };
26
27 #endif /* ABSTRACTVIEW_H */

```

Листинг 6.1: AbstractView.h

The abstract class AbstractPresenter.h is inherited from the ROOT's TQObject class in order to be able to accept the ROOT Signals (events) from the View and Model. Model Signals are connected to Presenter's slots in the connectModelSignals() method. Presenter being a middle man, holds references to the Model and the View.

```

1 #ifndef ABSTRACTPRESENTER_H
2 #define ABSTRACTPRESENTER_H
3

```

```
4 #include <TQObject.h>
5 #include <iostream>
6
7 template<class M, class V> class AbstractPresenter: public TQObject {
8 public:
9     AbstractPresenter(V* v){
10         view = v;
11     }
12
13     ~AbstractPresenter(){
14         delete model;
15         delete view;
16     }
17
18 protected:
19     M* model = nullptr;
20     V* view = nullptr;
21
22     virtual M* instantiateModel()=0;
23     virtual void connectModelSignals()=0;
24     virtual void updateViewState()=0;
25
26     ClassDef(AbstractPresenter,0)
27 };
28
29 #endif /* ABSTRACTPRESENTER_H */
```

Листинг 6.2: AbstractPresenter.h

Application has only one View class that contains three UI elements: number input (its value will be the only entry in the Model) and two buttons to load and save the View state.

Class MyView.h overrides pure virtual methods in the base class AbstractView.h. The code takes advantage of the override keywords. Thereby the ClassDef macro is replaced by the ClassDefOverride [115]. View implementation is following:

```
1 #ifndef MYVIEW_H
2 #define MYVIEW_H
3
4 #include "AbstractView.h"
5 #include "MyPresenter.h"
6 #include <TGNumberEntry.h>
7
8 class MyPresenter;
9
10 class MyView : public AbstractView<MyPresenter> {
11 public:
12     MyView(const TGWindow *w = 0);
13     virtual ~MyView();
14
15     // Expose getters and setters to Presenter
16     void setMyNumber(Double_t);
17     Double_t getMyNumber();
18
19 protected:
20     // Override base class virtual functions
```

```

21     MyPresenter* instantiatePresenter() override;
22
23     void connectPresenterSignals() override;
24
25     void initializeUI () override;
26
27
28     // Declaration of UI elements
29
30     TGNumberEntry* myNumberEntry;
31
32     TGTextButton* saveDataButton;
33
34     TGTextButton* loadDataButton;
35
36
37     ClassDefOverride(MyView,0)
38
39 };
40
41
42 #endif /* MYVIEW_H */

```

Листинг 6.3: MyView.h

The View notifies the Presenter about the user interactions via standard ROOT Signal and Slot mechanism. Signals from the user interface elements are directly connected to the slots in the Presenter object.

```

1 #include "MyView.h"
2
3 #include "MyPresenter.h"
4
5 #include <TGFrame.h>
6
7
8 MyView::MyView(const TGWindow* w) : AbstractView<MyPresenter>(w) {
9
10     initializeUI ();
11
12     presenter = instantiatePresenter();
13
14     connectPresenterSignals();
15 }

```

```
10
11 MyView::~MyView() {
12     Cleanup();
13 }
14
15 // Initialize UI widgets
16 void MyView::initializeUI(){
17     SetLayoutManager(new TGVerticalLayout(this));
18     // Number textbox
19     myNumberEntry = new TGNumberEntry(this, 0, 6, -1,
20         TGNumberFormat::kNESRealTwo, TGNumberFormat::kNEAAnyNumber,
21         TGNumberFormat::kNELLimitMinMax, 0, 100);
22     AddFrame(myNumberEntry, new TGLayoutHints(kLHintsCenterX | kLHintsTop,
23         100, 100, 50, 10));
24     // Save database button
25     saveDataButton = new TGTextButton(this, "Save_data");
26     AddFrame(saveDataButton, new TGLayoutHints(kLHintsCenterX | kLHintsTop,
27         0, 0, 0, 10));
28     // Load database button
29     loadDataButton = new TGTextButton(this, "Load_data");
30     AddFrame(loadDataButton, new TGLayoutHints(kLHintsCenterX | kLHintsTop,
31         0, 0, 0, 50));
32 }
33
34 // Instantinate the Presenter
35 MyPresenter* MyView::instantinatePresenter() {
36     return new MyPresenter(this);
```

```

32 }
33
34 // Connect View signals to Presenter slots
35 void MyView::connectPresenterSignals(){
36     myNumberEntry->Connect("ValueSet(Long_t)", "MyPresenter", presenter,
37                             "onViewMyNumberSet()");
38     saveDataButton->Connect("Clicked()", "MyPresenter", presenter,
39                             "onViewSaveDataButtonClick()");
40     loadDataButton->Connect("Clicked()", "MyPresenter", presenter,
41                             "onViewLoadDataButtonClick()");
42 }
43
44 // Setters and getters
45
46 void MyView::setMyNumber(Double_t number) {
47     myNumberEntry->SetNumber(number);
48 }
49
50 Double_t MyView::getMyNumber(){
51     return myNumberEntry->GetNumberEntry()->GetNumber();
52 }
```

Листинг 6.4: MyView.cpp

The Presenter receives user input from the view and passes the values of the user interface elements to the Model. Optionally Presenter can perform validation of the input data.

```

1 #ifndef MYPRESENTER_H
2 #define MYPRESENTER_H
3
```

```
4 #include "AbstractPresenter.h"
5 #include "MyView.h"
6 #include "Model.h"
7
8 class MyView;
9
10 class MyPresenter : public AbstractPresenter<Model, MyView> {
11 public:
12     MyPresenter(MyView* view);
13
14     // Slots for View Signals
15     void onViewMyNumberSet();
16     void onViewSaveButtonClick();
17     void onViewLoadButtonClick();
18
19     // Slots for Model Signals
20     void onModelMyNumberSet(Double_t);
21     void onModelDataLoaded();
22
23 protected:
24     // Override base class virtual methods
25     Model* instantiateModel() override;
26     void connectModelSignals() override;
27     void updateViewState() override;
28
29     ClassDefOverride(MyPresenter, 0)
30 };
```

```
31
32 #endif /* MyPRESENTER_H */
```

Листинг 6.5: MyPresenter.h

When Presenter is instantiated it updates the View state. Default values are pulled from the Model and populated into the View in the `updateViewState()` method.

```
1 #include "MyPresenter.h"  
2  
3 #include "MyView.h"  
4  
5 MyPresenter::MyPresenter(MyView* view) : AbstractPresenter<Model, MyView>(view) {  
6     connectModelSignals();  
7     updateViewState();  
8 }  
9  
10 Model* MyPresenter::instantinateModel() {  
11     return Model::getInstance();  
12 }  
13  
14 void MyPresenter::connectModelSignals() {  
15     model->Connect("myNumberSet(Double_t)", "MyPresenter", this,  
16                     "onModelMyNumberSet(Double_t)");  
17     model->Connect("dataLoaded()", "MyPresenter", this, "onModelDataLoaded()");  
18 }  
19 void MyPresenter::updateViewState(){  
20     view->setMyNumber(model->getMyNumber());
```

```
21 }  
22  
23 // Slots for View Signals  
24 void MyPresenter::onViewMyNumberSet(){  
25     Double_t number = view->getMyNumber();  
26     model->setMyNumber(number);  
27 }  
28  
29 void MyPresenter::onViewSaveButtonClick(){  
30     model->saveData();  
31 }  
32  
33 void MyPresenter::onViewLoadButtonClick(){  
34     model->loadData();  
35 }  
36  
37 // Slots for Model Signals  
38 void MyPresenter::onModelMyNumberSet(Double_t number){  
39     view->setMyNumber(number);  
40 }  
41  
42 void MyPresenter::onModelDataLoaded(){  
43     updateViewState();  
44 }
```

Листинг 6.6: MyPresenter.cxx

In the current program the Model is a singleton class that owns application data set

(Database). The Model exposes setters and getters to the Presenter to manipulate the values in the data set.

When a value in the data set was modified, the Model emits a notification signal. Presenter is subscribed to this notifications and updates the View accordingly.

```
1 #ifndef MODEL_H
2 #define MODEL_H
3
4 #include <RtypesCore.h>
5 #include <iostream>
6 #include <TQObject.h>
7 #include "Database.h"
8
9 class Model : public TQObject {
10 public:
11     static Model* getInstance();
12
13     // Data setters and getters
14     void setMyNumber(Double_t num);
15     Double_t getMyNumber();
16
17     // Save and load data methods
18     void saveData();
19     void loadData();
20
21     // Signals to Presenter
22     void myNumberSet(Double_t num); // *SIGNAL*
23     void dataLoaded();           // *SIGNAL*
```

```

24
25 private:
26     Model();
27     static Model* instance;
28
29     Database* data;
30     TString* dataFileName;
31
32     ClassDef(Model, 0)
33 };
34
35 #endif /* MODEL_H */

```

Листинг 6.7: Model.h

The Model can save and restore application state stored in the data set (Database) into the file on the hard drive. This functionality is achieved via standard ROOT Input and Output mechanisms.

```

1 #include "Model.h"
2 #include <TFile.h>
3 #include <TTree.h>
4
5 // Singleton
6 Model* Model::instance = NULL;
7
8 Model* Model::getInstance(){
9     if (!instance){
10         instance = new Model();
11     }
12     return instance;
13 }

```

```
11     }
12
13     return instance;
14
15 Model::Model(){
16
17     // Initialize the database
18
19     data = new Database();
20
21     // Set default database values
22
23     data->myNumber = 50;
24
25     // Set database filename
26
27     dataFileName = new TString("database.root");
28
29 };
30
31
32 // Write database to file
33
34 void Model::saveData(){
35
36     TFile * file = new TFile(dataFileName->Data(), "RECREATE");
37
38     TTree *tree = new TTree("tree", "ROOT_Tree");
39
40     tree->Branch("DatabaseBranch", "Database", &data, 16000, 0);
41
42     tree->Fill();
43
44     file ->Write();
45
46     file ->Close();
47
48 }
49
50
51 // Read database from file
52
53 void Model::loadData(){
54
55     TFile * file = new TFile(dataFileName->Data());
56
57     TTree *tree = (TTree*)file->Get("tree");
58 }
```

```

38     tree->SetBranchAddress("DatabaseBranch",&data);
39
40     tree->GetEntry(0);
41
42     file ->Close();
43
44 // Data setters and getters
45 void Model::setMyNumber(Double_t number){
46
47     data->myNumber = number;
48
49     myNumberSet(data->myNumber); // Emit signal
50 }
51
52 Double_t Model::getMyNumber(){
53
54     return data->myNumber;
55 }
56
57 // Model Signals
58 void Model::myNumberSet(Double_t n){
59
60     Emit("myNumberSet(Double_t)", n);
61 }
62
63 void Model::dataLoaded(){
64
65     Emit("dataLoaded()");
66 }

```

Листинг 6.8: Model.cpp

The data structure is represented with a Database class in the application. It is a descen-

dent of the TObject. This not only inherits the ROOT's Write method but also allows the Database to be a part of a ROOT collection.

In our trivial example we store one value in the Database that corresponds to the number entry value.

```

1 #ifndef SRC_DATABASE_H_
2 #define SRC_DATABASE_H_
3
4 #include <RtypesCore.h>
5 #include <TObject.h>
6
7 class Database : public TObject {
8 public:
9     Double_t myNumber;
10
11     ClassDef(Database, 1)
12 };
13
14 #endif /* SRC_DATABASE_H_ */
```

Листинг 6.9: Database.h

To summarize, in this section we have described the code of the three fundamental components of a ROOT-based GUI application built with the MVP architecture – View, Presenter and Model. Additionally we showed how the View's state can be stored in the Database class, saved and restored from the hard drive. The complete program code can be accessed on GitHub [114].

6.8 RooPositron program

RooPositron is a flexible positron lifetime fitting software that was developed as a part of this research [17]. It Supports the integration of custom models. The program is a console application. List of the implemented features:

- Implementation of custom fitting models (some c++ knowledge is required).
- In-depth control of the convolution operation. Change convolution bins number to balance fitting speed and precision.
- Fitting models support evaluation of the indirect parameters as functions of regular model parameters.
- Simultaneous fitting of multiple spectra with various channel widths.
- Plotting functionality and output of raster and vector plots.
- ASCII file output for plotting in other software.

The program is written in object-oriented C++ using CERN ROOT libraries. Fitting is performed via RooFit package functionality. Following fitting models are supported: multi-exponential, standard trapping model (STM), diffusion trapping model (DTM), dielectric powders model, liquids and solutions.

6.8.1 Installation

To install the program on Windows 10, first set up Ubuntu Linux inside Windows Subsystem for Linux (WSL) as described in 6.2. Launch Ubuntu Linux by selecting Start -> Ubuntu. Proceed with the setup on Ubuntu linux as described below.

In order to install the program in Linux or macOS first install CERN ROOT libraries. Instructions can be found in Section 6.1. Next, open Terminal and clone the program on the hard drive:

```
mkdir -p ~/Downloads && cd ~/Downloads
git clone https://github.com/petrstepanov/roopositron
cd ./roopositron
```

Compile the source code and link with ROOT libraries into a binary executable:

```
make
```

```
make install
```

Once the program is installed, you will be able to run it in Terminal with the “roopositron” command. Program is a console application, user interface implementation is in progress.

6.8.2 How to start the fit

RooPositron uses ORTEC’s Maestro file format for the input spectra. Place your spectra .Spe files in a folder, navigate into it and run “roopositron”.

Application creates “./constants.txt” file located in the same folder; this stores spectrum properties and fitting directions. For every fit RooPositron creates a child folder with the following set of files:

- “parameters.txt” is a file containing all the parameters of the fit. These parameters include resolution function information, fitting model parameters and width of the channel for every spectrum.
- “fit-* png” and “fit-* root” are raster and vector images of the fit
- “data-* txt” ASCII files generated from the plots with columns that allow plotting in other programs.

Variable	Default value	Description
channels	8192	Total number of channels to read from input files

defaultChannelWidth	0.006186	Default width of analyzer channel, in nanoseconds. In case of fitting multiple spectra, individual channel width for every spectrum can be set later in “constants.txt” file.
skipLines	12	Number of lines to skip in input .Spe files. Usually, Maestro files have a header with some information.
minChannel	600	Trim spectra on the left by setting the minimum channel number for the fit. Please make sure the spectrum range [minChannel, minChannel+backgroundBins] is flat without humps. These bins are used for automatic background level evaluation.
maxChannel	4000	Trim spectra on the right end.
excludeMinChannel and excludeMaxChannel	0	Exclude a range of channels from the spectra fit and χ^2 . Useful if experimental spectra have parasite humps. Set values to 0 to avoid excluding regions from a fit.
minimizerType	Minuit	Type of minimizer function to be used during the fit. Use one of the following values: Minuit, Minuit2, Fumili, GSLMultiMin.

decayModel	exp	Name of the fitting model to be used. Following models are currently available: exp, 2exp, 3exp, trapping, grain, powder, liquid. It is possible to specify two comma-separated models together, e.g. trapping,exp. The resulting fitting model will be a linear combination of separate fitting models.
resolutionFunction	2gauss	Number of Gaussians in resolution function. Currently support the following: 1gauss, 2gauss or 3gauss.
sourceComponents	1	Number of exponential components in source contribution. Use integer values: 1, 2, 3... For instance, if e+ source is sealed in Kapton, use 1 - one component.
commonParameters	comma-separated list of parameter names	For multiple spectra fitting. List of fitting parameter names that are common for all spectra during the fit. By default, common parameters are number of bins in spectrum (bins), channel width (channelWidth), parameters of the resolution function (FWHM_gauss1, FWHM_gauss2, FWHM_gauss3, Int_gauss2, Int_gauss3), and source contribution decay parameters (#tau_source, Int_source, #tau1_source, #tau2_source, #tau3_source, Int_expSource2, Int_expSource3).

bufferFraction	0.2	Convolution operation parameter Default value is 20% of the spectrum width. Increase this value if the tail of your spectrum does not approach the background level.
convolutionBins	1024	Binning of the convolution observable. Affects the sampling density of the FFT convolution operation. Increase to 2048 or 4096 if working with shorter lifetimes or higher channel width.
backgroundBins	150	Number of first spectrum bins used for background level estimation. Set to 0 to make background free during the fit. Fitting works best with the fixed automatic background.
asciiDelimiter	t	Column delimiter used in ASCII plot output files. C++ escaped. The default is tab.
imageWidth	1200	Width of the raster plot images.
imageHeight	800	Height of the raster plot images.

When launched, application checks the existence of the Constants file in the project folder. In case the file is missing the application will create Constants file with default values. List of variables in “./constants.txt” is presented in the table above.

If the value of a parameter is a combination of comma-separated items, make sure that there are no spaces between them. Any missing parameter in the “./constants.txt” file it will be replaced by the default one on the first program run.

6.8.3 Integrated fitting models

Currently, RooPositron supports a number of conventional fitting models. Model descriptions along with their fitting parameter names are demonstrated in the Table 6.2. On order

to use a certain fitting model please set the decayModel variable value in “./parameters.txt” to a certain model’s identifier. Additionally, you can specify a comma-separated list of models’ identifiers as a value of decayModel parameter. For instance, exp,exp,exp,exp would give a four-component exponential decay.

Every model accounts for an extra contribution of the annihilation of positrons in the source material.

6.8.4 How to adjust model fitting parameters

Once the program constants are defined we move on to setting the default model parameters for the fit. Run roopositron command from the Terminal. It will prompt to enter the starting parameters selected model. Input values using the keyboard.

Alternatively, you can interrupt the program by CTRL+C and navigate to the automatically generated “parameters.txt” file in a child folder. Use any text editor to open the “parameters.txt” (see Fig. 6.12). Set starting values, limits and select certain parameters to be fixed or free during the fit. Using a text editor is much quicker rather than entering model values from the keyboard. Especially when working with models that have many parameters.

Parameter name	Value	Minimum	Maximum	Error	Unit	Type
1 #lambda_+	2.430005	0.001000	100.000000	0.001440	1/ns	free
3 #lambda_2#gamma	6.250000	6.250000	6.250000	0.000000	1/ns	fixed
4 #lambda_b	20.000000	0.001000	100.000000	0.000000	1/ns	fixed
5 #lambda_po	0.252084	0.100000	100.000000	0.000144	1/ns	free
6 #tau1_source	0.150000	0.100000	2.000000	0.000000	ns	fixed
7 #tau2_source	0.380000	0.100000	5.000000	0.000000	ns	fixed
8 #tau3_source	1.800000	0.100000	10.000000	0.000000	ns	fixed
9 FWHM_gauss1	0.273959	0.100000	0.500000	0.000090	ns	free
10 FWHM_gauss2	1.104457	0.400000	2.000000	0.009972	ns	free
11 Int_expSource2	50.000000	0.000000	100.000000	0.000000	%	fixed
12 Int_expSource3	18.000000	0.000000	100.000000	0.000000	%	fixed
13 Int_gauss2	1.000000	0.000000	20.000000	0.000000	%	fixed
14 Int_source	12.000000	5.000000	20.000000	0.000000	%	fixed

Fig. 6.12 Editing fitting parameter values and limits in plain text editor.

6.8.5 How to implement a custom fitting Model

To implement a custom fitting model it is needed to have some object-oriented C++ knowledge. We have to create two classes. One will be responsible for the model equation

Table 6.2 List of fitting models supported by RooPositron

Model name	Identifier	Description
Mono-exponential	exp	For fitting spectra from reference defect-free samples.
Two-exponential	2exp	For materials saturated with one type of defects. Trapping speed is supposed to be very high.
Three-exponential	3exp	Three-exponential decay. Conventional deconvolution.
Multi-exponential	exp,exp,exp,exp	Multi-exponential deconvolution. Please specify as many comma-separated exp entries as you need.
Trapping model	stm	One state trapping model.
Diffusion-trapping model	dtm	For grained materials with point defects. The model accounts for: positron annihilation in bulk; e+ trapping into the vacancies and annihilation therein; e+ diffusion towards the grain boundaries; trapping and annihilation from intergrain space.
Powder model	powder	For dielectric nanopowders. The model accounts for: e+ annihilation in bulk of crystallites; e+ trapping and annihilation in vacancies within crystallites; Ps formation and escape outside of the crystallites; Ps thermalization and annihilation in inter-crystalline space.
Two-state powder model	powder2	Powder model with additional bounded state of the Ps atom on the powder surface.
Liquids and solutions	liquid	For liquids and liquid solutions. The model accounts for: formation of qf-Ps and its annihilation; transformation of qf-Ps into a bubble state; pick-off annihilation of Ps from bubble state; possible reactions of Ps with solvents and intratrack radicals (oxidation and ortho-para conversion).

and optional analytical integral. Another will provide default values for model parameters as well as formulas for the indirect model parameters calculated after the fit. Finally, we will have to come up with the new model identifier (name) and map the model with its identifier in the ModelProvider class.

1. Defining the Model equation

Extend the base `RooAbsPdf` class to define the model parameters and equation. Create your `CustomModel.cpp` and `CustomModel.h` files. Conventional location for model classes is `./src/roofit/pdfs/`. Apparently your `CustomModel` filename has to be unique. Override `RooAbsPdf::evaluate()` function and return your model equation there.

In order to dramatically improve the convolution speed please provide the numeric value of the function integral by overriding functions `RooAbsPdf::getAnalyticalIntegral()` and `RooAbsPdf::analyticalIntegral()`.

Since lifetime spectra are one-dimensional and integration is carried out along one variable, just return the value of 1 in function `getAnalyticalIntegral()`. For a given range provided as an `analyticalIntegral()` function argument you have to return the value of the definite integral of your model equation.

It is reasonable to calculate the definite integral using the Newton-Leibniz formula. If you refer to the existing models in the program you will see that `analyticalIntegral()` simply does return `indefiniteIntegral(x2) - indefiniteIntegral(x1);`. An indefinite integral is evaluated in `indefiniteIntegral()` function of your model class.

It is reasonable to use computational software (we used a Wolfram Mathematica in trial mode) to calculate the indefinite integrals for models' equations. Mathematica's `CForm[%]` command outputs any expression as C++ code. So user can copy expression from Mathematica and directly paste it in C++ `indefiniteIntegral()` function. Examples of Mathematica scripts that calculate indefinite integrals for already implemented models are located in the `./wolfram` folder.

2. Specifying default Model parameter values

Next, implement a wrapper class for your custom model. Conventional way to name it is `CustomModelProvider.class`. PDF wrppers are located in `./src/roofit/providers/`. In RooFit every function variable is an object. So the wrapper instantiates model parameter objects with default values. Next wrapper passes them to the Model and returns it.

Optionally if you want your model to calculate some indirect parameters please override `getIndirectParameters()` method in your `CustomModelProvider` class. The list of formulas (`RooFormulaVar` objects) you return in this function will be displayed in the legend on the plots along with regular model parameters.

3. Adding Model identificator

Lastly in order to be able to use our model we need to give it an identifier (char string used in `“./constants.txt”`). In order to do so modify the `PdfFactory` class. First, in `PdfFactory.h` add a new value to the `PdfHashNames` enumeration.

Come up with a model identifier and map it to the enumeration in `PdfFactory::hashPdfName`. Add a new case for the switch statement in `PdfFactory::getPdf()` and return your new `CustomModel` object.

If your model has indirect parameters, add a new case to the switch statement in `PdfFactory::getIndirectParameters` and return the list of your indirect parameters.

6.8.6 How to contribute

Contributors are welcome. Please clone the repository, make your changes and submit the Pull Request on GitHub platform [17]. Feel free to contact the author, Petr Stepanov with questions about `RooPositron` at `stepanovps@gmail.com`.

Summary

- Fully-digital CDB spectrometer with a software coincidence unit is assembled at Bowling Green State University. Special attention is paid to determination of the energy resolution of the apparatus (≈ 1.2 keV) and subtraction of the background contribution in the region close to the annihilation peak (511 keV). A computer program TLIST Processor is developed that subtracts the background on a two-dimensional energy spectrum and exports CDB spectrum. Another program – SW Calculator – was developed as a part of current research in order to perform deconvolution of the CDB spectrum into different contributions (e^+ annihilation on conduction and inner shell electrons, para-Ps annihilation in pores and so on). Additionally SW Calculator evaluates S- and W-parameters of the CDB spectra and allows calculation of the Fermi energy and binding energies of core electrons.
- Experimental spectra of pure and well annealed Al, Fe, Cu and Zn samples are measured and processed with a help of the developed software. The obtained values of the Fermi energies and binding energies of core electrons are in a good agreement with the reference values for the investigated metals. This result validates the correct operation of the CDB setup.
- Tuning of electronic circuits and optimization of geometry of the detection unit of the conventional analog PAL spectrometer is carried out. The regular spectrometer maintenance was performed every year. Maintenance included following procedures: time calibration, measurement of the amplitude spectra and adjustment of the CFDD thresholds, determination of the source correction and time resolution function.
- Three e^+ sources were produced from aqueous solution of $^{22}\text{NaCl}$. A convenient technology that allows sealing the $^{22}\text{NaCl}$ activity in between of thin Kapton foils that utilizes double-sided adhesive Kapton tape was suggested and implemented. All the e^+

sources were used in experiments during current research.

- New computer software RooPositron that allows processing the LT-spectra is developed. Program can account on a type of the studied materials (metals, powders, liquids) and positron reactions therein. The main advantage of the program is incorporation of the different physical fitting models that describe e^+ behavior in the studied media. Namely, multi-exponential deconvolution, standard trapping model, diffusion trapping models, Ps formation and thermalization in nanopowders, quasi-free Ps formation and kinetics of the intratrack chemical reactions in liquids (Ps oxidation, ortho-para conversion), Ps bubble formation. Additionally RooPositron supports integration of the custom fitting models. Program is distributed on the open-source basis which allows easy collaboration.
- LT spectra acquired at different recording time intervals and CDB spectra of Al_2O_3 0.05, 0.3,1 and 3 μm nanopowders were measured and interpreted by means of the RooPositron software. It was shown that consistent interpretation of the data is possible when thermalization process of the “hot” Ps atom in the intercrystalline space in nanopowders is taken into account. Kinetics of the Ps thermalization is essentially non-exponential, but the developed software is able to proceed with this.
- More detailed model of the Ps formation in liquids is suggested. Important novelty is taking into account the intermediate/transient Ps state – the quasifree positronium and its further transformation into the bubble state. It allowed us to explain reasonably the nature of deviation of I_1/I_3 ratio from the value of 1/3 in the conventional three-exponential decomposition of the spectra. It also explains the “juvenile broadening” effect observable in ACAR experiments.
- The application of the developed software made it possible to visualize the thermalization process of the “hot” Ps atom in the intercrystalline space in Al_2O_3 nanopowders. The rate constants of the Ps oxidation and the ortho-para conversion in liquids with

various concentrations of dissolved O₂ were obtained. It is impossible to distinguish these contributions using conventional three-exponential deconvolution.

- All the developed software is released under an open-source license; the program code can be accessed and improved by the researchers in the field.

References

- [1] R. Krause-Rehberg, H.S. Leipner “Positron Annihilation in Semiconductors. Defect Studies”. (Springer series in solid-state sciences. V. 127) Berlin: Springer 1999
- [2] “Positron spectroscopy of solids”. Eds. A. Dupasquier and A.P. Mills, Jr. IOS, Amsterdam, 1995
- [3] Positron and Positronium Chemistry; Schrader, D. M., Jean, Y. C., Eds.; Studies in physical and theoretical chemistry; Elsevier: Amsterdam [The Netherlands]; New York, 1988.
- [4] “Principles and applications of positron and positronium chemistry”. Eds. Y.C.Jean, P.E.Mallone, and D.M. Schrader (World Scientific Publications, Singapore, 2003)
- [5] Y. Kobayashi “Positron Chemistry in Polymers”, Defect and Diffusion Forum. V.331, pp.253-274 (2012) doi:10.4028/www.scientific.net/DDF.331.253
- [6] Kubicz, Ewelina, et al. “Novel J-PET Scanner Combined with Positron Annihilation Lifetime Spectroscopy Technique as a Tool for Morphometric Imaging.” Physica Medica, vol. 32, Sept. 2016, pp. 231–32. DOI.org (Crossref), doi:10.1016/j.ejmp.2016.07.478.
- [7] B. Jasinska, B. Zgardzinska, G. Cholubek et al. “Human Tissue Investigations Using PALS Technique – Free Radicals Influence”. Acta Physica Polonica A, V.132(5), pp.1556-1558 (2017)
- [8] Ewelina Kubicz and for the J-PET collaboration “Potential for biomedical applications of positron annihilation lifetime spectroscopy (PALS)” AIP Conference Proceedings 2182, 050004 (2019); <https://doi.org/10.1063/1.5135847>

- [9] E. Fernandez et al. “Tests of quantum electrodynamics with two-, three-, and four-photon final states from e^+e^- annihilation at $\sqrt{s}=29$ GeV. Phys.Rev.D, V.35, p.1 (1987) <https://doi.org/10.1103/PhysRevD.35.1>
- [10] Fee, M. S., et al. “Measurement of the Positronium 1^3S_1 – 2^3S_1 Interval by Continuous-Wave Two-Photon Excitation”. Physical Review A, V.48(1), pp.192-219 (1993) doi:10.1103/PhysRevA.48.192.
- [11] Gribakin, G. F., et al. “Positron-Molecule Interactions: Resonant Attachment, Annihilation, and Bound States.” Reviews of Modern Physics, vol. 82, no. 3, Sept. 2010, pp. 2557–607. DOI.org (Crossref), doi:10.1103/RevModPhys.82.2557.
- [12] Cassidy, D. B., et al. “Optical Spectroscopy of Molecular Positronium.” Physical Review Letters, vol. 108, no. 13, Mar. 2012, p. 133402. DOI.org (Crossref), doi:10.1103/PhysRevLett.108.133402.
- [13] Mills, Allen P. Possible Experiments with High Density Positronium. 2019, p. 030001. DOI.org (Crossref), doi:10.1063/1.5135824.
- [14] http://www.techno-ap.com/img/PositronLifetimeMeasurementSystem_e.pdf
- [15] P.S. Stepanov TLIST Processor. A Software Designed to Process Two-Dimensional Doppler Energy Spectra. <https://github.com/petrstepanov/tlist-processor>
- [16] P.S. Stepanov SW Calculator. A Computer Program for Calculating Line-Shape Parameters, Valence and Core Electron Energies. <https://github.com/petrstepanov/sw-calculator>
- [17] P.S. Stepanov RooPositron. A flexible positron lifetime fitting software. <https://github.com/petrstepanov/roopositron>

- [18] Brown, R., et al. "Effective Radius of Ground- and Excited-State Positronium in Collisions with Hard Walls." Physical Review A, vol. 95, no. 3, Mar. 2017, p. 032705. DOI.org (Crossref), doi:10.1103/PhysRevA.95.032705.
- [19] P.A.M. Dirac Proc. R. Soc. London Ser. A126 360 (1930);
P.A.M. Dirac Proc. Cambrige Philos. Soc. 26 361 (1930)
- [20] C.D. Anderson "The positive electron". Phys. Rev. 43 491 (1933)
- [21] V.B. Berestetskii, E.M. Lifshitz, L.P. Pitaevskii "Quantum electrodynamicsics" (Landau and Lufshitz Course of theoretical physics. V.4). Oxford: Butterworth-Heinemann, 2008
- [22] X-RAY DATA BOOKLET, Center for X-ray Optics and Advanced Light Source, Lawrence Berkeley National Laboratory <https://xdb.lbl.gov/xdb.pdf>
- [23] M. Deutsch "Evidence for the Formation of Positronium in Gases", Phys. Rev., V. 82, pp. 455-456 (1951)
- [24] Martin Deutsch Discovery of postronium. In "Adventures in Experimental Physics", V.4, pp. 67-81. World Science Communications, 1974.
- [25] Л.Д. Ландау, В.Б. Берестецкий 'О взаимодействии между электроном и позитроном", ЖЭТФ, т.19, с.67 (1949)
- [26] S. DeBenedetti, H.C. Corben "Positronium" Annu. Rev. Nucl. Sci., V.4, pp. 191-218 (1954)
- [27] V.W. Hughes, S. Marder, C.S. Wu Phys.Rev., V.106(5), pp. 934-947 (1957)
- [28] M.Eldrup, D.Lightbody, J.N.Sherwood "The temperature dependence of positron lifetimes in solid pivalic acid". Chem. Phys. 63 51-58 (1981)
- [29] R.A.Ferrel "Long lifetime of positronium in liquid helium". Phys. Rev., V. 108, 167-168 (1957)

- [30] S.V. Stepanov, D.S. Zvezhinskiy, V.M. Byakov “Beyond the Point Ps Approximation”, Materials Science Forum Vol. 733, pp 7-14 (2013) doi:10.4028/www.scientific.net/MSF.733.7
- [31] A.Sommerfeld, H.Walker. Ann. Phys. 32 56-65 (1938)
- [32] P.S. Stepanov, S.V. Stepanov, V.M. Byakov, F.A. Selim “Developing New Routine for Processing Two-Dimensional Coincidence Doppler Energy Spectra and Evaluation of Electron Subsystem Properties in Metals” Acta Physica Polonica A, Vol. 132(5), pp. 1628-1633 (2017) doi:10.12693/APhysPolA.132.1628
- [33] Christoph Hugenschmidt “Positrons in surface physics”, Surface Science Reports, V.71(4), pp.547-594 (2016) doi.org/10.1016/j.surfrept.2016.09.002
- [34] A. van Veen, H.Schut, J. de Roode, F.Labohm, C.V.Flaub, S.W.H.Eljt, P.E.Mijnarends “Intense positron sources and their applications”. Materials Science Forum 363-365 415-419 (2001)
- [35] P.S. Stepanov, F.A. Selim, S.V. Stepanov, A.V. Bokov, O.V. Ilyukhina, G. Duplatre, V.M. Byakov “Interaction of positronium with dissolved oxygen in liquids”, Physical Chemistry Chemical Physics (2020), doi 10.1039/C9CP06105C
- [36] A.T.Stewart “Positron annihilation in metals” in Positron annihilation, Edts. A.T.Stewart, L.O.Roelling. Academic Press, New York, London, 1967
- [37] Z.Tang, M.Hasegawa, Y.Nagai, M.Saito, Y.Kawazoe “First-principles calculation of coincidence Doppler broadening of positron annihilation radiation”. Phys. Rev. B 65 045108 (2002)
- [38] Cai-Lin Wang, Y.Kobayashi, K.Hirata “Positron mobilities in isoctane, n-hexane and hexafluorobenzene”. Radiat. Phys. Chem. 58(5-6) 451 (2000)

- [39] S.V. Stepanov, V.M. Byakov, G. Duplatre, P.S. Stepanov, A.V. Bokov "Track Effects in Positronium Formation", *Acta Physica Polonica A*, Vol. 132(5), p. 1461-1465, 2017
DOI: 10.12693/APhysPolA.132.1461
- [40] F.A.Selim, D.P.Wells, J.F.Harmon, W.Scates, J.Kwofie, R.SpaULDING, S.P.DuttaGupta, J.L.Jones, T.White, T.Roney "Doppler broadening measurements of positron annihilation using bremsstrahlung radiation". *Nuclear Instruments and Methods in Physics Research B* 192 197-201 (2002)
- [41] F.A.Selim, D.P.Wells, J.F.Harmon, J.Kwofie, G.Erikson, T.Roney "New positron annihilation spectroscopy techniques for thick materials". *Radiat. Phys. Chem.* 68 427 (2003)
- [42] E. do Nascimento, O. Helene, C. Takiya, V.R. Vanin *Nuclear Instruments and Methods in Physics Research, A* 538, pp. 723-730 (2005) doi:10.1016/j.nima.2004.09.013
- [43] E.D. Nascimento, O. Helene, V. Vanin, M.D. Cruz, and M. Morales, *Nuclear Instruments and Methods in Physics Research Section A: Accelerators, Spectrometers, Detectors and Associated Equipment* 609, 244-249 (2009). doi: 10.1016/j.nima.2009.07.051
- [44] E. do Nascimento, V.R. Vanin, N.L. Maidana, and O. Helene, *Journal of Physics: Conference Series* 443, 012024 (2013). doi:10.1088/1742-6596/443/1/012024
- [45] M. Haaks, T. Staab, and K. Maier, *Nuclear Instruments and Methods in Physics Research Section A: Accelerators, Spectrometers, Detectors and Associated Equipment* 569, 829 (2006). doi: 10.1016/j.nima.2006.08.117
- [46] C.Y. Xi, B.J. Ye, W. Kong, H.M. Weng, X.Y. Zhou, and R.D. Han, *Measurement Science and Technology* 16, 1212 (2005). doi: 10.1088/0957-0233/16/5/022

- [47] P. Pikart and C. Hugenschmidt, Nuclear Instruments and Methods in Physics Research Section A: Accelerators, Spectrometers, Detectors and Associated Equipment 750, 61 (2014). doi: 10.1016/j.nima.2014.01.066
- [48] V.B. Beresteckij, E.M. Lifshitz, L.P. Pitaevskij “Quantum electrodynamics” (Butterworth-Heinemann, Oxford, 2008). isbn: 978-0750633710
- [49] N.W. Ashcroft and N.D. Mermin, Solid state physics (Brooks/Cole Thomson Learning, South Melbourne, 2012). isbn: 978-0030839931
- [50] W. Lotz, J. Opt. Soc. Am., 2, 60, (1970), 206.
- [51] B. Bergersen “The effect of vacancy formation on the temperature dependence of the positron lifetime” Solid State Comm., V.7, pp.1203-1205 (1969)
- [52] D.C. Connors, R.N. West “Positron annihilation and defects in metals” Physics letters, V.30(1), pp. 24-25 (1969)
- [53] A. Dupasquier, R. Romero, A. Somoza “Positron trapping at grain boundaries” Phys. Rev. B, V.48(13) 9235-9245 (1993)
- [54] M.J.Puska, R.M.Nieminen “Theory of positrons in solids and on solid surfaces”, Reviews of Modern Physics, v. 66(3), p.841 (1994)
- [55] Jakub Cizek, Ivan Prochazka, Miroslav Cieslar, Radomir Kuzel, Jan Kuriplach, Frantisek Chmelik, Ivana Stulikova, Frantisek Becvar, Oksana Melikhova “Thermal stability of ultrafine grained copper”, Physical Review B, V.65, 094106 (2002)
- [56] B. Oberdorfer, R. Wurschum “Positron trapping model for point defects and grain boundaries in polycrystalline materials”, Physical Review B, V.79, 184103 (2009)
- [57] S.V. Stepanov, V.M. Byakov “To the theory of nonstationary diffusion-controlled tunnelling chemical reactions”, Radiation Physics and Chemistry, V.68 pp.643-646 (2003)

- [58] F.S.Dzheparov, J.-F.Jacquinot, S.V.Stepanov “Nuclear Relaxation via Paramagnetic Impurities”, Physics of Atomic Nuclei, v.65(11), 2052-2063 (2002). Translated from Yadernaya Fizika, v.65(11), 2113-2124 (2002)
- [59] Table of Integrals, Series, and Products. Eighth edition. I.S. Gradshteyn and I.M. Ryzhik. Ed. D.Zwillinger. Elsevier Inc., Amsterdam, 2015. ISBN 978-0-12-384933-5
- [60] C. Dauwe, T. Van Hoecke, D. Segers “Positronium Physics in fine powders of insulating oxides”, Proceedings of XXX Zakopane School of Physics “Condensed Matter Studies by Nuclear Methods”, Eds. K. Tomala and E.A. Gorlich, Zakopane, Poland, 6-13.05.1995
- [61] B. Van Waeyenberge, C. Dauwe “The interaction of positronium with paramagnetic surface defect at low temperatures in fine Al_2O_3 powders”, Radiation Physics and Chemistry, V. 68, pp. 553-556 (2003) doi:10.1016/S0969-806X(03)00229-9
- [62] P.S. Stepanov, F.A. Selim, S.V. Stepanov, V.M. Byakov “A Model for Joint Processing of LT and CDB Spectra of Dielectric Nano-sized Powders”, AIP Conference Proceedings 2182, 040004 (2019); <https://doi.org/10.1063/1.5135836>
- [63] P.S. Stepanov, F.A. Selim, S.V. Stepanov, V.M. Byakov “Positron and Positronium in Al_2O_3 nanopowders”, AIP Conference Proceedings 2182, 050008 (2019); <https://doi.org/10.1063/1.5135851>
- [64] K. Sudarshan, D. Dutta, S.K. Sharma, A. Goswami. P.K. Pujari “Air quenching of positronium in mesoporous materials: positron porosimetry” J. Phys.: Condens. Matter Vol. 19, 386204 (2007) doi:10.1088/0953-8984/19/38/386204
- [65] Y.Sang, H.Qin, H.Liu et al. J. Eur. Ceramic Soc., V.33(13-14), P. 2617-2623 (2013) <https://doi.org/10.1016/j.jeurceramsoc.2013.04.009>

- [66] G. Duplatre, I. Billard “Organic and Inorganic Chemistry of the Positron and Positronium” in Principles and Applications of Positron & Positronium Chemistry; Jean, Y. C., Mallon, P. E., Schrader, D. M., Eds.; World Scientific: Singapore; Hong Kong, 2003.
- [67] G. Consolati I. Genco M. Pegoraro L. Zanderighi “Positron annihilation lifetime (PAL) in poly[1-(trimethyl-silyl)propine] (PTMSP): Free volume determination and time dependence of permeability” J. Polym. Sci. B Polym. Phys., V.34(2), pp.357-367 (1996) [https://doi.org/10.1002/\(SICI\)1099-0488\(19960130\)34:2<357::AID-POLB17>3.0.CO;2-I](https://doi.org/10.1002/(SICI)1099-0488(19960130)34:2<357::AID-POLB17>3.0.CO;2-I)
- [68] B. Jasinska, B. Zgardzinska, G. Cholubek et al. “Human Tissue Investigations Using PALS Technique – Free Radicals Influence”. Acta Physica Polonica A, V.132(5), pp.1556-1558 (2017)
- [69] Ewelina Kubicz and for the J-PET collaboration “Potential for biomedical applications of positron annihilation lifetime spectroscopy (PALS)” AIP Conference Proceedings 2182, 050004 (2019); <https://doi.org/10.1063/1.5135847>
- [70] P. Moskal et al. “Feasibility study of the positronium imaging with the J-PET tomograph”. Phys. Med. Biol. 64 055017 (2019) <https://doi.org/10.1088/1361-6560/aafe20>
- [71] J. Lee, G.J. Celitans “Oxygen and Nitric Oxide Quenching of Positronium in Liquids” The Journal of Chemical Physics, V.44, p.2506 (1966); doi: 10.1063/1.1727072
- [72] Y. Kobayashi J. Chem. Soc. Faraday Trans., V.87, p. 3641 (1991)
- [73] O.E. Mogensen “Positron Annihilation in Chemistry”, Springer Verlag, Berlin, Heidelberg, New York, London, Paris, Tokyo, Hong Kong, Barcelona, Budapest, 1995
- [74] B. Zgardzinska, W. Bialko, B. Jasinska “Ortho-para spin conversion of Ps by paramagnetic O₂ dissolved in organic compounds”. Nukleonika, V.60(4) pp.801-804 (2015) DOI: <https://doi.org/10.1515/nuka-2015-0144>

- [75] A. Karbowski, K. Fedus, K. Suzewski, J. Bruzdowska, G. Karwasz Acta Physica Polonica A, V.132(5), P.1466 (2017) doi:10.12693/APhysPolA.132.1466
- [76] <http://prac.us.edu.pl/~kansy/index.php?id=lt10>
- [77] A. Bisi, G. Consolati, G. Gambarini, L. Zappa Nuovo Cimento, V.65B(2), p.442 (1981); Nuovo Cimento, V.1D(6), p.725 (1982); Nuovo Cimento, V.5D, p.358 (1985)
- [78] I. Billard, J.-Ch. Abbe, G. Duplatre J. Phys. Chem, V.95, p. 2501 (1991)
- [79] S.V. Stepanov, G. Duplatre, V.M. Byakov, D.S. Zvezhinskiy, V.S. Subrahmanyam “Formation of quasi-free and bubble positronium states in water and aqueous solutions”. Acta Physica Polonica A. V. 125(3), pp. 770-774, (2014) DOI: 10.12693/APhysPolA.125.770.
- [80] S.V. Stepanov, V.M. Byakov, G. Duplatre, D.S. Zvezhinskiy, P.S. Stepanov, A.G. Zaluzhnyi “Early processes in positron and positronium chemistry: possible scavenging of epithermal e^+ by nitrate ion in aqueous solutions”. J. Phys. Conf. Ser., V.618, 012003 (2015) doi:10.1088/1742-6596/618/1/012003
- [81] D.S. Zvezhinskiy, M. Butterling, A. Wagner, R. Krause-Rehberg, S.V. Stepanov “Account of the intratrack radiolytic processes for interpretation of the AMOC spectrum of liquid water”. J. Phys. Conf. Ser., V.443, 012057 (2013) doi:10.1088/1742-6596/443/1/012057
- [82] D.S. Zvezhinskiy, M. Butterling, A. Wagner, R. Krause-Rehberg, S.V. Stepanov “The evidence of quasi-free positronium state in GiPS-AMOC spectra of glycerol”. Acta Physica Polonica A. V. 125(3), pp. 821-824, (2014) DOI: 10.12693/APhysPolA.125.821
- [83] H.L. Clever, R. Battino, H. Miyamoto, Yu. Yampolski, C.L. Young “IUPAC-NIST Solubility Data Series. 103. Oxygen and Ozone in Water, Aqueous Solutions, and Organic Liquids (Supplement to Solubility Data Series Volume 7)”, Journal of Physical and Chemical Reference Data 43, 033102 (2014); <http://dx.doi.org/10.1063/1.4883876>

- [84] C.B. Kretschmer, Janina Nowakowska, Richard Wiebe “Solubility of Oxygen and Nitrogen in Organic Solvents from -25 to 50 C”. Industrial and Engineering Chemistry, Vol. 38(5), P.506-509 (1946)
- [85] R. Battino, T.R. Rettich, T. Tominaga “The Solubility of Oxygen and Ozone in Liquids” Journal of Physical and Chemical Reference Data, V.12, P.163-178 (1983); <https://doi.org/10.1063/1.555680>
- [86] V.M. Byakov, V.R. Petukhov J. Radioanal. Nucl. Chem. Letters. Vol.85(1), p.67 (1984)
- [87] S.V. Stepanov, V.M. Byakov “To the Theory of Nonstationary Diffusion-Controlled Tunelling Chemical Reactions”, Radiation Physics and Chemistry, v.68, p.643-646 (2003) doi:10.1016/S0969-806X(03)00284-6
- [88] F. Bockstahl, G. Duplâtre Phys. “Quantitative determination of a sodium dodecyl sulfate micellar radius through positron annihilation lifetime spectroscopy” Chem. Chem. Phys., 1, pp. 2767-2772 (1999); doi:10.1039/A901518C
- [89] D.P. Kerr, A.M. Cooper, B.G. Hogg Canad. J. Phys., V.43, P.963 (1965)
- [90] <http://palsfit.dk/>
- [91] I. Antcheva, M. Ballintijn, B. Bellenot, M. Biskup, R. Brun, N. Buncic, Ph. Canal, D. Casadei, O. Couet, V. Fine, L. Franco, G. Ganis, A. Gheata, D.G. Maline, M. Goto, J. Iwaszkiewicz, A. Kreshuk, D.M. Segura, R. Maunder, L. Moneta, A. Naumann, E. Offermann, V. Onuchin, S. Panacek, F. Rademakers, P. Russo, and M. Tadel, Computer Physics Communications 180, 2499 (2009); <https://doi.org/10.1016/j.cpc.2009.08.005>.
- [92] W. Verkerke and D. Kirkby. RooFit Users Manual v2.91. http://root.cern.ch/download/doc/RooFit_Users_Manual_2.91-33.pdf
- [93] Antcheva, I.; Ballintijn, M.; Bellenot, B.; Biskup, M.; Brun, R.; Buncic, N.; Canal, Ph.; Casadei, D.; Couet, O.; Fine, V.; et al. ROOT — A C++ Framework for Petabyte Da-

- ta Storage, Statistical Analysis and Visualization. Computer Physics Communications 2009, 180 (12), 2499–2512. <https://doi.org/10.1016/j.cpc.2009.08.005>.
- [94] Verkerke, W.; Kirkby, D. The RooFit Toolkit for Data Modeling. In Statistical Problems in Particle Physics, Astrophysics and Cosmology; Published by imperial college press and distributed by world scientific publishing co., 2006; pp 186–189. https://doi.org/10.1142/9781860948985_0039.
- [95] Stepanov, P. RooFit’s convolution fails linearity test <https://sft.its.cern.ch/jira/browse ROOT-9653>.
- [96] Downloading ROOT | ROOT a Data analysis Framework <https://root.cern.ch/downloading-root> (accessed Feb 21, 2020).
- [97] XQuartz - Releases <https://www.xquartz.org/releases/index.html> (accessed Feb 21, 2020).
- [98] Build Prerequisites | ROOT a Data analysis Framework <https://root.cern.ch/build-prerequisites> (accessed Feb 21, 2020).
- [99] Xcode Versions Information – MacPorts <https://trac.macports.org/wiki/XcodeVersionInfo> (accessed Feb 21, 2020).
- [100] More Software Downloads - Apple Developer <https://developer.apple.com/download/more/> (accessed Feb 21, 2020).
- [101] Building ROOT | ROOT a Data analysis Framework <https://root.cern.ch/building-root> (accessed Feb 21, 2020).
- [102] Compiling ROOT 6 executable on Windows <https://root-forum.cern.ch/t/compiling-root-6-executable-on-windows/33276> (accessed Feb 21, 2020).
- [103] Chrome OS - Linux Apps. Wikipedia; 2020. https://en.wikipedia.org/wiki/Chrome_OS#Linux_Apps

- [104] Xming X Server for Windows <https://sourceforge.net/projects/xming/> (accessed Feb 21, 2020).
- [105] Brun, R. ROOT User's Guide <https://root.cern.ch/root/htmldoc/guides/users-guide/ROOTUsersGuide.html> (accessed Feb 21, 2020).
- [106] GNU make reference <https://www.gnu.org/software/make/manual/make.html> (accessed Feb 22, 2020).
- [107] The GNU C++ Library Manual <https://gcc.gnu.org/onlinedocs/gcc-4.9.2/libstdc++-manual/> (accessed Feb 22, 2020).
- [108] Freedesktop.Org Project. Wikipedia; 2020. <https://en.wikipedia.org/wiki/Freedesktop.org>
- [109] Desktop Entry Specification <https://specifications.freedesktop.org/desktop-entry-spec/desktop-entry-spec-latest.html> (accessed Feb 22, 2020).
- [110] Download Free Java Software <https://www.java.com/en/download/> (accessed Feb 23, 2020).
- [111] How to setup gdb and Eclipse to debug C++ files on macOS Catalina <https://www.thomasvitale.com/how-to-setup-gdb-and-eclipse-to-debug-c-files-on-macos-sierra/> (accessed Feb 23, 2020).
- [112] Eclipse Downloads. The Eclipse Foundation <https://www.eclipse.org/downloads/> (accessed Feb 23, 2020).
- [113] Publish–Subscribe Pattern. Wikipedia; 2020. https://en.wikipedia.org/wiki/Publish%20%80%93subscribe_pattern
- [114] Stepanov, P. ROOT MVP GUI. Program That Illustrates Trivial MVP Implementation with the CERN ROOT Framework.; 2020. <https://github.com/petrstepanov/root-mvp-gui>

- [115] How to use the ClassDef Preprocessor Macro <https://root.cern.ch/how/how-use-classdef-preprocessor-macro> (accessed Feb 29, 2020).
- [116] Lynx Digital Signal Analyzer. <https://www.mirion.com/products/lynx-digital-signal-analyzer> (accessed 28 Mar, 2020).

The simplest view on γ -spectroscopy

Usually, γ -radiation from nuclei is initiated by preceding α - or β -decays of the “mother” nuclides. In many cases β -particles (and α -particles even more), emitted as a result of radioactive transformations of the nuclei, can not reach sensitive area of the detectors. As a rule, they are absorbed in the substance of the radioactive source itself.

In γ -detectors, the projectile gammas do not detected directly, but via generation of the secondary charged particles (usually electrons) as a result of interaction of the primary γ -quanta with the active substance of the detector. When projectile γ -quantum hits the scintillator, the secondary charged particles are generated as a result of the following three processes: the photoelectric effect, the Compton effect and the creation of electron-positron pairs.

Probability (or cross-section) of the photoelectric effect is proportional to Z^5 , where Z is the charge of the nucleus of the atom which is hit by the photon. For example, if we use BaF_2 as a scintillator, Z is equal to 56 – atomic number of barium. The electron knocked out as a result of the photoelectric effect acquires the energy

$$E_e = E_\gamma - E_b - E_r, \quad (1)$$

where E_γ is the energy of the primary γ -quantum, E_b is the binding energy of the knocked out electron, and E_r is the recoil energy of the nucleus (usually it can be neglected).

Usually the photoelectric effect is accompanied by emission of characteristic X-rays and Auger electrons. Characteristic X-rays, in turn, can also cause a photoelectric effect. Electrons formed as a result of all these processes are formed almost simultaneously. They all spend their energy in the detector producing ion-electron pairs. Thus, almost all the energy of the primary γ -quantum is transferred to kinetic energy of the secondary electrons. As a result the detector registers a photopeak (or the peak of “total absorption”) at the energy of

$$E = E_\gamma.$$

At the Compton scattering, only a part of energy of the primary photon is transferred to the knocked-out electron:

$$E_e = E_\gamma - E_{\gamma 2}, \quad E_{\gamma 2} = \frac{E_\gamma}{1 + E_\gamma(1 - \cos \theta)/mc^2}. \quad (2)$$

Here E_e is the energy of the knocked out electron, $mc^2 = 511$ keV is the rest energy of an electron, E_γ and $E_{\gamma 2}$ are the energies of γ -quanta before and after scattering, θ is the scattering angle.

If the scattering angle is $\theta = 180^\circ$, ($\cos \theta = -1$), then the electron acquires the maximal possible energy:

$$E_e^{max} = \frac{E_\gamma}{1 + mc^2/2E_\gamma}. \quad (3)$$

In this case it moves forward (along the initial direction of the projectile γ -quantum hitting the detector. In this case, the scattered photon (the Compton photon) flies strictly backwards and carries out the minimal possible energy $E_{2\gamma}^{min}$:

$$E_{2\gamma}^{min} = \frac{E_\gamma}{1 + 2E_\gamma/mc^2} \equiv E_{BS}, \quad E_{BS} = E_\gamma - E_e^{max}. \quad (4)$$

This is the case of “backscattering”.

The maximal energy which is transferred to the Compton electron E_e^{max} is called the upper edge of the Compton spectrum (or the Compton shoulder). In the Table 3 we present the energies of the Compton edges for some typical γ -emitters calculated according to Eqs. (3)-(4).

Table 3 The Compton-edge energies and energies of backscattered photons for some γ -emitters, calculated according to Eqs. (3)-(4).

E_γ , keV	annihilation	Cs-137	Ne-22	K-40
E_e^{max} , keV	511	662	1275	1450
$E_{BS} = E_\gamma - E_e^{max}$, keV	341	478	1062	1243

Smearing of the Compton edge (from the high-energy side) is due to the fact that backscattered photons (especially in detectors with big scintillators) can, in its turn, experience the Compton scattering again and thereby release some additional energy in the active volume of the detector. In Fig. 13 we presented the γ -spectrum of Cs-137 measured in our laboratory. It is a typical example of a γ -spectrum illustrating the photoelectric effect and the corresponding Compton scattering. The characteristic kink corresponding to the Compton edge at $E_e^{max} = 478$ keV is clearly seen. If the Compton effect occurs not in the active substance of the detector, but in its housing, and if the produced Compton photon hits again the active substance of the detector, and if this photon experienced the photoelectric effect therein, then it leads to a certain increase of the number of the produced ion-electron pairs in the detector. As a result some step up on the γ -spectrum appears at energies $E > E_{BS} = E_\gamma - E_e^{max} = 184$ keV (backscattering), and this increment lasts up to E_γ .

In our laboratory (where all the experiments were carried out) the γ -background spectrum was measured periodically twice a year using both Ge-detectors. During all the measurements, the sensitive elements of the detectors were shielded with lead bricks, Fig. 14. It decreased the background several times (in each detector). The spectra measured in summer 2019 are shown in Fig. 13 and 17 in green. Characteristic photopeak from K-40 and its Compton edge as well as many other characteristic lines are clearly seen in the spectrum. In particular, there is a line from Ne-22. After thorough washing of the lead bricks in autumn 2019, its intensity decreased by 2 times, but it did not completely disappear. We have found that it comes from the storage room, where all the positron sources are kept.

Cross-sections of the photoelectric effect and the Compton scattering rapidly decrease with the energy of γ -quanta, Fig. 15. If the photon energy becomes greater than $2mc^2 = 1022$ keV, then such a γ -quantum, flying close to a nucleus, can generate an e^+e^- pair and disappear. The energy difference $E_\gamma - 2mc^2$ is transformed into kinetic energy of the created electron and positron. Probability of this pair production process increases rapidly with

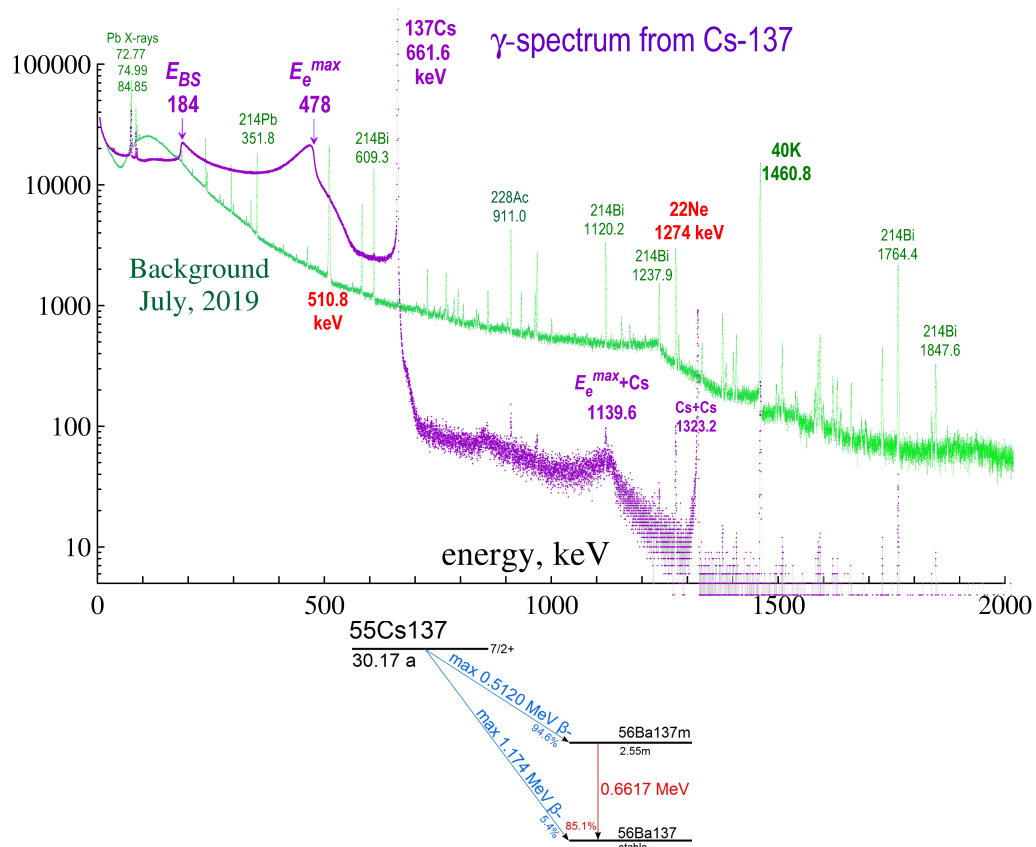


Fig. 13 γ -spectrum and the decay scheme of Cs-137. This isotope emits photons with $E_\gamma = 662$ keV. In green we have shown the background γ -spectrum in our laboratory.



Fig. 14 Position of the γ -source and the lead shielding of the sensitive volume of the HPGe γ -detector.

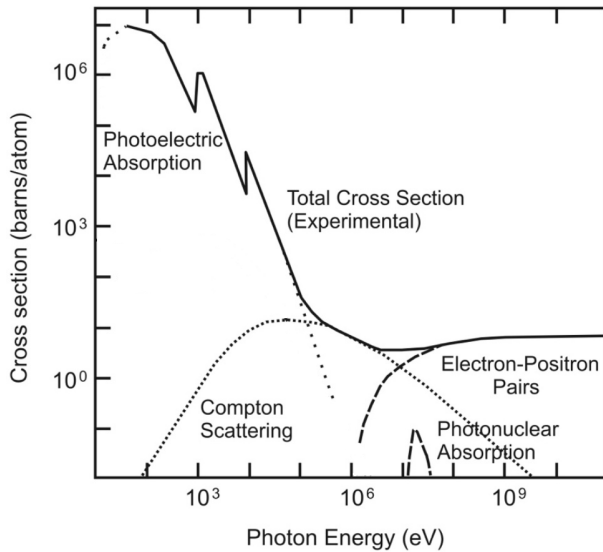


Fig. 15 Dependencies of cross-sections of the photoelectric effect, Compton effect and pair production vs. energy of the incident γ -quanta irradiated metallic copper.

increasing energy of the projectile γ -quantum, Fig. 15. If the pair production occurred in the detector volume, the created electron and positron are usually stopped therein also. It leads to the absorption of the energy $E_\gamma - 2mc^2$ in it.

The produced positron can annihilate with some electron, forming of two annihilation 511 keV photons. If both these photons experience a photoelectric effect (be absorbed in the detector), then the total absorbed energy will be equal to E_γ , and this event is undistinguishable from an ordinary photoabsorption of the original γ -quantum. However, if one of the annihilation photons leaves the detector without absorption, then a peak appears at lower energy $E_\gamma - mc^2$ (SE = single-escape peak). If both annihilation photons fly away the detector without being absorbed in it, a peak will be detected at the energy $E_\gamma - 2mc^2$ (DE = double-escape peak). These peaks are clearly visible, for example, in the case of decay of K-40 nuclei. 11% of decays of this isotope proceed by the e-capture. In this case, an excited nucleus Ar-40 is formed, which immediately emits 1460 keV γ -quantum. The latter creates e^+e^- pairs in the detector, Fig. 16.

It is often happen that in the studied sample occurs very quick sequence of γ -transitions, as compared with time needed for registration of γ -quanta in the detector. So the detector considers all these γ -quanta as one quantum and sums their energies. For example, when 1.274 MeV γ -quantum accompanying the β^+ -decay of Na-22 hits the detector (Fig. 17), very

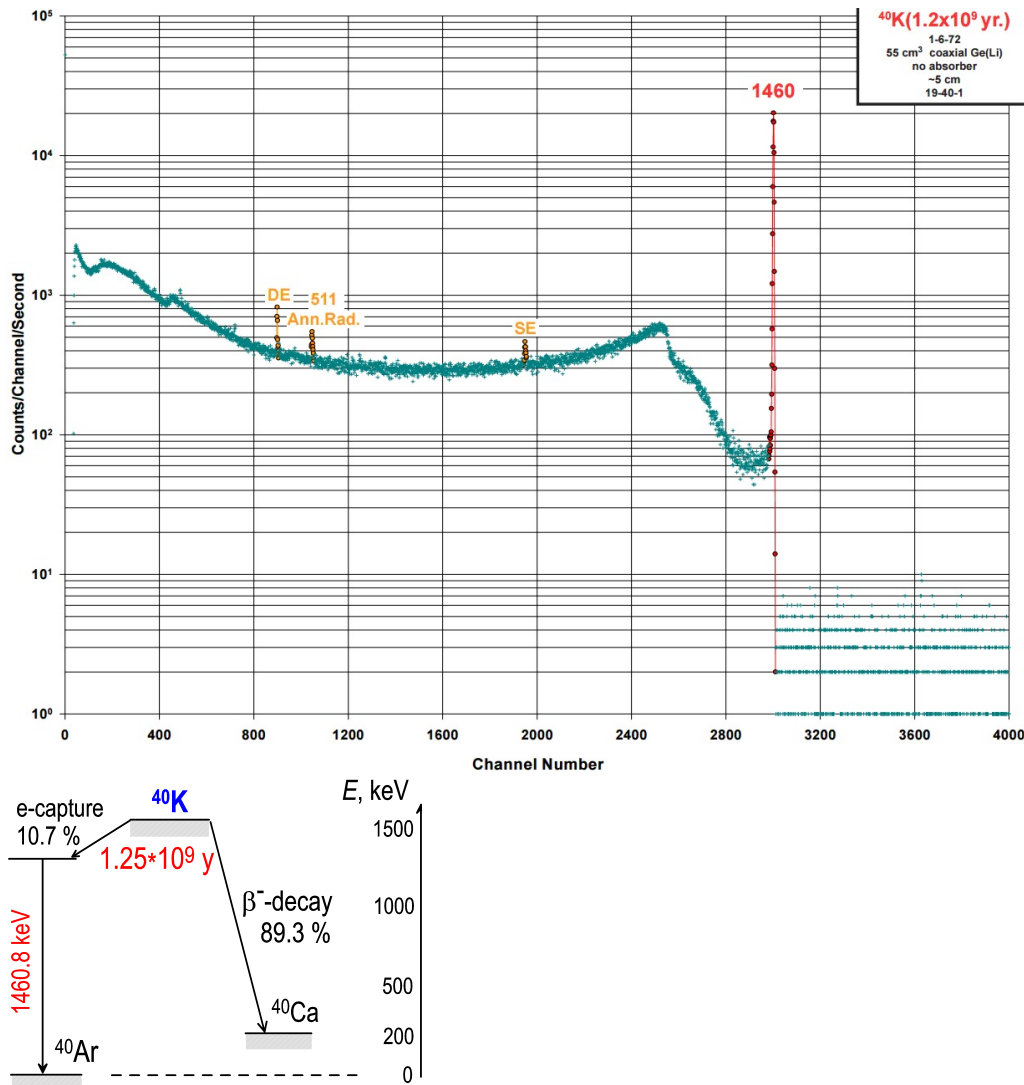


Fig. 16 γ -spectrum of K-40 and its decay scheme. Since the energy of the emitted photons is quite high (1460 keV), the pair production process is possible. Single-escape and double-escape peaks are located to the left of the photopeak on 511 and 1022 keV, respectively. The characteristic Compton edge is at $E_e^{max} = 1243$ keV and the backscattering peak is at $E_{BS} = E_\gamma - E_e^{max} = 1460 - 1243 = 217$ keV [Idaho National Laboratory “Gamma-ray Spectrum Catalogue” <https://gammaray.inl.gov/SiteAssets/catalogs/ge/pdf/k40.pdf>]

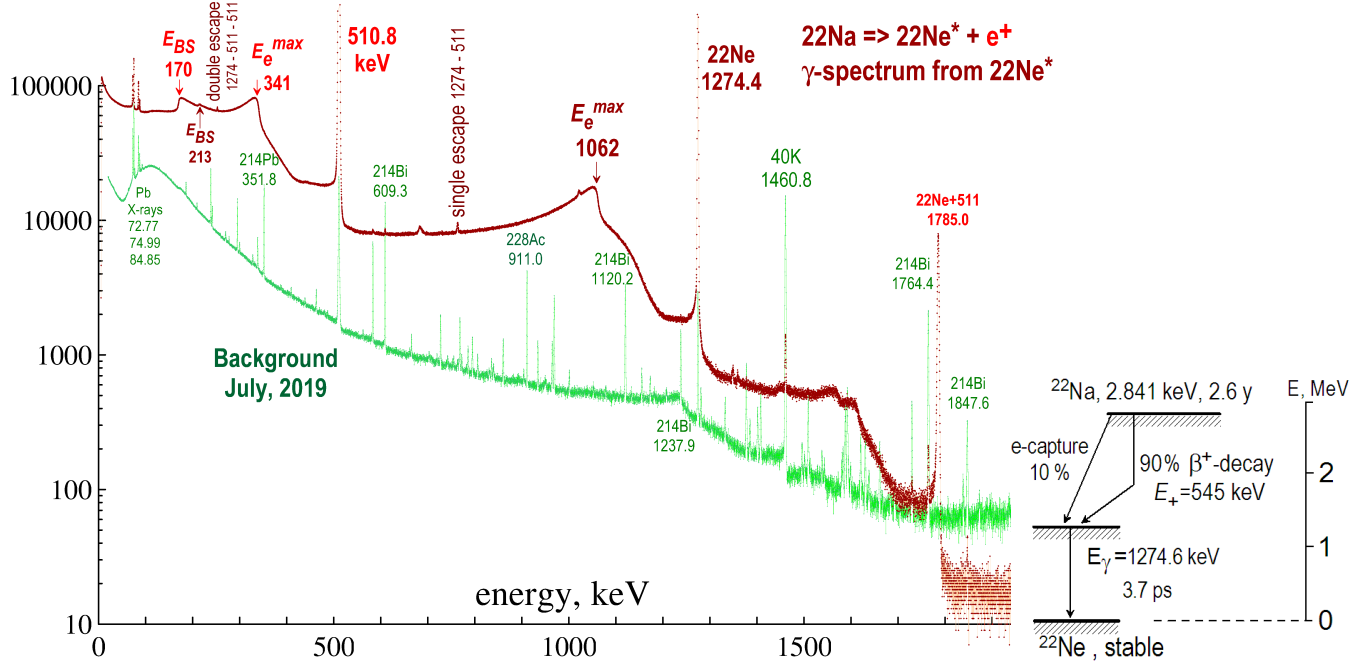


Fig. 17 γ -spectrum and the decay scheme of ^{22}Na . As a result of β^+ -decay an excited state of ^{22}Ne is formed. Within 3.7 ps it emits 1.274 MeV quantum and goes to the ground state. Annihilation of positrons leads to formation of 511 keV γ -quanta. Both these lines and other peculiarities at $E_e^{\max} = 1062$ keV, $E_{BS} = E_{\gamma} - E_e^{\max} = 1274 - 1062 = 212$ keV are seen on the spectrum. The γ -background in our laboratory is shown in green.

soon after that one of the annihilation 511 keV quantum may hit the detector as well. In this case, the detector detects a peak corresponding to the sum of the energies of 511 and 1.274 MeV. This peak is the pile-up peak.

Similar situation arises when Co-60 β^- -decay happens and Ni-60 nucleus in excited state is produced. Within 0.7 ps Ni-60 successively emitted two γ -quanta 1.17 and 1.33 MeV. Because the delay time between emission of these photons is very small in comparison with the detector time-resolution (which is about 1 μs), the detector records them as one photon at $1.17+1.33$ MeV.

Making positron sources from $^{22}\text{NaCl}$ aqueous solution

Everything is not as easy as it seems...

The research positron laboratories mainly use radioactive β^+ -decay sources. The ^{22}Na is the most common positron source used in the lifetime spectroscopy. The emission of e^+ is tagged by the emission of photon of 1.275 MeV, see Fig. 3.1.

Careful manufacturing of the e^+ radioactive source is very important for doing good PALS experiments. Usually positroners do it themselves. The first step is purchasing pure water solution of $^{22}\text{NaCl}$. In June 2017 F.Selim's lab bought 100 microCurie ($100 \mu\text{Ci} = 3.7 \text{ MBq}$) of ^{22}Na activity, Fig. 18.

EXPRESS DANGEROUS GOODS RADIOACTIVE MATERIALS (UN NO. 2811/1RST)							
Pg 1 of 1 Pgs		PRESS HARD - 5 PART FORM - USE BALL POINT PEN ONLY				Yellow III	
					<input type="checkbox"/> Check Box for Placarding		
UN #	Proper Shipping Name			Class (Subrskrs)	Pkg. Group	Quantity & Type of Packing	Pkg Instr
UN2915	RADIOACTIVE MATERIAL, TYPE A PACKAGE			7		1 Type A Package	
Radionuclide (Product Code)	Phys & Chemical Form	Activity	Label Category	TI	Box Dimension (If Applicable)	Tracking #	
Na-22	LIQUID/SALT	0.003719GBq	II-YELLOW	0.2	25Lx15Wx13H cm	648690079683	
Origin	Dest	Shipment Type (Delete Non-Applicable)		This Shipment is Within The Limitations Prescribed For (Delete Non-Applicable)		Remarks/Approvals/Authorizations	
ET FOXA TOLA	XXXXXX	Non-Radioactive	Radioactive	Passenger Aircraft	XXXXXXXXXX	57711922	
I hereby declare that the contents of this consignment are fully and accurately described above by the proper shipping name, and are classified, packaged, marked and labelled/placarded, and are in all respects in proper condition for transport according to applicable international and national governmental regulations. I declare that all of the applicable air transport requirements have been met. For radioactive material shipment acceptable for passenger aircraft the shipment contains radioactive material intended for use in or incident to research, medical diagnosis, or treatment.					24 hr. Emergency Telephone # 703-527-3887		
Shipper's Name and Address		Place/Date		Recipient's Name and Address			
PerkinElmer Inc. Shipping Manager 331 Treble Cove Road Building 250-1 North Billerica, MA 01862 Signature Brian McDonough		06/14/2017		BOWLING GREEN STATE UNIVERSITY 1851 N RESEARCH DR ENVIRONMENTAL & HEALTH SAFETY BOWLING GREEN, OH 43403 24/06/2017			
Title							
Typewritten Signature Acceptable							

Fig. 18 Shipping invoice for aqueous solution of radioactive $^{22}\text{NaCl}$ salt.

Typical dose rate is shown in Fig. 19. At 90°-degree geometry of the detector arrangement (which is the most adequate from the experimental viewpoint – annihilation photon cannot hit the scintillator of the start-detector), the counting rate from the vial with total activity



Fig. 19 Dose rate at 10 cm distance far from the vial with $^{22}\text{NaCl}$.

is rather low (it means that there was bought small amount of ^{22}Na activity), Fig. 19 and 20.



Fig. 20 Typical count rate from the original vial with radioactive salt $^{22}\text{NaCl}$.

Next, we need to make an envelope for the positron source. Many positroners make it from a thin kapton film (7-8 μm thick). Kapton is the most convenient substance for producing of the e^+ sources because 1) it is highly radioresistant polymer, 2) positronium atoms are not formed in kapton. So there is no long-lived component in the LT spectra related with the contribution from the e^+ annihilation in the e^+ source material. The source correction usually can be described by a single exponent with a typical lifetime 0.38 ns. To attribute some rigidity to the source, we make a “frame” for it from a double-side kapton tape, (its both sides are covered by a 30 μm layer of a silicon glue, to which we attach two thin kapton films of the envelope, Fig. 21.

The next step is preparation of the aqueous solution. Since the initial vial with the

radioactive salt is usually supplied in dry form, one needs to add small amount of pure water (about 100-300 μl) to dissolve $^{22}\text{NaCl}$ radioactive salt, Fig. 22.

Then we put the vial on a shaker for 5-10 minutes (to wash salt from walls of the vial) and then we drip a small drop of the radioactive solution onto a kapton film/substrate with a help of 10 μl syringe (typical volume of the drop is about 5 μl). After that we evaporate extra water slightly heating kapton film for about 10 min, Fig. 23. We proceed with dropping-drying cycles many times in order to deposit as much activity as possible to the kapton film and to make the e^+ source of a sufficient activity (about 3 MBq for the LT measurements). For the Doppler measurements, it is enough to have 10 times less active e^+ source.

When the necessary amount of $^{22}\text{NaCl}$ salt has been transferred to the Kapton film, we peel off the top film covering the adhesive layer of the double-sided Kapton tape and cover the active spot with another 8 μm Kapton film. As a result we obtain fairly well-sealed e^+ source, suitable for PALS measurements, Fig. 24.

In 2017 we also did one more e^+ source (having small activity) for the Doppler measurements.

Then we measured LT spectra of the reference (i.e. well-annealed and defect-free) samples of Al (165 ps – e^+ lifetime therein), Si (220 ps) and Fe (110 ps), so we succeeded to obtain the source corrections for both e^+ sources, which are the fractions of positron, annihilating within the sources themselves. It turned out that the source corrections (for Fe samples) is about 12% and can be described well with a help of two exponentials: $I_1 = 98\%$ $\tau_1 = 0.39$ ns (this component well correlates with the e^+ lifetime in kapton) and $I_2 = 2\%$ $\tau_2 = 1.6$ ns which probably corresponds to e^+ annihilation within the silicon glue. The source correction for Al and Si is $\approx 10\%$.



Fig. 21 Punching the kapton tape and attaching $8 \mu\text{m}$ kapton film to the double-side kapton tape.

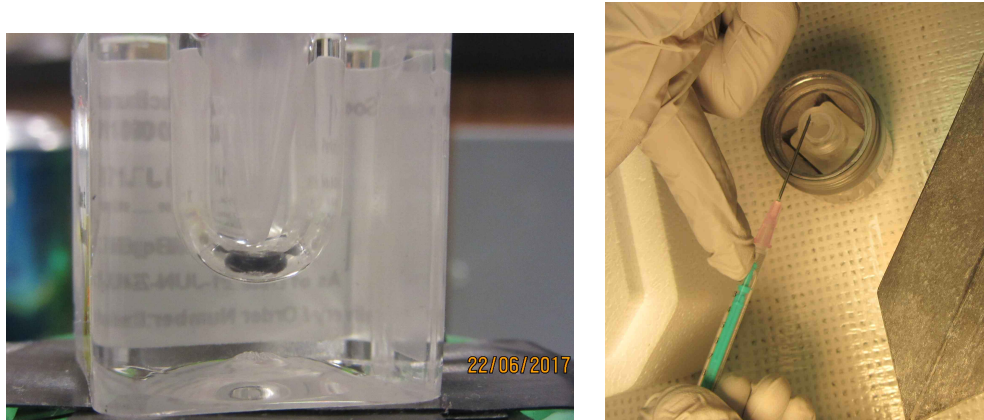


Fig. 22 Dropping water into a vial with ^{22}Na activity.



Fig. 23 Dropping $^{22}\text{NaCl}$ aqueous solution on the Kapton film.

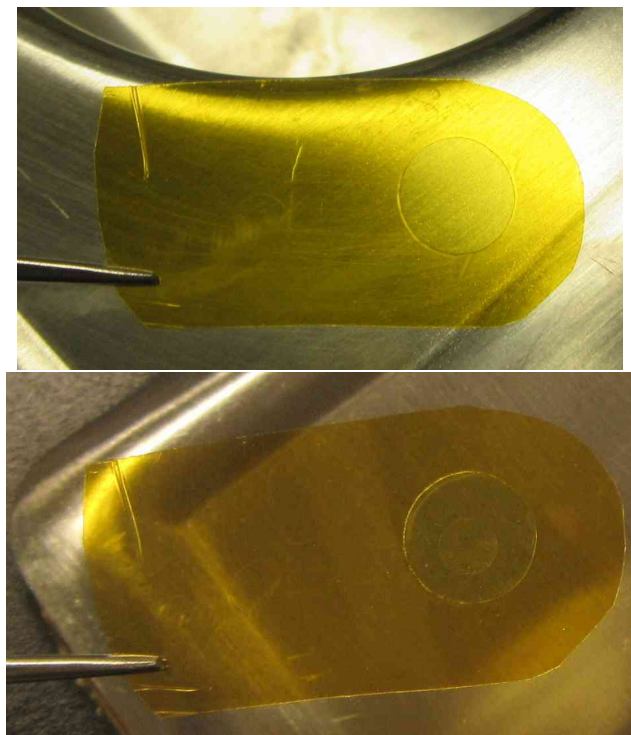


Fig. 24 Ready-to-use ^{22}Na positron source.

Adjustment and tuning of the Positron Annihilation Lifetime Setup

.1 Choice of the appropriate high voltage (HV) for Hamamatsu H3177 photomultipliers (PMTs)

Recommended HV for Hamamatsu H3177 PMT (it should be H3378-51????) is 2.5 kV (maximum HV = 3 kV). At HV=2.5 kV the amplitude of anode signals are high enough 2-3 V (Fig. 25), so no need to increase HV (when HV is high, close to 3 kV, the PMTs degrade faster).

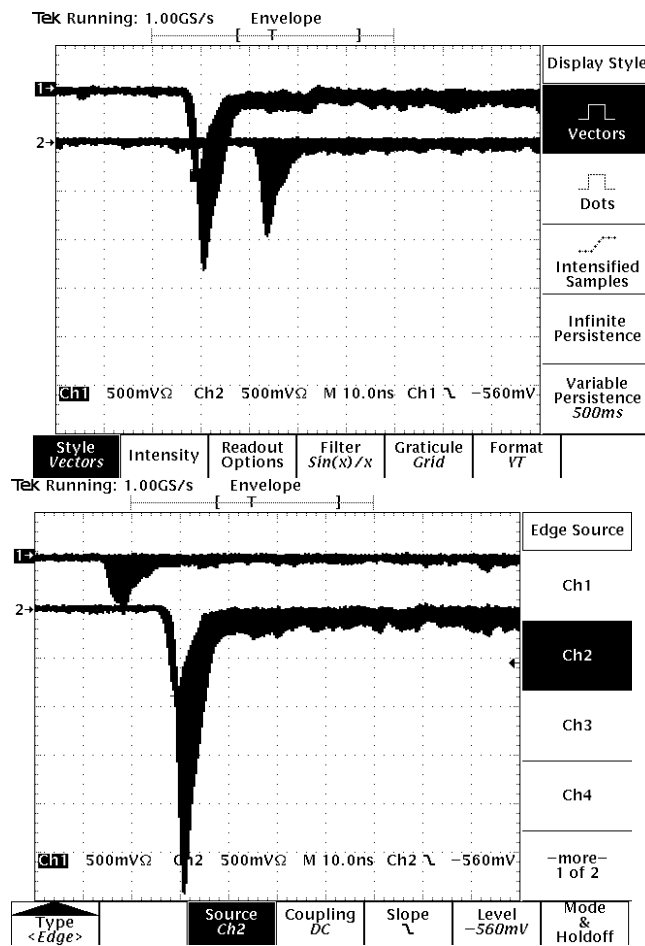


Fig. 25 Left: Anode signals from the Detector 1 (s/n BA 1773; see signals on the channel No.1, upper curves). This detector is supposed to be the START detector, because its signals are somewhat lower than that for the Detector 2. Right: Anode signals from the Detector 2 (s/n BA 1739; see signals on the channel No.2, lower curves). This detector is supposed to be the STOP detector, because its signals are higher than that from the Detector 1.

It is seen that the output voltage (of the anode signals) from the second detector is larger, so it is reasonable to assign it as a STOP detector (to have higher amplitudes on 511-photons and higher energy thresholds on the CFDD).

Note that the usage of the second anode output affects the signal of the first anode output! The best results are obtained when the second anode output does not used (no cables and no 50 Ohm terminators are inserted in the 2d anode output jack). In Fig. 26

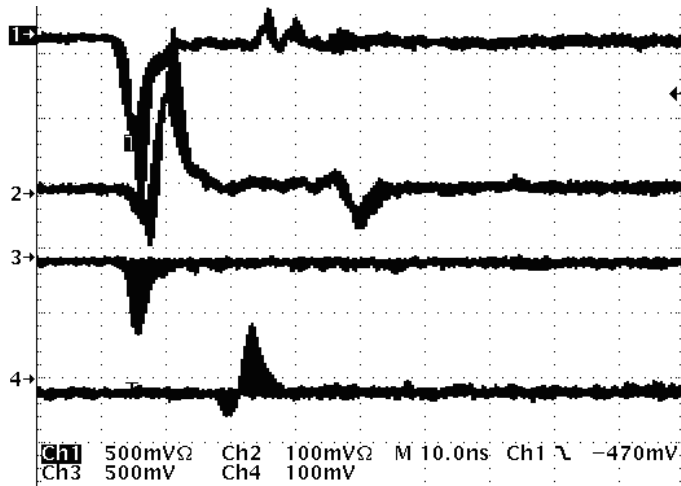


Fig. 26 Anode and dynode signals from both detectors (D1 — channels 1, 2; D2 — channels 3 and 4).

.2 Measurements of the amplitude spectra

To measure the amplitude spectra, the following procedure was applied for both detectors one by one.

The first anode output signal (A_1) of the detector 1 is connected to CFDD1 (for D2 – to CFDD2). Second anode output we leave EMPTY(!). The dynode signal (D_y) is plugged to the amplifier Ortec 471 (gain=100; input positive). The unipolar output from the amplifier we connect to the MCA input jack.

The dynode signal must be amplified before connecting to the Multi-Channel Analyzer (MCA), because MCA does not accept short (in time) and small (in amplitude) signals. The MCA input signal must be $+1\ldots 10$ V, and has a duration about $1 \mu s$.

To measure the amplitude spectra we must significantly decrease the detector loading, otherwise the amplified dynode signals will be overlapped (it this case measuring of the

amplitude spectra is not possible). So we put the source/sample sandwich 10-15 cm aside from the detector scintillators. Firstly we measure full amplitude spectra (when MCA is switched NOT in a coincidence mode; Coincidence = OFF). These spectra are shown for both detectors in Fig. 26 in black and in blue. All the spectra were accumulated during 600 s.

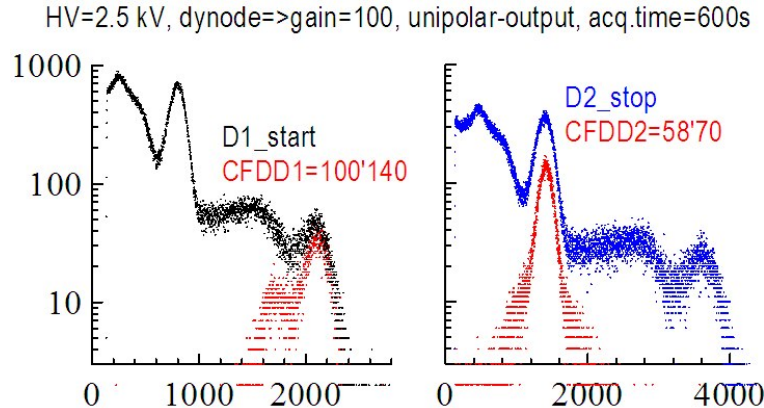


Fig. 27 Amplitude spectra from the START and STOP detectors. All spectra were measured with the CFDD external delay cable =25 cm.

Then we switch the MCA in the coincidence mode (the INPUT signal must coincide with the GATE signal) and we measure the amplitude spectra again. To proceed with this we must send the VALID START output signal from the rare panel of TAC to the GATE input of MCA. This signal indicate that the amplitude of the anode signal from the γ -detector falls inside the CFDD energy window. To generate this VALID START signal we send the fast timing output signal from CFDD1 (or CFDD2) to the START input of the TAC. IMPORTANT: TAC multiplier must be switched to x100 (instead of 1 as usually used for the LT measurements), see the PALS User manual. So we collect only those anode signals, which passed through the energy window of the discriminator. Adjusting the CFDD low and high energy thresholds (LL and HL parameters), we select just needed photons in the START and STOP channels. The obtained spectra are shown in red in Fig. 27.

.3 Calibration of the Time-to-Amplitude Converter (TAC)

To measure time duration of the MCA channel, we proceed with the following:

- 1) Put the source-sample sandwich near any γ -detector;

2) Take two fast timing outputs from any CFDD. One of its fast-timing output signal plug directly to the TAC START. The second fast-timing output plug to the variable Time Delay unit, which can delay the incoming signal by 8, 12, ..., 40 ns. Then output delayed signal plug into the TAC STOP.

3) Main TAC output connect to the MCA and start to collect spectrum during, say, 10 s. Then increase Time Delay by 4 ns step by step. So we obtain the spectra shown in Fig. 28, left. Knowing number of channels between the peaks, we calculate duration of 1 channel. It is 6.17 ps (Fig. 28, right):

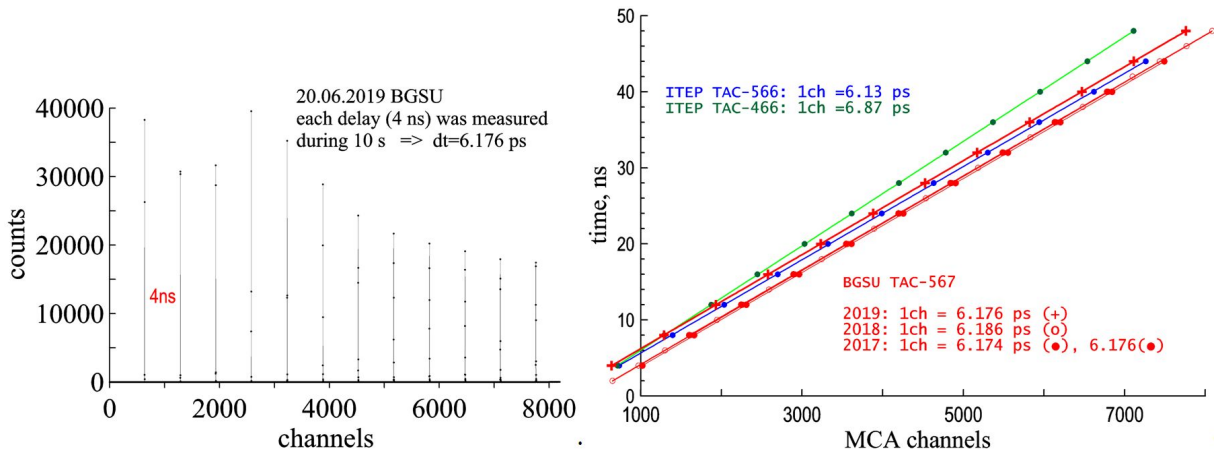


Fig. 28 Time calibration of TAC (June 19, 2019). Duration of 1 MCA channel is 6.176 ps.

We did time calibration of our TAC once per year, and it turned out very stable.

.4 Determination of the source correction and parameters of the resolution function

To obtain the fraction of the positrons annihilating within the e^+ source itself, we must measure the LT spectra from the “reference samples” (with the known e^+ lifetime). We used annealed Fe (900 C, 1 hour), $\tau_{e+} = 110$ ps; single crystal Si, $\tau_{e+} = 218$ ps and annealed Al ($\tau_{e+} = 165$ ps). Example of the LT spectra of Fe is shown below, Fig. 29.

Fitting the spectra from Fe reference sample one obtains that the source correction is 13% (94% 0.4 ns; 6% 2.8 ns). The resolution function is described with a help of two Gaussians: FWHM = 0.367 ns, 0.5% 0.8-1 ns

For the single crystal Si (218 ps): the source correction is 10% (= 0.4 ns (fixed) + 7%

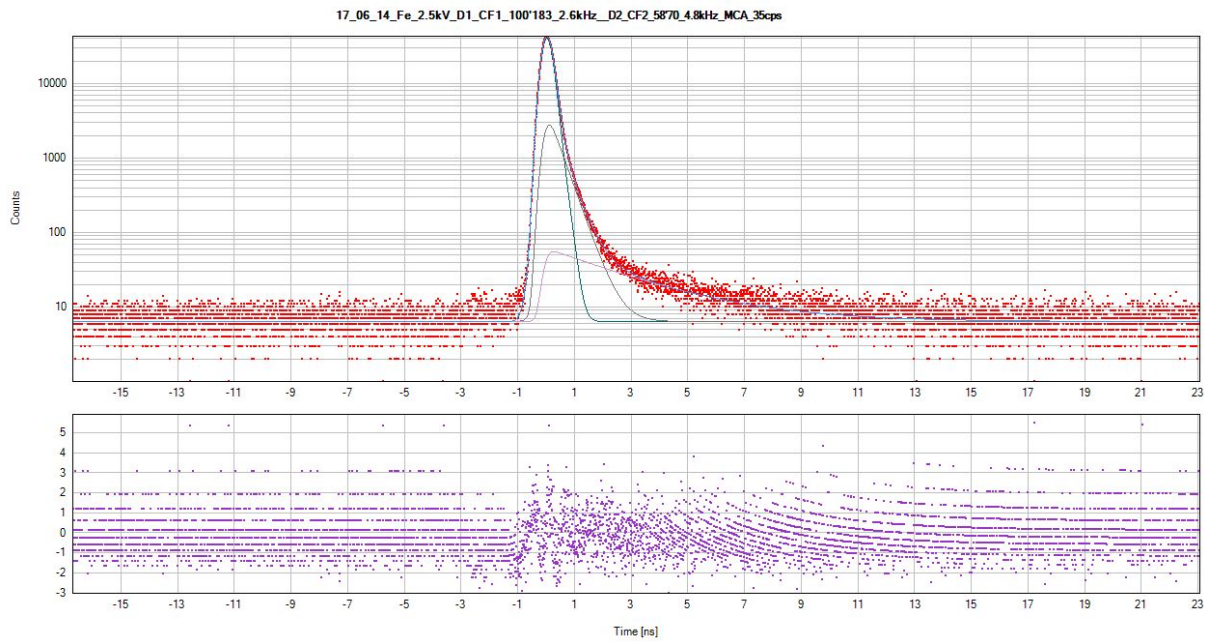


Fig. 29 LT spectrum of well-annealed iron (reference sample).

2.5-2.8 ns) The resolution function: FWHM = 0.36-0.37 ns (+ 0.2-0.6% 0.8-1 ns)

Unfortunately at the end of 2018 the e^+ source for LT measurements (LT source) was damaged. Then it was covered by an additional Kapton envelope. In June 2019 its activity was about 50-60 microCuri and activity of the Doppler source is about 10 microCuri:

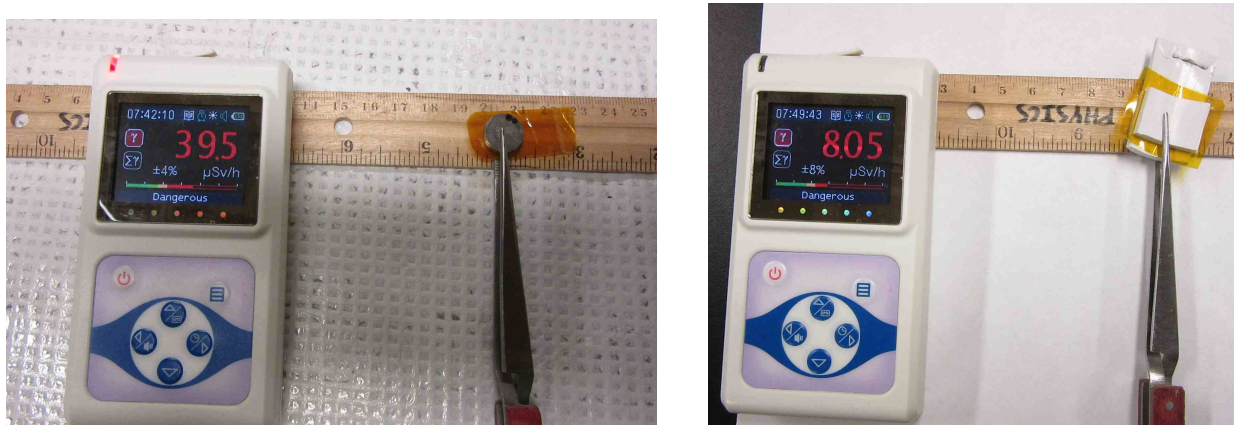


Fig. 30 Measuring of the dose rate from the e^+ sources for LT (left) and CDB (right) experiments.

The source corrections was re-measured (for all available e^+ sources) with a help of three different reference samples.

The e^+ -source for LT measurements:

Al (165 ps): 22% [0.38 ns (fixed) +4.8% 2.9 ns] $3.9 * 10^6$ counts;

FWHM1=0.37ns +0.3% FWHM2=1.3 ns

Si (220 ps): 23% [0.38 ns (fixed) +4.8% 3.2 ns] $4.1 * 10^6$ counts;

FWHM1=0.37ns +0.5% FWHM2=1 ns

W (110 ps): 30% [0.38 ns (fixed) +5.2% 3.0 ns] $8.8 * 10^6$ counts;

FWHM1=0.37ns +0.5% FWHM2=1 ns.

The e^+ -source for CDB measurements:

Si (220 ps): 14% [0.38 ns (fixed) +2% 1.7 ns].

.5 Final tuning of the LT setup

The last attempt to optimize geometry (arrangement of the detectors and source-samples sandwich) was done in July, 2019. It was confirmed that the 120° -degree geometry is the optimal compromise between the count rate and quality of the LT spectra. In this geometry, the second annihilation photon cannot hit the scintillator of the start-detector. We have made high-quality silver-plated cables connecting detectors and discriminators. Then we also adjusted as the lengths of the external delay cables on discriminators. At the same time, we tuned the upper and lower thresholds on both discriminators.

In Fig. 31 it is shown the optimal geometry, which is used now, and the LT spectrum of the defect-free Al. The coincidence count rate at this geometry is 35 cps. Shape of the spectrum (accumulated during 24h) is also shown in Fig. 31. Other experimental parameters are given on top of the spectrum.

Source contribution (for Al) is 22% (95% 0.38 ns + 5% 3.5 ns)

Resolution function: FWHM1 = 0.39 ns, + 0.5% FWHM2 = 1.1 ns

For 90-degree geometry the coincidence count rate drops down to 15 cps, which is unacceptably small.

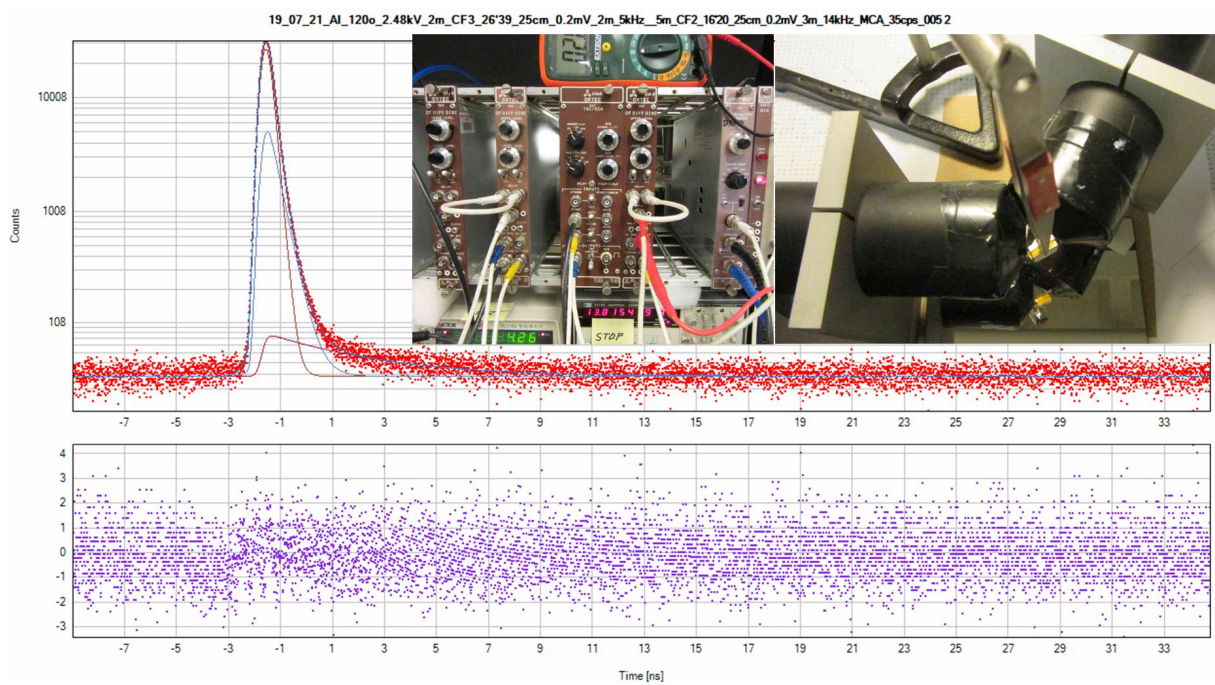


Fig. 31 The LT spectrum of the defect-free Al.

Calculation of the positron flux towards the grain boundary

It is usually believed that the grain boundary is a sink for the quasi-free positrons e_b^+ (“bulk” positrons). Similar situation may also occur when quasi-free Ps diffuses within the crystallites towards their boundary in powders.

Having reached the boundary e_b^+ transforms into e_g^+ (“grain” positrons). Here we also take into account e_b^+ trapping by defects (vacancies): $e_b^+ \rightarrow e_v^+$. We assume that the defects are uniformly distributed in the bulk. Of course, e_b^+ may also annihilate with the rate λ_b . Let us adopt that a grain (of a polycrystalline sample or a powder) has a spherical shape with the radius R , $V_R = 4\pi R^3/3$ is the volume of the grain.

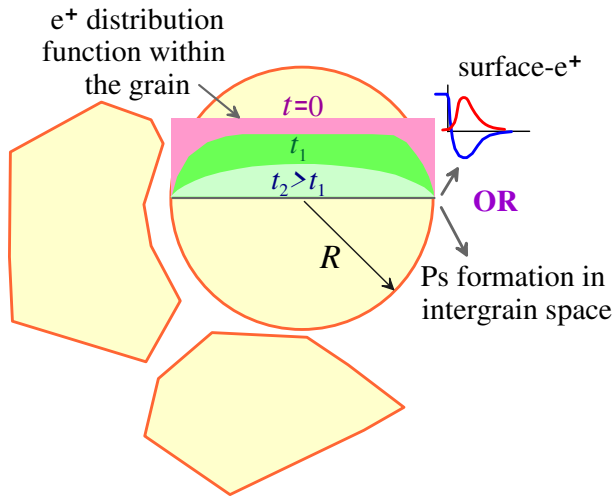


Fig. 32 Diffusion of a positron towards a grain boundary.

Now let us calculate the diffusion flux of the positrons on the spherical boundary, assuming that at $t = 0$ they were uniformly distributed over the grain volume. Behavior of the positrons is described by the following diffusion equation:

$$\frac{\partial c(r, t)}{\partial t} = D_+ \Delta_r c - \lambda c, \quad c(R, t) = 0, \quad c(r, 0) = \frac{\vartheta(r < R)}{V_R}, \quad V_R = \frac{4\pi R^3}{3}. \quad (5)$$

Here $c(r, t)$ is the local concentration (spatial distribution function) of e_b^+ , $n_b(t) = \int c(r, t) d^3 r$, $\lambda = \lambda_b + \kappa_v$ is their rate of disappearance due to annihilation and trapping by vacancies and

Δ_r is the radial part of the Laplace operator.

Denoting $\tilde{c}(r, t) = rc(r, t)$, we can separate space and time variables. Let's substitute $\tilde{c}(r, t) = T(t)R(r)$ to the previous equation. If we denote the separation constant as $-k^2$ ($R''/R = -k^2$), one obtains:

$$T' = -D_+ k^2 T - \lambda T \quad \text{and} \quad R'' = -k^2 R. \quad (6)$$

Solving these equations, we find the following infinite set of basis solutions:

$$\tilde{c}_m(r, t) \propto e^{-\lambda t - D_+ k_m^2 t} \cdot \sin(k_m r), \quad \text{where} \quad k_m = \pi m / L, \quad m = 1, 2, \dots \quad (7)$$

Here the discrete values of k_m appeared because of the boundary condition $R(r = L) = \sin k_m L = 0$.

Expression for $\tilde{c}(r, t)$ can be written as a linear combination of basis solutions:

$$\tilde{c}(r, t) = \sum_m A_m \tilde{c}_m(r, t), \quad (8)$$

where the coefficients A_m are determined from expansion of the initial condition into a series of sines:

$$\tilde{c}(r, t = 0) = \frac{r}{V_L} = \sum_m A_m \sin(k_m r). \quad (9)$$

In fact, multiplying both sides of this equation by $\sin(k_n r)$ and integrating over r and utilizing the orthogonality of the sines: $\int_0^L \sin(k_m r) \sin(k_n r) dr = \delta_{mn} L / 2$, we obtain

$$\int_0^L \frac{r dr}{V_L} \sin(k_m r) = A_m \frac{L}{2} \quad \rightarrow \quad A_m = \frac{2 \cdot (-1)^{m+1}}{k_m V_L} = \frac{3 \cdot (-1)^{m+1}}{2m\pi^2 L^2}. \quad (10)$$

Thus, solution of Eq. (5) is as follows:

$$c(r, t) = \sum_{n=1}^{\infty} A_n \frac{\sin(k_n r)}{r} \cdot e^{-\lambda t - D_+ k_n^2 t}, \quad A_n = \frac{(-1)^{n+1} \cdot 3}{2\pi^2 L^2 n}. \quad (11)$$

Note, that this expression fulfills normalization of the initial condition, namely:

$$1 = \int_{V_L} c(r, t=0) d^3r = \sum_{m=1}^{\infty} A_m \int_0^L \frac{\sin k_m r}{r} \cdot 4\pi r^2 dr = \sum_{m=1}^{\infty} \frac{8\pi L}{k_m^2 V_L} = \sum_{m=1}^{\infty} \frac{6}{\pi^2 m^2} = 1. \quad (12)$$

Integrating (11) over all volume of the grain at any time, we obtain a decrease in the number of quasifree positrons within the grain:

$$n_b(t) = \int_{V_L} c(r, t) d^3r = e^{-\lambda t} \sum_{m=1}^{\infty} \frac{6}{\pi^2 m^2} \cdot e^{-D_+ k_m^2 t} = \frac{6e^{-\lambda t}}{\pi^2} \sum_{m=1}^{\infty} \frac{e^{-\lambda_J m^2 t}}{m^2}, \quad \text{where } \lambda_J = \frac{\pi^2 D_+}{R^2}. \quad (13)$$

Here we introduced λ_J which we will call below as the “diffusion rate”. This final expression describes the decay kinetics of e_b^+ .

To obtain expression for the e_b^+ diffusion flux to the grain boundary (and differential equation for n_b), let us differentiate (13) over t :

$$\dot{n}_b = \frac{d}{dt} \left[\int_{V_L} c(r, t) \cdot d^3r \right] = \int_{V_L} \frac{\partial c(r, t)}{\partial t} d^3r. \quad (14)$$

Substituting here the diffusion equation (5) written in the form

$$\frac{\partial c(r, t)}{\partial t} = -\operatorname{div} \mathbf{j} - \lambda c, \quad \text{where } \mathbf{j} = -D_+ \nabla c,$$

and then using the Gauss theorem,

$$\int_{V_L} \operatorname{div} \mathbf{j} d^3r = \int_{S_L} \mathbf{j} \cdot d\mathbf{S} = J(t),$$

we get

$$\dot{n}_b(t) = -\lambda n_b(t) - J(t), \quad \text{where } J(t) = 4\pi L^2 D_+ |\nabla c(r, t)|_{r=L}. \quad (15)$$

To find an explicit expression for the diffusion flux $J(t)$, let us calculate a gradient from

$c(r, t)$ in (11). Because of

$$\left(\frac{\sin k_m r}{r} \right)' \Big|_{r=L} = \frac{(-1)^m k_m}{L} = \frac{(-1)^m \pi m}{L^2},$$

the diffusion flux takes the form (compare with Eqs. (4.18) and (4.29)):

$$J(t, \lambda, \lambda_J) = \frac{6D_+ e^{-\lambda t}}{L^2} \sum_{m=1}^{\infty} e^{-D_+ \pi^2 m^2 t / L^2} = \frac{6\lambda_J e^{-\lambda t}}{\pi^2} \sum_{m=1}^{\infty} e^{-\lambda_J m^2 t}. \quad (16)$$

Substituting this relationship into (15), we can again solve Eq. (15) and obtain expression for $n_b(t)$:

$$n_b(t) = e^{-\lambda t} \left[1 - \int_0^t J(\tau) e^{\lambda \tau} d\tau \right], \quad (17)$$

which after taking into account

$$\int_0^t J(\tau) e^{\lambda_{ps} \tau} d\tau = \frac{6}{\pi^2} \sum_{m=1}^{\infty} \lambda_J \int_0^t e^{-\lambda_J m^2 \tau} d\tau = \frac{6}{\pi^2} \sum_{m=1}^{\infty} \frac{1 - e^{-m^2 \lambda_J t}}{m^2} = 1 - \frac{6}{\pi^2} \sum_{m=1}^{\infty} \frac{e^{-m^2 \lambda_J t}}{m^2}.$$

exactly reproduces the above Eq. (13) for $n_b(t)$.

Calculation of expressions $a \sum_{n=1}^{\infty} \exp(-an^2)$ and $\frac{6}{\pi^2} \sum_{n=1}^{\infty} \frac{\exp(-an^2)}{n^2}$

Let us consider the sum $a \sum_{n=1}^{\infty} \exp(-an^2)$, which appears in the expression for the diffusion flux of the positrons to the grain boundary, see Eqs. (4.18), (4.29) and (4.30). Exact value as a function of a is shown by circles in Fig. 33).

If $a \ll 1$ (exponentials are small), then the terms of the summed series are slightly different from each other. In this case, summation can be replaced by integration:

$$a \sum_{n=1}^{\infty} \exp(-an^2) \approx a \int_0^{\infty} \exp(-an^2) dn = \sqrt{\frac{\pi a}{2}}. \quad (18)$$

This asymptotic behavior at small a is shown in green in Fig. 33).

When $a \gg 1$ in the sum we may keep the first two terms only (blue curve):

$$a \sum_{n=1}^{\infty} e^{-an^2} \approx a(e^{-a} + e^{-4a}). \quad (19)$$

Reasonable matching of these two asymptotes can be easily done as follows:

$$a \sum_{n=1}^{\infty} e^{-an^2} \approx \sqrt{\frac{\pi a}{2}} \cdot e^{-\sqrt{33a}} + a(e^{-a} + e^{-4a}). \quad (20)$$

It is shown in pink in Fig. 33, on the left.

Now let us consider the second sum, $S(a) = \frac{6}{\pi^2} \sum_{n=1}^{\infty} \frac{\exp(-an^2)}{n^2}$. When $a \ll 1$, we can again replace the sum $\sum_{n=1}^{\infty}$ with the integral $\int_b^{\infty} ... dn$, considering b as an adjustable parameter:

$$S(a) \approx \frac{6}{\pi^2} \int_b^{\infty} \frac{\exp(-an^2)}{n^2} dn, \quad S(0) = 1. \quad (21)$$

At small a the dependence $S(a)$ is non-analytical. To obtain it, let us calculate the derivative

$$S'(a) = -\frac{6}{\pi^2} \int_b^{\infty} e^{-an^2} dn = -\frac{6}{\pi^2 \sqrt{a}} \int_{b\sqrt{a}}^{\infty} e^{-x^2} dx \approx -\frac{6}{\pi^2 \sqrt{a}} \int_0^{\infty} e^{-x^2} dx = -\frac{3}{\pi \sqrt{\pi a}}.$$

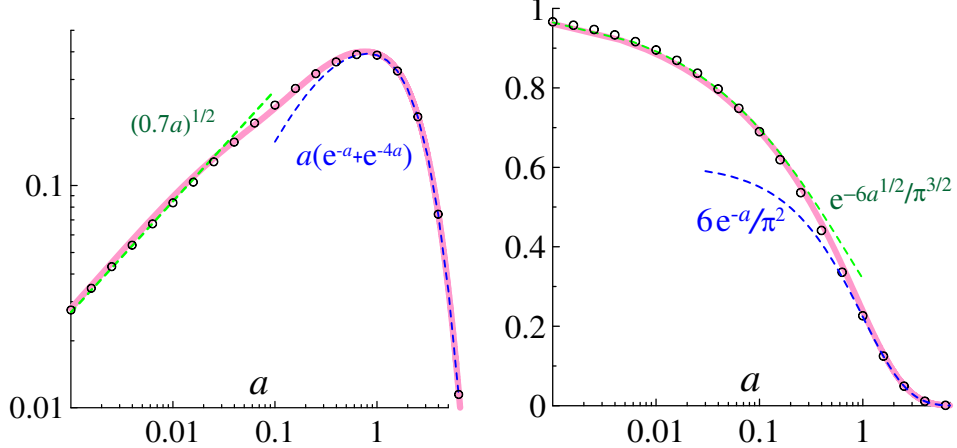


Fig. 33 Approximations of the sums $a \sum_{n=1}^{\infty} \exp(-an^2)$ and $\frac{6}{\pi^2} \sum_{n=1}^{\infty} \frac{\exp(-an^2)}{n^2}$ at different a .

It is seen that it diverges at small a . Nevertheless, integration of this expression over a , gives:

$$S(a \ll 1) = S(a = 0) - \frac{6\sqrt{a}}{\pi^{3/2}} = 1 - \frac{6\sqrt{a}}{\pi^{3/2}} \approx \exp\left(-\frac{6\sqrt{a}}{\pi^{3/2}}\right). \quad (22)$$

This dependence is shown in green in Fig. 33, the right plot.

When $a \gg 1$ we can hold only the first term in the series expansion of $S(a)$ (Fig. 33, the right plot, blue curve):

$$\frac{6}{\pi^2} \sum_{n=1}^{\infty} \frac{\exp(-an^2)}{n^2} \approx \frac{6e^{-a}}{\pi^2} = 0.61e^{-a}. \quad (23)$$

Now, we should match the asymptotic dependencies (22) and (23). Rather accurate approximation may be written as follows:

$$\frac{6}{\pi^2} \sum_{n=1}^{\infty} \frac{\exp(-an^2)}{n^2} \approx 0.39e^{-3.27\sqrt{a}} + 0.61e^{-a}. \quad (24)$$

It is shown in Fig. 33, right plot, the pink curve.

Thermalization kinetics of the positronium atom due to its collisions with crystallites and molecules of air in the intergrain space

We assume that the quasi-free positronium escapes a crystallite with some kinetic energy E_0 , which is determined by its work function (about 1-3 eV). Later on, the fate of p-Ps and o-Ps becomes different. The annihilation rate is determined by the spin state of the Ps: the para-state rapidly annihilates into two photons with the rate $\lambda_{2\gamma}$ (it is so-called intrinsic annihilation), but the ortho-state mainly undergoes conversion to p-Ps in collisions with O₂ molecules in the gas phase or with O₂ molecules adsorbed on the surface of crystallites. Apparently, when these collisions are frequent (nanopowders are stored in air), the rates of o-Ps intrinsic 3 γ -annihilation and o-Ps pick-off annihilation are small in comparison with its ortho-para-conversion rate.

We assume that $\lambda_{opc}(t)$ is proportional to the Ps collision frequency with crystallites

$$\lambda_{opc}(t) = \frac{\mu v(t)}{\ell},$$

where μ is the proportionality coefficient and ℓ is the o-Ps mean free path, which is comparable with the characteristic size L of the crystallites.

In each collision Ps loses the following amount of energy $\Delta E = \frac{4m}{M}(E - E_{th})$, where $E = mv^2/2$ is the Ps kinetic energy, $E_{th} = mv_{th}^2/2 = 3kT/2$ is the energy of the thermalized Ps, m is the mass of Ps, and M is the mass of an atom or a molecule which receive the recoil energy as a result of collisions. Let $\Delta t \approx \ell/v(t)$ is the time between two subsequent collisions, then:

$$\frac{dE}{dt} = -\frac{\Delta E}{\Delta t} = -\frac{4mv}{M\ell}(E - E_{th}), \quad \frac{dE}{dt} = mv \frac{dv}{dt}, \quad (25)$$

or

$$\frac{dv}{dt} = -\frac{2m}{M\ell}(v^2 - v_{th}^2), \quad v(0) = v_0. \quad (26)$$

At room temperature, the thermal velocity of Ps is $v_{th} = 8 \cdot 10^6$ cm/s. In this equation the variables (v and t) are straightforwardly separated, so the equation can be easily integrated:

$$v(t) = v_{th} \cdot \frac{1 + \nu e^{-\alpha t}}{1 - \nu e^{-\alpha t}}, \quad \nu = \frac{v_0 - v_{th}}{v_0 + v_{th}}, \quad \alpha = \frac{2mv_{th}}{M\ell}. \quad (27)$$

Positron annihilation in Al_2O_3 nanopowders of a different dispersion

There are several projects carried out by F.A. Selim research group aimed on manufacturing and investigations of transparent ceramics and nanophosphors (YAG garnets, ceramics doped with rear-earth ions, ZnO), which have wide applications in optical devices and electronics. Usually ceramics are grown by means of sintering of nanopowders of different oxides (Y_2O_3 , Al_2O_3 , SiO_2) with some additives [65]. Structural vacancy-type defects, defects raised after implantation of dopants as well as sorption of molecular oxygen from air strongly affect on transparency, light scattering and mechanical properties of the produced samples. Therefore, monitoring defects and impurities on each stage of the sample manufacturing is an important problem. In order to investigate it we made a series of LT and CDB measurements of Al_2O_3 nanopowders of a different grain size (50, 300 nm and 1 and 3 μm).

To fit the spectra we utilize a simplified version of the model (see Chapter 4.4) where we assume that positrons reach crystallite boundary ($\lambda_J \rightarrow \infty$, $\lambda_{Ps} \rightarrow 0$). In this case Ps atom can only be formed in between the grains and $n_{Ps}(t)$ disappears from the initial set of equations:

$$n_b(t) = (1 - P_{Ps})e^{-(\lambda_b + \kappa_v + \kappa_s)t}, \quad (28)$$

$$n_v(t) = (1 - P_{Ps}) \frac{\kappa_v [e^{-\lambda_v t} - e^{-(\lambda_b + \kappa_v + \kappa_s)t}]}{\lambda_b + \kappa_v + \kappa_s - \lambda_v}, \quad (29)$$

$$n_s(t) = (1 - P_{Ps}) \frac{\kappa_s [e^{-\lambda_s t} - e^{-(\lambda_b + \kappa_v + \kappa_s)t}]}{\lambda_b + \kappa_v + \kappa_s - \lambda_s}, \quad (30)$$

$$n_o(t) = \frac{3P_{Ps}}{4} \cdot \exp \left(- \int_0^t \frac{\lambda_{opc}(\tau)}{4} d\tau \right), \quad (31)$$

$$\dot{n}_p(t) = \frac{\lambda_{opc}(t)}{4} n_o - \lambda_{2\gamma} n_p, \quad n_p(0) = \frac{P_{Ps}}{4}. \quad (32)$$

Here $n_b(t)$, $n_v(t)$ and $n_s(t)$ are probabilities of observing a positron at a time moment t in following states, respectively: 1) quasi-free positron (qf-e $^+$) in the bulk of Al_2O_3 crystallite that annihilates with a rate λ_b ; 2) e $^+$ trapped in Al vacancy (vac-e $^+$) with annihilation rate

λ_v ; 3) e^+ localized in a bound state on the crystallite surface (surf- e^+), annihilates with a rate λ_s . Trapping rates of the qf- e^+ captured into the Al-vacancies and into surface bound states at the crystallite border are denoted as \varkappa_v and \varkappa_s .

First three Eqs. (28-30) describe behavior of a qf- e^+ that escaped Ps formation. These equations describe qf- e^+ annihilation in the bulk of crystallites, as well as their trapping by vacancies and transformation into surface-bound states.

Probability of Ps atom formation in between of the crystallites is denoted by P_{Ps} . Functions $n_o(t)$ and $n_p(t)$ stand for probabilities of observing o-Ps and p-Ps at a time moment t .

Usually an interaction of Ps with oxygen molecules (as well as some other molecules possessing oxidizing properties, like Cl_2 , Br_2 , I_2) is more important than with other neutral molecules, for example with nitrogen. In most cases interaction with O_2 leads to the Ps spin conversion and/or oxidation. Pick-off annihilation of Ps, which arises from so to say “elastic” collisions with gas molecules (N_2) or surface of crystallites, is usually less important, because time of these collisions is very short. One may say that interaction with oxygen molecules resembles a “sticky” collision (unstable complex formation), but not the elastic one. As a first step, below we restrict ourselves to the simplest case – accounting for the Ps interaction with O_2 , which leads to the Ps ortho-para conversion ($\lambda_{opc}(t)$ is the rate of this process, it depends on Ps velocity [60]). Later on we plan to take into account other possible contributions to annihilation of o-Ps (including its 3γ -annihilation, $\lambda_{3\gamma} = 0.007 \text{ ns}^{-1}$).

Expression for the ortho-para conversion rate of the Ps atom is given in [62]:

$$\lambda_{opc}(t) = \frac{\mu v_{th}}{\ell} \cdot \frac{1 + \nu e^{-\alpha t}}{1 - \nu e^{-\alpha t}}, \quad \nu = \frac{v_0 - v_{th}}{v_0 + v_{th}}, \quad \alpha = \frac{2mv_{th}}{M\ell}. \quad (33)$$

Here μ characterizes efficiency of ortho-para conversion at each collision, v_0 is the initial Ps velocity at the moment when qf-Ps escapes from the crystallite into intercrystallite space; $v_{th} \approx 8 \cdot 10^6 \text{ cm/s}$ is the velocity of Ps at room temperature. Mass of a Ps atom is expressed

by m whereas M is the mass of a crystallite volume that accepts the recoil energy colliding with Ps. Variable ℓ is the characteristic distance between the crystallites.

Substituting $\lambda_{opc}(t)$ into equation (31) for $n_o(t)$, we observe that kinetics of o-Ps annihilation has a non-exponential character:

$$n_o(t) = \frac{3P_{\text{Ps}}}{4} \exp \left(-\frac{\mu v_{th} t}{4\ell} - \frac{\mu M}{4m} \ln \frac{1 - \nu e^{-\alpha t}}{1 - \nu} \right). \quad (34)$$

Annihilation kinetics of the p-Ps can be obtained by solving equation (32). We take into account that the 2γ -annihilation rate of a p-Ps atom ($\lambda_{2\gamma} = 8 \text{ ns}^{-1}$) is significantly larger compared to all other annihilation rates:

$$n_p(t) \approx \frac{P_{\text{Ps}}}{4} e^{-\lambda_{2\gamma} t} + \int_0^t \frac{\lambda_{opc}(\tau) n_o(\tau)}{4} e^{-\lambda_{2\gamma}(t-\tau)} d\tau \approx \frac{P_{\text{Ps}}}{4} e^{-\lambda_{2\gamma} t} + \frac{\lambda_{opc}(t)}{4\lambda_{2\gamma}} n_o(t). \quad (35)$$

In order to estimate the value of this integral, we used the fact that the function $f(\tau > t) = 0$, $f(\tau < t) = \lambda_{2\gamma} e^{-\lambda_{2\gamma}(t-\tau)}$ at large $\lambda_{2\gamma}$ behaves like a δ -function. The first term in (35) describes annihilation of p-Ps, which was formed directly when e^+e^- pair entered the intercrystallite space; the second term is annihilation of p-Ps, formed via ortho-para conversion mechanism.

Now, we can calculate the shape of the LT spectrum:

$$C_{2\gamma}(t) \propto \lambda_b n_b + \lambda_v n_v + \lambda_s n_s + \lambda_{2\gamma} n_p = \lambda_b n_b + \lambda_v n_v + \lambda_s n_s + \frac{\lambda_{2\gamma} P_{\text{Ps}}}{4} e^{-\lambda_{2\gamma} t} + \frac{\lambda_{opc}(t)}{4} n_o(t). \quad (36)$$

The integral of the last term, which is needed to speed up the numerical calculations, can be easily taken:

$$\int_0^t \frac{\lambda_{opc}(\tau)}{4} n_o(\tau) d\tau = \frac{3P_{\text{Ps}}}{4} (1 - e^{-I(t)}), \quad I(t) = \int_0^t \lambda_{opc}(\tau) d\tau = \frac{\mu v_{th} t}{4\ell} + \frac{\mu M}{4m} \ln \frac{1 - \nu e^{-\alpha t}}{1 - \nu}.$$

The CDB and LT spectra were measured with a help of spectrometers described in

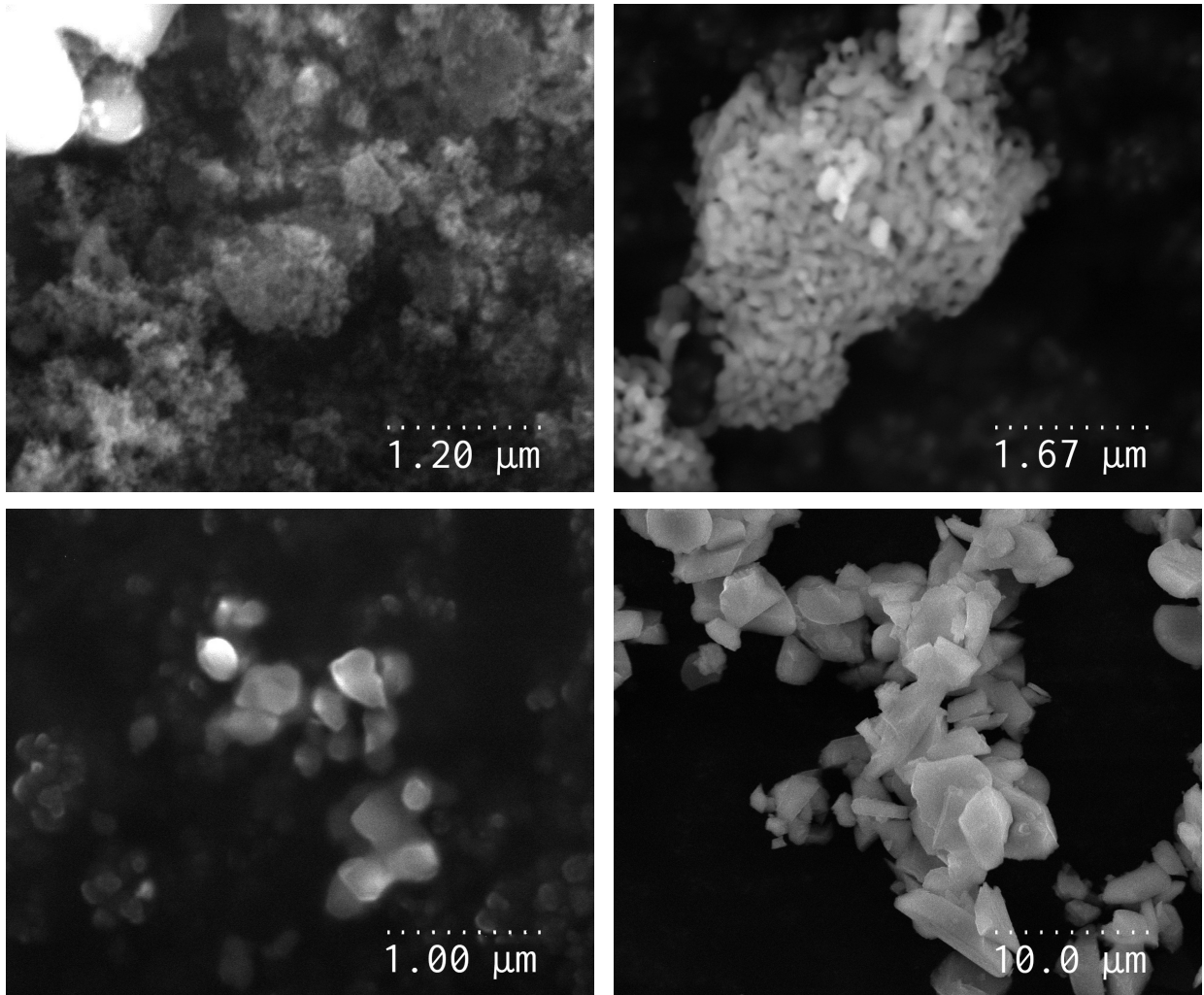


Fig. 34 SEM images of the investigated Al₂O₃ powders (left to right: 50 nm, 300 nm, 1 μm and 3 μm).

Appendices 6.8.6 and .5. Some Al₂O₃ sample spectra were acquired at a large time-scale (100 and 200 ns) of the Time-to-Amplitude Converter.

We start spectra analysis by fitting CDB spectra with a set of gaussian components corresponding to e⁺ annihilation with electrons of a different energies. The component of the CDB spectrum with the smallest FWHM of about 0.1 keV corresponds to the self-annihilation of the p-Ps atoms (see Fig. 35).

Since the qf-Ps state is excluded from the consideration in our model, the intensity of the narrow component is equal to the Ps formation probability: $Y_p = P_{\text{Ps}}$. Therefore the fitting of LT spectra was carried out with the value of P_{Ps} set to Y_p .

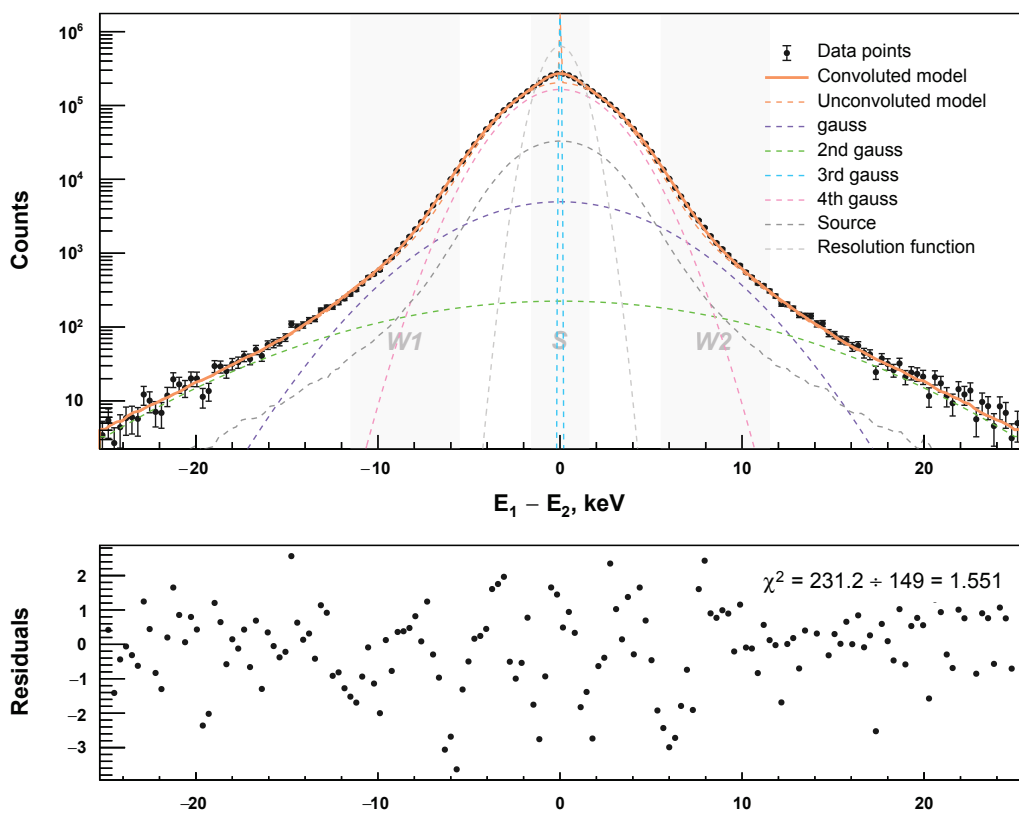


Fig. 35 CDB spectrum of a Al_2O_3 powder (50 nm powder size) deconvoluted into gaussian components. The most narrow component (3rd gauss) corresponds to annihilation of the p-Ps atoms.

The calculations of the characteristic distance ℓ between the crystallites for each studied sample are derived from the powder density measurements. We use trivial relationship $(1 + \ell/2R)^3 = \rho_{cryst}/\rho_{powder}$, where $2R$ is an average diameter of the crystallite, $\rho_{cryst} \simeq 4 \text{ g/cm}^3$ is the density of the crystalline Al_2O_3 and ρ_{powder} is its measured macroscopic density.

Diameter of the crystallites is calculated from the SEM images of the studied powders (see figure 34) with the help of the ImageJ software. Following diameter values are estimated: $60 \pm 40 \text{ nm}$ (50 nm powder), $170 \pm 110 \text{ nm}$ (300 nm powder), $0.28 \pm 0.23 \mu\text{m}$ (1 μm powder) and $3.5 \pm 2.7 \mu\text{m}$ (3 μm powder). The densities of the correspondent samples (ρ_{powder}) are measured as following: 0.45 g/cm^3 , 0.65 (300 nm), 0.85 (1 μm) and 2.0 (3 μm).

When processing the LT spectra it is important to estimate in advance the value of random coincidence background and fix it during the subsequent fit. This value is obtained from fitting the left part of the spectrum only (to the left from the annihilation peak).

The initial kinetic energy of positronium atom ejected from the bulk of crystallites was varied manually. We tried three reasonable values: 1, 2 and 3 eV. It seems that 2 eV (i.e. $v \approx 6 \cdot 10^7 \text{ cm/s}$, therefore $\nu \approx 0.76$ and $(1 + \nu)/(1 - \nu) \approx 7.3$) gives better agreement with experimental data.

The mass ratio m/M was also varied in a similar manner. The obtained value turned out to be $2 \cdot 10^{-6}$. This corresponds to an amount of 20 Al_2O_3 molecules that accept the recoil kinetic energy during collision of a Ps atom with a crystallite.

Results of the fit of the LT and CDB spectra of Al_2O_3 powders of different sizes are given in the Table 4. Spectra were fitted with the conventional 3-exponential model and with the model described above (labeled “Trapping + thermalization”). The results are the following:

- 1) Lifetime spectrum of a 3 μm γ - Al_2O_3 powder is almost mono-exponential. Here the crystallites are apparently defect-free single crystals, so the e^+ lifetime $\tau_b = 0.18 \text{ ns}$ can be naturally identified with the e^+ bulk lifetime in a defect-free Al_2O_3 crystal (our measurements show, this time is the same for α - and γ -phases).
- 2) Individual 3-exponential fits of the spectra of 50 nm and 100 nm powders measured

Table 4 Results of fitting of LT and CDB spectra of Al_2O_3 powders.

	TAC range	Total counts	Model	τ_1	I_1	τ_2	I_2	τ_3	I_3
$\gamma\text{-Al}_2\text{O}_3$ $\phi 50 \text{ nm}$	50 ns	3.6 M (35cps)	3-exp	0.23 ns	63%	0.5 ns	28%	24 ns	8%
	100 ns	1.2 M (7 cps)	3-exp	0.25 ns	73%	0.62 ns	16%	46 ns	11%
	200 ns	2.8 M (2 cps)	3-exp	0.26 ns	75%	0.67 ns	12%	59 ns	13%
Trapping model with thermalization $\tau_{\text{bulk}} = 0.18 \text{ ns}$ (fixed)				$\tau_v = 0.25 \text{ ns}$		$\tau_s = 0.47 \text{ ns}$		$P_{\text{Ps}} = \underline{\text{14.6\%}}$, $l = 60 \text{ nm}$	
CDB gaussians (FWHM, intensities)				$4 \pm 1 \text{ meV}, \underline{\text{14.6 \%}}$		15 eV, 80%	56 eV, 5%	217 eV, 0.4%	
$\alpha\text{-Al}_2\text{O}_3$ $\phi 300 \text{ nm}$	TAC range	Total counts	Model	τ_1	I_1	τ_2	I_2	τ_3	I_3
	50 ns	3.3 M	3-exp	0.21 ns	43 %	0.43 ns	54 %	23 ns	3 %
	100 ns	1.1 M	3-exp	0.28 ns	66 %	0.50 ns	29 %	40 ns	5 %
Trapping model with thermalization $\tau_{\text{bulk}} = 0.18 \text{ ns}$ (fixed)				$\tau_v = 0.26 \text{ ns}$		$\tau_s = 0.46 \text{ ns}$		$P_{\text{Ps}} = \underline{\text{4.3\%}}$, $l = 140 \text{ nm}$	
CDB gaussians (FWHM, intensities)				$4 \pm 6 \text{ meV}, \underline{\text{4.3\%}}$		15 eV, 90%	57 eV, 5%	236 eV, 0.4%	
$\alpha\text{-Al}_2\text{O}_3$ $\phi 1 \mu\text{m}$	TAC range	Total counts	Model	τ_1	I_1	τ_2	I_2	τ_3	I_3
	50 ns	3.4 M	3-exp	0.18 ns, 56 %		0.42 ns	42%	21 ns	1.8 %
	Trapping model with thermalization $\tau_{\text{bulk}} = 0.18 \text{ ns}$ (fixed)				$\tau_v = 0.22 \text{ ns}$		$\tau_s = 0.47 \text{ ns}$		$P_{\text{Ps}} = \underline{\text{1\%}}$, $l = 200 \text{ nm}$
CDB gaussians (FWHM, intensities)				$4 \pm 8 \text{ meV}, \underline{\text{1\%}}$		15 eV, 93%	69 eV, 5%	306 eV, 0.3%	
$\gamma\text{-Al}_2\text{O}_3$ $\phi 3 \mu\text{m}$	TAC range	Total counts	Model	τ_1	I_1	τ_2	I_2	τ_3	I_3
	50 ns	3.3 M	2-exp	0.18 ns	97 %	0.95 ns	3 %	—	
	Trapping model with thermalization $\tau_{\text{bulk}} = 0.18 \text{ ns}$ (fixed)				—		0.73 ns	$P_{\text{Ps}} = 0$, $l = 900 \text{ nm}$	
CDB gaussians (FWHM, intensities)				—		18 eV, 97%	97 eV, 3%	303 eV, 0.1%	

at different recording intervals (50, 100 and 200 ns), do not provide consistent values of the lifetimes τ_1 , τ_2 and τ_3 and intensities I_1 , I_2 and I_3 . Inconsistency is vary notable for the longer-living component τ_3 (highlighted in red in the Table 4). However, application of the two-state trapping model with Ps thermalization, issues consistent values for the fitting parameters τ_b , τ_v , τ_s , κ_v , κ_s , m/M and μ . Parameter P_{Ps} – Ps formation probability – was fixed to the intensity of the “narrow” component of the CDB spectrum (underlined in the Table 4).

3) Intensity of the “narrow” component of the CDB spectrum (Fig. 35) decreases with increase of the crystallite size. We explain this effect as follows. The qf-Ps is formed in a bulk of a crystallite as a result of combination of the thermalized e^+ with one of the track electrons knocked out by the energized e^+ . Then qf-Ps diffuses to the crystallite surface and escapes into the inter-crystallite space. In coarse powders qf-Ps has not enough time to reach the crystallite boundary and mostly annihilates in the bulk. For the sake of simplicity we

did not consider formation of the qf-Ps in the bulk and its diffusion to the crystallite surface (it will be done later on).

4) We believe that positron states with lifetimes of about 0.26 ns and 0.5 ns in $\gamma\text{-Al}_2\text{O}_3$ correspond to a positron trapped in Al-vacancy and in surf-e⁺ state bound on the crystallite surface.

5) For $\alpha\text{-Al}_2\text{O}_3$ powders the intensity of the positron surface state (with the lifetime about 0.5 ns) is notably shorter compared to the $\gamma\text{-Al}_2\text{O}_3$. It could be because of the deference of the e⁺ surface-bound states in these phases. This question needs further investigation.

6) It is likely that the parameter μ characterizes efficiency of Ps ortho-para conversion in collisions with oxygen. It may correlate with the sorption of O₂ on the surface of crystallites and with partial gas pressure of O₂. Our data seemingly indicate that the density of filling the surface with oxygen increases with the size of crystallites.

Experimental guide for the Coincidence Doppler Broadening Spectrometer

An experimental setup for the detection and registration of the energies of positron annihilation radiation was purchased from the Mirion Technologies (former Canberra) company. Spectrometer consists of two high purity germanium-based semiconductor detectors (HPGD) and two multichannel Lynx analyzers (MCA) that support acquisition in coincidence mode.

Acquisition or the coincidence CDB spectrum is a tedious process that consists of a number of milestones

- The Doppler spectrometer has to be assembled from parts.
- The local area network between computer and Lynx analyzers should be set up through a LAN switch
- Two programs – ProSpect and TLIST Data scanner – provided by the Mirion company need to be installed. ProSpect application
- The spectrometer needs to be calibrated with the reference radioactive samples; energy resolution of the detectors should be obtained.
- Export of the spectra to an external hard drive might be required.
- Certain positioning of the sample with respect to the detectors and their shielding is essential.
- The procedure of acquisition of the two-dimensional energy spectrum is not trivial; it requires setting up and launching ProSpect and Data Scanner applications simultaneously.
- In order to convert the two-dimensional energy spectrum into CDB spectrum a special TLIST Processor application was developed [15]. The application setup is not trivial;

it involves installing CERN ROOT libraries and compilation of the executable from source.

In this chapter we will describe the above steps in details to make it easy for the researchers to proceed with the Acquisition and analysis of the Doppler spectra.

.6 Coincidence Doppler spectrometer setup

A principle setup scheme of the Coincidence Doppler spectrometer is introduced on the Fig. 36. The facility operates as follows. The assembly consisting of the positron source enclosed in between a pair of samples is positioned between the detectors at equal distances. The typical source of positrons is ^{22}Na isotope. As a result of beta-decay, a positron with maximum of energy 0.543 MeV is emitted. The positron thermalizes in the bulk of investigated sample.

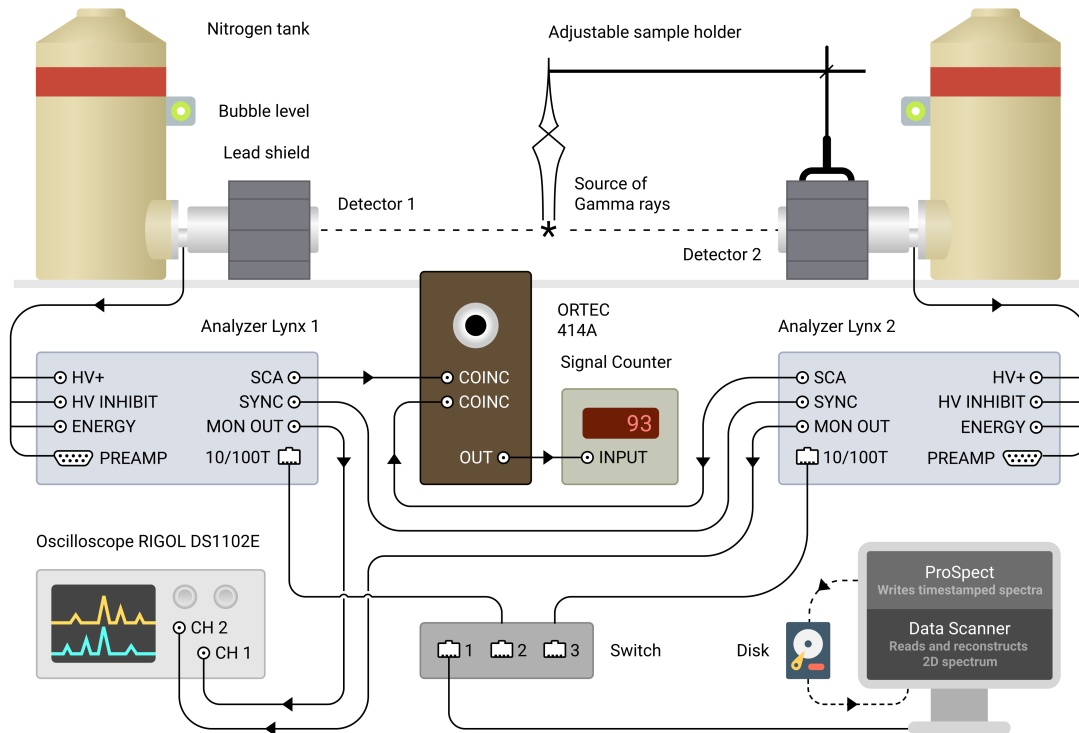


Fig. 36 Coincidence Doppler spectrometer setup diagram.

Thermalized positron annihilates either on a core electron or on a valence electron of an

atom of studied material. In majority of cases two photons are produced with energies from at about 500 to 520 keV. These photons are moving in anti-parallel directions.

The discrepancy in photon energies is caused by a non-zero momentum of center of mass of center positron-electron pair. When center of mass has zero momentum, photons have equal energy of 511 keV.

.6.1 High purity Germanium detectors

The conventional coaxial high-purity germanium (HPGe) detectors manufactured by the Mirion Technologies are used for detection of the gamma-radiation at BGSU. The detector is made of a cylinder-shaped piece of germanium with impurity level of about 10^{10} atoms/cc. The outer n-type diffused lithium contact is 0.5 mm thick. The p-type contact on the inner surface of an axial well is about 0.3 μm thick (see Fig. 37). The semiconductor is covered with a protective polished metal case.

Photon interaction within the active volume of the detector produces charge carriers which are swept by the electric field towards their collecting electrodes. A charge sensitive preamplifier converts this charge into a voltage pulse proportional to the energy deposited in the detector.

The Canberra Coaxial Ge detector can be shipped and stored without cooling. Like all germanium detectors, however, it must be cooled when operated to avoid excessive thermally generated leakage current. Cooling is performed with liquid nitrogen stored in the 8-liter Dewar flask that is directly connected to the germanium detector. Dewar flasks must be filled every four days.

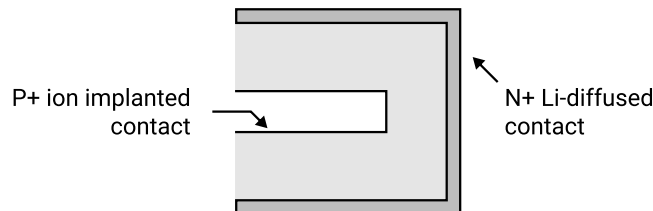


Fig. 37 Cross section of a coaxial Ge detector.

The relatively high energy resolution of the HPGe detectors is a feature that overshadows them from detectors of other type – BaF₂ or YAG. The energy resolution of the HPGe detectors was estimated to be 1.2 keV for Detector 1 and 1.4 keV for Detector 2 (see Fig. 3.13).

Unlike lithium-drifted detectors, high-purity germanium detectors may be cycled repeatedly between liquid nitrogen and room temperatures with no compromise in performance.

The lithium diffused outer contact will increase in thickness if the detector is kept warm for extended periods of time – months or years. This will affect the efficiency of the detector, particularly at low energies.

.6.2 Lynx Multichannel Analyzers

Lynx Multichannel Analyzers (MCA) produced by Canberra are one of the most advanced and promising digital-type analyzers on the market. The maximum supported number of analyzer bins is 32678.

Each analyzer is equipped with two built-in power supplies. Low-energy power supply generates voltage within the range of -200 to +200 V. High-energy power supply outputs range from 200 to 5000 V both positive and negative polarity.

Connection to computer can be established via different interfaces. Namely, 10/100 Mbps ethernet connection, universal Serial Bus (USB) and Serial Port (RS-232).

Lynx Analyzer supports a numerous different detectors (gamma, x-ray and alpha spectroscopy) and acquisition modes. Two acquisition modes that are important for Doppler spectroscopy are:

1. PHA (Pulse Height Analysis) is used for single-detector acquisition. Analyzer receives a signal from the detector and resolves its energy value. The count value in correspondent channel (bin) is increased. Over the time the cumulative spectrum of counts builds-up.
2. TLIST (Time-Stamped List Mode) is used for acquisition of the two-dimensional energy spectrum. Each event (photon, registered by detector) is stored in the analyzer's

memory as a pair of values – energy and timestamp. Series of these events are saved to a file every second. The Lynx’s timing resolution – accuracy of resolving the timestamp moment - tops at 100 ns.

.6.3 Observing the coincidence count rate

It is possible to monitor the coincidence count of the Lynx analyzers during the two-detector experiment. SCA outputs from the Lynx analyzers are connected to the ORTEC 414A Fast Coincidence unit (see Fig. 36). Coincidence window of the 414A is set to the maximum possible value of 110ns. The output from the 414A unit is connected to the signal counter that displays number of coincidence events in the real time.

.7 Geometry of the experiment

For the single detector experiment it is recommended to position the radioactive sample in front of the face of the detector. Two-detector experiment geometry must meet following criteria: detectors are aligned along the same line facing each other; sample is positioned in the middle of the imaginary line connecting centers of the front detector faces (see Fig. 36).

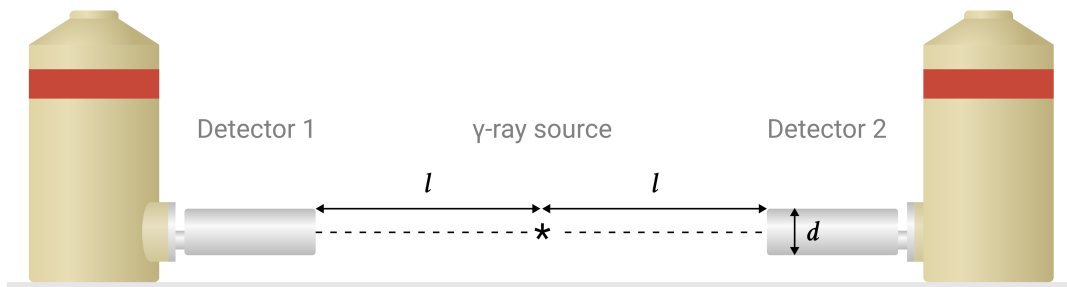


Fig. 38 Coincidence Doppler spectrometer setup diagram.

An important parameter is the distance between every detector and the radioactive sample. This distance has to be selected depending on following parameters: type of the experiment (single or two-detector), diameter of the HPGe detectors used, and the activity of the sample. Use following criteria to select the correct distance between sample and the detector:

- Keep the detectors' dead time value under 10% to prevent pile-up. When analyzer registers two or more annihilation photons within its time resolution interval, it sums their energy value. This effect is named pile-up and it leads to collection of false experimental data. It is known that HPGe detectors have a relatively poor timing resolution compared to BaF₂ scintillation detectors. Their timing resolution is 20 μ s. To prevent the pile-up of the signals it is recommended keep the detectors' count rate low – at around $5 \cdot 10^3$ cps (it corresponds to $\approx 10\%$ dead time). Increased count rates negatively affect the energy resolution. The pile-up events can be observed on the oscilloscope connected to the MON OUT output of the Lynx analyzer and should be avoided.
- For the two-detector Doppler experiment the distance between the detectors $2l$ has to be notably larger than the detector diameter: $2l > d$ (see 38). The equations of energy and momentum conservation for the two-detector Doppler experiment (put reference) rely on a fact that the annihilation photons are moving in anti-parallel directions and their full energy is registered. Realistically photons can scatter and loose energy outside of the active volume of the detector. When setting up the detectors in order for the majority of the registered photons to correspond to the above theoretical approximation the distance between the detectors has to be notably larger than their diameter.
- It is unfavorable to set the source relatively far $2l \gg d$ apart from the detector. In this case the count rate will be too small.

Usually a positron source with activity of about 10-30 μ Ci is used in Doppler experiments. Having the diameter of detectors 3 inches the experiments are carried out with the distance between the detectors set to about 20 inches (see 39).

A holder with the rod that pinpoints the center of the detectors' face is used to precisely position the sample. A combination of a two bubble levels and a floor jack under the table is used to horizontally align the detectors in space (see 39).

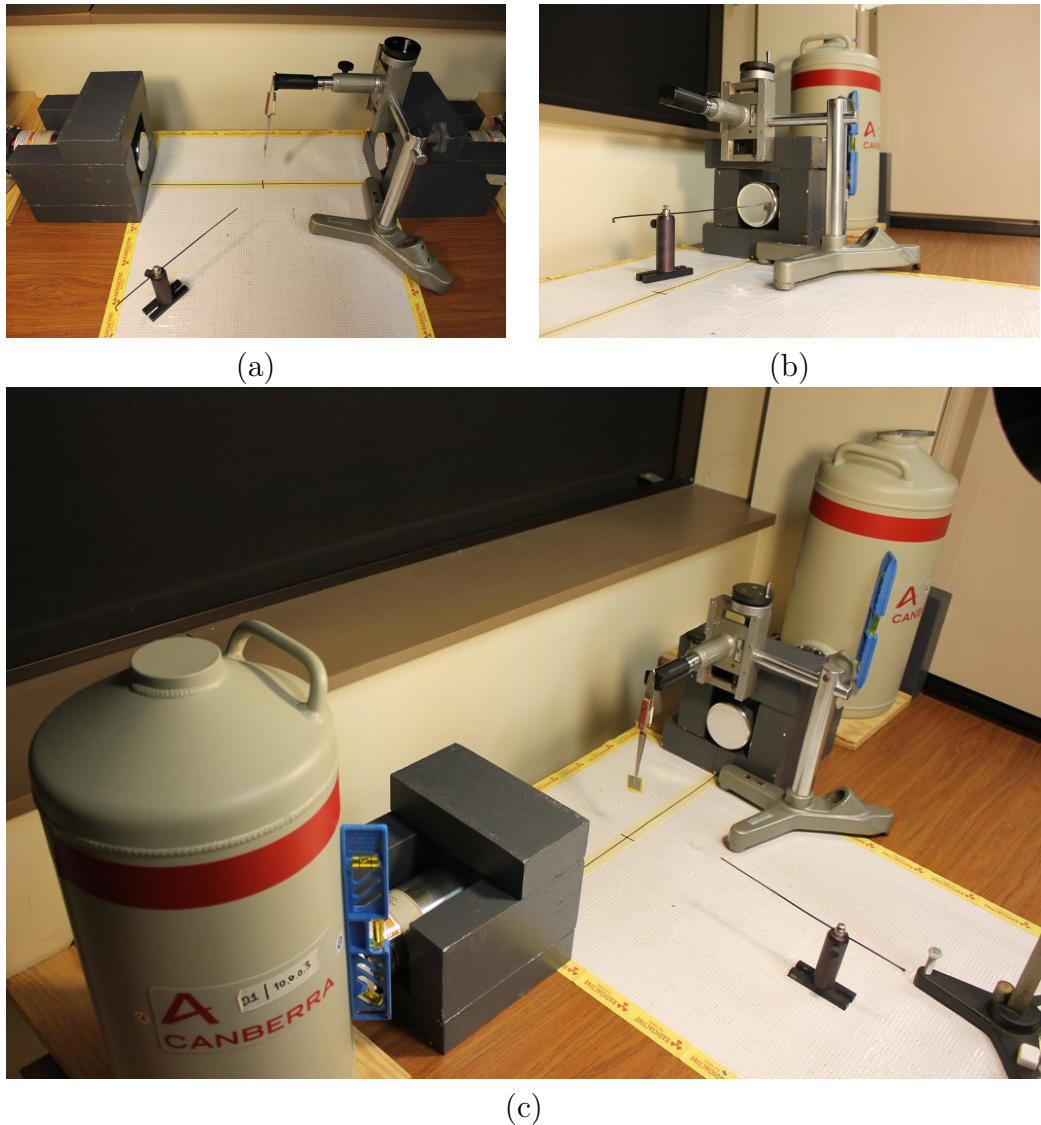


Fig. 39 Doppler spectrometer setup at Farida Selim lab at BGSU. (a, b) positioning the sample with respect to the detectors' orientation with the help of the pointer; (c) two-detector experiment setup; correct horizontal alignment of the detectors is asserted with the help of bubble levels

.8 Initial configuration

For fast local or remote connections, the 10/100 Base-TX Ethernet connection of the Lynx analyzers through the RJ-45 port is optimum.

In current research a dedicated network adapter was installed on the computer that collects data. This allows connecting the analyzers to the computer along with having an internet access. The computer and both Lynx analyzers were connected into a separate local area network (LAN) through a network switch. Dynamic Host Configuration Protocol (DHCP) was disabled over the local area network. Following static Internet Protocol (IP) v4 addresses were assigned to the devices on the network. Computer address set to 10.0.0.1; Lynx analyzers connected to the switch were assigned with 10.0.0.3 and 10.0.0.4 addresses.

After setting up the Ethernet connection of the Doppler spectrometer's hardware components it is important to perform the initial configuration of Lynx analyzers. Refer to the Lynx User's manual (can be requested on official website [116]) and perform following actions for each analyzer.

1. Update the Firmware to the most recent version. Depending on the version of the pre-installed firmware it might take two or more subsequent firmware updates for every unit.
2. Set up the administrator password.
3. Set unique Ethernet IP address for Lynx unit.
4. Synchronize each device's system time with the system time on the computer.

.8.1 Setting up the device Friendly Names

By default every Lynx analyzer has a default hardware name "Lynx". In order to be able to reconstruct the two-dimensional spectrum with the Data Scanner application the Lynx analyzers need to have different hardware identifiers (or Friendly Names).

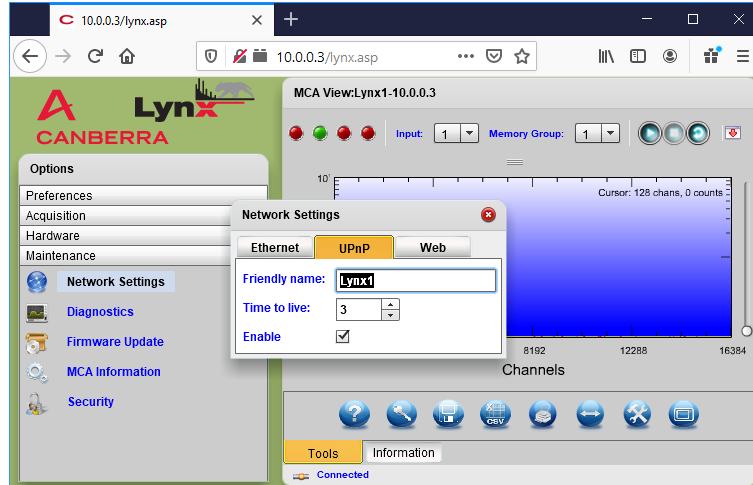


Fig. 40 Assigning a unique Friendly Name for the Lynx analyzer.

In the Lynx web interface navigate to the “Maintenance” section and open the “Network Settings” dialog. On the “UPnP” tab input a unique “Friendly name” for the analyzer (see Fig. 40).

Configure every analyzer to have a unique Friendly name. For instance, we assigned “Lynx1” and “Lynx2” friendly names to the Lynx analyzers.

.8.2 Getting started with the ProSpect software

Lynx analyzers support different types of communication interfaces. It is possible connect to the analyzers and run spectrum acquisition in PHA mode through the web browser via Adobe Flash and HTML5 web interfaces. Nevertheless the two-dimensional energy spectrum acquisition is only possible if the connection is established via the ProSpect program. Therefore, ProSpect application is the most suitable for positron Doppler spectroscopy.

Upon the first start the ProSpect application will require to enter the user license. Software license file along with the license information is located in “SelimLab” team BGSU SharePoint site folder: /LabDocuments/ProSpect License. **TODO: move to sharepoint.**

Connection to the analyzers can be established in ProSpect application in the “Connect to Device” modal dialog under the “Tools” tab. Enter the corresponding detector’s IP address and check the “Take Over” checkbox before clicking the “Connect” button (see Fig. 41).

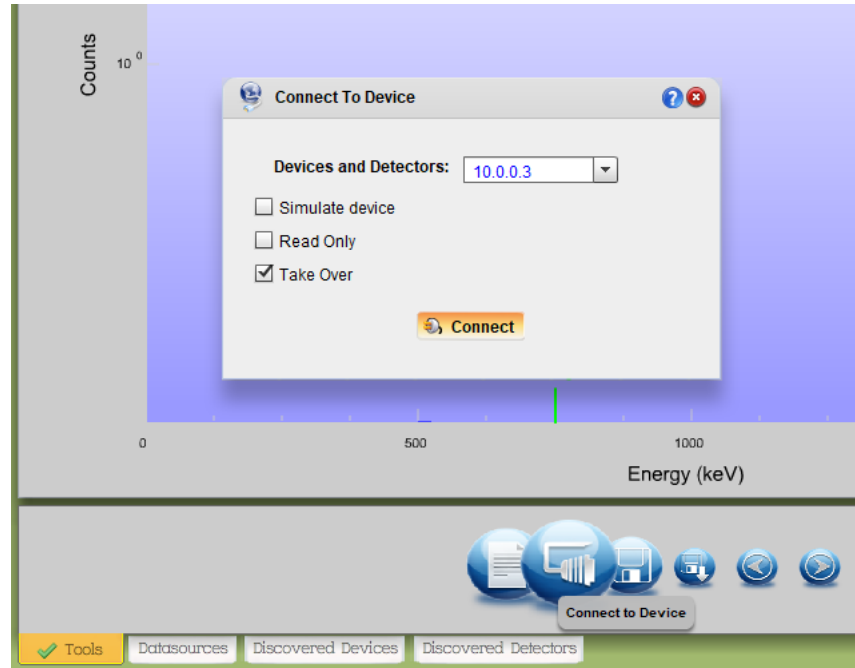


Fig. 41 Connecting to Lynx Analyzers in ProSpect application.

After successful connection both analyzers will be reflected under the “Datasources” tab. Double-clicking on the analyzer preview window under the “Datasources” tab will bring up correspondent analyzer settings in the user interface.

.8.3 Clearing the analyzer error status

Occasionally ProSpect application will display an error status of one or both analyzers. It is reflected by the orange color in the “Datasources” tab. In order to clear the error on a certain detector do following: select the detector by double-clicking on its preview in the “Datasources” tab. Double-click the yellow light circle on the top left while holding the SHIFT key. Confirm clearing the detector fault by clicking on “Yes” in the modal dialog (see Fig. 42).

.8.4 Ramping the voltage

The voltage on the detector preamplifiers needs to be ramped to the operational value of 4400 V.

In ProSpect application find the voltage settings under the “Detector” tab in the “High

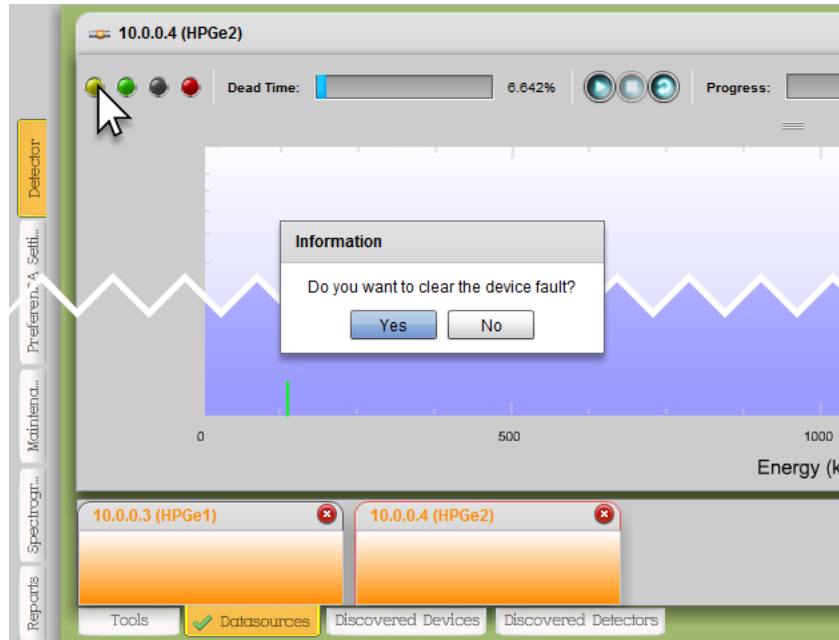


Fig. 42 Clearing the device fault in the ProSpect application.

Voltage Settings". Click the pencil icon to bring up the "High Voltage Power Supply" settings. According to the manufacturer recommendation the "Reading voltage" field should read 4400 V (add reference). Set the "Voltage" value in the modal dialog to a value that corresponds to a "Reading voltage" value of 4400 ± 1 V, Fig. 43.

.8.5 Timing signal shape adjustment

Before the acquisition is started it is important to make sure the shape of the timing signal from the preamplifier is correct. In order to do that proceed with the automatic pole-zero adjustment:

- In the "MCA Settings" tab on the left vertical tab bar click the pencil icon in the 'Filter Settings" palette.
- In the "Digital Filer" modal dialog go to "Miscellaneous" tab. Click "Start" button to the right of "Auto Pole Zero" label.

The shape of the preamplifier signals can be observed on the oscilloscope connected to the MON OUT outputs of the Lynx analyzers.

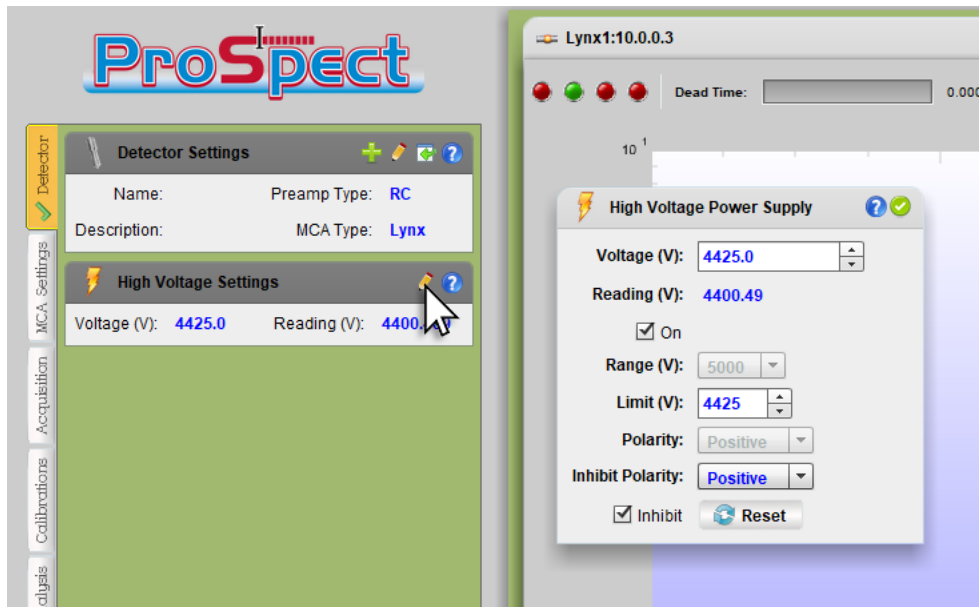


Fig. 43 Ramping voltage on the preamplifiers.

.8.6 Analyzer calibration

It is necessary to calibrate Lynx analyzers before acquiring the energy spectra. Reference radioactive samples emitting photons of a known energy values are used to calibrate each analyzer energy axis.

A list of radioactive isotopes with their reference energies values used to calibrate the spectrometer is given in the Table 5.

Table 5 List of radioactive isotopes and their photon energies used for calibration.

Isotope	Barium-133	Cobalt-60	Sodium-22	Cesium-137
Energies, keV	80.997	1173.228	511	661.657
	160.612	1332.492	1274.537	
	383.849			
	437.012			

Activities of every isotope used to acquire the calibration spectrum were estimated to be less than $0.1 \mu\text{Ci}$.

For accurate measurements the recommended value of the detectors' Dead Time should

not exceed 10%. During the acquisition of the calibration spectra the reference radioactive samples were positioned on a certain distance from the detectors. Detectors' dead time values were 6.39% and 6.15% respectively. Acquisition was running for 18 hours. Analyzers collected data individually in Peak Height Analysis (PHA) mode. Discriminator threshold levels were turned off.

ProSpect application has a built-in interface that performs the calibration. Calibration procedure is straightforward. User marks the regions of interest (ROI) on the spectrum and enters the expected energy value for the peak center (see Fig. 44).

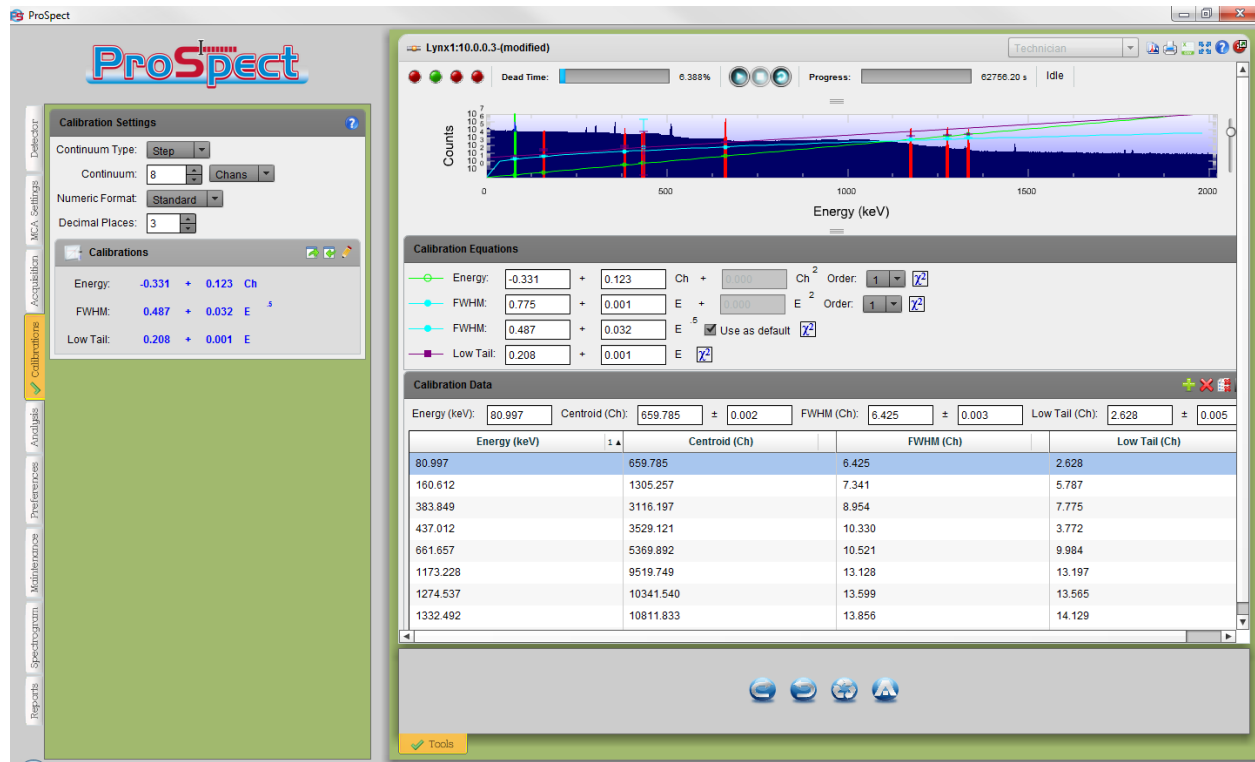


Fig. 44 Screenshot of the ProSpect calibration interface displaying spectrum and calibration points.

It is important to note that the 511 keV energy peak from Na-22 was not included in the calibration process, because it is inevitably broadened because annihilation occurs with atomic/molecular electrons, which contribute with their own momentum, which is transferred to annihilation photons. Position of the annihilation peak is slightly shifted from 511 keV to lower energies due to non-zero value of the binding energy of the electron that annihilates

with the positron.

Alternately it is possible to calibrate the analyzers without reference samples (see Sect. 3.6). A background spectrum with sufficient statistics can be used to calibrate the Lynx units. The downside of this approach is that the background spectrum acquisition takes considerably more amount of time.

.9 Setting discriminator levels

After the calibration is complete, we proceed with setting up analyzers' discriminator upper and lower levels. In Doppler positron spectroscopy the region of interest on the energy spectrum is the annihilation peak with the maximum at around 511 keV. In order to limit the amount of data to be processed by the computer we set the lower and upper discriminator levels for each analyzer.

The lower discriminator level must be in between of the Compton edge and the annihilation peak. Upper discriminator level is selected to be symmetrical to the lower level with respect to the photopeak. In ProSpect discriminator levels are specified in percents. In our case we set both analyzers' lower discriminator levels to 22% and upper discriminator levels to 30%.

After setting the discriminator values it is important to acquire individual energy spectra from every analyzer in PHA mode.

Photopeak energy spectra need to be saved to the hard drive and analyzed. Following histogram binning properties need to be obtained during the spectra analysis: histogram lower bin minimum energy, histogram upper bin maximum energy, and number of bins.

In our case for the conversion gain of 16384 bins, calibrated analyzers with discriminator window of 22% to 30% provided binning properties depicted in Table 6.

We will use of the above binning parameters during the acquisition of the two-dimensional Doppler energy spectrum in TLIST Data Scanner Application.

Table 6 Binning properties of analyzers to be used in TLIST Data Scanner application.

Analyzer	Histogram lower bin left edge	Histogram upper bin right edge	Number of bins
Lynx1 10.0.0.3	444.021099	605.637433	1311
Lynx2 10.0.0.4	435.6434437	594.1126407	1311

.10 Two-dimensional energy spectrum acquisition

Lynx analyzers have a special mode (TLIST) when they register events sharing using a single system clock. The analyzer that shares its system clock is named Master. The analyzer that takes advantage of the shared clock is named Slave.

During the acquisition both devices independently save pairs of registered timestamped events to the hard drive. Another software that is executed in parallel (TLIST Data Scanner) reads information with registered events from the hard drive. Due to the fact that analyzers share one system clock, Data Scanner can match energy events that were registered at a same moment of time and reconstruct two-dimensional energy spectrum.

For every analyzer ProSpect application creates a new file containing registered pairs of energy and time events every several seconds. In order to obtain the two-dimensional energy spectrum with reasonable statistics the acquisition should run for a minimum of about a day. This leads to millions? of generated files. Total amount of data can be over 500GB? How many per second?. Apparently it is important to keep these files on a separate physical drive.

.10.1 Hard drive requirements for spectrum acquisition

Having two programs communicating with the hard drive at the same time (ProSpect and TLIST Data Scanner) might result in a significant load on the hard drive. The amount of data being read and written on the hard drive depends on following factors:

1. Binning value (conversion gain) of analyzers. We use 16386 bins.

2. Count rate on each analyzer. We usually keep the detectors at a low count rate at about 5 kcps.
3. Upper and lower discriminator values on each analyzer. We use range of 22% to 30% to register only annihilation events from the photopeak.

Currently in our research lab we are using an external hard disk drive with NTFS file system connected via the USB3 interface. Tests in CrystalDiskMark application show the maximum possible of 90 Mb/s write speeds and 108 Mb/s read speeds. During the acquisition it is important to monitor the read and write hard drive speeds and make sure they do not exceed the maximum hard drive speeds.

In order to avoid the problems with the physical hard drive and its bus interface limiting the spectra processing speeds we highly recommend using their quickest possible combination. A great solution in 2020 is an internal SATA3 SSD or NVMe SSD hard drive.

For the better performance we recommend to disable the Windows 10 file indexing feature on the hard drive that stores timestamped spectra.

.10.2 Setting up the Prospect with separate physical drive

Due to a heavy load on the hard drive during the experiment It is a good idea to export the TLIST data on a separate physical drive. This way the system disk will be isolated from constant read and write operations. Unfortunately the ProSpect application does not have a functionality to specify the output location for the TLIST spectra. By default, ProSpect always saves spectra to the folder “./ProSpect/data” located in the “Documents” folder of the current user’s home folder. It is reasonable to use a following workaround. Remove ProSpect’s “data” folder and set up a symbolic link named “data” in the same location that will redirect to a different physical drive. In order to set up a symbolic link to a directory enter following command in the windows Command Prompt:

```
mklink /D C:\Users\your_user\Documents\ProSpect\data F:\data
```

Here second parameter is the path to the ProSpect’s “data” folder. Third parameter is the redirected location of the “data” folder on another physical drive.

Sometimes it is necessary to ensure that the symbolic link already exists. In order to do so list all the symbolic links in a specific directory with a command:

```
dir /AL /S C:\Users\your_user\Documents\ProSpect
```

Third parameter is the location of your ProSpect “data” folder. The output of the above command will show if the symbolic link exists.

.10.3 Acquisition in TLIST mode

Two software programs are used to obtain the two-dimensional Doppler energy spectrum. ProSpect application saves individual timestamped events from every analyzer to a hard drive. TLIST Data Scanner reads these spectra on the fly and determines pairs of energy events from every analyzer that happened within the same resolving time interval.

In order to run the spectrum acquisition in TLIST mode following actions need to be taken:

1. Set the proper geometry of the experiment. Ensure the correct alignment of the detectors with respect to each other. Properly position the sample.
2. Connect SYNC outputs of the Lynx analyzers with a BNC cable with the 50 Ohm terminators on each end.
3. Launch ProSpect application and establish connections with the analyzers. Make sure every analyzer has a unique Friendly name.
4. Ramp the voltage on every analyzer to a reading value of 4400 V.
5. For each analyzer navigate to MCA Settings and bring up the “External Synchronization” modal dialog. Ensure that synchronization “Status” is set to “Enabled” and “Mode” set to “Slave” for every analyzer.

6. Ensure that analyzers do not have error status. Reset error status if needed.
7. Format the drive where TLIST spectra are saved. Turn off the indexing on the drive. Create “data” and “scanned” folders in the drive’s root folder.
8. Launch TLIST Data Scanner program. Add “data” folder as a working directory. Enable option to move files after scan to the “scanned” folder. Click ‘Start All Scans’ button.
9. In the ProSpect program start simultaneous acquisition. Hold keyboard CTRL key and click “Start Acquisition”. Change the External Synchronization Mode of second analyzer from to “Master B” within 20 seconds. At this point ProSpect App starts exporting timestamped spectra to “data” folder.
10. In the Data Scanner App open “Scan Results” tab. Locate two entries in the table that correspond to the TLIST data from analyzers 45. Enter binning properties obtained on the calibration step (in Table 6), namely “Energy Low”, “Energy High” values and number of bins (# BINs). Set “Time BINs” value in the menu bar to 300.
11. Open “Analysis” tab in Data Scanner. Specify device friendly names, acquisition start times and set “Energy (keV)” as axis units. Press ‘Graph’ button.
12. After desired statistics is accumulated save the two-dimensional spectrum by clicking “Export Data” button.

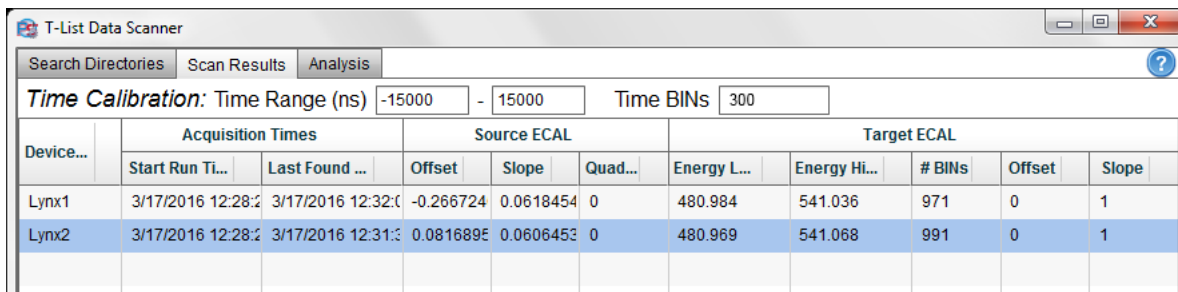


Fig. 45 Specifying axis binning for two-dimensional energy spectrum.